



Advanced Manufacture by Screen Printing

Sarah-Jane Potts

Thesis Submitted to Swansea University in fulfilment of
the requirements for the Degree of Engineering
Doctorate

College of Engineering, Swansea University

2020


Abstract

Screen-printing is the most widely used process in printed electronics, due to its ability to transfer materials with a wide range of functional properties at high thickness and solid loading. However, the science of screen printing is still rooted in the graphics era, with limited understanding of the fundamental science behind the ink transfer process. A multifaceted approach encompassing all aspects of the production of printed electronics from ink formulation, through screen-printing and post processing was therefore undertaken. With a focus on carbon inks due to their electrical conductivity, low cost, inertness and ability to be modified or functionalised. Parametric studies found that with blade squeegees, lower angles and softer blades led to increases in ink deposition, irrespective of ink rheology. However, the effects of print speed and snap distance were related to the rheology of the inks. Existing computational models were inaccurate and based on two contrasting theories. Extensional CaBER testing provided qualitative indications of the effect of separation speed and distance on deposition. However, this could only assess the effect of vertical, 2-dimensional forces and could not evaluate the influence of shear forces due to separation angle or the effects of the screen mesh. For this purpose, a screen-printing visualisation rig was specifically constructed, allowing the ink transfer mechanism to be captured for the first time. This identified similarities with one of the two theories, although existing models had oversimplified the process and did not account for variations in lengths of the separation regions or the contact angle between the mesh and substrate. It was also found that changes in the ink rheology and parameter settings changes the lengths of these regions, as well as the shape and presence of filaments formed during separation. The parameters of print speed, snap distance, solid loading and ink rheology were assessed and found to affect the mesh/substrate contact time and filamentation behaviour. This had a quantifiable effect on ink deposition, in terms of the amount of ink transfer, roughness and therefore conductivity. Finally, photonic annealing and subsequent compression rolling were found to enhance the conductivity of carbon inks by removing binder between particles and consolidating the ink film, leading to 8 times reduction in resistivity for a graphite-based ink and halving in resistivity for an ink

containing a combination of carbon black and graphite, where there was less potential for improvement due to the conductive bridges between the graphite flakes.

DECLARATION

This work has not previously been accepted in substance for any degree and is not being concurrently submitted in candidature for any degree.

Signed  (candidate)

Date 10/06/2020

STATEMENT 1

This thesis is the result of my own investigations, except where otherwise stated. Where correction services have been used, the extent and nature of the correction is clearly marked in a footnote(s).

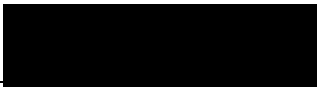
Other sources are acknowledged by footnotes giving explicit references. A bibliography is appended.

Signed  (candidate)

Date 10/06/2020

STATEMENT 2

I hereby give consent for my thesis, if accepted, to be available for photocopying and for inter-library loans after expiry of a bar on access approved by the Swansea University.

Signed  (candidate)

Date 10/06/2020

Acknowledgements

I would firstly like to acknowledge, with thanks, the Materials and Manufacture Academy (M2A), Engineering and Physical Sciences Research Council (EPSRC), European Social Fund, Coated² and my industrial sponsors, icm Print. I would also like to acknowledge the Welsh Centre for Printing and Coating for use of equipment, Swansea University AIM facility (EP/M028267/1, ERDF 80708 and Ser Solar) for access to their SEMs, Specific for access to a range of their laboratories and facilities as well as the Swansea University Materials Advanced Characterisation Centre (MACH1) for use of their compression roller.

I would like to thank Prof. Tim Claypole for providing me with this opportunity and for supervising my project. I would also like to thank Dr Chris Phillips for supervising me and providing me with support, guidance and encouragement when I needed it most. I would also like to thank all of the other staff and students in the Welsh Centre for Printing and Coating who have helped and guided me throughout this project, especially Yin Cheung Lau and Dr Ben Clifford. I would also like to thank Dr Eifion Jewell for his guidance, support and many chats about screen printing. I would also like to thank all of the M2A team for all of their help and support during this project.

I would especially like to thank, with love, my long-suffering partner Dr Thomas Dunlop. Without his continuous support, advice and kindness, this journey would have been a lot harder and a lot less enjoyable. I would also like to thank, with love, my family and friends whose love, friendship, kindness support and willingness to put up with me moaning has made my journey a lot more enjoyable. I would especially like to thank, with love, my Mum, Jane Stevens, who has stood by me through the thick and thin and without whose support, I would not be half the person I am today. I would also like to thank, with love, my Grandad Eric and Great Aunt Joan, as well as my sister Jenny and the rest of my family.

I would like to also give thanks and dedicate this thesis to my Secondary School Maths teacher, Mr Simon Meredith. Without whose kindness, patience and inspirational way of teaching, I would never have been able to accel at maths to the

extent where Engineering became an option for me. I will always be grateful for you making one of my hardest subjects both fun and possible for me.

I would like to thank Alex Holder and Tatyana Korochkina and the others who contributed to the P2CAR2 (Printing Process Control by Advanced Rheology 2) project, which was conducted as a project for the EPSRC Centre for Innovative Manufacture in Large-Area Electronics (CIMLAE). Part of this thesis conducts work which continues on from the findings of this investigation and presents the rheological analyses conducted by Alex holder and the ink making, printing, print topography and electrical characterisation results conducted by Tatyana Korochkina as a comparison with the work produced.

I would also like to thank my examiners, as their feedback me to improve the quality of this thesis. I would especially like to thank Prof. David Gethin for his both his feedback on this thesis and for inspiring me to get into printed electronics by showing me all of the cool projects that WCPC were working on, as well as his help and patience during my undergraduate degree.

The following people and institutions contributed to the publication of work undertaken as part of this thesis:

Paper 1: Effect of photonic flash annealing with subsequent compression rolling on the topography, microstructure and electrical performance of carbon-based inks. Published in Journal of Materials Science: June 2019, Volume 54, Issue 11, pp 8163–8176. DOI: 10.1007/s10853-019-03462-3

Located in Chapter 6

Candidate	Miss Sarah-Jane Potts, Swansea University
Author 1	Mr Yin Cheung Lau, Swansea University
Author 2	Dr Thomas Dunlop, Swansea University
Author 3	Prof. Tim Claypole, Swansea University
Author 4	Dr Chris Philips, Swansea University

Author details and their roles:

Candidate contributed: The main body of work including printing, topography analyses, electrical analyses, SEM and writing of the paper.

Author 1 contributed: The photonic annealing and assistance with the process description and analysis of the effects of photonic annealing.

Author 2 contributed: TGA analyses of the inks and resins, analysing the data and assisted with writing analyses of the results.

Author 3 contributed: Assisted with designs of experiments and editing the paper.

Author 4 contributed: Editing the paper.

Signed Candidate _____

Author 1 _____

Author 2 _____

Author 3 _____

Author 4 _____

Paper 2: High-Speed Imaging the Effect of Snap-Off Distance and Squeegee Speed on the Ink Transfer Mechanism of Screen-Printed Carbon Pastes. *J Coatings Technol Res.* 2019;1–13.

Located in Chapter 4

Candidate	Miss Sarah-Jane Potts, Swansea University
Author 1	Dr Chris Philips, Swansea University
Author 2	Dr Eifion Jewell, Swansea University
Author 3	Dr Ben Clifford, Swansea University
Author 4	Mr Yin Cheung Lau, Swansea University

Author 5	Prof. Tim Claypole, Swansea University
-----------------	--

Candidate contributed: Design and creation of the rig, conducted experiments on the rig, conducted rheological analyses of the inks, conducted topography analyses and electrical characterisation of the prints and analysed the data, conducted the comparison study on the DEK 248 and analysed the prints. Analysed and processed the data, then wrote the paper.

Author 2 Contributed: Assistance with the jig design and editing the paper

Author 3 contributed: Assistance with design of experiments and editing of the paper

Author 4 contributed: Assistance with the concept, design and creation of the jig.

Author 5 contributed: Assistance with the concept and design of the jig, designed the mesh design being assessed, helped edit the paper.

Author 6 contributed: Editing the paper.

Signed Candidate _____

Author 1 _____

Author 2 _____

Author 3 _____

Author 4 _____

Author 5 _____

Contents

Abstract	i
Acknowledgements	iv
Contents.....	viii
List of Figures	xiii
List of Tables.....	xxi
List of Equations	xxii
List of Abbreviations.....	xxiii
Chapter 1. Introduction	1
1.1. Aims and Objectives.....	1
1.2. Introduction to Screen-Printing	2
1.2.1. History of Screen-Printing	2
1.2.2. Flatbed Screen-Printing.....	3
1.2.3. Flatbed Screen-Printing Components	4
1.3. Chapter closure	9
Chapter 2. Literature Review	11
2.1. Introduction	11
2.2. Effect of Screen-Printing Parameters	11
2.2.1. Mesh Tension and Size	12
2.2.2. Squeegee Effects	13
2.2.3. Snap Distance.....	16
2.2.4. Squeegee Speed.....	17
2.3. Screen-Printing Inks	18
2.3.1. Rheological profile of screen inks.....	19
2.3.2. Functional Materials Used in Screen Printing Inks.....	19
2.3.3. Carbon-Based Screen-Printing Inks	21
2.4. Screen-Printing Models	24
2.4.1. Ink Flow Ahead of the Squeegee	24
2.4.2. Ink Flow Behind the Squeegee	26
2.5. Drying and Post Processing.....	30
2.5.1. Drying Techniques	30

2.5.2.	Post Processing.....	30
2.6.	Chapter Closure	31
2.6.1.	Effect of parameters on a graphite-based ink.....	32
2.6.2.	High speed imaging the ink transfer mechanism of screen-printed carbon pastes	33
2.6.3.	The effect of ink composition on ink transfer mechanisms	33
2.6.4.	Effect of photonic flash-annealing with subsequent compression rolling on the performance of carbon-based inks	34
Chapter 3.	Materials and Methods	35
3.1.	Screen-Printing	35
3.1.1.	Dek 248	35
3.1.2.	Svecia Matic.....	35
3.2.	Screen Printing inks.....	36
3.2.1.	Ink Making	36
3.2.2.	Rheological analyses of inks	38
3.3.	Drying and Post Processing.....	50
3.3.2.	Drying and Curing.....	50
3.3.3.	Compression Rolling.....	51
3.4.	Thermal Analyses	52
3.4.1.	Thermo-Gravimetric and Simultaneous Thermal Analysis	52
3.5.	Surface Characterisation.....	52
3.5.1.	White Light Interferometry	52
3.5.2.	Focus Variation Microscopy	57
3.5.3.	Scanning Electron Microscopy (SEM)	58
3.6.	Electrical Characterisation.....	60
3.6.1.	Sheet Resistance and Resistivity	61
3.6.2.	Line Resistance	62
3.7.	Chapter Closure	62
Chapter 4.	Effect of screen-printing parameters on a Graphite-Based Ink.....	64
4.1.	Introduction	64
4.2.	Materials and Methods	65
4.2.1.	Ink preparation	65
4.2.2.	Rheological Assessment.....	67
4.2.3.	Printing.....	67
4.2.4.	Topography Analyses.....	70

4.2.5.	Electrical Characterisation	70
4.3.	Results	71
4.3.1.	Rheological Analyses	71
4.3.2.	Effect of Mixing and Milling on Print Performance	73
4.3.3.	DEK 248 Parameter Study	78
4.3.4.	Svecia Parameter Study	81
4.4.	Discussions	101
4.5.	Conclusions	103
Chapter 5.	High speed imaging the ink transfer mechanism of screen-printed carbon pastes	106
5.1.	Introduction	106
5.2.	Materials and Methods	108
5.2.1.	Rheological and extensional testing	108
5.2.2.	Screen-printing visualisation method	109
5.2.3.	Comparison Screen Printing	110
5.2.4.	Printed line topography	112
5.2.5.	Electrical characterisation	113
5.3.	Results	114
5.3.1.	Rheological Analyses	114
5.3.2.	Print Topography of different line widths	118
5.3.3.	Classification of flow regions during screen-printing	120
5.3.4.	Effect of line width on deposition mechanism	122
5.3.5.	Discussion of effects of line widths	126
5.3.6.	Effect of snap distance and squeegee speed on the length of ink separation stages	127
5.3.7.	Assessment of snap off distance and squeegee speed on filamentation behaviour	129
5.3.8.	Effect of snap distance and squeegee speed on print topography	132
5.3.9.	Effect of snap distance and squeegee speed on electrical performance	133
5.3.10.	Full scale Press Comparison for the effects of snap off distance and print speed	134
5.3.11.	Discussion of the effects of snap off distance and print speed	139
5.4.	Discussion	142
5.5.	Conclusions	145
Chapter 6.	The effect of ink composition on ink transfer mechanisms	147

6.1.	Introduction	147
6.2.	Materials and Methods	149
6.2.1.	Inks	149
6.2.2.	Rheological and extensional testing.....	150
6.2.3.	Screen-printing visualisation method.....	151
6.2.4.	Printing on a commercial press	151
6.2.5.	Printed line topography	151
6.2.6.	Electrical characterisation	152
6.3.	Results	152
6.3.1.	Rheological analyses	152
6.3.2.	Print contact regions.....	162
6.3.3.	Print Characterisation.....	167
6.3.4.	Commercial Press Comparison	172
6.4.	Discussions	181
6.5.	Conclusions	185
Chapter 7.	Effect of photonic flash-annealing with subsequent compression rolling on the performance of carbon-based inks	187
7.1.	Introduction	187
7.2.	Materials and Methods	189
7.2.1.	Ink formulation.....	189
7.2.2.	Printing Methodology	190
7.2.3.	Print characterisation before and after processing	191
7.2.4.	Post Processing – photonic annealing and compression	192
7.2.5.	Thermogravimetric analysis of ink and binder	193
7.3.	Results	193
7.3.1.	Topography and microstructure of printed solid squares.....	193
7.3.2.	Sheet Resistance of printed squares	198
7.3.3.	Printed Lines	201
7.3.4.	TGA analysis of ink and binders.....	202
7.4.	Discussions	203
7.5.	Conclusions	205
Chapter 8.	Conclusions and Future Work.....	206
8.1.	Introduction	206
8.2.	Conclusions	206
8.3.	Future Work.....	212

I.	Appendix I Quantifying and controlling variables on Svecia Matic.....	A
	Controlling squeegee pressure	A
	Quantifying print speed.....	B
II.	Appendix II Development of Screen-Printing Visualisation Rig	F
	Prototype 1	F
	Prototype 2	G
	Motorised Screen-Printing Visualisation Rig	K
	References	N

List of Figures

Figure 1.1 Schematic of Flatbed Screen Printing.....	4
Figure 1.2 Diagram of mesh geometry consisting of mesh width (w), mesh thickness (D), nominal thread diameter (d) and pitch (p). With an emulsion-based stencil with labelled emulsion over mesh (EOM), stencil thickness and maximum printable ink film thickness.	6
Figure 1.3 Blade and diamond geometry squeegee geometries.....	9
Figure 2.1 Effect of squeegee material, pressure and angle on the deflection of single durometer blade squeegees	16
Figure 2.2 Illustration of Cling Zone.	17
Figure 2.3 Graphite atomic structure	22
Figure 2.4 Percolation of electrically conductive particles in a paste.....	24
Figure 2.5 Riemer and Messerschmitt’s theories of ink flow and separation behind the squeegee.	29
Figure 2.6 Cause and effect diagram of thesis components for improving the print performance of carbon-based screen-printing inks.....	32
Figure 3.1 Schematic diagram of three-roll miller.....	38
Figure 3.2 Diagram to show the different regions that the Cross model, Power-law model and Sisko model cover (97).....	40
Figure 3.3 Viscoelastic response of material with time lag between shear stress and strain.....	42
Figure 3.4 Shear rheometers plate and plate (left) and cone and plate (right) configurations.....	46
Figure 3.5 Filament profiles of the most commonly observed modes of capillary thinning and break up.....	50
Figure 3.6 Extensional rheology schematic diagram	50
Figure 3.7 Schematic diagram of a white light interferometer (WLI) (left) with breakdown of light beams forming intensity distribution fringes from constructive and destructive interfaces in recombining waves of light.	55
Figure 3.8 Michaelson (left diagram) and Mirau (right diagram) Interferometric Objectives used for white light interferometry	55
Figure 3.9 Analysis of average line width and height in Vision software.	56
Figure 3.10 Analysis of average print height of the edge of printed solid square in vision software.	56
Figure 3.11 Surface roughness values from Vision 64 software for print area.....	56
Figure 3.12 Schematic diagram of a Focus Variation Microscope (FVM).....	58
Figure 3.13 FVM working principle by calculating a focus value inside a windowing area.(119)	58
Figure 3.14 Schematic diagram of Scanning Electron Microscopy (SEM) (Field Emission SEM).	60
Figure 3.15 Mode of emission of Secondary Electrons in Scanning Electron Microscopy (SEM).....	60
Figure 3.16 Schematic diagram of the four-point collinear probe technique with probes evenly spaced apart (s) (left) with the probe positions on the printed square of	

length, L and width, W to find the average sheet resistance from 12 positions (right).	62
Figure 3.17 Measuring line resistance with 2-point probes	62
Figure 4.1 Changes in (a) Viscosity profiles and (b) Viscosity ramps from 1s^{-1} to 100s^{-1} for 60s then back to 1s^{-1} , then from 1s^{-1} to 200s^{-1} for 60s and back to 1s^{-1} to assess the ink recovery time with different mixing techniques (outliers removed)... 72	72
Figure 4.2 Viscoelastic profiles assessing changes in phase angle (δ), storage modulus (G') and loss modulus (G'') of the inks with different mixing techniques in the linear viscoelastic region at 1 Hz.	73
Figure 4.3 White light interferometry images of the edges of the printed squares for the printed graphite-based inks. Prepared with (a) stirring only, (b) triple roll milling followed by stirring, (c) triple roll milling followed by Speedmixing and (d) Speedmixing only. Conducted at 5 times magnification.	75
Figure 4.4 White light interferometry images of the $700\mu\text{m}$ nominal width lines for the printed graphite-based inks. Prepared with (a) stirring only, (b) triple roll milling followed by stirring, (c) triple roll milling followed by Speedmixing and (d) Speedmixing only. Conducted at 5 times magnification.	75
Figure 4.5 Average (a) film thickness and (b) line width for the different mixing techniques used on the graphite-based ink. (error bars for standard deviation, dashed lines to show nominal widths).....	76
Figure 4.6 Average (a) Surface roughness (S_a) and (b) maximum roughness (S_z) for the different mixing techniques used on the graphite-based ink. (error bars for standard deviation).	76
Figure 4.7 Average (a) Line Resistance, (b) sheet resistance and (c) sheet resistivity for the different mixing techniques used on the graphite-based ink. (error bars for standard deviation).	77
Figure 4.8 Changes in line resistance with different (a) snap off distance, (b) squeegee hardness and (c) squeegee pressure for lines produced perpendicular to the print direction.	79
Figure 4.9 Changes in line resistance of the $700\mu\text{m}$ lines with line orientation for different (a) snap off distance, (b) squeegee hardness and (c) squeegee pressure.	80
Figure 4.10 White light interferometry images of the $700\mu\text{m}$ nominal width lines for the printed graphite-based inks. At speed settings (a) 55 mm/s , (b) 880 mm/s and (c) 1600 mm/s . Conducted at 5 times magnification.....	83
Figure 4.11 Average (a) film thickness and (b) line width for different squeegee speeds (error bars for standard deviation).....	84
Figure 4.12 Average (a) Surface roughness (S_a) and (b) maximum roughness (S_z) for the different squeegee speeds (error bars for standard deviation).....	84
Figure 4.13 Average (a) Line Resistance, (b) sheet resistance and (c) sheet resistivity for the different squeegee speeds (error bars for standard deviation).	85
Figure 4.14 White light interferometry images of the $700\mu\text{m}$ nominal width lines for the printed graphite-based inks. At (a) 70, (b) 75 and (c) 80 Shore A hardness. Conducted at 5 times magnification.....	86
Figure 4.15 Average (a) film thickness and (b) line width for different squeegee hardness's (error bars for standard deviation).....	87

Figure 4.16 Average (a) Surface roughness (Sa) and (b) maximum roughness (Sz) for the different squeegee hardness's (error bars for standard deviation). 87

Figure 4.17 Average (a) Line Resistance, (b) sheet resistance and (c) sheet resistivity for the different squeegee hardness's (error bars for standard deviation). 88

Figure 4.18 White light interferometry images of the 700µm nominal width lines for the printed graphite-based inks. At (a) 70°, (b) 75° and (c) 80°. Conducted at 5 times magnification. 89

Figure 4.19 Average (a) film thickness and (b) line width for different squeegee angles (error bars for standard deviation). 89

Figure 4.20 Average (a) Surface roughness (Sa) and (b) maximum roughness (Sz) for the different squeegee angles (error bars for standard deviation). 90

Figure 4.21 Average (a) Line Resistance, (b) sheet resistance and (c) sheet resistivity for the different squeegee angles (error bars for standard deviation). 91

Figure 4.22 White light interferometry images of the 700µm nominal width lines for the printed graphite-based inks. At (a) 5mm, (b) 7.5mm and (c) 10mm. Conducted at 5 times magnification. 92

Figure 4.23 Average (a) film thickness and (b) line width for different snap off distances (error bars for standard deviation). 92

Figure 4.24 Average (a) Surface roughness (Sa) and (b) maximum roughness (Sz) for the different snap off distances (error bars for standard deviation). 93

Figure 4.25 Average (a) Line Resistance, (b) sheet resistance and (c) sheet resistivity for the different snap off distances (error bars for standard deviation). 94

Figure 4.26 White light interferometry images of the 700µm nominal width lines for the printed graphite-based inks. At (a) 70° and 70 Shore A hardness, (b) 75° and 75 Shore A hardness and (c) 80° and 80 Shore A hardness. Conducted at 5 times magnification. 96

Figure 4.27 Average (a) film thickness and (b) line width for different squeegee hardness's and angles (error bars for standard deviation). 96

Figure 4.28 Average (a) Surface roughness (Sa) and (b) maximum roughness (Sz) for the different squeegee hardness's and angles (error bars for standard deviation). 96

Figure 4.29 Average (a) Line Resistance, (b) sheet resistance and (c) sheet resistivity for the different squeegee hardness's and angles (error bars for standard deviation). 98

Figure 4.30 Changes in line resistance with line orientation for different (a) squeegee speeds, (b) squeegee hardness's, (c) squeegee angles and (d) snap off distances 100

Figure 5.1 Photograph (a) and schematic diagram (b) of the screen-printing simulation rig, showing the positioning of the high-speed camera. The zoomed in schematic diagram (c) shows a cross section through the point of contact during screen-printing as would be observed by the high-speed camera. 111

Figure 5.2 Print image design consisting of 6mm long sections reducing from 400µm to 25 µm (400 µm, 200 µm, 100 µm, 50 µm and 25 µm) in line width. 111

Figure 5.3 Viscosity profile (a) and viscoelastic profile assessing changes in phase angle (δ), storage modulus (G') and loss modulus (G'') with frequency (b) for the carbon ink assessed. 114

Figure 5.4 High speed images of separation at the point of film splitting with separation speed and separation distance. 117

Figure 5.5 Surface response of the percentage of the cross-sectional area of ink remaining on the bottom plate (a) and percentage length to separation point from the bottom plate (b) with changes in separation distance and separation speed.	117
Figure 5.6 Evolution of the minimum radius	118
Figure 5.7 Comparison of high-speed image of ink deposition with labelled microscopy image of print produced for 50 μm line.....	119
Figure 5.8 White light interferometry images of the prints conducted through the (a) the 50 μm line, (b)100 μm line, (c) 200 μm line and (d) the 400 μm line. Conducted at 5 times magnification.	120
Figure 5.9 Change in average printed film thickness and line width with increases in line width on mesh.	120
Figure 5.10 Labelled high-speed camera image of the squeegee forcing the mesh into contact with the substrate. Where the ink is deposited from the mesh to the substrate as the squeegee flows across the screen (above). With a cross sectional schematic diagram of the process (below).	122
Figure 5.11 High-speed camera images of the deposition of (a) the 50 μm line, (b)100 μm line, (c) 200 μm line and (d) the 400 μm line conducted at 5x magnification.	124
Figure 5.12 Change in contact regions with line width in relation to filament separation positions (a) and when conducted over regular time intervals (measurements conducted every 3 frames) (b).	125
Figure 5.13 Average distance between separation points for different line widths.	125
Figure 5.14 Schematic Diagram of the separation mechanisms occurring based on the results for the GEM carbon-based ink when printing a 100 μm or 200 μm line.	126
Figure 5.15 Comparison of filament separation positions and the topography profile of the printed 200 μm line	126
Figure 5.16 Quantification of print stage lengths for deposition using varying snap distances at fixed print speed of 300 mm min^{-1} (a to c) and at a range of print speeds using a fixed gap of 1.825 mm (d to f).....	129
Figure 5.17 High-speed camera images at 5x magnification of different stages of the deposition of the 200 μm line conducted at 300 mm min^{-1} with snap distances of (a) 1.475 mm and (b) 1.125 mm. As well as conducted with a snap distance of 1.825 mm with squeegee speeds of (c) 100 mm min^{-1} and (d) 500 mm min^{-1}	131
Figure 5.18 Changes in the optical microscopy images (10 x magnification) of the printed lines with standard settings (300 mm min^{-1} , 1.825 mm snap distance and at contact point) (a), with the snap distance reduced to 1.475 μm (b) and 1.125 μm (c). As well as with the print speed reduced to 100 mm min^{-1} (d) and increased to 500 mm min^{-1} (e).....	133
Figure 5.19 Variations in the average film thickness and average printed line width with changes in snap distance (a) and squeegee speed (b) (analysed using white light interferometry) (error bars represent standard deviation).	133
Figure 5.20 Changes in line resistance of the 200 μm lines with changes in snap distance (a) and speed (b) (error bars represent standard deviation).....	134
Figure 5.21 White light interferometry topography images of the 700 μm lines conducted on the DEK 248 Screen-printer, for prints conducted at 30 mm/s for snap speeds of 0.5 mm to 1.5 mm (a to c), 50 mm/s for snap speeds of 0.5 mm to 1.5 mm (d	

to f) and 70mm/s for snap speeds of 0.5mm to 1.5mm (g to i) at 5 times magnification.....	136
Figure 5.22 Average film thickness (a), line width (b) and cross-sectional area (CSA) of ink deposited (c) for the 700 μ m lines produced for combinations of snap off distance and print speed. (error bars for standard deviation)	137
Figure 5.23 Average film thickness (a) and average surface roughness (Sa) (b) for the printed squares produced for combinations of snap off distance and print speed. (error bars for standard deviation).....	137
Figure 5.24 Average line resistance for the 700 μ m lines (a), as well as average sheet resistance (b) and sheet resistivity (c) of the printed squares conducted on the DEK 248 Screen printer for combinations of snap off distance and print speed. (error bars for standard deviation)	139
Figure 6.1 Viscosity profiles (a) and viscoelastic profiles assessing changes in phase angle (δ) (b), storage modulus (G') (c) and loss modulus (G'') (d) of the different dilutions of the carbon ink.....	154
Figure 6.2 High speed images of the separation mechanism for inks diluted by (a) 0 wt%, (b) 2.5 wt%, (c) 5 wt%, (d) 7.5 wt% and (e) 10 wt% and a graph of the evolution in the (dimensional) radius as a function of time (f).....	155
Figure 6.3 Viscosity profiles (a) and viscoelastic profiles assessing changes in phase angle (δ) (b), storage modulus (G') (c) and loss modulus (G'') (d) of the varying carbon morphologies and loading percentages. (Error bars represent standard deviation).....	160
Figure 6.4 High speed images of the separation mechanism for the ethyl cellulose-based carbon inks loaded with varying amounts of graphite (a to c), carbon black (d to f) and GNPs (g to i), with a graph of the evolution in the (dimensional) radius as a function of time (j).	161
Figure 6.5 High-speed camera images at 5x magnification and quantification of the average print stage lengths for deposition of the carbon ink diluted by 0 wt% to 10 wt%.	163
Figure 6.6 High-speed camera images at 5x magnification and quantification of the average print stage lengths for deposition of the plain resin (a) along with the ethyl cellulose-based carbon inks loaded with varying amounts of graphite (b to d), GNPs (e to g) and carbon black (h to j).	166
Figure 6.7 High-speed camera images at 5x magnification of different stages of the deposition of the plain resin showing the merging of the filaments forming during separation.	167
Figure 6.8 White light interferometry topography images of the printed lines diluted by (a) 0 wt%, (b) 2.5 wt%, (c) 5 wt%, (d) 7.5 wt% and (e) 10 wt%, with a graph of the corresponding changes in film thickness and width below. (error bars represent standard deviation).	169
Figure 6.9 Comparison of the average cross sectional area of the printed line with the average flow to separation stage length during printing of the line.....	170
Figure 6.10 White light interferometry topography images of the printed lines produced with the ethyl cellulose-based carbon inks loaded with varying amounts of graphite (a to c), carbon black (d to f) and GNPs (g to i).	171

Figure 6.11 Changes in line width (a), film thickness (b) and the cross-sectional area of ink deposited (c) with ethyl cellulose-based carbon inks containing different carbon morphologies and different loading ratios.....	172
Figure 6.12 Comparison of the average cross sectional area of the printed line with the average full contact region (stages 1-4) during printing of different carbon morphologies and concentrations.....	172
Figure 6.13 White light interferometry topography images of 500 μ m printed lines conducted on the DEK 248 Screen-printer at 5 times magnification, diluted by (a) 0 wt%, (b) 2.5 wt%, (c) 5 wt%, (d) 7.5 wt% and (e) 10 wt%, with a graph of the corresponding changes in line width (e) and film thickness (f) below for the 500 μ m and 700 μ m lines, as well as the film thickness of the printed squares (error bars represent standard deviation).	174
Figure 6.14 The average surface roughness (sa) (left graph) and average maximum surface roughness (sz) (right graph) of the printed squares conducted on the DEK 248 Screen printer for the printed carbon inks diluted between 0 wt% and 10 wt%.	174
Figure 6.15 Average line resistance for the 500 μ m and 700 μ m lines (a), as well as average sheet resistance (b) and sheet resistivity (c) of the printed squares conducted on the DEK 248 Screen printer for the printed carbon inks diluted between 0 wt% and 10 wt%.....	176
Figure 6.16 Average film thickness (a) and line width (b) of the 500 μ m and 700 μ m lines produced by the ethyl cellulose-based carbon inks containing different carbon morphologies and different loading ratios. (error bars for standard deviation)	177
Figure 6.17 Average film thickness (a) and average surface roughness (Sa) (b) of the printed squares produced by the ethyl cellulose-based carbon inks containing different carbon morphologies and different loading ratios. (error bars for standard deviation).....	178
Figure 6.18 White light interferometry topography images of the printed solid area conducted on the DEK 248 Screen-printer, for the ethyl cellulose-based inks containing 15 wt% (a) and 25 wt% (b) graphite, 15 wt% (c) and 25 wt% (d) GNPs, as well as 10 wt% (e) and 20 wt% (f) carbon black at 5 times magnification.	178
Figure 6.19 Scanning Electron Microscope (SEM) images showing the microstructure of the ethyl cellulose-based inks containing 15 wt% graphite (a), 25 wt% graphite (b), 15 wt% GNPs (c) and 25 wt% GNPs (d) at 3,000 times magnification. As well as the inks containing 10 wt% carbon black (e) and 20 wt% carbon black (f) at 10,000 times magnification.	179
Figure 6.20 Average line resistance for the 500 μ m and 700 μ m lines (a), as well as average sheet resistance (b) and sheet resistivity (c) of the printed squares conducted on the DEK 248 Screen printer for the ethyl cellulose-based carbon inks containing different carbon morphologies and different loading ratios. (error bars for standard deviation).....	181
Figure 7.1 White light interferometry images of the edges of the printed squares for the printed graphite, GNP, graphite with carbon black inks both before post treatment (images a to c respectively) and after both photonic annealing and compression rolling (images d to f respectively) at 5 times magnification.....	196

Figure 7.2 Film thickness (a) and Average surface roughness (Sa) (b) for the various inks before and after photonic annealing and compression rolling (error bars show standard deviation). 196

Figure 7.3 Scanning Electron Microscope (SEM) images at 3000 times magnification showing the microstructure of the graphite-based inks which have received no post processing (a), after compression rolling only (b), after photonic annealing only (c) and after both photonic annealing and compression rolling (d). 197

Figure 7.4 Scanning Electron Microscope (SEM) images at 3000 times magnification showing the microstructure of the graphite nanoplatelet (GNP) -based inks which have received no post processing (a) and which have undergone both photonic annealing and compression rolling (b). 197

Figure 7.5 Scanning Electron Microscope (SEM) images at 3000 times magnification showing the microstructure of the graphite and carbon black -based inks which have received no post processing (left) and which have undergone both photonic annealing and compression rolling (right). 198

Figure 7.6 Sheet resistance of the printed squares before and after photonic curing and compression rolling for all inks (left) and graphite and carbon black based ink only (right). 200

Figure 7.7 Resistivity of the printed squares before and after photonic curing and compression rolling for all inks (left) and graphite and carbon black based ink only (right). 200

Figure 7.8 Ink film thickness for the printed 700 μm nominal width lines before and after photonic curing and compression rolling. 202

Figure 7.9 Resistance of the printed 700 μm nominal width lines before and after photonic curing and compression rolling for all inks (left) and graphite and carbon black based ink only (right). 202

Figure 7.10 TGA Analysis of the graphite ink and binder only up to 500°C. 203

Figure I.1 Substrate with eyelets and spring balance to measure horizontal interaction force between squeegee, mesh and substrate. B

Figure I.2 Prototype for speed tester D

Figure I.3 Speed tester design D

Figure I.4 Components for speed tester displaying the FDM printed casing, Arduino, LCD screen and LDRs with resistors. D

Figure I.5 Average speeds for different settings on the Svecia Matic screen-printer. .E

Figure II.1 Prototype 1 for the screen-printing visualisation jig G

Figure II.2 Dimensions of Screen Frame (Top) with the deflection (bottom left) and von mises stress (bottom right) distributions caused by a point load when supported by the jig design. I

Figure II.3 Print Design I

Figure II.4 Prototype 2 design in SolidWorks from the front (left) and rear (right) views. I

Figure II.5 Prototype 2 screen and substrate holder design with the deflection (left) and von mises stress (right) distributions caused by a point load. J

Figure II.6 Prototype 2 squeegee holder on moving slider design with the deflection (left) and von mises stress (right) distributions caused by the reaction of the downward squeegee force with the holder fixed from above. J

Figure II.7 Prototype 2 clamped in position with backlighting and high-speed camera positioned to the side.....J

Figure II.8 Screen and substrate holder for motorised jig (Top) with the deflection (bottom left) and von mises stress (bottom right) distributions caused by a point load estimated as the squeegee and screen forces.L

Figure II.9 Squeegee holder for motorised jig (Top) with the deflection (bottom left) and von mises stress (bottom right) distributions caused by a point load estimated as the squeegee and screen forces.M

Figure II.10 Motorised screen-printing visualisation rig from the front (left) and when in use (right).M

List of Tables

Table 3.1 Polydimethylsiloxane (PDMS) standard viscoelastic sample G' and G'' vales at 25°C.....	47
Table 4.1 Different Mixing Techniques used.	66
Table 4.2 Triple roll mill settings.....	66
Table 4.3 DEK 248 Screen-Printing Press Parameter Settings.....	69
Table 4.4 Svecia Matic Screen-Printing Press Parameter Settings.	69
Table 4.5 Design of experiments for parameter trial conducted on the Svecia Matic	82
Table 5.1 3 ² Full factorial analysis of snap off distance and print speed on the DEK 248 screen-printer.....	112
Table 5.2 Lengths of discrete ink deposits and gaps between deposits for printed 50 µm line.	119
Table 6.1 Ink batch composition for carbon-based inks	150
Table 6.2 Triple roll mill settings.....	150
Table 7.1 Ink formulations for graphite, GNP and combined graphite and carbon black-based inks.	190
Table 7.2 Triple roll mill settings.....	190
Table 7.3 Summary of changes in ink film thickness and roughness of solid area data – standard deviation in parentheses.....	198
Table 7.4 Summary sheet resistance and resistivity of solid area data – standard deviation in parentheses.	201
Table I.1 Table of average speeds for different settings on the Svecia Matic screen-printer.	E

List of Equations

Equation 2.1 Hagen-Poiseuille law	27
Equation 3.1 Shear Viscosity	38
Equation 3.2 The Cross model	39
Equation 3.3 The Power-law (or Ostwald-de Waele) model	40
Equation 3.4 The Sisko model	40
Equation 3.5 Resultant strain of viscoelastic material	41
Equation 3.6 Shear stress applied to viscoelastic material.....	41
Equation 3.7 Storage Modulus (G').....	42
Equation 3.8 Loss Modulus (G'').....	42
Equation 3.9 Complex shear modulus	42
Equation 3.10 Phase angle (loss factor)	42
Equation 3.11 Einstein's equation for infinitely dilute, non-interacting hard spheres	43
Equation 3.12 Barnes' equation for rod like (prolate) particles	43
Equation 3.13 Barnes' equation for disc-like (oblate) particles	43
Equation 3.14 Krieger-Dougherty (K-D) equation	44
Equation 3.15 Quemada equation	44
Equation 3.16 Shear rate of the cone and plate geometry	45
Equation 3.17 Extensional viscosity (η_E).....	48
Equation 3.18 Idealised elastic filament breakup.....	48
Equation 3.19 Midpoint radius for power-law fluid	49
Equation 3.20 Relationship between conductivity and resistivity	61
Equation 3.21 Relationship between Resistance and Resistivity.....	61

List of Abbreviations

The following table describes the various abbreviations and acronyms used throughout this thesis.

Abbreviation	Explanation
CaBER	Capillary breakup extensional rheology
CFD	Computational fluid dynamics
CMT	Combined motor-transducer
CNT	Carbon Nanotube
CSA	Cross sectional area
CVD	Chemical vapor deposition
c-PSC	Multi-layer screen printed mesoporous stack with carbon top electrode
EOM	Emulsion over mesh
FiSER	Filament stretching rheometer
FLG	Few layers graphene
FVM	Focus variation microscopy
GEM	Gwent Electronics Materials
GNP	Graphite nanoplatelet
GO	Graphite oxide
IPL	Intensive pulsed light
LDR	Light dependent resistor (photoresistor)
LVR	Linear viscoelastic region
P2CAR2	Printing Process Control by Advanced Rheology 2

PDMS	Polydimethylsiloxane
PSI	Phase shifting interferometry
PV	Photovoltaic
R2R	Roll to roll
RFID	Radio Frequency Identification
rpm	Revolutions per minute
SAOS	Small amplitude oscillatory shear
SE	Secondary electron
SEM	Scanning Electron Microscope
SMT	Separate motor-transducer
TEM	Transmission Electron Microscope
TGA	Thermogravimetric analysis
VSI	Vertical scanning interferometry
WLI	White light interferometry

Chapter 1. Introduction

1.1. Aims and Objectives

Screen printing is a technique which has been around for many years (1,2). It is a relatively cheap and simple process that can deposit a wide range of inks onto a variety of substrates. As it is capable of depositing highly viscous inks containing large functional materials and large concentrations of functional materials, this has led to it being widely used for the deposition of printed electronics.

Printed electronics are becoming increasingly popular as they offer an economic, low temperature alternative to conventional manufacturing methods. They can be produced in high volumes over large areas on a range of substrates. This has enabled electronic systems to be deposited onto a wide range of non-traditional substrates including paper, plastics, textiles, metals, organic materials and much more. Screen printing is used for the production of a wide range of printed electronics, including all layers of printed electroluminescence lighting (3) which can be used for shop signs and packaging. Printed resistive carbon heaters that can be used in underfloor heating when printed onto steel sheets that can be located under carpets (4,5). It is also used in producing photovoltaics (6,7), with screen printing used to deposit the majority of layers in carbon top electrode perovskite solar cells (C-PSC), providing an economical method for mass producing the cells. Additionally, it is also used in producing electrochemical and pressure sensors (8,9), such as glucose biosensors

There is a limited understanding of the fundamental science behind the ink transfer process due to the interaction of complex fluids in complex flows, with a number of press parameters. All of which have an impact on the print quality and performance, making it hard to produce predictive models and resulting in screen printing being viewed as a black art.

This has resulted in a limited understanding of the fundamental science involved in the deposition of the ink onto the substrate and the separation of the ink from the mesh during the screen-printing process. As well as a lack of understanding of the effect of press parameter settings on functional inks. This lack of understanding can result in a number of print defects which can affect the print consistency and

performance. Therefore, a better understanding of the effects of ink rheology, press parameters, post processes as well as the deposition process itself can enable improvements in the print performance.

To achieve this, this thesis will focus on three main areas:

- The effect of key parameters on print quality.
- Visualising the ink deposition and separation in screen-printing.
- The effect of post processing on print performance.

Carbon inks have been chosen as the functional material to be assessed for this thesis as they are widely used in the manufacture of a range of printed electronics applications due to their electrical conductivity and relatively low cost. However, identifying a technique to enable the analysis of the ink deposition and separation in screen printing could be beneficial for a range of functional inks.

Overall, these studies could be used to develop predictive methods, as well as improve the understanding of how to optimise print quality and performance for screen-printed functional materials.

1.2. Introduction to Screen-Printing

1.2.1. History of Screen-Printing

Screen printing is a versatile, and economically competitive printing technique. It is capable of printing a wide rheological range of inks. This includes highly viscous inks which are common with functional inks containing large particles or high concentrations of functional particles. This has led to screen printing being widely used in the manufacture of a range of printed electronics applications (10).

Its origins date back to ancient times, where the technique of attaching stencils to a gauze mesh was developed in eighth-century Japan. These stencils used fine strands of silk or human hair to hold together unconnected patterns (1,2). However, screen printing as it is known today only came about in the late nineteenth century, where it was used for producing packaging, advertising and labelling (2). Multicolour, automatic presses then came into existence in the early twentieth century (1,2,11). Following on from this, screen-printing started to be used as a medium for creating artwork in the 1920's (1). Its popularity then significantly increased in the 1960's, at which point it started being used as a process for decorating textiles, as well as the

medium for creating famous artworks by the likes of Eduardo Paolozzi and Andy Warhol (2). Recently, screen-printing has entered a new chapter and is currently responsible for producing a wide range of printed electronics. These include resistive heaters (4), electrochemical sensors (9), printed batteries (12), Perovskite PV (6,7), and energy harvesting in the form of printed pyroelectrics (13) and thermoelectrics (14).

1.2.2. Flatbed Screen-Printing

Flatbed screen printing is the oldest and simplest form of screen printing and is commonly used for producing printed electronics. It is available in a range of sizes and a number of forms including manually operated, hinge backed hand benches, semi-automatic hinge backed presses, as well as semi and fully automatic horizontal lift flatbed presses. This combined with its ability to print on a range of substrates including textiles, wallpapers, electronic circuit boards, polymers, ceramics etc. make it a very versatile process (15).

In flatbed screen printing, the screen and substrate remain stationary during printing, while the flow-coat and squeegee move from one side of the screen to the other. The flow-coat layer is optional and uses a metal blade to evenly distribute the ink over the mesh prior to printing, filling holes in the mesh with ink. Once the flow-coated layer has been applied, the squeegee then forces the mesh into contact with the substrate. This can be done without any gap between the mesh and substrate, known as contact mode. Or with a separation distance between the mesh and substrate, known as a snap off distance, as shown in Figure 1.1. The ink is then transferred from the mesh to the substrate, by the passage of the squeegee displacing the screen onto the substrate, with the ink passing through the gaps in the emulsion on the mesh.

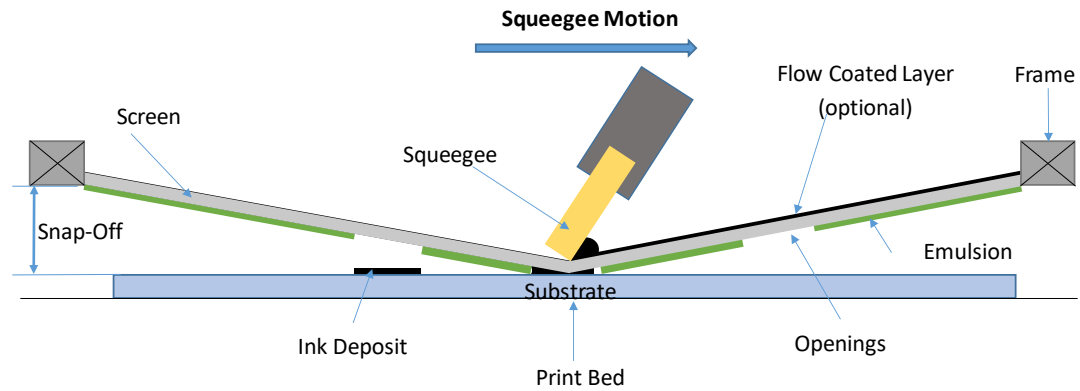


Figure 1.1 Schematic of Flatbed Screen Printing

1.2.3. Flatbed Screen-Printing Components

As flatbed screen printing is the dominant technique used for depositing functional materials, it was the press type chosen for analyses in this thesis.

1.2.3.1. Screen and Mesh

The screen is responsible for determining the print pattern and transferring the ink to the substrate. The screen consists of a frame which holds a tensioned mesh in place, with a stencil of the print on top of the mesh. The mesh is made by weaving thin threads of typically either polyester or stainless steel, to create a woven structure. The material choice is determined by the image tolerance and cost. Stainless steel meshes are capable of printing finer features, such as a 25 μ m continuous line. This is due to their larger open area between threads for ink to pass through, as stainless-steel threads can be made finer than polyester threads. Stainless steel meshes can also be subject to higher tension than polyester meshes. This minimises the required snap off gap between the mesh and substrate, therefore minimising distortion of the print. However, stainless steel meshes are more expensive than polyester meshes, by around ten times. Stainless steel meshes are also far more delicate than their polyester counterparts, with a lower elastic limit of around 3%, compared with 20% for polyester. As well as requiring only 15N/cm load for 1% elongation, while polyester screens can withstand around 40N/cm for the same elongation percentage. This means that local high stresses, including a small flick or too much pressure while cleaning, can result in plastic deformation.

The woven mesh is put under tension using a pneumatically or mechanically applied tensile force and held in place with clamps. The mesh consists of a warp and weft

direction. The straight threads are in the warp direction and the threads that weave up and down between the warp threads are the weft, as shown in Figure 1.2. When the mesh is at the desired tension, the frame can be attached.

Frames can be fixed or adjustable to vary mesh tension. Fixed frames are most common and are typically made from Aluminium due to its low density and corrosion resistance. The surface of the frame being bonded to the screen is usually roughened prior to adhesion, to increase the surface area and frictional bonding to improve the seal. To avoid the tension of the mesh causing plastic deformation on the frame from the inward forces, the frame is typically pushed inwards by pneumatic clamps along the edges as the mesh is stretched in the reverse direction. This provides a pre-compression force on the sides of the frames to counter the inward tension caused by the mesh.

The frame is attached by being raised from below, into contact with mesh and fixed in place with an adhesive. The adhesive is left to cure for around 24 hours with the screen under tension. The screen is then cut out along the edges of the frame and is ready for the stencil to be applied. The frame can be orientated to change the angle of the mesh to the frame according to the features which are being printed, to optimise print quality.

The stencil is then applied to the screen. The most common methods for creating the stencil are with direct emulsions or capillary films. Direct emulsion methods consist of coating a photo-polymeric, UV light sensitive emulsion onto the mesh which is then dried to physically harden the emulsion. The film positive of the pattern to be printed is then placed onto the emulsion and exposed to high intensity UV light, causing cross linking in areas not covered by the positive. The areas covered by the positive remain water soluble and are then washed off with high pressure water, before being dried in an oven. A number of layers of emulsion can be applied to change the emulsion thickness (Figure 1.2). This in turn determines the maximum printable film thickness, as well as the print roughness. Where thin emulsion thicknesses tend to conform to the topography of the mesh. Whereas multiple layers of emulsion can overcome this roughness.

The capillary film stencil is applied as a solid film. In this case the mesh is initially soaked in water. Then the photo-emulsion, which is mounted on a transparent carrier

polyester film, is applied as a sheet. The water on the mesh dissolves the stencil on the underside and the resultant liquid is drawn into the mesh through capillary flow. After it has been dried, the process is then the same as with the direct emulsion method where the film positive is applied and the exposed areas are cured with UV. The capillary film method tends to produce the higher quality prints as it is applied as a single, homogeneous sheet. This leads to more consistency in the film thickness of the print and no shrinkage due to drying, as it remains a solid for the whole procedure. However, the capillary film method is far more expensive than the direct emulsion method. It can also be unreliable as defects in the film can make it unusable or require touching up by hand. Therefore, the direct emulsion method is more popular, while the capillary film method is used for prints requiring high resolution, fine features. (15–17)

The mesh is characterised in terms of the thread diameter (d) and mesh ruling, quantified as the number of threads over a unit of distance (e.g. threads/cm), as shown in Figure 1.2. These in turn determine the length of the pitch (p) and mesh width (w), also known as mesh opening. These dictate the amount of ink which can pass through the mesh and the print resolution. The emulsion stencil is characterised in terms of the total stencil thickness, the amount of emulsion over the mesh (EOM) as well as the total thickness of the mesh and stencil. Which combines the total mesh thickness (D) with the height of the EOM. (15–17)

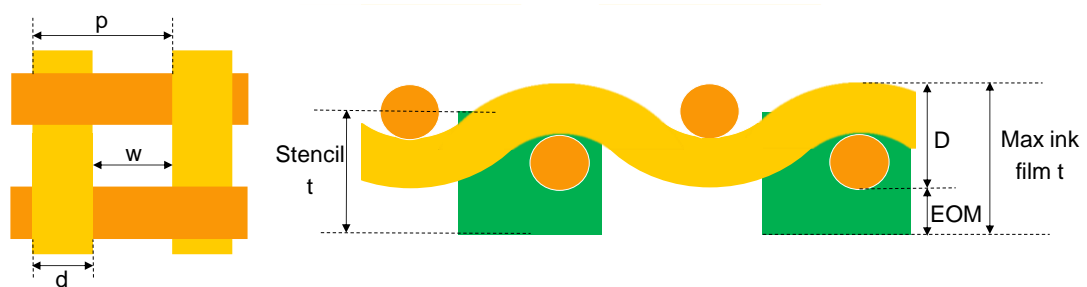


Figure 1.2 Diagram of mesh geometry consisting of mesh width (w), mesh thickness (D), nominal thread diameter (d) and pitch (p). With an emulsion-based stencil with labelled emulsion over mesh (EOM), stencil thickness and maximum printable ink film thickness.

1.2.3.2. Snap Off Distance

The snap off distance is the separation distance between the mesh and substrate during printing, which assists in the separation of ink between the mesh and substrate. The amount of snap off required is dependent on the rheological profile of the ink and the tension that the mesh is kept under. If too great a snap off distance is used, then this will induce mechanical stress in the mesh that can result in the printed image being distorted. Therefore, the snap off distance is kept as low as possible to ensure a clean separation between the mesh and substrate, while minimising distortion of the image or deformation of the mesh. Changes in snap distance can also influence the ink elongation and ink separation, although further experimental work is needed to improve the understanding of this relationship

1.2.3.3. Flow-coat

The flow-coater (flood bar), if used, is responsible for providing a consistent layer of ink over mesh prior to printing. It is typically conducted using a blade made from aluminium or stainless steel which fills the mesh with ink prior to printing, without pushing ink through the mesh or contacting the mesh to the substrate. This can be conducted in contact with the mesh, or a small set distance above the mesh, according to the application.

1.2.3.4. Squeegee hardness, geometry and pressure

The squeegee is then responsible for bringing the inked mesh into contact with the substrate and enabling printing as it flows over the mesh. Squeegees are typically cast polyurethane blades, with the mechanical properties stated as “Shore A” hardness in the screen-printing community. The hardness value is used to measure the resistance of the outer surface of the squeegee to deflection (18). The shore harness is varied to accommodate for a range of printing conditions, such as substrate surface energy, roughness and the desired quantity of ink to be deposited. Typically, the shore hardness ranges between 55 and 90 Shore A hardness. They are also available in a variety of different geometries and can be used at a range of angles to alter the print quality and film thickness. Polyurethane compounds are used as they are able to provide resistance to screen-printing inks and solvents, as well as resistance to abrasion. The squeegee must also be rigid enough to withstand the hydrodynamic and drag forces which act on it during printing. As well as able to absorb changes in height from the substrate and mesh roughness's.

The investigations in this thesis focussed on two squeegee geometries, the diamond squeegee and the single durometer blade squeegee (Figure 1.3), as they are the most commonly used geometries. The square profiled diamond squeegee is used with the point at 45 degrees to the mesh. This geometry is used in the electronics industry for producing relatively thick ink deposits and does not require the angle being adjusted (15). The other geometry was a single durometer blade squeegee. With blade squeegees, the angle at which the squeegee contacts with the mesh can be adjusted with the squeegee holder. This typically ranges between 60° and 80° and has a great effect on the quantity of ink deposited. Other squeegee geometries are also available, including those containing different materials or layers of different hardness polyurethane for support to minimise squeegee deflection. However, single durometers are still commonly used in industry and were the subject of previous studies covered in the literature (Chapter 2) which these results were compared against. Changes in the squeegee hardness and angle can lead to variations in the ink flow and separation from the mesh behind the squeegee, although further experimental work is required to better understand these changes.

The squeegees can also be set at a range of pressures, according to the desired print. The pressure used will depend on the squeegee hardness, geometry, angle, mesh tension and snap off used. It must ensure the squeegee sufficiently displaces the mesh to the substrate, without causing it to excessively deflect or warp at the tip. The squeegee pressure can be adjusted using either screw threads or pneumatic pistons. The screw thread method alters the pressure provided by the squeegee, by altering the vertical height of the squeegee. However, as squeegees come in a range of hardnesses and geometries, coupled with changes in the substrate profile, using the same vertical position does not translate to a consistent pressure being applied. The pneumatic systems are capable of setting the squeegee pressure in terms of load per unit length (N/m) or in terms of the downward squeegee load (Kg), which can be converted to N/m by accounting for the squeegee length. This provides a more reliable method for producing consistent squeegee pressures, which are easier to quantify. However, pneumatic systems are more complex than screw thread systems (15–17,19). The effects of squeegee geometry, hardness and pressure on print performance is discussed in the literature review.

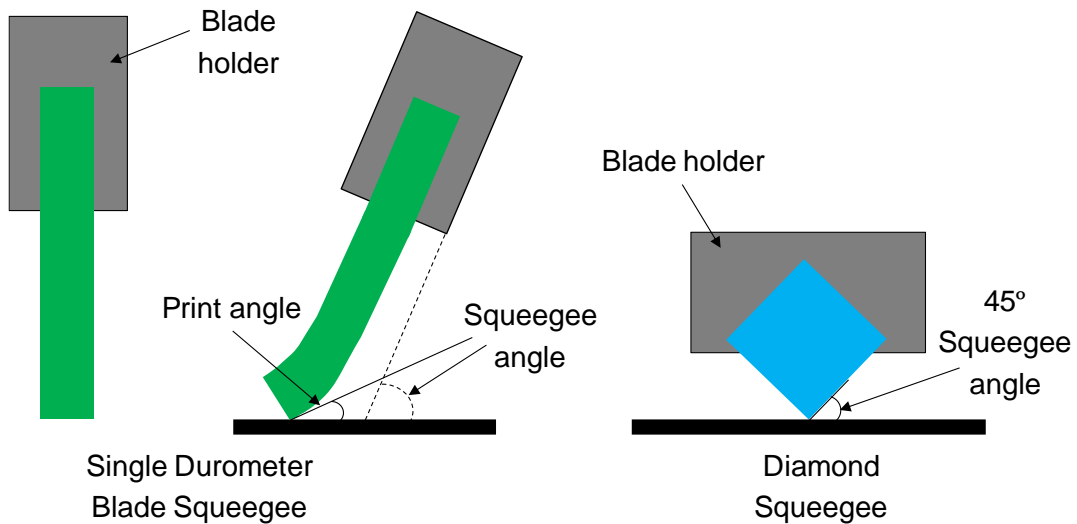


Figure 1.3 Blade and diamond geometry squeegee geometries.

1.2.3.5. Squeegee Speed

The squeegee speed is the rate of squeegee passage across the mesh during the print stroke. This determines the rate of ink deposition and subsequent separation between the mesh and substrate. The squeegee speed used will depend on the pseudoplasticity and elasticity of the ink, which would influence the separation mechanism and amount of shear required to thin down the ink.

1.3. Chapter closure

Therefore, to achieve these aims and objectives set out in 1.1, the thesis will consist of an Introduction, Literature Review, Materials and Methods, followed by four main chapters then Conclusions and Future Work. The first main chapter will focus on the effect of a range of press parameters. The following two chapters develop a technique, which for the first time has been able to visualise the deposition mechanism and assess how it varies with a range of variables including press parameters and ink rheology. The final main chapter then investigated the use of post processing techniques for enabling further improvements in print performance.

Chapter 4 will investigate the effect of press parameter settings to establish which parameters have significant effects on the print quality produced so that optimal settings can be identified. Chapter 5 will identify a visualisation method for assessing the ink deposition mechanism in screen-printing. As well as investigate

how the mechanism varies with line widths, snap distance and squeegee speed for a given carbon-based ink. Whereas Chapter 6 will identify how this mechanism alters with changing the rheological profile of a range of carbon-based inks. As well as identify links between ink rheology and print performance. Then finally, Chapter 7 will investigate the effect of post processing techniques. To identify if there are alternative drying, curing or other post processing methods which could enhance the print quality.

Chapter 2. Literature Review

2.1. Introduction

This chapter will review the current literature related to screen-printing. This can be separated into four main areas consisting of:

- The effects of different press parameters
- The rheological profiles of screen-printing inks and functional materials used in screen printing inks
- Screen printing models describing the ink deposition mechanisms
- Drying and post processing techniques used in screen printing

The press parameters can be separated into four main areas consisting of the mesh design, the squeegee used, the snap off distance and the squeegee print speed. All of which can have an effect on the print quality and performance. The effects of these parameters can also be affected by the rheological profile of the ink used, which vary according to the binder, solvent and particles used. With screen printing used to deposit a range of functional materials, this can range greatly, so this work will focus on carbon-based inks. With the parameters and ink rheologies used effecting the print quality and performance, analytical models are needed to minimise the need for trial and error, therefore existing analytical models on the ink flow and deposition mechanisms during screen printing will be investigated. In addition to these variables, the drying and post processing methods used after the print is produced can also have an effect on the print performance. Therefore, these were also investigated.

2.2. Effect of Screen-Printing Parameters

Past experiments have been conducted into identifying the effects of various screen-printing parameters. These include the mesh material and geometry (20–22), squeegee hardness, angle, pressure and geometry (23,24), as well as snap distance and print speed (23).

Optimising these parameters can both improve print performance and overcome print defects such as mesh marking, pinholes and crowning, as well as irregularities in printed lines. Mesh marking is the appearance of regular features corresponding with

the frequency of the mesh in the printed solid film (20,25,26). This causes increases in the print roughness and can cause issues when depositing multiple layers. It is typically caused by high viscosity inks, incorrect screen tension or the squeegee speed being used (25,26). Pinholes, consisting of small gaps in the print, as well as crowning, consisting of a small lip at the edge of prints, can also cause increases in roughness and reductions in print functionality. Crowning is believed to be an effect of the ink release mechanism from the screen (27,28). While typical line irregularities can consist of voids from non-continuous lines, shorts, or partial shorts from intrusions of the printed lines onto neighbouring lines. As well as line waviness and variation in line width (29). All of which can worsen print performance or render it useless.

2.2.1. Mesh Tension and Size

Changes in mesh tension, mesh materials, wear and the mesh dimensions can all have a significant effect on the print quality and film thickness produced.

Experiments have found that using a courser mesh tended to increase the quantity of ink transferred, due to larger mesh openings enabling a greater volume of ink to transfer through the mesh. Whereas a finer mesh led to reductions in the quantity of ink transferred (4,20–22,30). Some experiments on carbon based inks and silver based inks found that as the film thickness reduced with increasing the fineness of the mesh, there was an increase in the sheet resistance produced (20,22,30).

A study by Philip *et al.* (4) found that although film thickness reduced with using finer meshes, the lowest sheet resistance was obtained with the finest mesh used in that experiment, with 77 threads/cm and a 48 μm thread diameter. In this case, printing carbon-based pastes through coarser meshes led to large variations in the topographical profile of the prints due to lower shear stresses during ink deposition and subsequent separation from the mesh. This led to reductions in shear thinning of the ink, resulting in higher viscosities. This would prevent a continuous, consistent film from being deposited. Thus, leading to worse electrical performances in the prints.

Other studies investigating a finer range of mesh densities found the optimal mesh density to produce the best conductivity varied according to the solvent used in another carbon-based ink, where the coarsest mesh containing 32 threads/cm and 100

μm thread diameter was best for inks containing 4-Hydroxy-4-Methyl-2-Pentanone, 4-Hydroxy-4-Methyl-2-Pentanone & P-Menth-1-En-8-ol (Terpineol) or 2-Butoxyethanol as their solvent. While the mesh containing 90 threads/cm and 48 μm thread diameter was best for the ink containing P-Menth-1-En-8-ol (Terpineol). (21). Therefore, as there is an interaction between the ink rheology and particle sizes within the inks with the mesh sizes required, different meshes are required for optimising print performance with different inks. Further studies are needed to improve the understanding of the fluid dynamics occurring during screen printing it will be hard to predict optimal parameters.

Similar trends in film thickness have been seen when using a stainless-steel mesh rather than a polyester mesh. Increases in film thickness were found with coarser meshes for carbon and silver based inks, along with subsequent reductions in sheet resistance with thicker films (20,22). However, the line widths produced for comparable mesh rulings was found to be greater with the stainless steel meshes. This is due to the larger mesh openings from the finer stainless-steel strands, providing a larger internal volume for the ink to pass through.

Mesh tension has also been reported to have an effect on print quality. Where increases in mesh tension typically led to increases in the amount of ink deposited, although this was dependent on the substrate used (27). However, the effect of mesh tension had a strong interaction with the snap distance used. Where the effect of snap distance on the quantity of ink deposited was found to be dependent on the mesh tension (27,31). Studies have also identified the negative impact of creep and fibre realignment on mesh tension over time. Repeated use and vibrations from transportation were found to cause elongation and subsequent failure of mesh strands (18). The amount of tension loss over a given time period was found to be predictable using a power law equation, enabling the life span of a mesh to be estimated.

2.2.2. Squeegee Effects

A range of squeegee parameters have been found to have a significant impact on the film thickness and quality of the print. Interactions between the squeegee pressure, material properties such as hardness, angle of the tip and geometry of the squeegee

can influence the deformation of the squeegee during printing. This in turn can affect the ink pressure generated at the squeegee tip and subsequent print quality (16).

For a blade squeegee, altering the stiffness and angle of contact between the squeegee and mesh can have a significant impact on the deformation of the squeegee profile and tip. This can result in changes in the quantity of ink deposited and print topography. If the squeegee is too stiff, this can result in print defects such as bands and streaks due to the squeegee losing contact with the substrate. However if the squeegee is too compliant, this would result in the blade bending and deforming at high loads when using a blade geometry squeegee (Figure 2.1). This would then result in a high ink deposit with a lack of control over the film thickness as the squeegee loses contact with the mesh and substrate, potentially producing inconsistent prints (15–17,19). In screen printing studies, the squeegee's flexibility and durability are compared using shore hardness of the squeegee, ranging from soft and compliant, to hard and stiff.

Softer squeegees (60-70 Shore A hardness) tend to deposit more ink, producing greater film heights than harder squeegees (80-90 Shore A hardness) (18,23,27,31–33). This is due to the deflection of the softer squeegee forcing more ink to be deposited. However, other studies found that the medium hardness squeegees (70-75 Shore A hardness) produced film thicknesses slightly lower than that of the soft squeegee, when at squeegee angles of 65° or more. Although at squeegee angles of 60° or less, they were found to produce greater film thicknesses (32). Other studies found that medium hardness squeegees produced greater film thicknesses at angles greater than 60° as well (27,31). This is most likely due to the deflection profile of the squeegee where too hard a squeegee may cause scraping and too soft a squeegee could cause excessive deflection. The latter would result in a loss of control over the quantity of ink deposited in some circumstances. However, squeegee hardness is not always an indicator of how the squeegee will bend. There are also composite squeegees with harder cores which will deflect less than a single durometer squeegee. Although these investigations were all conducted on single durometer blade squeegees.

The angle of a blade squeegee also has a significant effect on the quantity of ink deposited, where a lower angle (around 60°) typically leads to a greater film

thickness and steeper angles reduce the quantity of ink transferred, as illustrated in Figure 2.1 (27,31,32). However, there were less significant differences in the film thicknesses produced at higher angles, such as 75° and 80°. Although for some substrates, angles of 80° were found to produce slightly greater film thicknesses than for 75°. Overall, this would suggest that using a soft squeegee with a shallow angle would generally produce the greatest ink deposit.

In the case of squeegee pressure, too little pressure can result in insufficient contact between the squeegee and substrate. This can cause the ink to not transfer properly onto the substrate, or completely remain on the mesh. If a hard squeegee is used, then too much pressure can cause the squeegee to scrape off some of the print. If the squeegee is soft, this can cause the squeegee to bend and deform, leading to increases in ink transfer (Figure 2.1). This could also cause loss of control over the quantity of ink deposited. As excessive squeegee deformation could cause loss of contact between the mesh and substrate.

In literature, a range of results have been found. Some studies found that low squeegee pressures were best for producing consistent, thick deposits of solder paste (34). Whereas others found that higher squeegee pressures produced greater film thicknesses (32). While some also found it to have no significant trend, with optimal pressure settings varying with different inks and substrates (23,27,31). However, these changes were less significant than those caused by varying squeegee hardness and angle.

Additionally, if the squeegee is worn down leading to alterations in the tip geometry through repeated use, this can cause changes in the print quality. Accelerated testing has been conducted on the effect of exposing a squeegee to inks, solvent absorption and wear from repeated use. Testing was accelerated by printing over abrasive paper while being lubricated by the ink (35,36). Squeegee wear from repeated use affected different squeegees to different degrees, but in general caused increases in ink transfer and wider lines (36). For printing fine line electronics, this can be highly problematic. As this would cause increased costs of inks and loss of line resolution. Repeated exposure to low boiling point solids in inks and cleaning fluids can cause reductions in the elastic modulus, as well as swelling of the squeegee causing increases in its mass and volume (35). However, the effects of these solvents can be

reversed by exposing the squeegee to elevated temperatures of up to 100°C to enable relaxation. Although this can only be done after printing and these things may change leading to issues over the duration of a long print run.

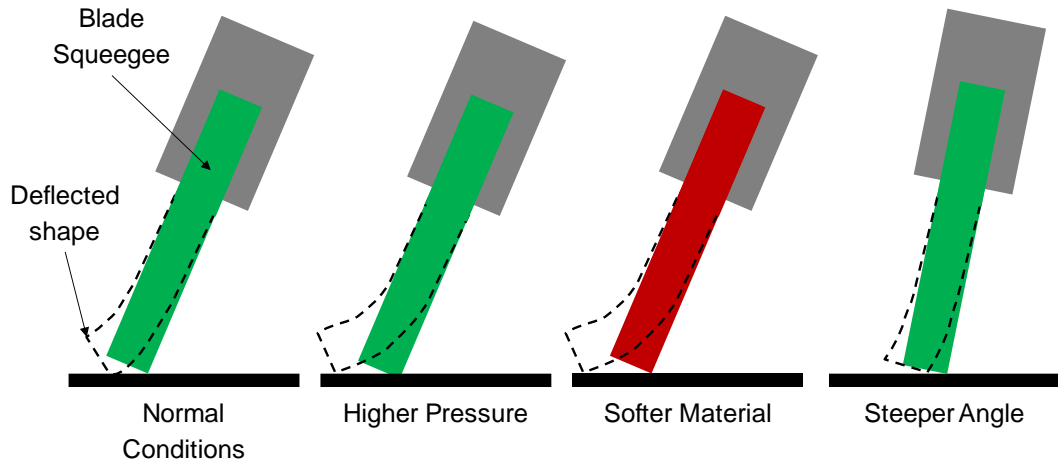


Figure 2.1 Effect of squeegee material, pressure and angle on the deflection of single durometer blade squeegees

2.2.3. Snap Distance

Changes in snap distance and print speed have been found to affect the print topography and electrical performance of the prints. In the case of snap distance, some studies found that increasing the snap distance led to increases in the ink deposit for a range of ink viscosities, although there were less pronounced trends for inks with the lower viscosities (37).

There is an optimal snap distance for a given ink and substrate to produce high quality, defect free prints. Snap off distances greater than this optimum distance lead to reductions in the area of the emulsion gasketing formed in front of the squeegee (38). This led to reductions in the resolution of the pattern edges and breaks between lines, as well as produced ghost images along the edges. Alternatively, distances smaller than this led to the mesh being unable to peel off of the substrate in time, causing printing defects such as pinholes and grains on the print pattern's surface (38). Riemer (39) suggested when the lifting force is smaller than the drag between the ink and mesh threads, the fabric can stick to the substrate behind the squeegee, known as the cling zone (Figure 2.2). Riemer (39) suggested that the cling zone is greatest when the mesh to substrate angle is at its lowest. Therefore, sufficient snap off distance is required to prevent the mesh from sticking to the substrate. Fox (40)

also found that too small a snap off distance could cause the mesh to adhere to the substrate. Additionally, Fox found that higher ink deposits could be achieved with a rotating roller squeegee when the snap off distance had been increased to a sufficient height due to increases in the hydrodynamic pressure in the ink flow ahead of the squeegee. Suggesting that the quantity of ink flowing through the mesh ahead of the squeegee could also affect the amount of ink deposited. Alternatively, other experiments have found that the snap off distance had no significant effects on the print quality of fine lines (23).

However, the effect of snap distance can be affected by the squeegee speed, which determines the rate at which the mesh separates from the printed substrate, known as snap off speed (37). By increasing the snap speed, the amount of time for the ink to be drawn out from the mesh is reduced, leading to a reduction in the ink quantity transferred (41).

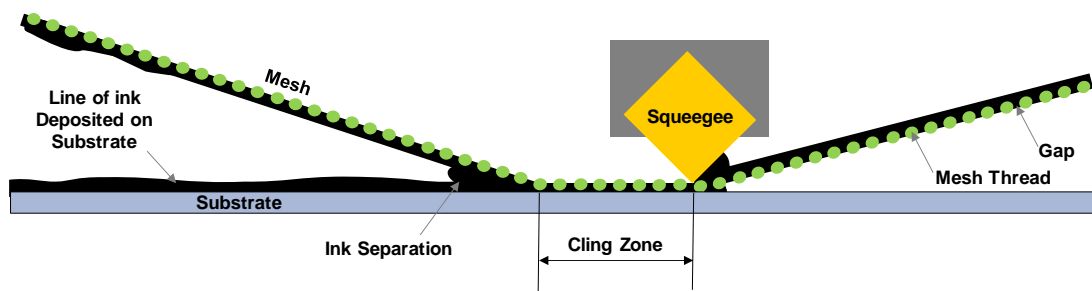


Figure 2.2 Illustration of Cling Zone.

2.2.4. Squeegee Speed

Increasing the squeegee speed has led to improvements in print quality. Increases in print speed led to improvements in the printed solid densities, due to the hydrodynamic effects (37,42). Increases in the hydrodynamic pressure were associated with an increase in the shear rate, due to the higher printing speeds. This led to a reduction in the ink viscosity and therefore a greater flow of ink during deposition.

Higher print speeds were also found to be beneficial for screen-printing of solder pastes, where increases in print speed were found to lead to increases in the film thickness of solder paste deposits (34,43). Other studies also found increases in print speed to have a positive effect on the print quality. Increases in the squeegee velocity from 4cm/s to 10cm/s led to reductions in line width and smoother edges, with

minimal signs of spreading as the screen has an optimal peel off time (38). However, further increases in print speed led to reductions in line edge quality, as the squeegee speed had become greater than the screen peel off speed.

Other studies found that increases in print speed led to reductions in print quality. This was found in terms of the printed line width and edge quality of fine lines, which worsened with increasing print speed (23). The optimal print speed may also be determined by the application of the print, with fine lines requiring different settings to printing large solid areas. In other cases, increases in print speed were found to cause reductions in dot gain (41). This was believed to be due to the high viscosity of the ink being assessed, which led to the squeegee lifting off the screen at high velocities. There were also increases in the snap-off velocity, reducing the amount of time that the ink had to separate from the mesh during ink transfer (41).

The extent to which snap distance and squeegee speed plays a role on print quality is strongly influenced by the ink characteristics, leading to no consistent trend. The behaviours of the inks would depend on their rheological profile, related to the molecular structures and particle interactions within them. (44) The extent of the effect of snap distance and squeegee speed may be linked to the viscoelasticity and pseudoplastic nature of screen-printing inks, as they tend to shear thin over a large shear range. Therefore, this would make the inks susceptible to the effect of snap distance and squeegee speed, which can alter the shear and shear rate applied to the ink. This is supported by studies which found that there was a strong interaction between the ink or paste being printed and the effect of print speed (45). In one study, one of the inks assessed showed a clear increase in the quantity of ink transferred with increases in speed, while another ink showed a reduction in the quantity of ink transferred with increases in print speed (45).

2.3. Screen-Printing Inks

Inks consist of a colour pigment, dye or functional material in the form of particles or flakes, which are dispersed in a resin matrix. In the case of solvent based inks, this is combined with solvents in which the resin is dissolved in. The ratio of solvent to resin can tailor the viscosity of the ink, as well as evaporate at the required rate to facilitate drying. There are also UV curable screen-printing inks which contain fluid cross-linkable monomers, rather than solvents (46).

2.3.1. Rheological profile of screen inks

Screen-printing inks are typically pseudoplastic (shear thinning) to enable the ink to remain stable on the mesh prior to printing. But flow readily during printing, to ensure a high-quality print is produced. The inks should also return to their resting viscosity in a suitable time. Allowing the print to settle enough to overcome marking from the mesh features, without spreading out at the edges of the print and leading to loss of resolution. They should also have a relatively high viscosity when compared with alternative printing processes such as inkjet and flexography, to ensure that the ink distributes evenly and only passes through the mesh with squeegee pressure (44).

These properties make screen printing suitable for producing printed electronics. Where functional inks typically have relatively large particle sizes and concentrations, leading to higher viscosity profiles.

2.3.2. Functional Materials Used in Screen Printing Inks

Due to its ability to print a wide viscosity range, screen printing is regularly used for depositing functional inks in manufacturing a range of printed electronics. This includes electroluminescent lamps, where screen printing can be used to deposit all layers including phosphor-based inks, insulating dielectrics and conductive electrodes. The conductive electrodes can be silver nanowire or carbon nanotube (CNT) based to produce a semi-transparent conductive layer (3). Electrochemical sensors also use screen-printing, to deposit conductive carbon and silver layers, along with the insulating dielectric layer (8). Perovskite solar cells are also partly screen-printed, where layers of mesoporous titanium dioxide (TiO_2), Zirconium dioxide (ZrO_2) and carbon inks are screen printed to build up the multi-layer screen printed mesoporous stack (c-PSC) (6).

Materials such as silver, copper and carbon are regularly used to produce conductive tracks and electrodes in screen-printed electronic devices. Silver inks can typically be characterised as three main forms. These include silver solutions, microparticle inks (particle size $> 1 \mu\text{m}$) and nano particle inks (particle size $< 1 \mu\text{m}$). Screen-printing is typically used for depositing microparticle inks or higher viscosity nanoparticle inks as it can accurately deposit thick, consistent films with minimum pressure, over a wide area at economical production rates (20). Screen printed silver inks and pastes are regularly used in producing a range of printed electronics which

require high electrical conductivity (46). Including silicon Photovoltaic (PV) solar cells, Radio Frequency Identification (RFID) aerials, as well as flexible and stretchable circuits for membrane switches and wearable thin film transistors (20,47,48).

However, silver is very expensive and its prices fluctuate over time, which leads to problems in cost estimation (46). Copper and carbon-based inks offer a more economical alternative for conductive inks. Copper inks can produce a resistance similar to that of silver inks, but copper tends to rapidly oxidise over time. As copper oxide (CuO) is insulating, this can lead to reductions in conductivity over time (46,49,50). As well as this, copper is typically printed in its precursor form of copper oxide as nanoparticles. To convert the copper oxide into conductive copper, the print must be sintered to create conductive pathways between the nanoparticles and increase their packing density (49). However, as copper has a high melting temperature and must avoid oxidising, sintering must occur quickly at high temperatures. This is not possible with conventional thermal sintering in dryers and ovens. This also limits their use with thermally sensitive substrates, such as cost-effective polymer films including PET and PEN which are regularly used in printed electronics (46,50). However, photonic methods such as intensive pulsed light (IPL) sintering and annealing, which provide a rapid burst of high energy, have been found to rapidly sinter the copper oxide nanoparticles. This can make them conductive without damaging heat sensitive substrates (49,50).

Carbon is also an alternative low-cost conductive material. It is more economically viable than silver and does not require high energy sintering like copper. Carbon also has other advantages, such as chemical inertness and its ability to be modified or functionalised through the addition of atoms of different elements to the edges of flakes, which is advantageous for electrochemical sensors. It is also able to act as an intercalating material for energy storage and is easier to dispose of than alternative conductive materials (26). Carbon is also available in a range of morphologies, making it viable for use in a wide range of applications. This made carbon the most viable material for conducting a range of investigations within this thesis.

2.3.3. Carbon-Based Screen-Printing Inks

Screen-printed carbon inks and pastes are widely used in the manufacture of a range of printed electronics applications due to their electrical conductivity and relatively low cost. These include resistive heaters (4,5), electrochemical sensors (9), printed batteries (12), Perovskite PV (6,7), as well as energy harvesting in the form of printed pyroelectrics (13) and thermoelectrics (14). These inks typically consist of a range of carbon morphologies to tailor the performance and cost of the inks.

2.3.3.1. Carbon Morphologies

Graphite, carbon black and graphite nanoplatelets (GNPs) are the primary forms of carbon used in a large proportion of these devices in industry and the focus of this thesis. This is due to their ease of use and economic advantage over other commercial conductive materials, such as silver and more recent derivatives of carbon such as graphene and carbon nanotubes (CNTs). Although graphene and CNTs are preferred for highly conductive, thin, flexible and semi-transparent applications.

Graphite is a multi-layered planar crystalline structure, consisting of stacks of parallel two-dimensional (2D) carbon layers held together by Van der Waals bonds. Individual carbon layers consist of sp^2 hybridized carbon atoms bonded in hexagonal rings (Figure 2.3) (51). Graphite flakes are typically tens of microns in length and are conductive primarily along their planes (26). Graphite is a very cheap morphology of carbon, although it can lead to worse print roughness and conductivity due to the geometry of the flakes. It is regularly used in combination with other carbon morphologies to reduce costs in conductive carbon inks. If the graphite flakes are partly exfoliated, then GNPs can be produced, which consist of tens to hundreds of carbon layers, with a platelet thickness of around 0.34 nm to 100 nm (51,52). These are a little more expensive than graphite, but due to their smaller size and better aspect ratio, can produce smoother prints. Randomly oriented graphite flakes can lead to greater deviations in the print profile than randomly oriented GNPs, leading to lower print roughness. The smaller sizes of the GNPs also enable them to be printed through finer meshes to produce finer print features. However, further work is required to understand the effect of screen printing on the orientation and interaction of the deposited particles and flakes.

Carbon black on is an amorphous form of carbon. It consists of nearly spherical primary particles, fused together in aggregates. This produces a submicron scale, roughly spherical particle with a high surface area (26,53). Carbon black is widely used due to its low cost. However, when compared with the other morphologies of carbon, carbon black has a high percolation threshold for electron conduction. This is due to the large contact resistance between carbon black particles (5). However, when it is combined with larger carbon morphologies such as graphite or GNPs in inks, they can be readily dispersed in the composite matrix. Here they form conductive bridges between neighbouring graphite flakes or GNPs to enhance the electrical conductivity of the ink (26,54).

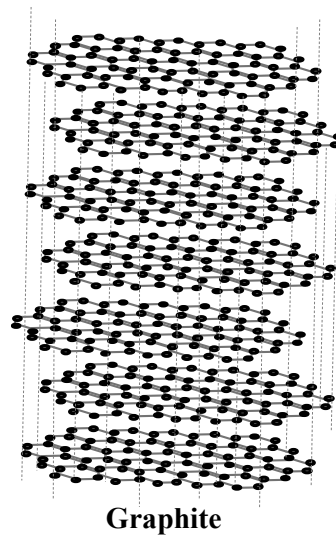


Figure 2.3 Graphite atomic structure

2.3.3.2. Carbon Concentrations

The concentration of carbon particles and flakes in an ink can determine the conductivity and resistivity of the composite printed film produced. Percolation models have been used to describe the relationship between resistivity and the concentration of conductive particles in an insulating matrix, such as a polymer base used in screen-printing inks (55–57).

For inks containing a low percentage of conductive particles and flakes, there would be an insufficient number of conductive pathways present for electrical conduction to penetrate or percolate through the ink. As the particles would be distributed throughout the volume of the insulating host (55,56). This creates a very high resistivity within the ink. When increasing the percentage loading of conductive

particles and flakes within the ink, a point will be reached where the number of agglomerating particles in the non-conductive matrix are sufficient. At this point, the first connected conductive pathway, extending through the composite is formed (55). This is illustrated in Figure 2.4.

Due to the effect of optimising the percentage loading of conductive particles on the electrical performance of screen-printed inks, past studies have assessed the effect of carbon concentrations and morphologies on print conductivity. Oxfall *et al.* (54) and Phillips *et al.* (26) investigated the effect of adding carbon black to graphite nanoplatelet (GNP) and graphite-based inks on the electrical performance of the prints respectively. Oxfall *et al.* (54) found that replacing 10 wt% of the conductive GNPs with carbon black led to a reduction in the electrical percolation threshold from 6.9% to 4.6%, leading to more conductive inks with a similar rheological profile and print quality. Phillips *et al.* (26) identified the optimal ratio of carbon black to graphite carbon morphologies in an ink, for producing the highest conductivity. Where inks containing a carbon loading of 29.4% by mass achieved optimal conductivity ($0.029 \Omega \text{ cm}$) at a graphite to carbon black ratio of 2.6 to 1. Whereas a carbon loading of 21.7% (Mass) had a lower optimal ratio of 1.8 to 1.

Both experiments found the changes in concentrations and ratio of carbon morphologies led to alterations in the rheological profiles of the inks. Thus, leading to subsequent changes in the ink transfer mechanism. As well as changes in the topographical profiles of the prints, due to the roughness of the carbon morphologies. Experiments have also been conducted to optimise the carbon concentration in an ink through dilution studies, to assess how print performance alters with incremental changes in viscosity and viscoelasticity (22,55). These analyses identified the gradual reduction in the rate of improvement in conductivity with increases in conductive particles. The optimal loading concentration was also identified, after which no further improvements were made in the print conductivity.

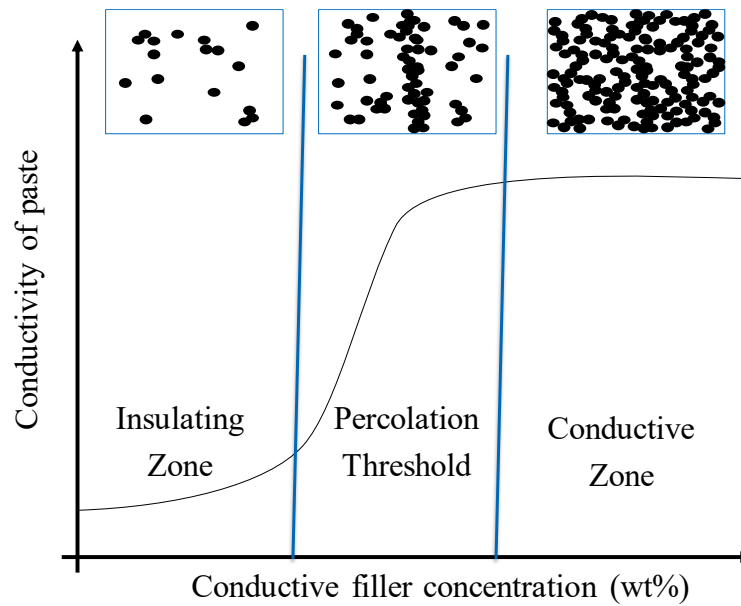


Figure 2.4 Percolation of electrically conductive particles in a paste

2.4. Screen-Printing Models

Despite there being a range of literature on the effects of altering press parameters settings and ink rheology on the print quality and performance, there is a limited understanding of how the ink is deposited during screen-printing. In terms of how it transfers from the mesh to the substrate and how it is subsequently separated. This is due to limitations in modelling the rheological properties of screen-printing inks, which are typically pseudoplastic and viscoelastic (44,58,59). This makes it hard to develop predictive models of the screen-printing process. As well as leaving a lack of understanding in the physical mechanisms, which enable screen printing to occur. The deposition process can be split up into two main sections. The first is the ink flow occurring ahead of the squeegee, including the ink in front of and below the squeegee. Followed by the ink flow occurring behind the squeegee, including the separation of ink from the mesh to the substrate.

2.4.1. Ink Flow Ahead of the Squeegee

The flow regimes occurring in the paste flow region ahead of the squeegee have been theorised and computationally simulated in a number of papers. Early mathematical models were suggested by Riemer, based on first principles with maximum pressure at the squeegee tip (39,60,61). As well as by Owczarek and Howland, as three separate flow regions rather than one (62).

Riemer (39) created flow patterns and pressure profiles based on experiments investigating the ink roll ahead of the squeegee. From which, a theoretical model was developed, based on the Navier-Stokes equation. On solving for stream function (ψ) this can be used to generate a plot of streamlines, which Riemer assessed for a range of angles between the squeegee and substrate. For all flow patterns generated, the streamlines were created by incrementing the stream function in a way that creates a constant flow between the traces. Where the separation between parallel streamlines was related to the velocity of ink flow in that region, with smaller gaps representing higher velocities. The locus of maximum pressure was directed towards the intersection of the mesh and squeegee edge, which would provide high pressure for ink injection into the mesh.

Owczarek and Howland (62,63) suggested that the developed flow field in front of the squeegee could be split into three main regions rather than one. These consisted of a pressurisation region, where the viscous and pressure forces dominate, located around where the squeegee contacts the substrate. The downward screen cross flow region, where viscous, gravity and pressure forces are in control. Then finally the paste collection region, which is mainly affected by the inertia and gravity forces at the front of the ink flow.

Following on from these theories, a number of computational fluid dynamics (CFD) models were developed to assess both Newtonian and Non-Newtonian inks (64–66). The work by Jewell and Claypole (66) assessed a range of Newtonian and non-Newtonian inks and the effect of varying viscosities at a range of squeegee angles, nip gaps and squeegee speeds. The fluid pressure was at a maximum at the squeegee tip, but then rapidly decreased with distance away from the squeegee tip. The majority of the ink roll was at zero pressure, complimenting the theory by Riemer. Of those parameters tested, the viscosity and nip gap had the most significant effect on the fluid pressure, whereas the speed and angle were found to be secondary parameters. The size of the ink roll was found to have a negligible effect on the pressure generated at the squeegee tip, with minimal effect on ink transfer or print quality.

Glinski *et al.* (64) assessed the effect of both Newtonian and Non-Newtonian fluids at a range of squeegee contact angles. The results deviated from Riemer's model,

which was designed for an infinite quantity of paste, where the pressure never reduced to atmospheric at any squeegee distance. As the stencil, paste and air contact points are in atmospheric pressure in this case, the results deviate at distances further away from the blade tip. However, there is a good correspondence between Glinski *et al.* and Riemer's Pressure profiles close to the blade tip. When comparing the Newtonian and Non-Newtonian CFD simulations, there were clear differences between the two, with the Newtonian ink behaving similarly to Riemer's model. The velocity streamlines and pressure distribution curves produced for the Newtonian ink show great similarities with Riemer's analytical model, particularly around the blade tip. However, with the non-Newtonian profiles, the area in which the hydrodynamic forces appear to dominate over the gravitational forces occurs over the whole paste flow front. This leads to a quick increase in the paste viscosity after a given distance in front of the contact point due to lower strain.

Clements *et al.* (65) also developed a mathematical model, to predict the pressure profiles produced in the ink flow ahead of the squeegee. In this case, the squeegee blade could be both curved or linear. As with the calculations by Owczarek and Howland, it was assumed only Stokes flow was present and the pressure only depended on the distance measured from the squeegee tip. Fox (40,42) also investigated the effect of the squeegee nip contact area on the ink flow both ahead of and behind the squeegee for a roller squeegee. Here the variation in ink velocity and viscosity was modelled based on an equation derived from the Reynolds equation by Dowson (67) using Stokes equation and continuity which gave a better correspondence with the experimental results.

2.4.2. Ink Flow Behind the Squeegee

The contact of the squeegee, mesh and substrate leading to ink deposition, followed by the separation of the mesh from the substrate has been mathematically theorised by Riemer (39,60,61,68,69) and Messerschmitt (70). Riemer (68) suggested the ink deposition mechanism in screen printing was due to the adhesion of the ink to the substrate, where a pure wetting phenomenon on the ink was great enough to separate the ink from the mesh. This was based on a theory of a two-dimensional rope deflecting under a given load, to calculate the forces required to separate the mesh from the print on the substrate. In later work, Riemer (39) presented an alternative model, describing the function of the wires in the screen mesh as acting in the

manner of pistons in a syringe, or a vacuum pump, as is illustrated in Figure 2.5. In this case, the openings in the mesh are likened to tubes, forcing the ink into the mesh in accordance with the Hagen-Poiseuille law, given in Equation 2.1. (39,69). Where Q is the flow rate, P is the pressure, r is the radius, η is the fluid viscosity and l is the length of the pipe/tubing. This provided a way of calculating the volumetric flow rate through a capillary, which in this case is the holes in the mesh. This can be used to assess the maximum ink velocity possible in a given mesh during snap-off.

$$Q = \frac{\pi Pr^4}{8\eta l}$$

Equation 2.1 Hagen-Poiseuille law

Riemer (39) also suggested that there were two key forces occurring during separation, where the wires are pulled up by the forces acting in the mesh and countered by a downward force acting between the paste and mesh. However, the Hagen-Poiseuille law is designed for incompressible, Newtonian fluids, and assumes the gaps in the mesh behave in the same manner as a pipe. Based on this, he also illustrated that a greater force between the paste and mesh, than that of the lifting force, would result in the mesh strands sticking to the substrate. This is known as the “cling zone”. Whereas a greater lifting force would result in the ink columns being pulled from the meshes during snap-off and transferred to the substrate. After this, the columns would lose their supporting walls and collapse in a region he called the “separation zone”. Although, for optimal print quality, Riemer suggested the separation should occur without a cling zone behind the screen.

Messerschmitt (70) suggested an alternative theory to those identified by Riemer. Messerschmitt believed that the adhesive forces between the substrate and ink could not be the driving force for printing, as suggested by Riemer (68) due to the surface area of the mesh containing the ink, being greater than that of the area of the substrate being printed onto, as that would result in the majority of the ink remaining on the screen and not sufficiently transferring to the substrate. The effect of pressure differentials, gravity and air pressure were also called into question, as it had been found possible to print against gravity and in a vacuum. (71)

Messerschmitt suggested that although these separation forces would be insufficient to break the adhesion between the ink and the mesh, it would be enough to induce a

flow. From which, a shearing action within the ink would be created, which could then cause a cohesive failure. (66,72) Thus enabling the ink to separate between the mesh and substrate. This process was described by Messerschmitt as four key stages of the transfer of the ink to the substrate. These consisted of adhesion, extension, flow and separation, as is illustrated in Figure 2.5. Where the final stage consisted of the ink splitting. Leaving ink remaining on both the surface of the mesh, as well as on the surface of the substrate as the print. (70)

Based on the work by Riemer (39) and Messerschmitt (70), Kapur *et al.* (71) produced a CFD model based on the Landau-Levich equation and capillary number (ratio of viscous forces to surface tension forces), to calculate the volume of ink transferred during the screen-printing process. The model consisted of two main flow regimes, including shear flow occurring over the mesh strand, as well as extensional flow occurring between the mesh strand and substrate, where extensional filament separation occurred during the mesh release phase, as described in Messerschmitt's four key stages of ink transfer. The ink separation mechanism was modelled using boundary conditions based on those used in capillary breakup extensional rheology (CaBER) models. Where filament profiles have been previously developed for both shear thinning and viscoelastic fluids being extended at a constant rate between two plates (73,74).

However, this model was based on contact screen printing methods. Thus, neglecting the effect of angular forces, resulting from angular contact between the mesh and substrate, during more typically used off contact screen-printing methods. There is also a lack of CaBER experimental data on fluids which are both shear thinning and viscoelastic, with most research being conducted on Newtonian and low viscosity elastic fluids (75–77). Therefore, screen printing inks would require combinations of the existing filament profiles for different rheological models, which are discussed more in Section 3.2.2.7 (74).

Xu and Willenbacher (78) conducted a rheology and high-speed video imaging study on fine line screen printed ZnO pastes in which they assessed the interaction between the rheological properties of the inks and pastes with the actual screen-printing process. Their study imaged the deposition of ink during screen printing with a commercial screen printer and high-speed camera fixed directly below the substrate,

looking up at the print. This was used to capture the motion of the paste, squeegee, screen and the flow of the ink after deposition. Their work identified three main regions, including a length of ink deposited ahead of the squeegee, defined as the pre-injection zone. A length between the nip contact point and snap off position as defined by Riemer (1989) as the cling zone. Which Xu and Willenbacher (2018) found to be linearly related to the fracture strain of the ink, assessed using CaBER testing. The final stage consisted of paste spreading, which is where the ink slumps after it has been deposited. Which in this case was used to assess the effect of the spreading time on the width and resolution of the printed pattern.

Although this provides an insight into the size of the cling zone and quantity of paste spreading after print deposition, it does not confirm whether the separation models suggested by Riemer or Messerschmitt were in fact correct. There is currently no experimental proof to determine whether either of these models actually describe the mechanism by which ink is transferred from the mesh to the substrate. Therefore, to identify the true ink transfer mechanism occurring, experimental studies are required to provide validation and potential boundary conditions for future computational models.

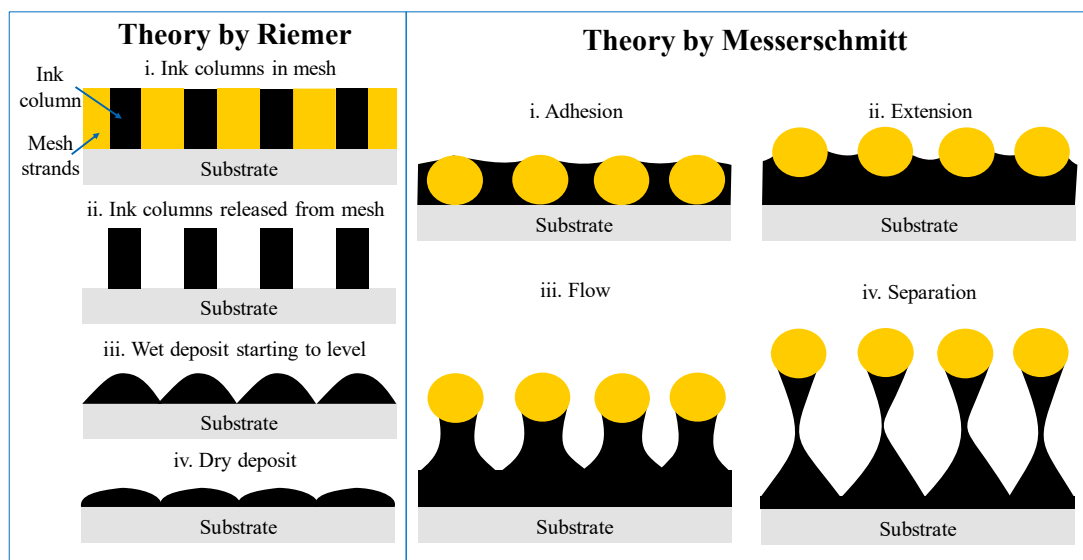


Figure 2.5 Riemer and Messerschmitt's theories of ink flow and separation behind the squeegee.

2.5. Drying and Post Processing

2.5.1. Drying Techniques

As many screen-printed electronics inks are water or solvent based, drying is typically done using an in-line conveyor dryer or oven (26,79). However, the settings used depend on a combination of the boiling point of the solvent(s) used in the ink and the maximum temperature at which the substrate is stable (e.g. glass transition temperature of polymer substrates) (80). This can result in long drying times.

2.5.2. Post Processing

2.5.2.1. Photonic Annealing

Photonic methods, in the form of intensive pulsed light (IPL) sintering and annealing, have been used as a method of providing further improvements in print performance after traditional drying methods have been conducted. It provides a rapid burst of high energy to heat materials, such as metal nanoparticles and copper oxide. This allows them to sinter and become conductive. It can also heat the print to high temperatures without damaging low cost substrates, such as polymer films or paper (49,50). This provides opportunities for low cost plastic electronics. IPL sintering and annealing has been used in a range of printed electronics, such as photovoltaic applications (81–83), enhancing the electrical performance of RFID (radio frequency identification) tags (84,85) and other forms of printed electronics (86,87). As a result, photonic annealing has been identified as a lower cost alternative to high energy, thermal processes. This enables a higher throughput, along with improvements in the surface roughness, edge resolution and conductivity of the prints. Arapov *et al.* (88) used photonic annealing to reduce the resistance of printed binder-based graphene inks from 200 Ω /square after thermal drying at 100 °C for 5 minutes (based on 6 μ m dry film thickness), to 40 Ω /square after photonic annealing.

Despite improvements in electrical performance, it was noted that photonic annealing also resulted in a reduction in layer adhesion and cohesion. The degradation of the binder caused a decrease in the number of contact points between the graphene sheets and therefore a loss of structural integrity. (88).

2.5.2.2. *Compression Rolling*

To counteract this disruption, Arapov *et al.* (88) used compression rolling to improve the structural integrity of the prints. This also provided further improvements to resistivity, reducing it to 20 Ω /square, along with a reduction in film thickness and surface roughness from 6 μm and 0.945 μm respectively after thermal drying to 1.7 μm and 0.065 μm respectively after photonic annealing followed by compression rolling. (88) Compression rolling alone has also been investigated as a possible post processing method for a range of applications, including radio frequency identification (RFID) antenna and other graphene-based prints and coatings. These cases used binder free deposits, where it produced improvements in the electrical and thermal conductivity of the devices due to better flake alignment (88–91). There are also reports of compression rolling leading to improvements in the electrochemical performance of screen printed lithium ion batteries, with electrodes consisting of graphite (92–94) and amorphous carbon (95). In these cases, the compression rolling process has been found to reduce the roughness of the electrode by compressing the graphite flakes to become orientated with the basal plane, parallel to the current connector. (94) This led to increases in the electrode's density and a reduction in porosity, which enabled improvements in the ionic and electrical conductive pathways. (92,93)

Although these analyses assess the effect of photonic annealing and compression rolling on single morphologies of carbon, these processes could also provide an effective method for improving the electrical performance of inks containing a range of carbon morphologies, without having to change the ink formulations.

2.6. Chapter Closure

There is literature on the effect of ink rheology and process parameters as well as modelling techniques. However, there is an issue in how these all link together. Studies of process parameters have often been limited to a certain ink type. As the effects of press parameters alter with the ink being used, further investigation is required. As well as this, modelling techniques for the screen-printing process have not been considered for many years, with theories developed prior to the growth of

printed electronics. This identifies a knowledge gap that must be filled with original research.

Therefore, this thesis will follow a multifaceted approach encompassing all aspects of the production of printed carbon inks from ink formulation, through screen-printing, to drying and post processing, as illustrated in Figure 2.6. These experiments were conducted to provide a better understanding of the effect of press parameters and post processing techniques on screen-printed functional materials. As well as providing an insight into how the ink is deposited from the mesh to the substrate to provide possible validation for one of the existing models. Such insights could lead to the development of predictive methods as well as improve the understanding of how to optimise the print quality and performance of screen-printed functional materials. This is elaborated as summarised in the following subsections

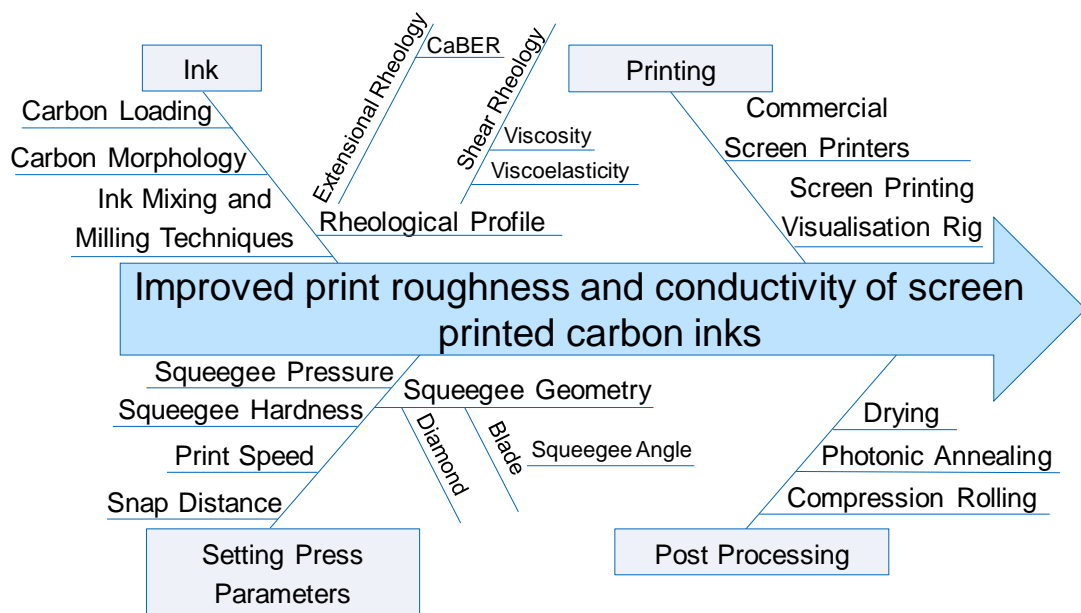


Figure 2.6 Cause and effect diagram of thesis components for improving the print performance of carbon-based screen-printing inks.

2.6.1. Effect of parameters on a graphite-based ink

Screen-printing press parameter settings have been found in the literature to have a range of effects on the print quality produced depending on the print pattern, substrate and ink used. Therefore, the fourth chapter of this thesis will explore the effect of altering a range of press parameters for a simple, carbon-based ink.

Whereas the literature has explored the effect of commercial inks, this simple ink

containing only one carbon morphology in a plain resin without any additives limits the number of variables which may interact with the parameter settings

To ensure the ink is prepared using the optimal methods and created consistently between batches, a study will also be conducted on the effect of optimising ink mixing and milling techniques to improve the print performance.

2.6.2. High speed imaging the ink transfer mechanism of screen-printed carbon pastes

The literature has identified a lack of understanding of the mechanism by which the ink is transferred through the mesh and onto the substrate. There are two main mathematical models by Messerschmitt (70) and Riemer (39), but these models provide contradicting theories, lack experimental validation and date back to the 1980s. Therefore, the fifth chapter in this thesis will focus on developing a method by which the deposition and separation mechanism can be visualised. Enabling a way of identifying whether the mechanism resembles either of the models and if the effect of parameter settings can be visualised, quantified and compared to the print quality produced.

2.6.3. The effect of ink composition on ink transfer mechanisms

The literature identified a link between the rheological profile of the ink and the optimal parameter settings, suggesting there are interactions between process parameters and ink properties. Therefore, the sixth chapter of this thesis will investigate a range of carbon inks with different rheological profiles, to assess whether they follow a similar deposition and separation mechanism. As well as whether there are quantifiable changes between the deposition mechanisms of the different inks. This will identify the effect of gradually diluting a commercial carbon ink containing a range of carbon morphologies on incremental changes in rheology and subsequent separation methods. Followed by investigations into the effect of inks containing only 1 carbon morphology at a time in various concentrations, to identify how alterations in individual elements of the ink influence the deposition mechanisms. Assessments of the topography and print performance will also be conducted to compare changes in print quality with changes in the deposition mechanism. Overall, this will provide a better understanding of the effect of rheological profiles, as well as the geometry and concentration of functional

materials on the deposition mechanism and how it relates to the conductivity and topography of the prints produced.

2.6.4. Effect of photonic flash-annealing with subsequent compression rolling on the performance of carbon-based inks

The literature identified possible post processing techniques for improving the electrical performance of prints. Photonic annealing was able to lead to improvements in the electrical performance of prints without causing damage to heat sensitive substrates. This could offer a viable method for enhancing the performance of carbon prints on polymer substrates which would typically become damaged by comparable temperatures with traditional drying methods.

However, some studies found that photonic annealing led to reductions in the mechanical stability of the print but found that subsequent compression rolling could be conducted to restore the mechanical stability. It also provided further improvements in the electrical performance. In the seventh chapter, the effect of photonic flash annealing with subsequent compression rolling was assessed for carbon inks containing a range of carbon morphologies. Therefore, the effect of the post processes on the topography, microstructure and electrical performance of carbon-based inks could be assessed as well as establishing which carbon morphologies, or combinations of morphologies benefitted from the processes.

Chapter 3. Materials and Methods

3.1. Screen-Printing

Screen-printing was conducted on flatbed presses to assess the effect of parameter settings and ink rheology on print quality. For the experiments conducted, two presses detailed below were used to conduct parametric studies in order to assess a range of settings. A minimum of ten prints were conducted for every setting to provide sufficient prints for a statistically robust analysis.

3.1.1. Dek 248

The Dek 248 is a semi-automatic flatbed screen printing press. It can be used with a range of different mesh sizes and materials, squeegee geometries and hardnesses, squeegee speeds, snap off distances and quantifiable squeegee pressures. It is capable of printing at squeegee speeds of up to 70 mm s^{-1} and can take frame sizes of $508 \text{ mm} \times 508 \text{ mm}$. Although screens of $300 \text{ mm} \times 240 \text{ mm}$ can be used with an adapter frame. The snap off distance is set digitally and can be adjusted between 0 and 25 mm. While the squeegee pressure is set with a physical dial and can be adjusted in terms of the downward squeegee force, between 0 and 15kg. It can have up to two squeegees fitted to enable printing in both directions. Or a flow coater blade fitted along with a squeegee to produce a flow coat prior to printing. It also has a 2-camera system to enable alignment for producing multiple layers.

In these experiments, a $300 \text{ mm} \times 240 \text{ mm}$ screen was used with a polyester mesh containing 61 threads per cm, a $64 \mu\text{m}$ thread diameter, with 13-micron emulsion and the mesh mounted at 24° to the frame. The substrate used was PET (polyethylene terephthalate— Melinex® 339, DuPont Teijin Films ($175 \mu\text{m}$ thickness) opaque white). This mesh and substrate were chosen as they were suitable for the carbon-based inks being printed. The inks and other parameters used were varied to study their effects on print quality.

3.1.2. Svecia Matic

The Svecia Matic is a three-quarter-automatic flatbed screen printer. Like the DEK screen printer, it is capable of assessing different parameters but is also capable of taking larger screens of up to $550 \text{ mm} \times 750 \text{ mm}$ and printing at far higher speeds. The range of $0.05\text{-}2 \text{ m s}^{-1}$ ($50\text{-}2000 \text{ mm s}^{-1}$) would enable a more thorough analysis

of the effects of speed, which are comparable with those used in industry. It is also capable of adjusting the squeegee angle from 60° to 90° to the substrate, whereas the Dek could only use diamond squeegees or squeegee blades at fixed angles. This enables a more thorough analysis of squeegee effects. As with the Dek, it can also have a flow coater blade fitted alongside the squeegee to produce a flow coat prior to printing. The snap distance is set manually and measured. The snap distance on the Svecia was set to the nearest 0.5 mm. As well as this, the squeegee pressure was controlled by a screw thread system, which adjusted the linear height of the squeegee. This made it harder to keep constant, although this was partially overcome using a piece of substrate attached to two spring balance sets (Appendix I). The speed of the press was measured using an Arduino controlled LDR system (Appendix I).

These experiments used the same substrate and mesh properties as with the DEK trials to provide comparison. Although the prints were conducted with a larger screen, with a frame size of 508mm x 508mm to accommodate for the larger press and squeegees. As with the DEK trials, the press parameters used were varied to study their effects on print quality.

3.2. Screen Printing inks

3.2.1. Ink Making

3.2.1.1. Resin Preparation

Resins were prepared by measuring out the required mass of powdered resin and placing that in a pot to be decanted. The required mass of solvent was then measured into a glass beaker, which was fixed in place on a hotplate with an overhead stirrer placed into the beaker. Magnetic stirrers were used instead of overhead stirrers for lower viscosity formulations, with the magnetic stirrer mode on the hotplate enabled. Solvents were preheated to a set temperature required to melt the polymer being added (typically around 70°C). Once the solvent was at temperature, the powdered resin would be gradually added, increasing stirring speeds as the polymer content increased, until all of the powdered resin was added. To ensure the granules were definitely dissolved, the resin was heated and stirred for one hour after all polymer granules had ceased to be visible, leaving a clear resin.

3.2.1.2. Mixing and Milling in Functional Materials

Once the resin was cool, the required mass of resin for an ink was weighed into a pot. The required mass of functional materials was then weighed out, gradually added and stirred into the resin by hand. The ink slurry was then dispersed in a paint shaker, then left to wet overnight before milling. Milling was conducted with an EXAKT80E three-roll mill (EXAKT Advanced Technologies GmbH). The three-roll mill works by passing the ink slurry through rollers with a smaller gap size between the final two rollers (Figure 3.1). The gaps between the back and middle rollers, as well as between the middle and front rollers, could be set according to the degree of milling required. Along with the speed of the front roller to set the rate. Milling techniques such as bead milling and three roll milling can be used for wetting, grinding and dispersing solids into liquids to refine the dispersion of the pigment in the ink. This is popular with highly viscous inks with large, agglomerated particles, such as those being used in these experiments.

Stirring techniques, such as using an overhead stirrer are simple and well-established processes. which can be used to improve the distribution of the particles in the ink. However, traditional overhead stirrers tend to have the propeller located in one area of the pot of ink being stirred and may cause some areas to shear more than others. This leads to potential areas of high and low shear in the ink. Overhead stirring was used as one of the two mixing/stirring processes assessed for improving ink homogeneity. This was conducted on the Heidolph overhead mechanical stirrer (model RZR 2021), with a stainless-steel propeller containing 4 straight blades (50mm diameter).

Centrifugal mixing was assessed as an alternative to overhead stirring. The system being used was a Speedmixer™ DAC 150.1 (FVZ-K) which uses dual asymmetric centrifugal mixing. This is designed to enable rapid mixing and grinding of materials and is a faster process than overhead stirring. To identify which process was best for creating the most conductive, homogeneous ink, a mixing study was conducted in Section 4.3.2, with the technique which created the most conductive ink used for

producing the inks in all parametric studies.

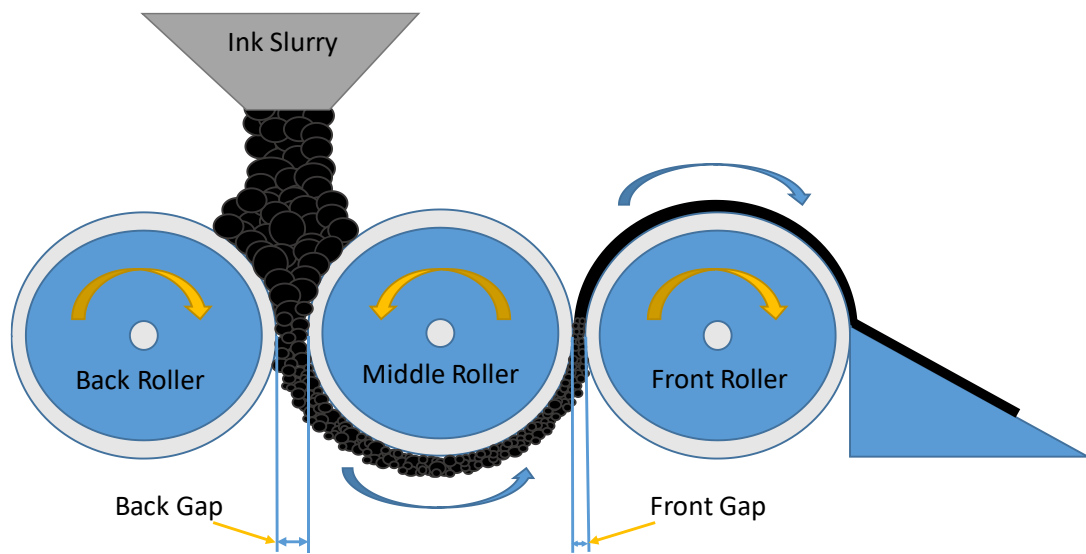


Figure 3.1 Schematic diagram of three-roll miller

3.2.2. Rheological analyses of inks

3.2.2.1. Ink Rheology

As inks are non-Newtonian fluids, they can be characterised in terms of their rheological profile. Rheology is defined as the study of flow and deformation of matter. In the case of inks, rheological analyses can be used to determine how the ink will behave in a range of conditions, which it will be subject to during the printing processes.

3.2.2.2. Viscosity

Viscosity (η) is defined as a liquid's resistance to flow. It was quantified by Newton as the force per unit area of shear stress required to induce a steady, simple flow, as given in Equation 3.1. Where σ is the shear stress and $\dot{\gamma}$ is the shear rate, defined as the change in velocity (v) for a given change in distance (h) (96).

$$\sigma = \eta \dot{\gamma} = \eta \frac{\delta v}{\delta h}$$

Equation 3.1 Shear Viscosity

In the case of Newtonian fluids, the viscosity is constant with changes in shear rate and time, with a linear relationship between shear stress and shear rate. Non-Newtonian fluids display changes in viscosity with changes in shear rate. Fluids with time dependent viscosities can either be rheopectic or thixotropic. Where thixotropic

fluids will reduce in viscosity with increasing shear time, while rheopectic fluids increase in viscosity with increasing shear time. In both cases, the material will gradually return to its initial viscosity when shearing ceases.

Whereas fluids which change in viscosity with the rate of shear can be characterised as shear thinning (pseudoplastic) fluids, shear thickening (dilatant) fluids or Bingham plastics. In the case of Bingham plastics, there is no flow observed below a critical yield stress. After the yield stress is reached, the stress appears to observe a linear relationship between shear stress and shear rate, as with a Newtonian fluid. In the case of Dilatant fluids, as shear rate increases the particles in the fluid start to interlock, causing increases in viscosity. With pseudoplastic fluids increases in shear rate led to particles aligning with the flow, leading to reductions in viscosity. This is the case with most paints and inks which can be pseudoplastic or thixotropic and therefore influenced by the speed of printing or the duration over which it is printed.

As viscosity is not constant for non-Newtonian fluids, Newtons equation is not capable of determining their viscosity. To try and mathematically model the apparent viscosity of pseudoplastic fluids as a function of shear rate, a number of mathematic models have been produced. These describe different stages of the changes in viscosity with shear rate (Figure 3.2) (97). The Cross model is able to describe the whole curve of the changes in viscosity with shear rate of a pseudoplastic fluid, as given in Equation 3.2. Where η is the measured viscosity, η_0 is the zero-shear viscosity, η_∞ is infinite-shear viscosity, while K and m are constants. In this case, K provides the dimensions of time and m is a dimensionless constant between 0 and 1. Where 0 defines a Newtonian fluid and 1 is the most shear thinning possible (97).

$$\frac{\eta - \eta_\infty}{\eta_0 - \eta_\infty} = \frac{1}{1 + (K\dot{\gamma})^m}$$

Equation 3.2 The Cross model

However, this can be quite a complex model. When simplified, the Cross model can be reduced to the Power-law and Sisko models. The Power-law model is given in Equation 3.3 and the Sisko model is given in Equation 3.4. Where $k=K^n$ and is known as the consistency (Pa.sⁿ), while n is a dimensionless constant known as the power law index. As with m, the power law index (n) ranges from 1 for Newtonian liquids towards 0 for very non-Newtonian liquids. The Power-law model can be used

for fluids at shear rates of around 1 s^{-1} to 1000 s^{-1} . Whereas the Sisko model can be used for shear rates between 0.1 s^{-1} to 1000 s^{-1} (97,98). Therefore, the Power-law model can be used to fit the viscosity range found in screen printing inks and is referred to later when identifying the ink separation mechanisms observed in screen printing in Sections 5.3.1.2 and 6.3.1. However, these models only consider the shear thinning nature of screen inks, which can also be viscoelastic.

$$\sigma = k\dot{\gamma} \text{ or } \eta = k\dot{\gamma}^{n-1}$$

Equation 3.3 The Power-law (or Ostwald-de Waele) model

$$\sigma = k\dot{\gamma}^n + \eta_{\infty}\dot{\gamma} \text{ or } \eta = k\dot{\gamma}^{n-1} + \eta_{\infty}$$

Equation 3.4 The Sisko model

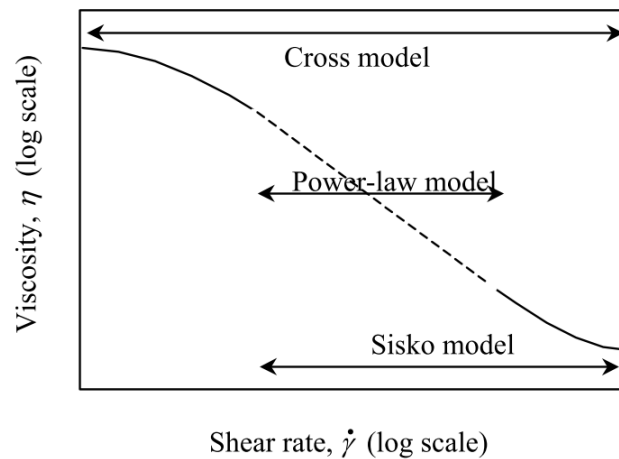


Figure 3.2 Diagram to show the different regions that the Cross model, Power-law model and Sisko model cover (97)

3.2.2.3. Viscoelasticity

Viscoelasticity is a property of fluids that exhibit both elastic and viscous behaviours during deformation (99). Most structural fluids exhibit a degree of viscoelasticity, as there is a natural rest condition. This represents a minimum energy state, which the fluids will try to return to following deformation. The movement from the rest state represents a storage of energy, in the form of an elastic force which will try to return to the minimum energy state (97). In the case of a polymer dispersion, elasticity may be seen due to polymer chains acting like unfolding springs.

To determine the stress and strain interactions of the viscoelastic materials, the fluids can be modelled by defining their viscous and elastic components (99,100). Using a rotational rheometer, a range of tests can be conducted to assess the viscoelastic response of a fluid under a range of conditions. The effect of creep can be assessed by applying a constant stress to the fluid under assessment, with the resultant strain recorded. Oscillatory testing can be conducted to assess the effect of frequency and amplitude, by applying an oscillating stress or strain to the fluid and assessing the resultant oscillatory strain or stress produced. As well as this, stress relaxation can be monitored by applying a sudden, constant strain, where the decay in resultant stress over time is monitored (97).

The experiments conducted in this thesis assessed the changes in the elastic and viscous components with oscillatory tests over a range of frequencies and amplitudes. Oscillatory tests are conducted with a sine-wave-shaped input of either stress or strain, which is resolved into resultant sinusoidal stress or strain outputs. From this, the in phase regions are the solid-like responses and the out of phase regions are the liquid like responses, as shown in Figure 3.3 (97,101).

The material is subject to an oscillatory strain with the angular frequency (ω), given as $2\pi f$ where f is the frequency in hertz (Hz). From Figure 3.3, expressions can be derived for strain (γ) and shear stress (τ), shown in Equation 3.5 and Equation 3.6 respectively (101). Where t is time, γ_o is the strain amplitude, τ_o is the shear stress amplitude and δ is the phase angle (loss factor, phase lag) between the shear stress and strain.

$$\gamma(t) = \gamma_o \sin(\omega t + \delta)$$

Equation 3.5 Resultant strain of viscoelastic material

$$\tau(t) = \tau_o \sin(\omega t)$$

Equation 3.6 Shear stress applied to viscoelastic material

From these expressions, the dynamic moduli for the solid and liquid components can be given. The solid component is defined as the storage modulus (G'), as shown in Equation 3.7. Whereas the liquid component is defined as the loss modulus (G''), given in Equation 3.8. The units of both moduli are in Pascals (Pa) (17,101).

$$G' = \frac{\tau_o}{\gamma_o} \cos (\delta)$$

Equation 3.7 Storage Modulus (G')

$$G'' = \frac{\tau_o}{\gamma_o} \sin (\delta)$$

Equation 3.8 Loss Modulus (G'')

By combining G' and G'' together, the complex shear modulus (G*) is produced, as shown in Equation 3.9 When there is an ideal elastic solid G''=0 and G*=G'.

Whereas an ideal fluid is present when G'=0 and G*=G''. The ratio of the viscous and elastic moduli is defined as the phase angle (δ), which is a dimensionless value, as shown in Equation 3.10. Where a phase angle of 0° would be a complete solid and an angle of 90° would be a complete liquid (97).

$$G^* = G' + iG''$$

Equation 3.9 Complex shear modulus

$$\tan \delta = \frac{G''}{G'}$$

Equation 3.10 Phase angle (loss factor)

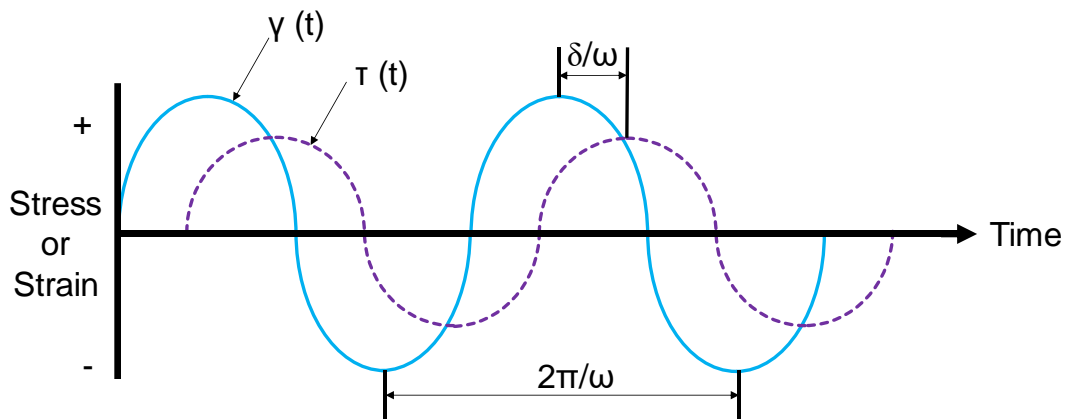


Figure 3.3 Viscoelastic response of material with time lag between shear stress and strain.

3.2.2.4. Packing factor

In screen printing, functional inks typically contain particles and flakes of sizes greater than 1 μm, such as graphite, creating coarse dispersions or suspensions.

Although they can also come in the form of colloidal dispersions containing particles smaller than 1 μm , such as carbon black. The rheological profile of the ink can be influenced by the particle size, geometry and concentration which can influence the ink flow due to particle interactions and the way the flow diverges around them.

Einstein's equation for infinitely dilute, non-interacting hard spheres first described the relationship between the concentration of particles in dispersion and the viscosity of the dispersion medium (97,102–104). This is given in Equation 3.11, where η is the measured viscosity, η_0 is the Newtonian continuous phase viscosity, and ϕ is the volume fraction of spheres in the suspension (97,102). Additionally, $[\eta]$ is the intrinsic viscosity of spheres, found to be 5/2 by Einstein.

$$\eta = \eta_0(1 + [\eta]\phi)$$

Equation 3.11 Einstein's equation for infinitely dilute, non-interacting hard spheres

However, Einstein's equation did not account for the shape of the particles, which can also affect rheology. Due to the particle geometry influencing the streamlines in flow, non-spherical particles can increase the viscosity of the dispersion as the flow must diverge more around these geometries. Barnes created the equations given in Equation 3.12 and Equation 3.13 to account for this in the cases of rod like and oblique particles, where p is the axial ratio (97). Rods have the greatest effect on the relative viscosity of a dilution, followed by plates, then grains, with spheres having the least effect on increasing the viscosity.

$$[\eta] = \frac{7}{100}p^{\frac{5}{3}}$$

Equation 3.12 Barnes' equation for rod like (prolate) particles

$$[\eta] = \frac{3}{10}p$$

Equation 3.13 Barnes' equation for disc-like (oblate) particles

Although Barnes equation accounts for shapes, it is only true for low concentrations of suspended particles, as with Einstein's equation. To overcome this, equations for medium-to-high concentrations of particles were also developed. Krieger and Dougherty developed a semi-empirical equation for the concentration dependence of

the viscosity, as shown in Equation 3.14 (96,105). Where ϕ_m is the maximum packing fraction, or volume fractions at which just enough particles are in the dispersion for the viscosity to become infinite (96,97). ϕ_m is dependent on the particle size and shape, therefore providing more freedom for non-spherical geometries than the previous equations.

$$\eta = \eta_o \left(1 - \frac{\phi}{\phi_m}\right)^{-[\eta]\phi_m}$$

Equation 3.14 Krieger-Dougherty (K-D) equation

Quemada simplified the K-D equation based on experimental works which found that $-\left[\eta\right]\phi_m$ typically simplifies to around 2 (97,106). The Quemada equation is given in Equation 3.15 (106).

$$\eta = \eta_o \left(1 - \frac{\phi}{\phi_m}\right)^{-2}$$

Equation 3.15 Quemada equation

However, there are also cases where inks can contain a range of particle sizes and shapes, which can lead to higher theoretical packing factors than those obtained with single geometries. As the smaller particles can slot into the gaps between the larger particles, mixtures of particle sizes can lead to reductions in the ink viscosity. This is particularly useful for high concentration suspensions (97). Therefore, a range of carbon morphologies were assessed in a range of concentrations in this thesis to experimentally assess the effect of carbon morphologies and concentrations on print performance.

3.2.2.5. Stability of dispersions

In the case of coarse dispersions, particles are likely to wet out over time. This can cause the particles to settle out of the resin and lose homogeneity. Whereas colloidal dispersions are unlikely to settle out, but the particles are subject to small movements by Brownian motion. The homogeneity of the dispersions can also be lost by flocculation of the particles. In which case, particles can form clusters and come out of the colloidal suspension (96,97). Such occurrences can be due to the addition of clarifying agents, or the effect of Van der Waals forces. Due to all particles being attracted together by Van der Waals forces and are held stable by

electrical charges (electrostatically stabilised) or are attached to polymer layers (sterically stabilised). However, this can be overcome by applying a shear force to break down flocs and redistribute the flakes. Therefore, sufficient mixing or stirring of the ink prior to printing was conducted to overcome these issues.

3.2.2.6. Shear Rheology

The viscosity profile and recovery time of an ink from a given shear rate, as well as the viscoelasticity profiles of the inks were assessed using shear rheometers.

Rotational rheometers have three main geometries, consisting of a cone and plate pair, plate and plate pair and a coaxial cylinder system. Screen printing inks are typically measured using a parallel plate or cone and plate system (Figure 3.4). In the case of cone and plate systems, there is an even shear rate ($\dot{\gamma}$) across all of the ink, which are good for highly viscous inks, as described in Equation 3.16. Here δu is the speed and δh is the distance between the cone and plate. If the cone angle is small, at 4° or less, then the gap between the cone and plate can be given as $r\theta$. Where r is the radius and θ is the angle between the cone and plate in radians. Thus, the shear rate can be simplified into terms of the rotational rate (ω) and θ (97).

$$\dot{\gamma} = \frac{\delta u}{\delta h} = \frac{2\pi r/t}{r\theta} = \frac{r\omega}{r\theta} = \frac{\omega}{\theta}$$

Equation 3.16 Shear rate of the cone and plate geometry

However, the small gap at the tip of the cone can trap large particles. Parallel plate systems on the other hand do not have this issue as the gap between the plates can be adjusted. This allows the gap size to be optimised to prevent particles jamming, overcome inertia, while also preventing slip from occurring. Although, with some highly viscous screen-printing inks it can be hard to overcome slip. In such cases, a roughened plate can be used.

The rheometers can either be stress (torque) controlled or strain (rate) controlled. Controlled-stress rheometers have a combined motor-transducer (CMT), where a single motor is used for the top geometry to provide both the motion and torque for measurement. Controlled-strain rheometers use a separate motor-transducer (SMT), where there are two motors rather than one which work synchronously. The motor for the bottom plate works as a torque transducer, while the motor for the top cone/plate is used as a drive unit (107,108). Both rheometers used in these

experiments were CMT rheometers as they are more suitable for higher viscosity fluids.

Shear viscosity measurements were carried out on a Malvern Bohlin rotational rheometer (Gemini Bohlin Nano, Malvern Instruments) with a 2° 20 mm stainless steel cone and a parallel plate (right diagram in Figure 3.4) held at 25 °C. A viscosity test going from 1 s⁻¹ to 100 s⁻¹ and back down was conducted on 30Pa silicon oil (Brookfield Viscosity Standard silicon oil). The sample was specified as having a viscosity of 29840 mPa.s at 25°C. The results were found to be within 3% of the specified value and to behave in a Newtonian manner over the tests conducted. The Bohlin rheometer was chosen to conduct viscosity tests on as it is accurate at low torques, producing smooth results across the full range of strain rates assessed.

Viscoelastic measurements were carried out on a Malvern Kinexus Pro Rheometer (Malvern Instruments) with a 40mm roughened plate and roughened parallel plate (to minimise the effect of slip) (left diagram in Figure 3.4) with tests conducted at 25°C. A SAOS frequency sweep test from 0.1Hz to 10Hz was conducted on a standard viscoelastic material: Polydimethylsiloxane (PDMS) with defined elastic (G') and viscous (G'') shear moduli as defined in Table 3.1 to ensure accurate results were produced. The results on the Kinexus aligned with those defined in Table 3.1. Both tests were conducted a minimum of three times to ensure repeatability of results.

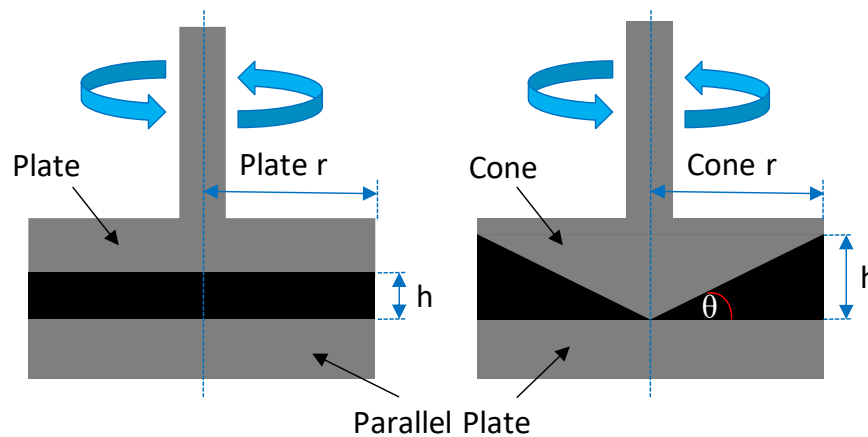


Figure 3.4 Shear rheometers plate and plate (left) and cone and plate (right) configurations

Table 3.1 Polydimethylsiloxane (PDMS) standard viscoelastic sample G' and G'' values at 25°C

Frequency (Hz)	Elastic Modulus (G')	Viscous Modulus (G'')
0.1	3922	8802
0.886	27081	26491
10	82504	37871

3.2.2.7. Extensional Rheology

During ink deposition in screen printing, the ink is subject to extensional flow during the separation of the mesh from the substrate. To investigate whether the extensional rheological profile of the inks relate to the method of ink separation and resultant print quality, extensional rheology tests were conducted. These filament profiles were then compared with those identified during screen printing for different inks. The effects of separation speed and distance on the separation mechanism and quantity of ink left on the lower plate were also assessed and compared with the effect of snap distance and print speed on ink separation mechanisms and print quality seen in screen printing.

There are two main forms of extensional rheometers used for assessing the separation of a body of ink between two surfaces. The filament stretching rheometer (FiSER) and the capillary breakup extensional rheometer (CaBER) (109–111).

Both techniques involve subjecting a sample of ink, between two rigid plates, to uniaxial extensional flow. In both tests, this leads to the formation of a liquid bridge between the separating endplates. However, the techniques for controllably stretching the ink is different. With FiSER tests, the ink is separated at a defined rate profile until the filament breaks. Whereas CaBER tests involve the end plates being separated linearly or exponentially in a rapid step stretch (109,112). Once the plates have reached their separation distance, a liquid bridge is formed between the two endplates. The profile of the liquid bridge then evolves and subsequently breaks under the action of capillary pressure. While the necking (localised rate of thinning) of the liquid filament is resisted by the viscous and elastic stresses in the liquid

bridge (74,111,113). The subsequent evolution of the mid-filament diameter (D_{mid}) is then monitored in relation to time (t) during the process of necking (113). The filament profiles of the most commonly observed modes of capillary thinning are given in Figure 3.5 (74).

For a Newtonian Liquid, the change in D_{mid} with t can be used to calculate the extensional viscosity (η_E), as shown in Equation 3.17. Where σ is the ink surface tension and X is a dimensionless variable dependent on the tensile force and radius of the filament (76,113).

$$\eta_E = (2X - 1) \frac{\sigma}{-\delta D_{mid} / \delta t}$$

Equation 3.17 Extensional viscosity (η_E)

In the case of elastic fluids, the diameter typically decays exponentially. Whereas with Newtonian fluids the filament diameter decays linearly (Figure 3.5) (110). The idealised elastic filament breakup can be modelled as shown in Equation 3.18. Where D_1 is the mid-filament diameter following extension and λ_E is the characteristic relaxation time of the fluid for the elastocapillary thinning action (113,114).

$$\frac{D_{mid}(t)}{D_1} = \exp(-t/3\lambda_E)$$

Equation 3.18 Idealised elastic filament breakup

However, screen printing inks are pseudoplastic as well as viscoelastic, leading to alterations in the extensional viscosity with the amount of shear applied and the relaxation time of the ink. Some pseudoplastic fluids have been found to exhibit sharp necking during filamentation. This can be described with a power-law model based on a cylindrical filament approximation, as shown in Figure 3.5 (115). In the case of a power-law fluid which compiles with the equation $\tau = (K\dot{\gamma}^{n-1}) \dot{\gamma}$, the midpoint radius varies as shown in Equation 3.19. Where n is the power-law exponent, K is the consistency index and $\Phi(n)$ is a numerical constant.

$$\frac{R_{mid}}{R_o} = \Phi(n) \frac{\sigma}{K} (t_c - t)^n$$

Equation 3.19 Midpoint radius for power-law fluid

In this case, where filamentation leads to a singular point of breakup, the midpoint radius is described by a power-law of slope n. However, this has only been found to work for inelastic, pseudoplastic behaving fluids such as foods and consumer products, as well as carbon nanotube (CNT) suspensions (74,116,117). Therefore, with screen-printing inks which are both pseudoplastic and viscoelastic, combinations of the two behaviours may be seen according to the strain and strain rate applied.

Extensional testing of the inks was assessed using a purpose-built capillary breakup extensional rheometer (CaBER) to characterise the uniaxial extensional properties of the inks. Ink samples were placed between two parallel 3 mm diameter stainless steel plates held at a 1mm gap. The upper plate was then moved upwards at a constant velocity to a fixed separation. The change in minimum diameter over time until separation point was measured. The extension and separation of the cylindrical liquid bridges were captured using a high-speed camera (Photron FastCam Mini High-Speed Camera). The images were used to assess the change in minimum radius over time and the relative material flow from bottom to top plates in terms of cross-sectional area of ink split between the plates. As well as the length to separation point from the bottom plate and the volume of ink left behind on the bottom plate, as shown in Figure 3.6. The effect of ink rheology, separation speed and gap size on the filament profile could then be compared with the amount of ink deposited and the ink filament profile observed during screen printing.

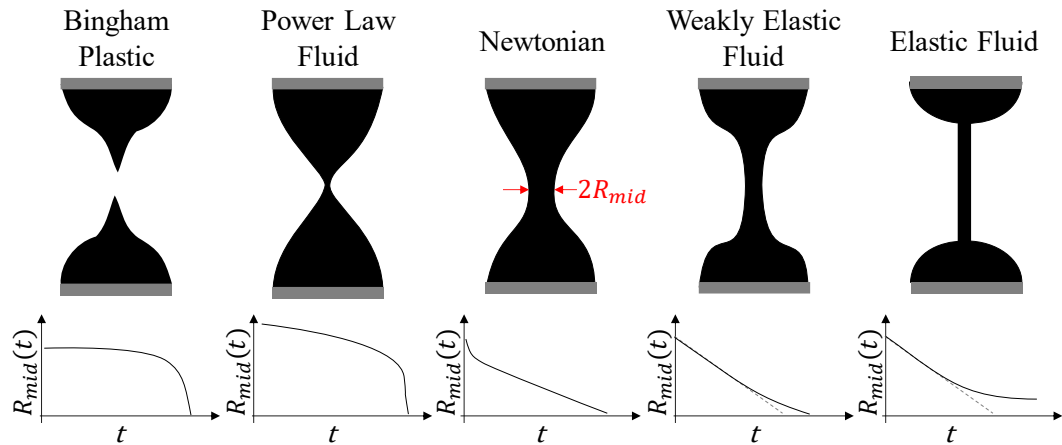


Figure 3.5 Filament profiles of the most commonly observed modes of capillary thinning and break up

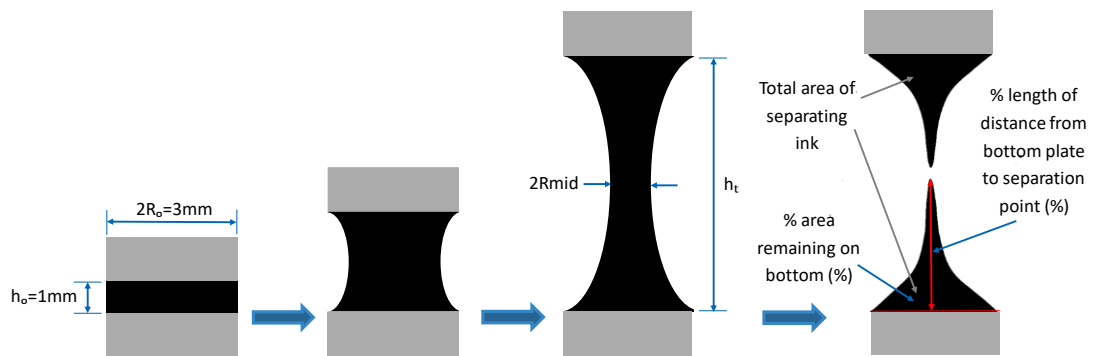


Figure 3.6 Extensional rheology schematic diagram

3.3. Drying and Post Processing

3.3.2. Drying and Curing

3.3.2.1. Dryers & Ovens

As the inks being printed for these experiments were solvent based, the samples could be dried in an oven or conveyor dryer. Temperatures and durations were set to accommodate for the boiling points of the solvent(s) used in the carbon-based inks and the maximum temperature at which the substrate, PET is stable. When dried in the oven, prints were left to dry at between 80 °C - 100 °C for 30 minutes. Whereas samples dried in the conveyor dryer were passed through at 100 °C for 5 minutes.

3.3.2.2. Photonic Annealing

Photonic Annealing using intensive pulsed light (IPL) was assessed for its ability to provide a rapid burst of high energy to heat materials such as metal nanoparticles and copper oxide. This enables the conductive particles to be sintered, enhancing their

conductive pathways, by selectively heating the print to high temperatures without causing potential damage to low cost substrates such as polymer films or paper (49,50). This provides a high-throughput method to enhance the performance of low-cost plastic electronics, rather than more expensive high-energy, thermal processes.

Photonic annealing was performed using a PulseForge® 1200 (NovaCentrix, Austin, TX, USA). A preliminary study was used to optimise voltage, pulse pattern and duration to produce the greatest improvement in conductivity in the prints. The pulse envelope of 2 ms in length and 260 V was used to provide a total energy of 1.10 J cm⁻² to the samples. A single pulse of high energy resulted in catastrophic ablation and delamination of the print due to rapid gasification of binders within the ink. Therefore, an envelope comprised of 10 micro-pulses and a duty cycle of 80% of total energy was used to raise the temperature of the printed features more gradually to remove the binders in a more controlled manner. Using the NovaCentrix SimPulse thermal simulation package, the peak temperature of the ink during photonic annealing was estimated to be 307 °C. This was based on measured layer thickness and a database of thermal characteristics of the materials. As the carbon-based prints assessed were black, and the PET substrate used was opaque white, light absorbance in the visible spectrum was far greater for the print than it was for the substrate. This allowed the PulseForge to selectively heat the printed features to a very high temperature, whilst the unprinted area remained below its glass transition temperature and was not distorted.

3.3.3. Compression Rolling

Although photonic annealing was found to produce notable improvements in the electrical performance of carbon prints assessed, it also resulted in loss of layer adhesion and cohesion in the prints due to degradation of the binder leading to loss of structural integrity. Compression rolling was assessed as a method to regain structural integrity in the prints as well as provide further improvements in electrical performance.

Compression rolling was performed using a Durston DRM 150 Rolling Mill (W Durston Ltd, UK). The compression pressure could not be directly measured but was manipulated by setting the gap between the rollers. Gap sizes from 0.05 to 0.25 mm were assessed, and a gap size of 0.125 mm was found in preliminary studies to

generate the greatest improvement in conductivity without causing warpage of the substrate. To evaluate the relative effects of photonic annealing followed by compression and compression alone, samples of printed graphite ink were also compression rolled without prior photonic annealing.

3.4. Thermal Analyses

3.4.1. Thermo-Gravimetric and Simultaneous Thermal Analysis

Thermogravimetric analysis (TGA) tests were conducted to establish the equivalent temperatures and durations required to remove the binder in the inks using traditional thermal drying methods when compared to photonic annealing. Samples of a resin binder (15% polymer by mass) and graphite ink used for assessing the effects of photonic annealing and compression rolling were analysed. Testing was carried out on a PerkinElmer STA 6000 with a temperature ramp to 500°C over 50 min (10 °C min⁻¹) in a nitrogen atmosphere.

3.5. Surface Characterisation

3.5.1. White Light Interferometry

White light interferometry is a non-contact method used to produce quick three-dimensional scans of a range of samples. As it does not require any sample preparation, it is a very useful method for assessing prints without damaging them, although it does not produce a colour image like alternative non-contact methods such as focus variation microscopy.

White light interferometry was used to assess the topographic profiles of the prints produced. White light interferometry works by passing a beam of white light through a condenser lens, from which collimated white light is split by a beam splitter, directing the beam towards the print sample (left diagram, Figure 3.7). This then passes through an objective lens to a beam splitter, which produces an object beam and a reference beam. The reference beam is then directed towards a reference mirror and reflected back towards the beam splitter while the object beam is sent to the surface of the sample and reflected back up towards the beam splitter (Figure 3.7, right diagram). When the two beams recombine, they produce a series of interference fringes. Where waves of light that are completely in phase with one another produce constructive interference, creating bright areas, while waves that are completely out of phase cancel each other out and produce destructive interference, creating dark

areas. During measurement, the interference measurement is varied by changing the optical path and length between the object and reference beams by either phase shifting or vertical scanning techniques (118). Vertical scanning interferometry (VSI) is used for the majority of applications, while phase shifting interferometry (PSI) is used for producing higher resolution scans for samples with a scanning range of up to 0.16 μm . VSI on the other hand can be conducted on a depth range of up to 0.5mm. VSI works by moving the objective (Figure 3.7) relative to the test surface with either a piezoelectric transducer or motor scanner, with the movement of interference fringes over the sample surface building up an interference map of the sample's topography.

Lenses between 2.5- and 50-times magnification can be used on the Veeco Wyco NT9300 Wide Area White Light Interferometer used for these experiments. Different objective lens configurations are used according to the magnification, with Michaelson interferometers used for 2.5 to 5 times magnification and Mirau interferometers used for 10 to 50 times magnification lenses. Michaelson interferometers (left diagram, Figure 3.8) consist of an objective, a beam-splitter and a separate reference surface. As 2.5 to 5 times magnification lenses have a long working distance, the beam splitter can be fitted in between the objective and the surface, with the reference mirror positioned off to the side. However, with greater magnifications, the working distance becomes shorter, meaning that the beam splitter cube located in the Michaelson interferometer would not fit. Therefore, the Mirau interferometer is used instead, consisting of two small glass plates between the objective and the test surface (right diagram, Figure 3.8). A small reflective spot is located on one of the plates to act as the reference surface, while also acting as a compensating plate. The other plate is coated on one side to act as a beam-splitter (118). However, the Mirau interferometer cannot be used for the lower magnifications of below 10 times. As at these magnifications, the reference spot obscures too much of the aperture. This reference spot has to be larger than the objects field of view as it is a surface conjugate to the best focus plane of the object (118).

In these experiments, the 5 times Michaelson interferometer (working distance of around 6.7mm and optical resolution of around 2.23 (μm)³) was used on the Veeco Wyco NT9300 Wide Area White Light Interferometer to assess the three-

dimensional surface profile of printed lines and squares. As 5 times magnification was used, a measurement area of 1.2 mm by 0.93 mm was taken for each scan (at a resolution of 736×480 pixels with sampling at $1.67 \mu\text{m}$ intervals). In both instances, the ink film thickness was then calculated as the average height of the substrate subtracted from the average height of the ink (Figures Z and T). Printed lines were assessed at intervals of either 3 or 4 even spaces across the lines, with lines assessed on three different prints produced across the print run to calculate the averages and standard deviations. The average line width and print height for each scan was obtained by averaging the cross-sectional profile across the scan length, as shown in Figure 3.9. Where the average width is taken from the edges of the prints and the average print height was taken as the difference between the average height of the substrate and the average height of the top surface of the print.

For the printed squares, analyses were conducted in the centre of the print for average surface roughness (Sa) and average maximum surface roughness (Sz) values. As well as over the edge of the solid print, so that the printed ink film thickness could be evaluated. The print height analyses were conducted on the centre of each four edges on the square for each print (Figure 3.10) and the surface roughness values were assessed conducting scans of four evenly spaced positions within the centre of the square (Figure 3.11), with the surface roughness values automatically generated in the Vision 64 software for the area scanned. The average print height for each scan assessing the edge of the squares was found as shown in Figure 3.10. Where the average height of the print surface was subtracted from the average height of the substrate. These scans were conducted on three different prints produced across the print runs to assess averages and standard deviations.

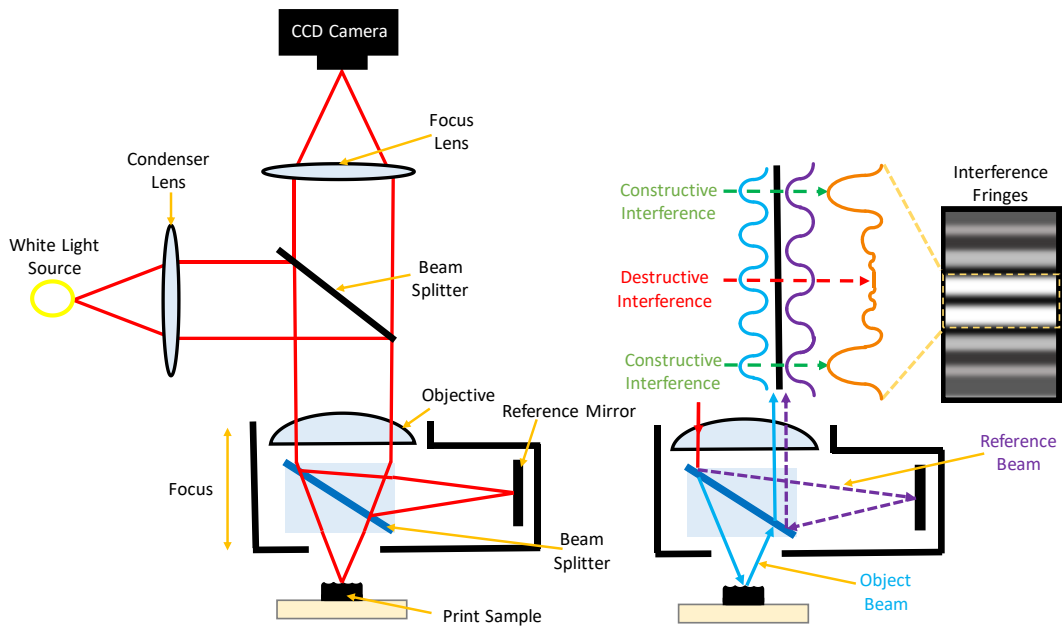


Figure 3.7 Schematic diagram of a white light interferometer (WLI) (left) with breakdown of light beams forming intensity distribution fringes from constructive and destructive interfaces in recombining waves of light.

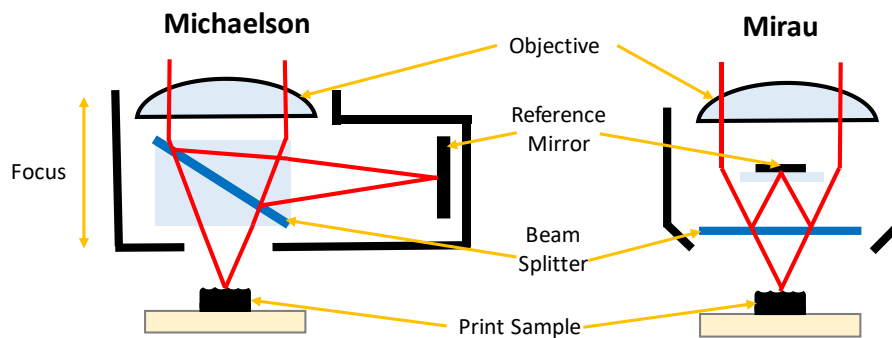


Figure 3.8 Michaelson (left diagram) and Mirau (right diagram) Interferometric Objectives used for white light interferometry

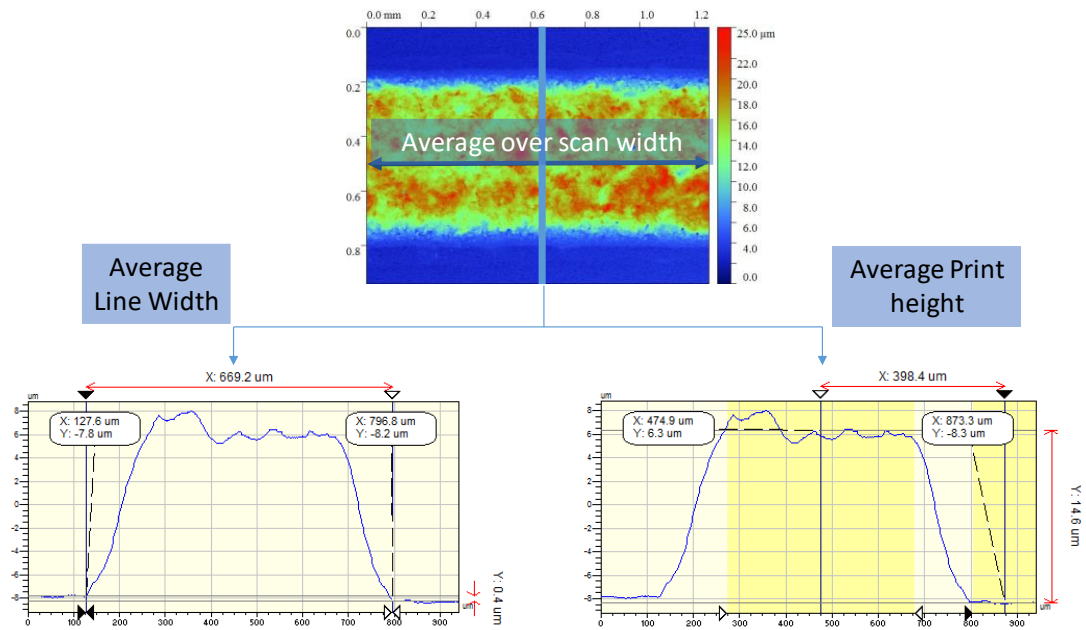


Figure 3.9 Analysis of average line width and height in Vision software.

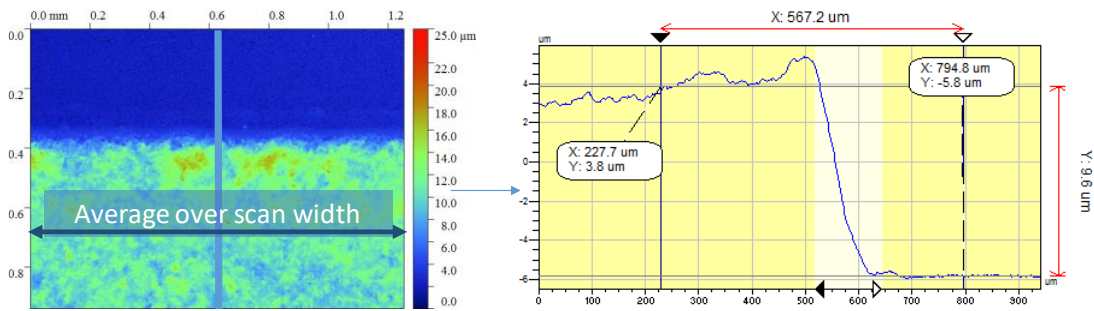


Figure 3.10 Analysis of average print height of the edge of printed solid square in vision software.

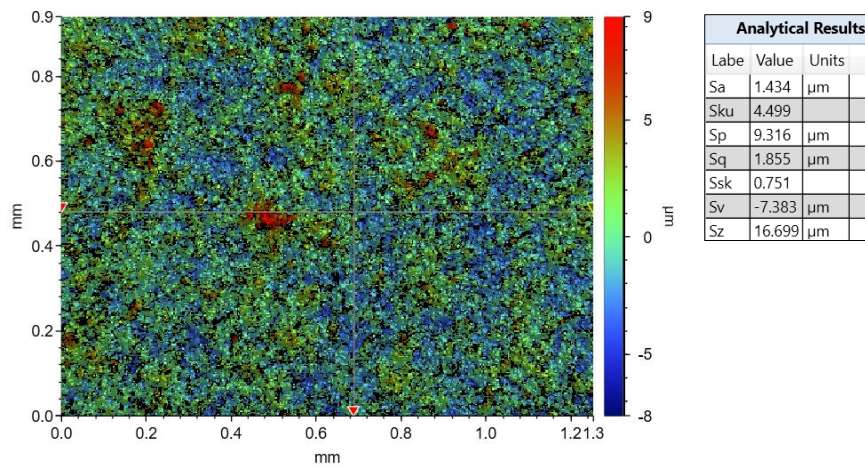


Figure 3.11 Surface roughness values from Vision 64 software for print area

3.5.2. Focus Variation Microscopy

Focus variation microscopy is a non-contact surface characterisation method, like white light interferometry, but instead measures the surface topography of samples using optics. As it compiles a series of optical images rather than assessing the position of features with interference fringes, it has the advantage that it can produce a true colour, three-dimensional image, while the white light interferometer can only produce the topographic profile. This is done by conducting a stack of images at a specified frequency over the z range, which is obtained by the objective lens mechanically moving through the z range (Figure 3.12).

For every pixel on each of the Z levels scanned for the stack, a focus value $F_z(x,y)$ (a constant of a pixel with respect to its neighbouring pixels) is calculated. In general, a more in focus image will have a higher focus value. A mathematical fitting procedure can then be used for each pixel to establish the calculated focus values for each level and the detected z-coordinate of a point for a particular z level with the highest $F_z(x,y)$ (119) (Figure 3.13). By extracting the in-focus pixels from each of the scans and compiling them together, a topographic image is produced along with a true colour image. The Alicona Infinite Focus G5 microscope (Alicona Imaging GmbH) was used for capturing the true colour surface form of the prints at 5- and 10- times magnification.

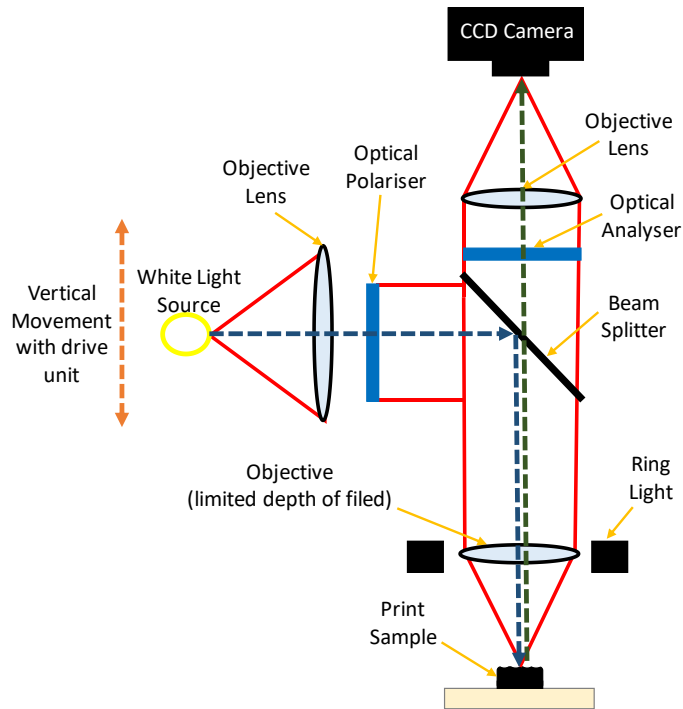


Figure 3.12 Schematic diagram of a Focus Variation Microscope (FVM)

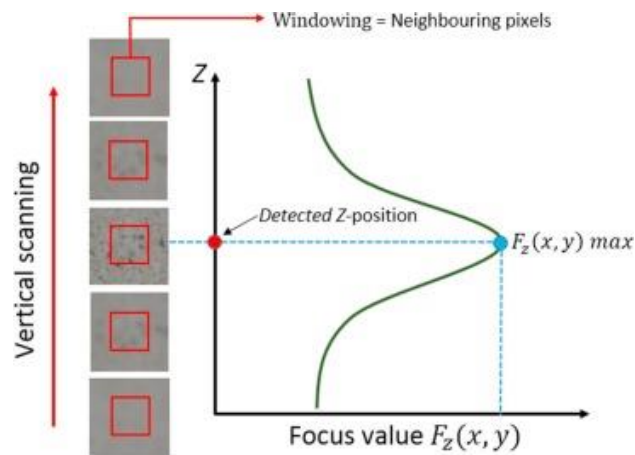


Figure 3.13 FVM working principle by calculating a focus value inside a windowing area.(119)

3.5.3. Scanning Electron Microscopy (SEM)

Scanning Electron Microscopy (SEM) is a form of microscopy that is capable of imaging up to 1,000,000 times magnification, which is substantially higher than what is achievable with visible light microscopy. This is due to the shorter wavelength of electrons, where visible light has a wavelength of 400-700 nm and electrons have a wavelength of 0.001-0.004 nm. This makes it ideal for assessing the particle interactions of screen-printed functional materials. It is capable of producing

resolutions of 1-10nm and has a far better depth of field than light-based microscopy. However, as it uses electrons instead of light, it can only produce greyscale images.

3.5.3.1. Sample Preparation

Sections of the printed squares produced during print trials were assessed by removing around 3 mm x 3 mm areas from the centre of the squares with a scalpel. Print samples were mounted onto aluminium sample stubs which could be fitted into the machine. This was done using a fast-drying silver DAG paint and copper tape coated in carbon-based adhesive on the adhesive side to hold the prints in place, as well as provide a conductive pathway onto the stubs. Once mounted, the samples were then sputter coated on a Quorum Metal Evaporator (Sputter Coater) with 5nm of platinum to ensure samples were conductive enough to produce high resolution images.

3.5.3.2. SEM Imaging

SEM Analysis was conducted on a JEOL 7800F FEG scanning electron microscope (SEM) to assess the particle geometries, distribution and orientations in the range of prints produced.

SEM works by focussing an electron beam, typically with an energy ranging from 0.2 to 40keV, by one or two condenser lenses onto an area of around 0.4 to 5nm on the sample below (Figure 3.14). The beam is passed through pairs of scanning coils or deflector plates in the electron column, typically with a final lens. This will deflect the beam in the x and y axes so that it scans over an area of the sample surface (120).

Analyses were conducted using the Secondary Electron (SE) detectors (Figure 3.14). Secondary electrons were used as they provide good surface detail and topography by penetrating up to 10nm into the sample. Secondary electrons are the more common, low energy form of electrons which are used for high resolution imaging due to their high abundance. They are emitted by atoms excited by an electron beam, and are produced by inelastic scattering (Figure 3.15). The number of secondary electrons emitted is a function of the angle between the surface and the beam. (121,122).

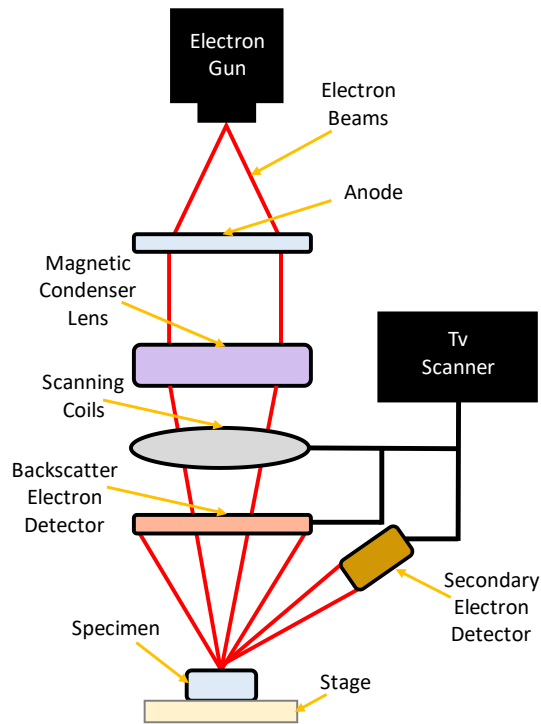


Figure 3.14 Schematic diagram of Scanning Electron Microscopy (SEM) (Field Emission SEM).

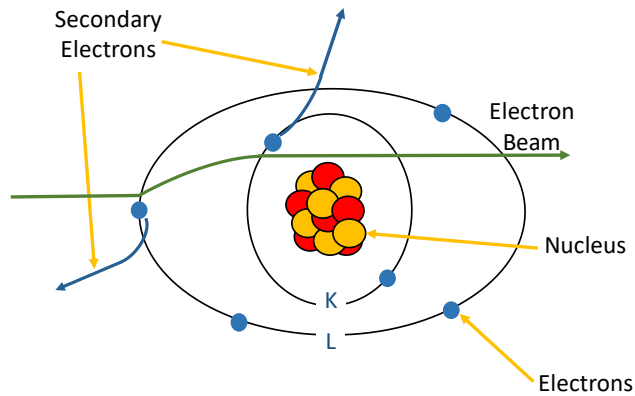


Figure 3.15 Mode of emission of Secondary Electrons in Scanning Electron Microscopy (SEM)

3.6. Electrical Characterisation

Electrical characterisation was conducted to provide comparisons in the conductivity of prints produced with different parameter settings and inks. Two- and four-point probe measurements were conducted to find the line resistance, sheet resistance and resistivity values of printed lines and squares. As resistivity (ρ) is the reciprocal of

conductivity (σ), this can provide an inverse comparison of the conductivity of the prints (Equation 3.20).

$$\sigma = \frac{1}{\rho}$$

Equation 3.20 Relationship between conductivity and resistivity

3.6.1. Sheet Resistance and Resistivity

The four-point probe collinear probe technique is commonly used to assess the sheet resistance and resistivity of semiconductors, thin films and conductive coatings. The method involves four, equally spaced, electrically conducting pins in contact with the sample being assessed and is typically placed towards the centre of the sample (123). The two outer probes are used to provide DC current while the two inner probes are used to measure the voltage drop, as shown in Figure 3.16 (left).

The sheet resistance measurements were conducted on printed 45x45 mm squares using a SDKR-13 probe (NAGY Messsysteme GmbH) 4-point probe with a tip distance of 1.3 mm. It was used with a Keithley 2400 digital Sourcemeter, with subsequent conversion to sheet resistance using the appropriate correction factor from the data table proposed by Smits (124) based on the dimensions of the square and the tip distance. A constant current (1mA with 2.1v) was passed through the print by the outer two probes with a DC power source.

Sheet resistances were then compared (with the correction factor) to assess the effect of parameters and ink rheology on conductivity. To account for the variation in film thickness after post processing, resistivities were also calculated as the product of sheet resistance and ink film thickness using Equation 3.21. Where R is the measured resistance, ρ is the resistivity, L and W are the length and width of the square (which in this case are equal, meaning that length divided by width gives one) and t is the thickness of the square. In this case, the thickness of the square is the average film thickness of the printed square which was measured using white light interferometry as described earlier.

$$R = \frac{\rho L}{t W}$$

Equation 3.21 Relationship between Resistance and Resistivity.

For each print assessed, measurements were conducted twelve times on each square in four positions near the centre with the probes orientated to the width, to the length and at 45° (Figure 3.16, right). This was conducted on three to five prints produced over the print run with all of the measurements used to produce an average and standard deviation to identify any changes in performance across the centre of the print or over the duration of the print run.

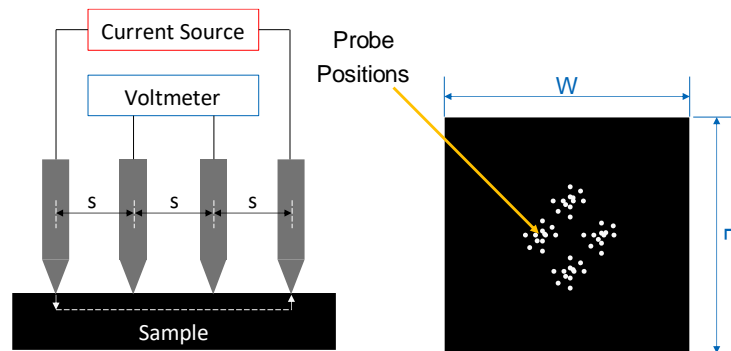


Figure 3.16 Schematic diagram of the four-point collinear probe technique with probes evenly spaced apart (s) (left) with the probe positions on the printed square of length, L and width, W to find the average sheet resistance from 12 positions (right).

3.6.2. Line Resistance

Line resistance was measured using the same multimeter in two-point mode for 700 μm , 600 μm and 500 μm nominal width lines, all of which were 25mm in length. Probes were placed in the centre of the contact squares at the end of the lines as shown in Figure 3.17. Measurements were also conducted on the 200 μm nominal width lines produced with the rig mesh, which were 6 mm long.



Figure 3.17 Measuring line resistance with 2-point probes

3.7. Chapter Closure

The range of equipment which will be used to conduct the experiments in this thesis has been identified. The ink making methodology is optimised in Section 4.3.2, and

used in all following experiments for consistency. All inks were rheologically assessed with a minimum of three repeats to establish the pseudoplasticity and viscoelasticity of the inks, as well as the extensional rheological properties for the inks which will be used in the visualisation tests. The screen-printing visualisation method developed during this investigation is described at the beginning of Chapter 5. Analyses of prints was conducted using white light interferometry and focus variation microscopy to assess the print topography, scanning electron microscopy to assess particle orientations and interactions, along with two- and four-point probe resistivity measurements to assess the conductivity of the prints. A minimum of ten prints for each of the parametric ensured there were sufficient number of samples to be assessed to ensure statistical robustness of the topography and electrical characterisations described in more detail in further methods sections that are specific to the work in Chapters 4, 5, 6 and 7.

Chapter 4. Effect of screen-printing parameters on a Graphite-Based Ink

4.1. Introduction

This chapter focusses on the effect of press parameters on a simple carbon-based ink, containing only one carbon morphology (graphite) in a resin without any additives. This was to limit the number of variables which could interact with the parameter settings. Graphite was chosen as it is used in a wide range of conductive inks and is relatively low cost, making it ideal for conducting a number of experiments with.

To ensure the ink preparation methods produced a well dispersed, conductive ink, various mixing and milling combinations were tested to identify the optimal method. This ensured that the inks used in the parameter tests were consistent between batches and well dispersed, to prevent variation in the rheological profiles of the inks.

The press parameters investigated were the snap off distance, squeegee speed, squeegee hardness, squeegee angle, squeegee pressure and squeegee geometry. The snap off distance is the distance between the mesh and substrate which is set to enable the ink to separate from the mesh after deposition. Where the optimal distance is required to enable a clean separation of the ink between the mesh and substrate, without over deflecting the mesh which could cause to loss of print resolution (18). However, the effect of snap distance on the print quality varies with inks, most likely due to the range of viscoelasticity profiles in screen printing inks (37,38)

Squeegee pressure is also critical for enabling a good print. With too little pressure preventing the squeegee from bringing the mesh to the substrate and resulting in insufficient contact between the squeegee and substrate, resulting in poor ink transfer. While too much can also cause loss of resolution and poor print quality. As too high a squeegee pressure can cause the squeegee to deform and change the hydrodynamic conditions between the screen and squeegee while pressing the screen

firmly to the substrate. If the squeegee is soft, this can cause the squeegee to deflect away from the mesh and cause more ink to be deposited. Whereas if the squeegee is hard, the increase in interaction between the squeegee, mesh and substrate can cause poor ink transfer between the mesh and substrate, leading to inconsistent prints with overall less ink deposited. The amount of pressure needed is coupled with the amount of snap off distance used, with greater pressures required for larger snap off distances. As with snap off distance, the effect of squeegee pressure on the print quality is also related to the viscoelasticity of the ink (23,27,31,32,34).

The squeegee angle and hardness can also have a significant impact on the deflection of the squeegee profile and tip, with harder squeegees typically being better for producing fine features on smooth surfaces, while the deflection of a softer squeegee at a shallow angle can enable a greater deposit and the ability to print onto rougher substrates. The effects of these settings were also found to vary with the rheological profile of the ink, with some studies finding that a soft squeegee at a shallow angle produced a thicker and more consistent deposit, while others with different inks found other hardnesses and angles to produce more greater ink deposits (18,23,27,32,33). Studies were also conducted on the effect of line orientation, with work by Barden (33) identifying some interaction between print parameter settings and the line orientation in graphics inks.

Studies by Jewell *et al.* (27) and Pan *et al.* (23) found that all of these parameters interacted. In order to identify the effects of single parameters at a time, Barden (33) and Peterson (17) conducted analyses changing only one variable at a time. However, these studies were conducted on graphics inks. As the literature identified that the effect of these parameters changed with the rheological profile of the ink used, this work will assess how the parameter settings influence both the print topography and electrical performance of a simple carbon-based ink.

4.2. Materials and Methods

4.2.1. Ink preparation

The graphite model ink consisted of 22.5% graphite (Timrex® SFG15, Imerys Graphite, with Carbon—typical D90 17.9 μm , according to the manufacturer) and 77.5% pre-made vinyl resin base (with 15% by weight dry polymer, VINNOL

(Wacker Chemie AG) in 4-hydroxy-4-methylpentan-2-one). This concentration was chosen as this was found to produce a good compromise between print quality and conductivity. It was prepared in four 100g batches. The graphite was gradually added to the resin and stirred in by hand. The ink slurries were then allowed to wet overnight before being prepared using the four mixing techniques outlined in Table 4.1. These four different mixing procedures are assessed in Section 4.3.2 in order to develop a mixing technique which would produce the best print quality and conductivity. As method 3 was found to produce the best print quality, it was then used for preparing all inks used in the parametric studies in Sections 4.3.3. and 4.3.4.

Table 4.1 Different Mixing Techniques used.

Ink	Mixing Techniques
1	Stirring only
2	Triple roll milled then stirred
3	Triple roll milled then Speedmixed
4	Speedmixed only

For inks 1 and 2, the stirring was conducted with a Heidolph overhead mechanical stirrer (model RZR 2021) with a stainless-steel propeller, containing 4 straight blades (50mm diameter). The inks were mixed for 15 minutes at 1000 rpm. These settings were used for stirring both inks 1 and 2.

For inks 2 and 3, milling was conducted using an EXAKT80E 3 roll mill (also known as triple roll mill) (EXAKT Advanced Technologies GmbH). The conditions used are presented in Table 4.2. The same settings were used for both inks 2 and 3.

Table 4.2 Triple roll mill settings

Pass number	Band Gap (µm)	Front Gap (µm)	Speed (rpm)
1	60	15	200
2	40	10	200
3	20	5	200

For inks 3 and 4, mixing was conducted in a Speedmixer™ DAC 150.1 (FVZ-K), which provides dual centrifugal mixing by spinning the ink while it is in a sealed container. Mixing was conducted for 5 minutes at 2500 rpm. The same settings were used for both inks 3 and 4.

The technique which produced the best print consistency and electrical performance was then used for preparing all inks used in the parametric studies.

4.2.2. Rheological Assessment

Rheological evaluation was carried out on each of the inks using a combination of shear, viscoelastic and extensional measurements. Shear viscosity measurements were carried out on a Malvern Bohlin rotational rheometer (Gemini Bohlin Nano, Malvern Instruments) with a 2° 20 mm stainless steel cone and a parallel plate held at 25 °C. Ink viscosity was measured as the shear rate was gradually increased to 100 s⁻¹ and then reduced back to 1 s⁻¹. A shear ramp was also conducted by increasing the viscosity instantaneously from 1 s⁻¹ to 100 s⁻¹, where it was held for 60 seconds and then instantaneously dropped back down to 1 s⁻¹. Following this, it was also instantaneously increased again, this time from 1 s⁻¹ to 200 s⁻¹, where it was held for 60 seconds, before being instantaneously dropped back down to 1 s⁻¹. This was done to assess the rate of recovery from different shear rates. In both cases, the inks were pre-sheared at a rate of 50 s⁻¹ followed by a recovery period of 60 seconds prior to testing so that the inks would have the same initial viscosity during tests.

Viscoelastic measurements were carried out on a Malvern Kinexus Pro Rheometer (Malvern Instruments) with a 40mm roughened plate and roughened parallel plate (to minimise the effect of slip). Amplitude (strain) sweep measurements were conducted to establish the linear viscoelastic range at 0.1, 1 and 10Hz. As the results showed comparable trends, the values from the linear viscoelastic range of the test conducted at 1Hz were chosen for comparison.

4.2.3. Printing

The DEK 248 was used to optimise the mixing techniques for the inks and assess the effect of squeegee hardness, pressure and snap off distance for a diamond squeegee. However, the DEK could not assess the effect of using blade squeegees with different hardnesses or contact angles, or the effect of print speed, as its maximum

print speed was 70 mm s^{-1} . The Svecia Matic flatbed screen printer was used to assess these, along with snap off distance. The Svecia was not able to print with a diamond squeegee and its squeegee pressure was set in terms of linear distance with a screw thread, rather than actual squeegee force as with the DEK which was set using pneumatic pistons. Therefore, both presses were required to assess the full set of parameters. The diamond squeegee had a contact angle between the mesh and squeegee tip of 45° . However, the blade squeegee would have deflected excessively if used at 45° , so a starting angle of 70° was used which is more suitable for the blade geometry and comparable with previous experiments reported by Jewell *et al* (125) and Anderson (18).

The preliminary evaluation of the inks produced with different mixing techniques were conducted on a DEK 248 flatbed screen printing machine using a 300 mm x 240 mm frame with a polyester mesh with 61 threads per cm, $64 \mu\text{m}$ thread diameter and 13-micron emulsion, 1 mm snap-off, 70 Shore A hardness diamond squeegee of 130 mm length with a 8-kg squeegee force and print/flood speeds of 70 mm s^{-1} . The substrate was PET (polyethylene terephthalate—Melinex® 339, DuPont Teijin Films ($175 \mu\text{m}$ thickness) opaque white). The print image included a series of 25-mm-long lines of nominal widths from $100 \mu\text{m}$ to $700 \mu\text{m}$ and a 45-mm square solid patch for sheet resistance assessment. The print contained series of lines in three orientations, so that the effect printing lines perpendicular, parallel and at 45° to the print direction could be assessed. Ten prints were produced for each of the inks. Printed samples were dried in a conveyor dryer at 100°C for 4 minutes.

The parameter study on the DEK 248 was conducted with the same mesh, substrate, drying conditions and number of prints produced, along with the ink mixed with the settings which produced the most consistent and conductive prints. A range of settings were used for the hardness of the diamond squeegees, the snap off distance and the squeegee pressure (quantified as squeegee force), as shown in Table 4.3. Each parameter was changed while the other settings were held constant. The settings used were comparable with those used by Jewell *et al* (27) and Anderson (18) who also assessed these parameters over three levels for graphics based inks.

Table 4.3 DEK 248 Screen-Printing Press Parameter Settings.

Parameters	Settings		
Squeegee Hardness (Shore A)	70	75	80
Snap off (mm)	0.7	1	1.3
Squeegee Pressure (kg)	7	8	9

The other parameter trials were conducted on the Svecia Matic flatbed screen printer due to its ability to print at a wide range of squeegee speeds and alter the angle of the blade squeegee. This enabled squeegee speed, angle and hardness to be assessed.

The same substrate, mesh features and design were used as with the DEK 248 trials. Although the screen frame was 508 mm x 508 mm. The range of snap off distances, squeegee speeds, hardnesses and angles used are given in Table 4.4. Each parameter was changed while the other settings were held constant. As the literature had found the effects of squeegee angle and hardness for blade squeegees to be interlinked and to be consistent irrespective of ink used, the effect of maximising and minimising both squeegee angle and hardness together were also assessed, while other parameters were held constant. The range of squeegee hardnesses and angles used were the same as those used by Jewell *et al.* (27) for assessing a range of graphics based inks for comparable results. Ten prints were produced for each of the inks. Printed samples were dried in a conveyor dryer at 100°C for 4 minutes.

Table 4.4 Svecia Matic Screen-Printing Press Parameter Settings.

Parameters	Settings		
Speed (Setting (mm s⁻¹))	1 (55)	5 (880)	9 (1600)
Snap off (mm)	5	7.5	10
Squeegee Angle (°)	70	75	80
Squeegee Hardness (Shore A)	70	75	80

4.2.4. Topography Analyses

White light interferometry (NT9300, Veeco Instruments, Inc., Plainview, NY, USA) was used to measure a full three-dimensional surface profile over the edge of the solid print so that the printed ink film thickness could be evaluated. 5 times magnification was used, giving a measurement area of 1.2 mm by 0.93 mm (at a resolution of 736×480 pixels with sampling at $1.67 \mu\text{m}$ intervals). The ink film thickness was calculated as the average height of the substrate subtracted from the average height of the ink, excluding the print edges where there tended to be a lip or a decline in ink film thickness depending on the print orientation. A total of 36 measurements were taken for each ink type or press parameter assessed. This was obtained over three print samples with 12 evenly spaced points around the perimeter of the printed square for each print. Average surface roughness measurements (S_a) over the printed area were also taken away from the edges. From this the average in film height and roughness was calculated.

Printed line geometry was also assessed at five times magnification. $700 \mu\text{m}$, $600 \mu\text{m}$ and $500 \mu\text{m}$ nominal width lines (produced perpendicular to the print direction) were each measured in 3 evenly spaced points. A total of 9 measurements were taken for each line width for each test conducted. This was obtained over three print samples with 3 evenly spaced points across the lines. From this the average and standard deviation in line width and thickness was calculated.

4.2.5. Electrical Characterisation

Resistance measurements were conducted to identify how conductive the prints were, in order to link the effect of press parameters and print topography with electrical performance of the prints. Sheet resistance measurements were conducted on the printed 45×45 mm squares using a 4-point probe method. A SDKR-13 probe (NAGY Messsysteme GmbH) with a tip distance of 1.3 mm was used with a Keithley 2400 digital Sourcemeter, with subsequent conversion to sheet resistance using the appropriate correction factor from the data table proposed by Smits (124). Sheet resistances are displayed as measured (with the correction factor) and, to account for the variation in film thickness after post processing, resistivities were also calculated as the product of sheet resistance and ink film thickness. A total of 12 sheet resistance values were taken across the centre of each printed square to account for any deviation

in print quality or effects of compression across the area. Line resistance was measured using the same multimeter in two-point mode for 700 μm , 600 μm and 500 μm nominal width lines in each orientation, as the print designs contained lines perpendicular, parallel and at 45° to the print direction. For the mixing study, the lines produced perpendicular to print direction were compared. These measurements were conducted on three samples from each of the print runs to obtain averages and standard deviations.

4.3. Results

4.3.1. Rheological Analyses

4.3.1.1. Viscosity

All of the inks were shear thinning, with the most significant reductions in viscosity occurring between 1 s^{-1} and 50 s^{-1} (Figure 4.1 (a)). The inks were slow to recover to their rest viscosities, exhibiting hysteresis when reducing the shear rate back down from 100 s^{-1} to 1 s^{-1} . The inks took around 20 seconds to recover back to their initial viscosities when increased to a shear rate of 100 s^{-1} and around 30 seconds to recover from 200 s^{-1} (Figure 4.1 (b)). While recovery was relatively slow, the shear thinning process was almost instantaneous. Out of the mixing techniques assessed, the ink which was Speedmixed only exhibited the highest viscosity between 20 s^{-1} and 100 s^{-1} , although inks which were stirred only or triple roll milled followed by Speedmixed exhibited higher initial viscosities. However, after the inks were reduced back down to 1 s^{-1} , their final viscosity was lower than that of the ink which was Speedmixed only. Whereas the ink which was triple roll milled followed by stirring had the lowest viscosity at all shear rates assessed, with a viscosity of 14 Pas at 100 s^{-1} . While the ink which was Speedmixed only had a viscosity of 17.2 Pas and the ink which was triple roll milled followed by Speedmixed had a viscosity of 15.7 Pas at shear rates of 100 s^{-1} . This suggests that the triple roll milling technique used can reduce the viscosity of the ink, as stirring or Speedmixing alone cannot break up the agglomerates. By improving the dispersion of the graphite flakes in the ink and ensuring consistent sizes of the graphite flakes from milling the inks. This would allow the ink to flow more readily during the screen-printing process, enabling more consistent print deposits.

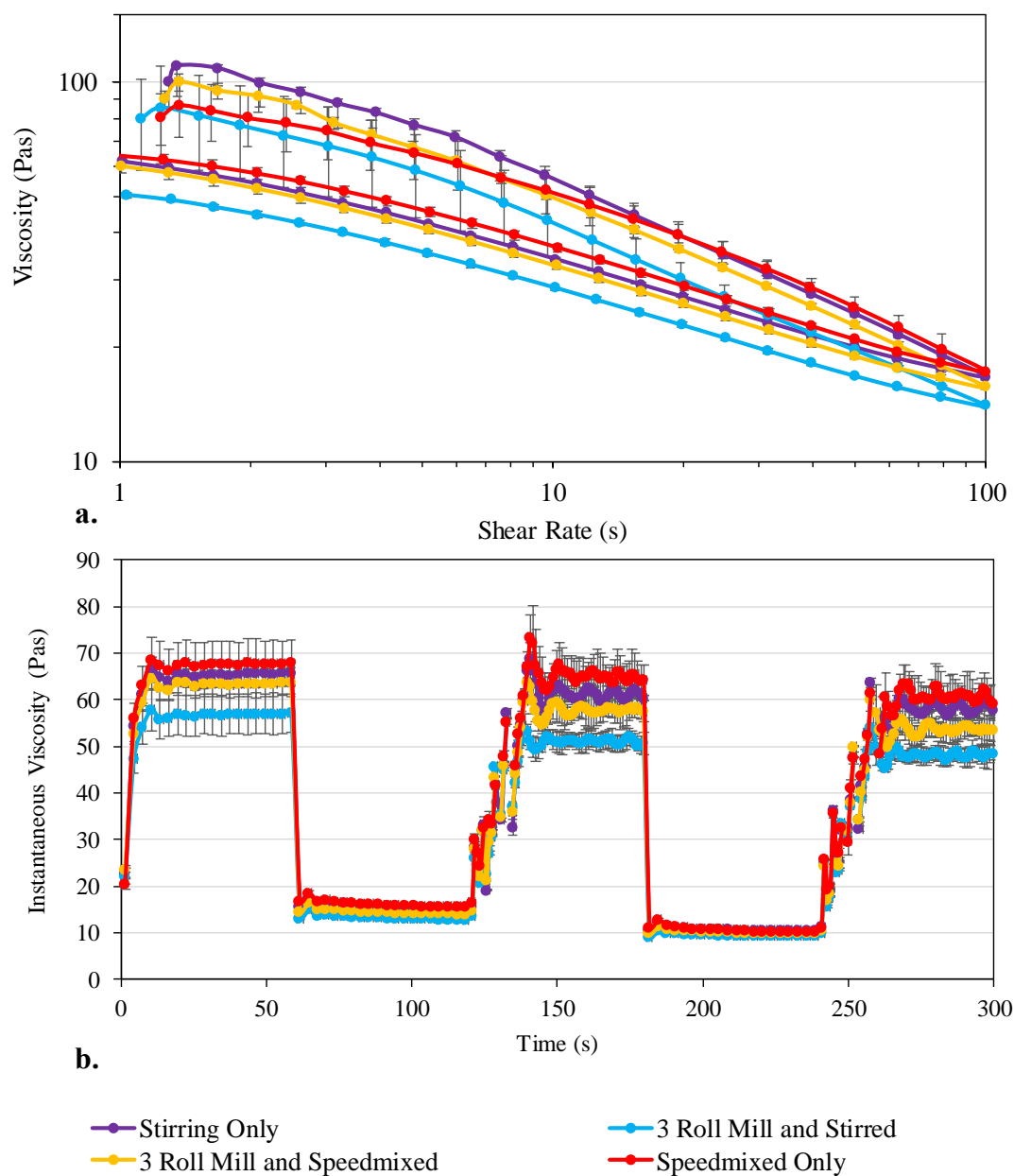


Figure 4.1 Changes in (a) Viscosity profiles and (b) Viscosity ramps from $1s^{-1}$ to $100s^{-1}$ for 60s then back to $1s^{-1}$, then from $1s^{-1}$ to $200s^{-1}$ for 60s and back to $1s^{-1}$ to assess the ink recovery time with different mixing techniques (outliers removed).

4.3.1.2. Viscoelasticity

The inks which were triple roll milled were found to have a lower phase angle (δ) than those which were not, therefore behaving in a more elastic manner than those which were not triple roll milled (Figure 4.2). Both inks which were triple roll milled had a δ of around 61.5° , while the ink which was stirred only has an δ of 65.9° and the ink that was Speedmixed only had a δ of 66.9° . The inks which were triple roll

milled behaved in a more elastic manner, as the graphite flakes would be better dispersed, enabling more particle to particle interactions. The volume fraction of graphite would be the same in all inks, but the number of flakes would be greater after the agglomerates were dispersed during triple roll milling. In all cases, the inks behaved in a predominantly liquid like manner as indicated by the δ , where the viscous modulus (G'') was greater than the elastic modulus (G') in all cases.

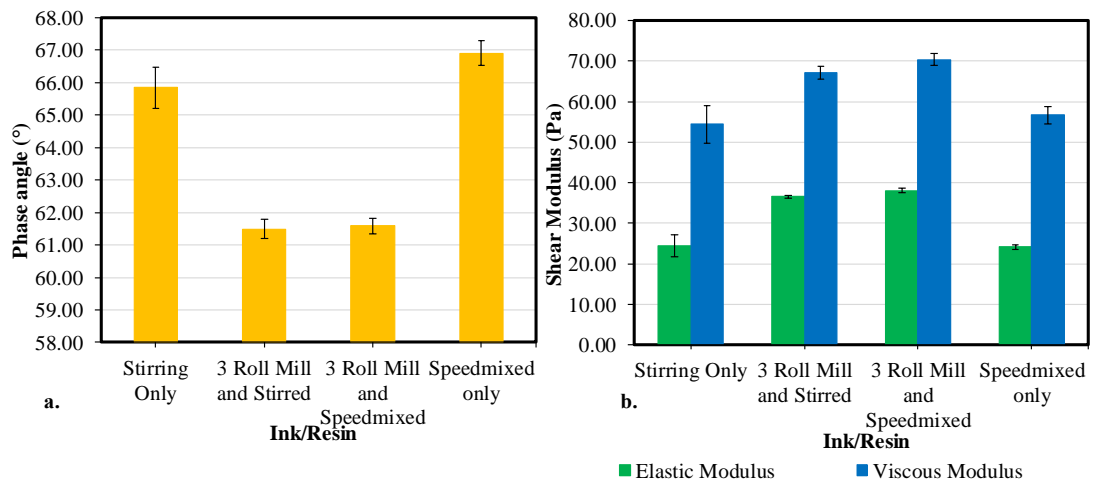


Figure 4.2 Viscoelastic profiles assessing changes in phase angle (δ), storage modulus (G') and loss modulus (G'') of the inks with different mixing techniques in the linear viscoelastic region at 1 Hz.

4.3.2. Effect of Mixing and Milling on Print Performance

4.3.2.1. Topography of prints

The print topography of both the printed solid areas and printed lines were found to vary with the mixing techniques used for producing the graphite-based inks. As shown in the topography plots of the print surface in Figure 4.3 and Figure 4.4, all prints were relatively rough with some pin holes, due to the geometry of the graphite flakes. However, the most inconsistent print profiles were produced with the inks which were stirred only or triple roll mixed then stirred, as shown in images (a) and (b) of Figure 4.3 and Figure 4.4. These prints exhibited the greatest number of pinholes, as well as large areas without ink deposit leading to gaps in the conductive pathways in both the printed squares and lines. These were only stirred by the overhead stirrer, which stirs around the centre of the pot. This would provide uneven amounts of mixing in the pot of ink which could lead to inhomogeneity. These print

defects would limit the number of conductive pathways across the ink, leading to the worst electrical performances.

The best print quality with the most consistent print height and least number of pinholes was produced by triple roll milling then Speedmixing the ink, as shown in image (c) of Figure 4.3 and Figure 4.4. While inks produced with Speedmixing alone, shown in image (d) of Figure 4.3 and Figure 4.4, produced a print consistency similar to that of the inks produced by triple roll milling followed by Speedmixing, although the print height was not as consistent. Similar trends were shown with variations in film thickness and line width of the printed lines, as shown in Figure 4.5. The improvement in print roughness and consistency with the inks which were both triple roll milled and speed mixed were due to the better ink homogeneity. As the triple roll milling enabled better flake dispersion and consistency in flake size, while the subsequent Speedmixing would provide an even amount of mixing across the ink, improving its homogeneity and therefore producing more even ink distribution in prints. This improvement in print homogeneity would enable more conductive pathways across the print which would improve the prints electrical performance. The inks which were stirred also produced average line widths smaller than that of the nominal line widths on the mesh (Figure 4.5 (b)). This is due to the agglomerations of carbon flakes in the ink leading to wavy line edges and large patches where ink has not deposited from the screen, leading to a lower average width (Figure 4.4).

The inks which were Speedmixed deposited greater film thicknesses and line widths than inks which were stirred. The variations in print roughness, are given in Figure 4.6. inks which were Speedmixed produced a greater average surface roughness (S_a) than those which were stirred, with a similar maximum surface roughness (S_z) to those which were stirred. This is due to all prints containing some pinholes and the Speedmixed inks producing greater film thicknesses than those which were stirred. For conductive carbon prints in applications such as resistive heaters, thicker, more consistent print deposits would enable better conductive pathways and improve the electrical performance of the prints.

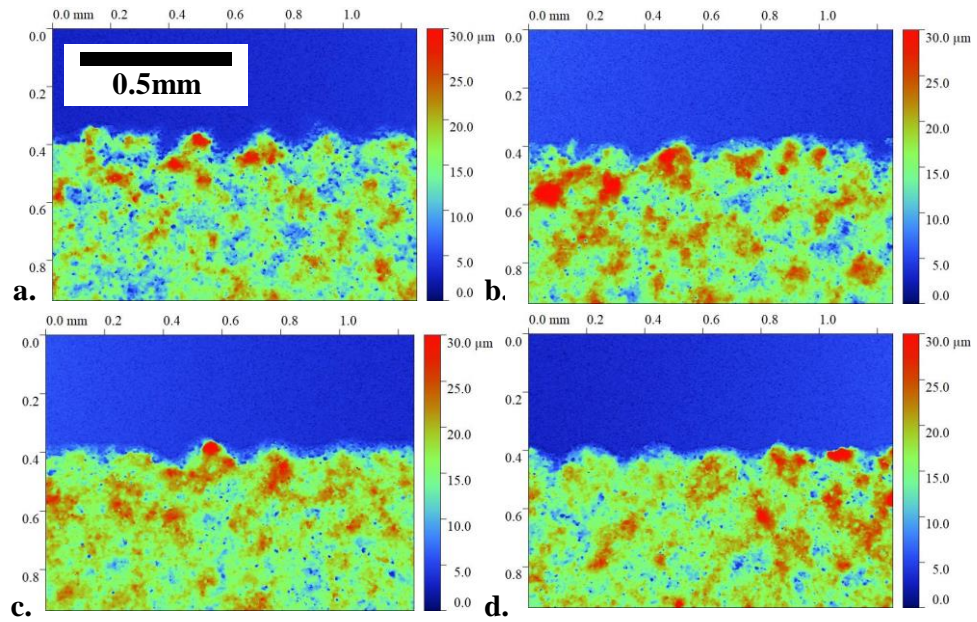


Figure 4.3 White light interferometry images of the edges of the printed squares for the printed graphite-based inks. Prepared with (a) stirring only, (b) triple roll milling followed by stirring, (c) triple roll milling followed by Speedmixing and (d) Speedmixing only. Conducted at 5 times magnification.

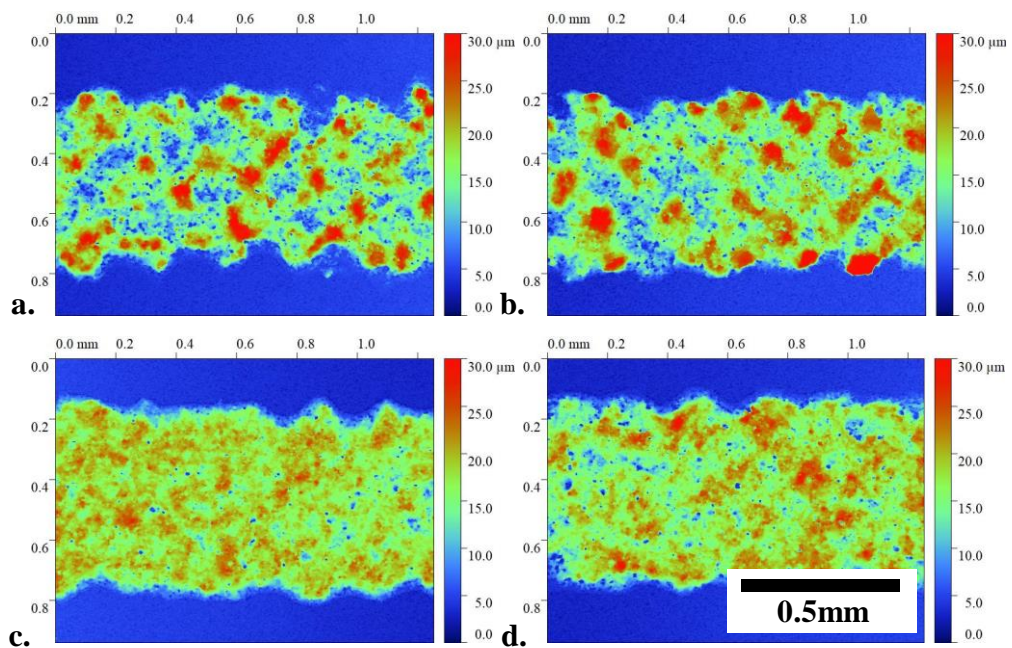


Figure 4.4 White light interferometry images of the 700µm nominal width lines for the printed graphite-based inks. Prepared with (a) stirring only, (b) triple roll milling followed by stirring, (c) triple roll milling followed by Speedmixing and (d) Speedmixing only. Conducted at 5 times magnification.

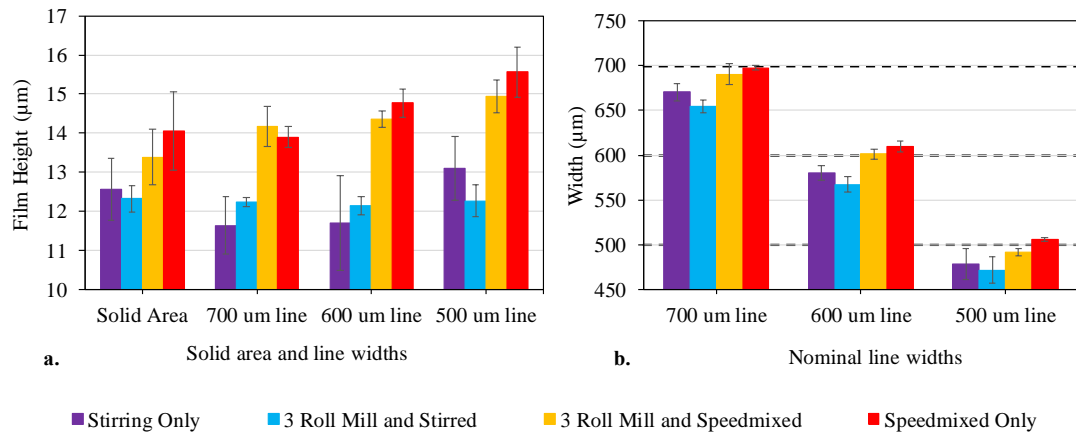


Figure 4.5 Average (a) film thickness and (b) line width for the different mixing techniques used on the graphite-based ink. (error bars for standard deviation, dashed lines to show nominal widths).

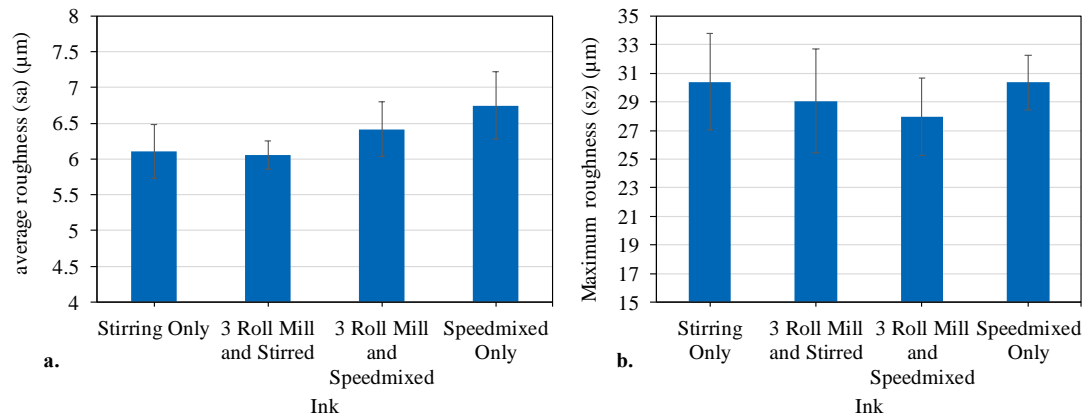


Figure 4.6 Average (a) Surface roughness (S_a) and (b) maximum roughness (S_z) for the different mixing techniques used on the graphite-based ink. (error bars for standard deviation).

4.3.2.2. Electrical characterisation of prints

The electrical performances of the prints were found to be inversely related to the amount of ink deposited and the homogeneity of the prints (Figure 4.7). The prints which were Speedmixed deposited the greatest film thicknesses and best print consistency with the least number of defects (defined by the area of pinholes on the print) were also found to have the lowest sheet and line resistances, as shown in (a) and (b) of Figure 4.7. This would be expected as a more homogeneous print would enable better conductive pathways. However, when film thickness was accounted for, the resistivities of the prints were within standard deviation. Calculated from

fluctuations in electrical performance both across the area of the printed square and over the print cycle. This is shown in graph (c) of Figure 4.7, where the prints which were triple roll milled had lower average resistivities of around 1.71 Ω .cm, while the prints which were stirred only or Speedmixed only had average resistivities of around 1.85 Ω .cm.

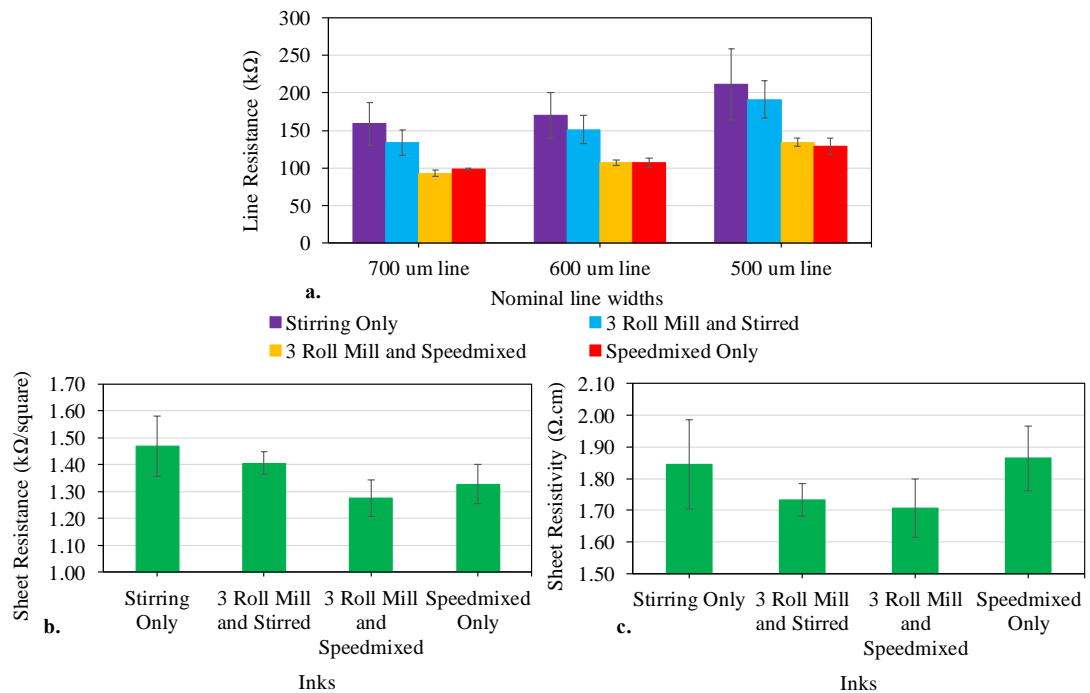


Figure 4.7 Average (a) Line Resistance, (b) sheet resistance and (c) sheet resistivity for the different mixing techniques used on the graphite-based ink. (error bars for standard deviation).

4.3.2.3. Discussions of mixing effects

The inks which were Speedmixed produced a more consistent print topography with less defects than those which were stirred. Speedmixing provided even shear to the whole ink, whereas the traditional overhead stirrer used a blade which only provided localised shear. This could lead to sections of the ink containing worse distribution of graphite, which would cause increases in print inconsistencies, shown in the results. However, the inks which were triple roll milled prior to Speedmixing produced the best results in terms of both print consistency and electrical performance. The milling enabling the graphite flakes to become well dispersed in the ink prior to mixing. Thus, leading to further improvements in ink homogeneity, which in turn led to better print performance. The ink which was triple roll milled

prior to being Speedmixed had the lowest viscosity, with one of the lowest phase angles. This will have enabled it to flow better during printing. Triple roll milling followed by Speedmixing was used for preparing the inks used in the parameter studies.

Therefore, optimal mixing techniques for producing a graphite-based ink with best consistency and performance were identified as consisting of triple roll milling followed by Speedmixing. This was then used for producing the inks to be assessed for the press parameter studies.

4.3.3. DEK 248 Parameter Study

4.3.3.1. Diamond Squeegee Parameter Study

There were no significant changes in print performance with changes in squeegee hardness or pressure, as shown in the line resistance values displayed in Figure 4.8 ((a) and (b)). The variation lay within the standard deviations, which resulted from fluctuations in print topography across the print run as later prints produced higher resistances as the ink dried in, for all line widths assessed. However, there was a slight reduction in the average line resistance produced with increases in snap off distance (Figure 4.8 (a)). The standard deviations seen with the results for changes in snap off and pressure were due to changes in print consistency over the print run and the position measured on the line. As all studies were conducted across the same number of prints and on the same positions on the lines, the trends seen are valid.

The effect of line orientation on line resistance was also assessed to see whether the print direction had any interaction with the squeegee hardness or pressures used (Figure 4.9). No significant effects were seen with squeegee pressure for all line orientations, although the lines produced parallel to the print direction had the highest line resistance and those produced perpendicular to the print direction had the lowest line resistance. In the case of squeegee hardness, the highest resistance was consistently produced by the lines printed parallel to the print direction and the lowest were by those perpendicular to the print direction. However, the lines produced parallel or at 45° to the print direction were found to have higher line resistances at 70 Shore A and 80 Shore A squeegee hardness, although these values were within standard deviation. In the case of snap off distance, the lines produced

parallel to or at 45 ° to the print direction were also found have higher line resistances than those produced perpendicular to the print direction. There was also a change in the trend caused by snap off distance, where the lines produced parallel or at 45° to the print direction saw increases in line resistance between 1mm and 1.3mm snap off distances.

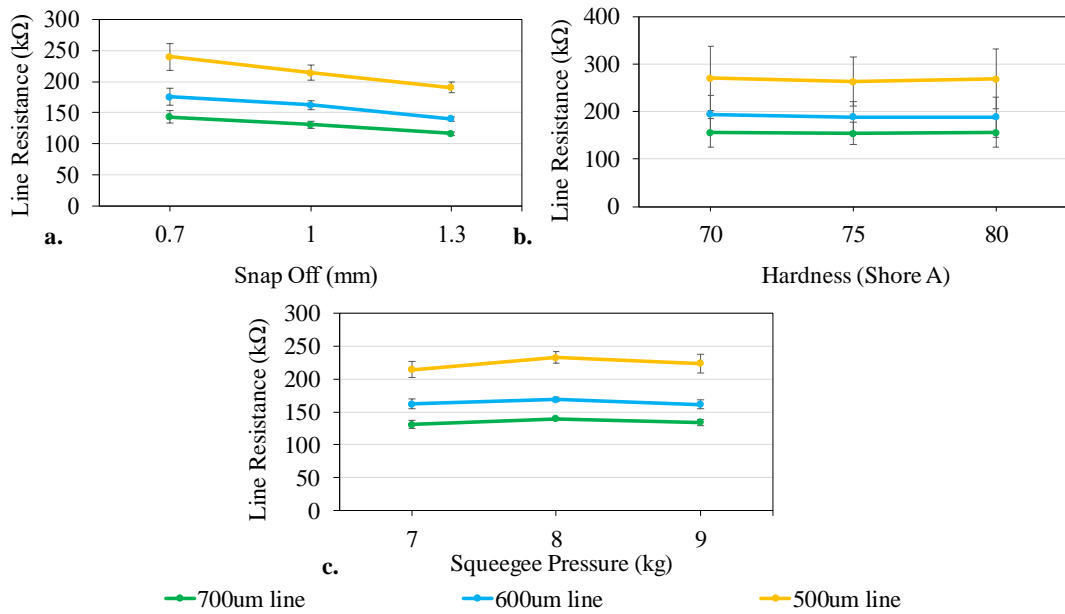


Figure 4.8 Changes in line resistance with different (a) snap off distance, (b) squeegee hardness and (c) squeegee pressure for lines produced perpendicular to the print direction.

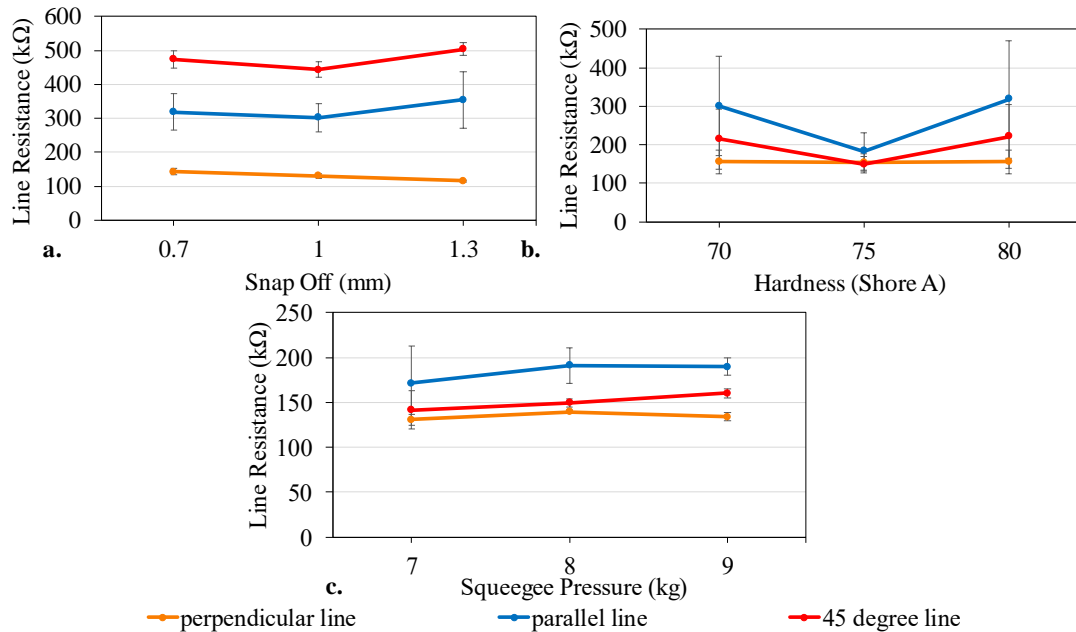


Figure 4.9 Changes in line resistance of the 700 μ m lines with line orientation for different (a) snap off distance, (b) squeegee hardness and (c) squeegee pressure.

4.3.3.2. Discussions of DEK parameter study

The squeegee hardness and pressure had no significant effect on the print performance. Although increases in snap off distance led to gradual reductions in line resistance. This could be as the lower snap off distances were not sufficient for a clean and consistent separation of ink between the mesh and substrate.

The lines produced at 45° to and parallel to the print direction were typically found to have higher line resistances than those produced perpendicular to the print direction. This may be as the squeegee deposits the ink for the perpendicular lines simultaneously, enabling even separation between the mesh and substrate across the length of the line. Whereas the lines at 45° and parallel to the print direction would be deposited from one side of the line's length to the other, this could lead to a less consistent separation and resultant print profile. This could also be due to the orientation of the mesh in relation to the line directions, with less open areas between the mesh strands in the lines at 45° and parallel to the print direction. In the case of squeegee pressure, there were no significant changes in line resistance with changes in pressure at any of the line orientations. With squeegee hardness, the 70 Shore A and 80 Shore A hardness squeegees were found to produce a higher line resistance than the 75 Shore A hardness squeegee, when printed either parallel or perpendicular to the print direction. This may be due to the harder squeegees being too rigid and

causing the ink to be scraped partially off after deposition. While the softer squeegees may conform too much, creating a large contact area which could also reduce the amount of ink remaining on the substrate. Therefore, in these cases the medium hardness (75 Shore A) squeegee was found to produce the lowest line resistance. In the case of snap off distance, different trends were seen for the lines produced parallel or at 45° to the print direction with increases in line resistance between 1mm and 1.3mm snap off distances. While the lines produced perpendicular to print direction saw reductions in line resistance for the same increase in snap distance. When the lines are oriented parallel or at 45° to the print direction, this amount of snap distance may be excessive and cause the mesh to warp, producing an inconsistent line.

4.3.4. Svecia Parameter Study

The parameter studies conducted on the Svecia Matic flatbed screen printer assessed the effect of altering the snap off distance, squeegee speed, angle and hardness by altering one parameter at a time. This was done to identify the effects of individual parameters without the influence of complex interactions between other parameters. In addition, the effect of maximising both squeegee hardness and angle were also assessed, as shown in Table 4.1. From this, the effect of these parameters on print topography and electrical performance were investigated.

Table 4.5 Design of experiments for parameter trial conducted on the Svecia Matic

Assess	Experiment	Squeegee Speed (mm/s)	snap off distance (mm)	Squeegee Angle (°)	Squeegee Hardness (shore A)
Standard Settings	1	55	5	75	75
Squeegee Speed	2	880	5	75	75
	3	1600	5	75	75
Squeegee Hardness	4	55	5	75	70
	5	55	5	75	80
Squeegee Angle	6	55	5	70	75
	7	55	5	80	75
Snap Off Distance	8	55	7.5	75	75
	9	55	10	75	75
Angle and Hardness	10	55	5	70	70
	11	55	5	80	80

4.3.4.1. Speed

Topography Analyses

Speeds were ranged from the lowest press speed setting 1 (55mm/s), to the highest press speed setting 9 (1600mm/s) with speed setting 5 (880mm/s) in the middle. Increases in print speed lead to improvements in print consistency (Figure 4.10). Prints conducted at lower speeds exhibited mesh marking (marking which relates to the frequency of the mesh strands), which is characteristic of higher viscosity inks due to poor separation between the mesh and substrate. Leading to areas with no ink deposited and greatly limiting the number of conductive pathways across the print. At higher speeds, there was better print consistency, although there were still some areas with pinholes and variations in print height. This is also shown in the changes in print height ((a) of Figure 4.11), where there was a gradual increase in average film thickness with increases in speed. This was due to increases in the shearing of the ink leading to reductions in the ink viscosity and allowing greater ink deposits and more homogeneous prints.

However, there was a reduction in the average line width of all lines with increases in print speed, between the lowest print speed and the medium print speed, which then levelled off at the highest speed ((b) of Figure 4.11). This was due to reductions in the amount of ink spreading at the line edges with increases in speed, where prints produced at the lowest speed had inconsistent line edges due to the mesh marking. The print produced at the medium speed had the lowest print roughness (Figure 4.12). Although all print roughness's were within the calculated standard deviation of one another, as the average print roughness was a feature of the random orientation of the graphite flakes rather than the print quality. However, the maximum print roughness, depicting the distance between the peaks and troughs in the print showed that the print conducted at the highest speed had the greatest maximum roughness. Although the highest print speed deposited the thickest deposits, it still had areas without ink deposited and others with agglomerates of ink, as shown in Figure 4.10, while the medium print speed had a more consistent print deposit. However, further improvements may be made with further increases in speed as there is a linear increase in film thickness with print speed (Figure 4.11 (a)).

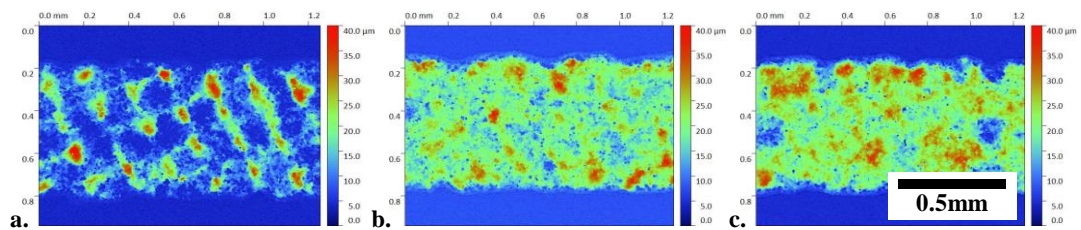


Figure 4.10 White light interferometry images of the 700µm nominal width lines for the printed graphite-based inks. At speed settings (a) 55 mm/s, (b) 880 mm/s and (c) 1600 mm/s. Conducted at 5 times magnification.

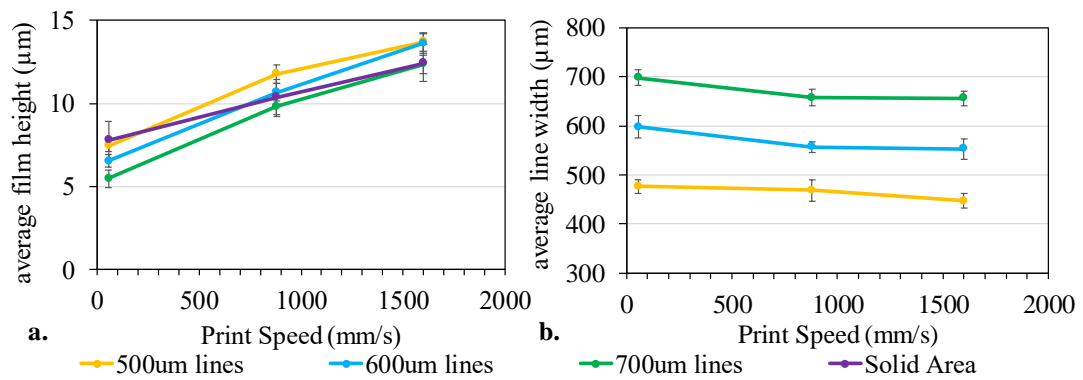


Figure 4.11 Average (a) film thickness and (b) line width for different squeegee speeds (error bars for standard deviation).

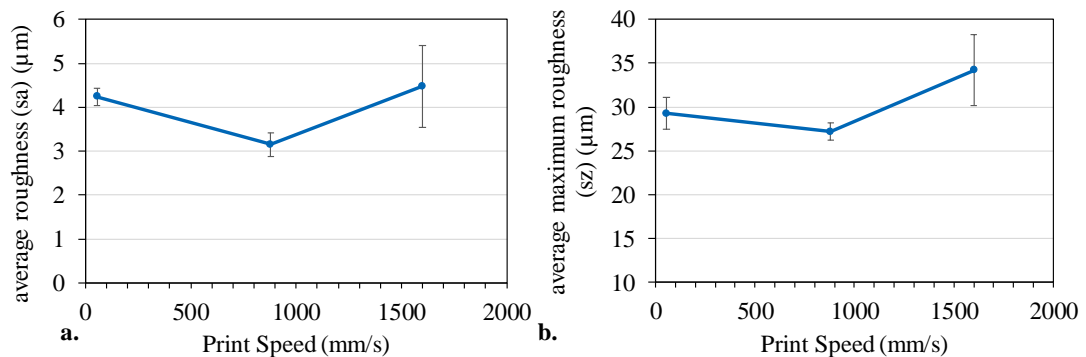


Figure 4.12 Average (a) Surface roughness (Sa) and (b) maximum roughness (Sz) for the different squeegee speeds (error bars for standard deviation).

Electrical Characterisation

The line resistances of the prints were inversely related to the amount of ink deposited, and the print homogeneity as shown in graph (a) of Figure 4.13. With the more consistent prints produced at the higher speeds providing more conductive pathways and therefore better electrical performances for all line widths assessed. There was a less significant difference between the line resistances produced by the medium and high speeds tested than between the medium speed and the lowest speed. Which corresponds with the substantially worse print consistency of the print conducted at speed 1 which had severe mesh marking with few connections between isolated ink deposits.

Slightly different trends were produced for the sheet resistances, shown in graph (b) of Figure 4.13, where the lowest sheet resistance of 1.5 kΩ/square was produced by the medium speed. However, this value was within calculated standard deviation of

the print produced at the highest speed, most likely due to the fluctuation in print quality across the printed square. Although this larger standard deviation for the prints produced at the highest speed suggests that higher speeds led to less consistent print topography and performance. When print film thickness was taken into consideration, the medium print speed still produced the best electrical performance, as shown in graph (c) of Figure 4.13. Where the medium speed produced a sheet resistivity of $1.6 \Omega\cdot\text{cm}$, while the highest print speed produced the highest sheet resistivity of $2.2 \Omega\cdot\text{cm}$. The medium speed had the best electrical performance for the printed squares produced, most likely due to the highest print speed depositing thicker deposits, but the medium speed had a more homogeneous print with less pinholes and therefore more conductive pathways

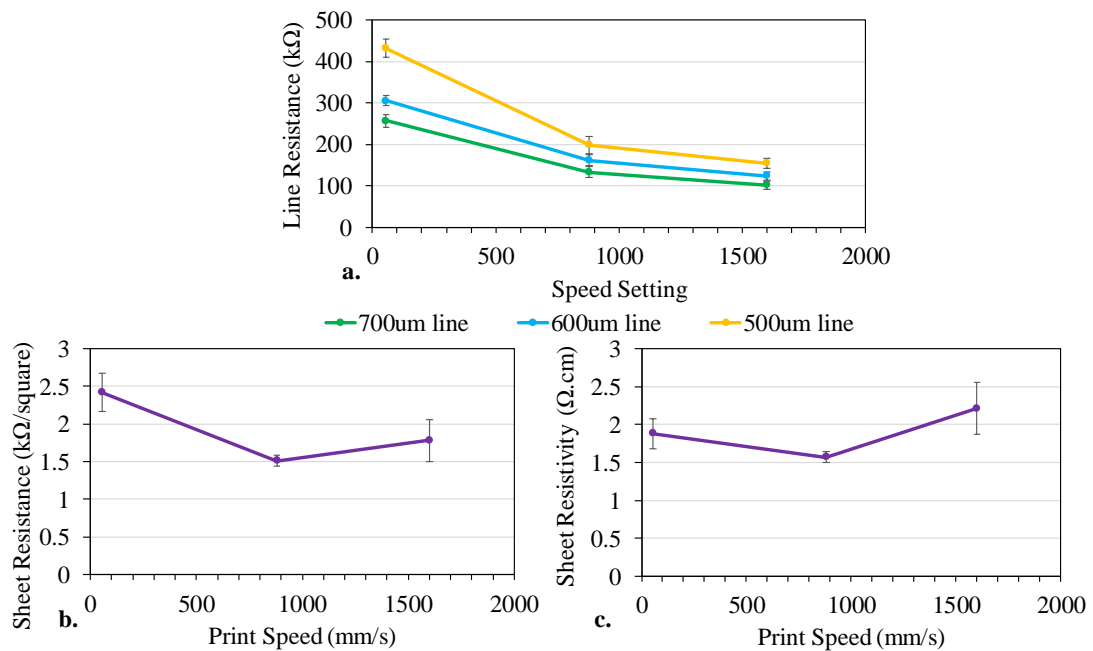


Figure 4.13 Average (a) Line Resistance, (b) sheet resistance and (c) sheet resistivity for the different squeegee speeds (error bars for standard deviation).

4.3.4.2. Squeegee Hardness

Topography Analyses

Increases in squeegee hardness were found to cause mesh marking and worsening of the print topography (Figure 4.14). The prints produced with the lowest squeegee hardness had the most consistent print topography. All prints showed some degree of mesh marking, most likely as they were all conducted at the lowest print speed as this enabled the effects of the other parameters to be more significant. The worst case of

mesh marking was shown for the prints produced with the hardest squeegee, producing the largest gaps in the printed films. This is supported by changes in the average film thicknesses, where there was an overall reduction in film thickness with increases in squeegee hardness, as shown in graph (a) of Figure 4.15. The lowest squeegee hardness deposited the greatest average film thickness for both the printed square and all lines assessed. There was a significant reduction in the average film thickness of the printed lines between 70 Shore A and 75 Shore A hardness, with a less significant reduction between 75 Shore A and 80 Shore A. Whereas there was a more gradual reduction in the film thickness of the printed squares, with the 70 shore A and 75 Shore A hardness squeegees producing similar print topographies on the printed squares. Although there was no significant change in the line widths of the printed lines with changes in squeegee hardness, as shown in graph (b) of Figure 4.15. There was a clear increase in the print roughness with increases in squeegee hardness (Figure 4.16) due to the increase in mesh marking with squeegee hardness, leading to areas with very high ink depositions and other areas with no ink deposited at all. This is due to the increased interaction between the squeegee and substrate leading to worse ink separation between the mesh and substrate, causing more ink to remain on the mesh during separation. This was also seen by Jewell *et al* (27) and Barden (33) when studying the effects of squeegee hardness. Therefore, producing areas of isolated ink deposits with few conductive pathways.

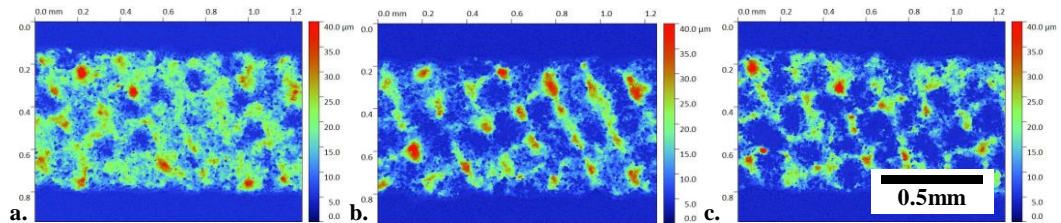


Figure 4.14 White light interferometry images of the 700 μ m nominal width lines for the printed graphite-based inks. At (a) 70, (b) 75 and (c) 80 Shore A hardness. Conducted at 5 times magnification.

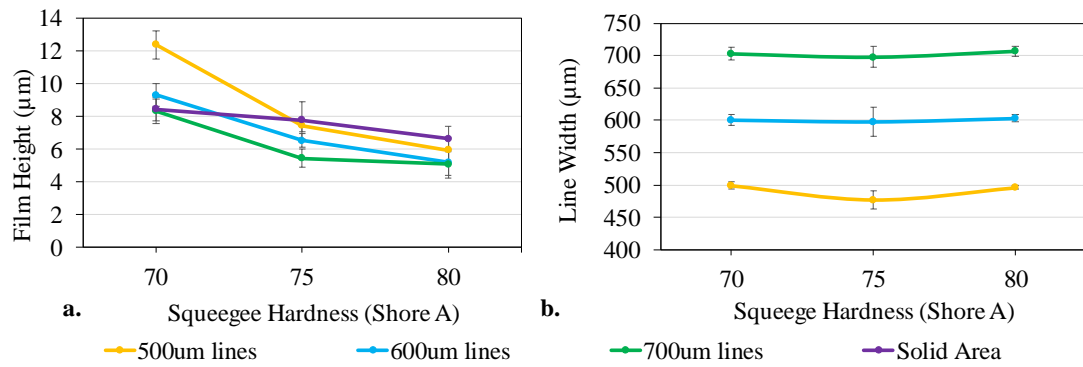


Figure 4.15 Average (a) film thickness and (b) line width for different squeegee hardness's (error bars for standard deviation).

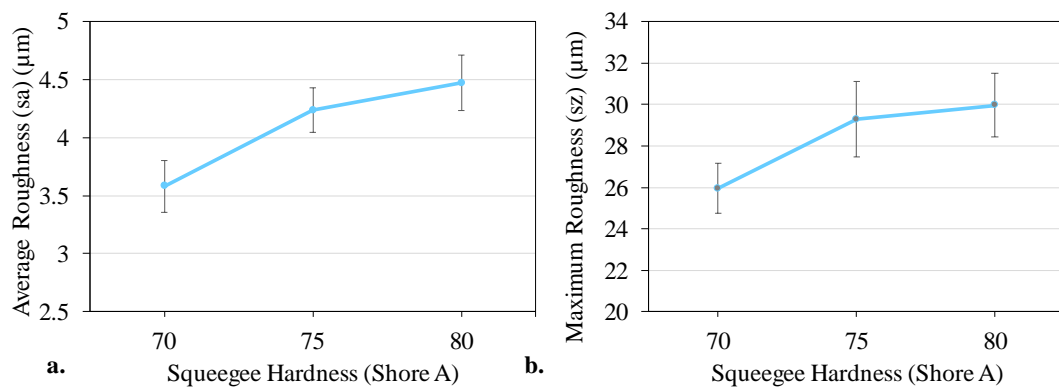


Figure 4.16 Average (a) Surface roughness (Sa) and (b) maximum roughness (Sz) for the different squeegee hardness's (error bars for standard deviation).

Electrical Characterisation

The electrical performance was inversely related to the film thickness and print consistency (Figure 4.17). The lowest line resistance values were produced with the softest squeegee of 70 Shore A hardness for all line widths assessed, as shown in graph (a). This corresponds with the changes in film height of the lines. Although there was a less significant difference between the line resistances produced at 75 Shore A and 80 Shore A hardness, which lay within standard deviation. The sheet resistance values also corresponded with the changes in film thicknesses of the printed squares. The sheet resistance produced at 75 Shore A, of 2.4 kΩ/square, was only slightly higher than that produced at 70 Shore A, which had a sheet resistance of 2.2 kΩ/square. Although the sheet resistance for the 80 Shore A hardness squeegee was significantly higher than those produced at 75 Shore A, at 3.7 kΩ/square. When film thickness was accounted for, an average sheet resistivity of

1.9 Ω .cm was produced for both 70 Shore A and 75 Shore A hardness squeegees. Whereas the 80 shore A squeegee still produced a far worse electrical performance, with a resistivity of 2.5 Ω .cm.

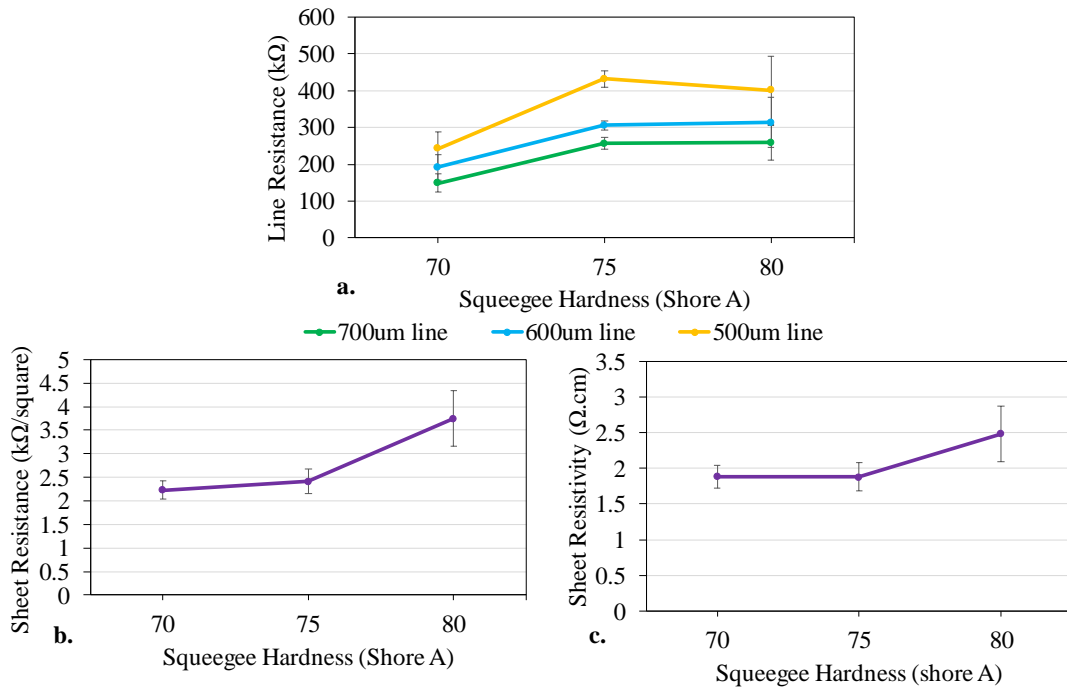


Figure 4.17 Average (a) Line Resistance, (b) sheet resistance and (c) sheet resistivity for the different squeegee hardness's (error bars for standard deviation).

4.3.4.3. Squeegee Angle

Topography Analyses

The lowest squeegee angle, of 70°, was found to produce the most consistent print out of the angles assessed (Figure 4.18). This corresponds with the work done by Jewell *et al* (27), Anderson (24)(18) and Barden (33), with the shallower angles producing more deflection and allowing more ink to be deposited. While the prints conducted at greater angles of 75° and 80° produced too much interaction between the squeegee and substrate. Causing more of the ink to remain on the mesh and producing multiple pin holes in the print, mesh marking and isolated areas of ink deposits. Which led to worse electrical performance due to a lack of conductive pathways.

This corresponds with the changes in average film thickness for the printed lines, where the 70° angle produced the greatest film thicknesses and the 75° angle produced the lowest film thicknesses (Figure 4.19). However, there was a more

significant difference between the film thicknesses produced at 70° and 75° than there was between 75° and 80°. Although there was no significant change in the width of the lines produced with changes in squeegee angle. In the case of the printed squares, there was a linear reduction in film thickness with increases in squeegee angle from 70° to 80°.

There were also significant changes in the average surface roughness (Sa) (Figure 4.20). The greatest Sa was produced at a squeegee angle of 75°, due to mesh marking causing there to be regions with high ink deposits and others with no ink deposits. The 80° angle produced similar roughness's to that of the 75° angle, although it had a lower maximum roughness as it was less affected by mesh marking. This suggests that the 75° created the worse interaction between the mesh and squeegee. The lowest Sa was produced with a squeegee angle of 70°, which corresponds with the observations as it produced the most homogeneous print. Although there were insignificant changes in the maximum roughness, as all prints contained some pin holes leading to deviations of the full print height in all cases.

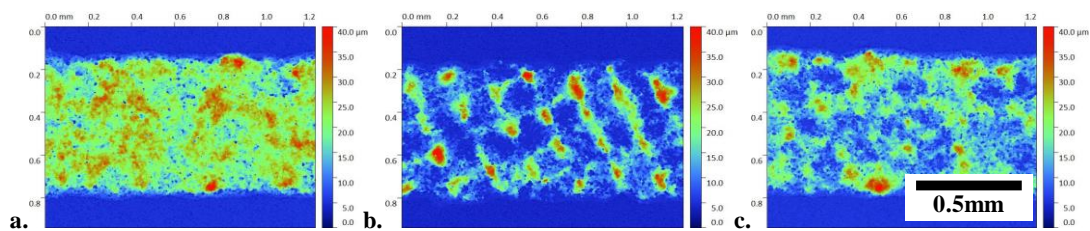


Figure 4.18 White light interferometry images of the 700µm nominal width lines for the printed graphite-based inks. At (a) 70°, (b) 75° and (c) 80°. Conducted at 5 times magnification.

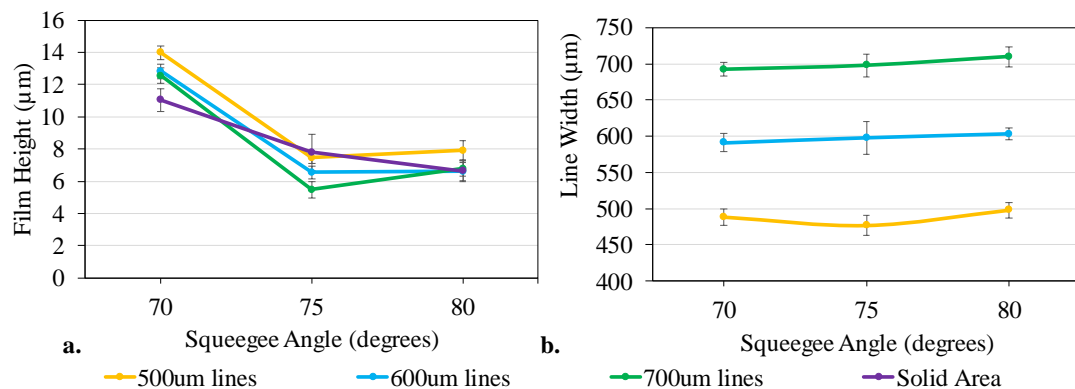


Figure 4.19 Average (a) film thickness and (b) line width for different squeegee angles (error bars for standard deviation).

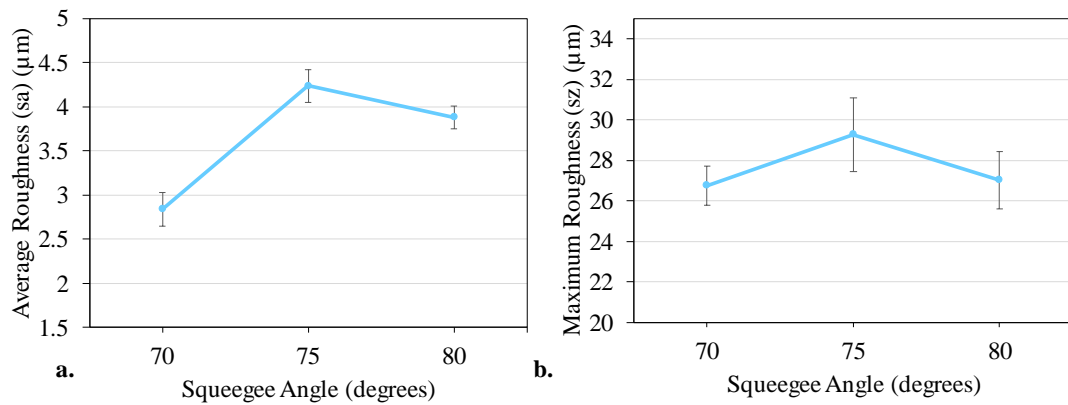


Figure 4.20 Average (a) Surface roughness (Sa) and (b) maximum roughness (Sz) for the different squeegee angles (error bars for standard deviation).

Electrical Characterisation

As with the previous results, the changes in both line and sheet resistance were inversely related to the changes in film thickness as well as roughness with changes in squeegee angle (Figure 4.21). For all line widths assessed, the 70° squeegee angle produced the lowest line resistance, whereas the 75° squeegee angle produced the highest line resistance. The 80° angle produced lower line resistances than the 75° angle, although they were significantly higher than those produced by 70° in all cases. Whereas the printed square displayed a linear increase in sheet resistance with squeegee angle, from 1.5 kΩ/square at 70° to 3.4 kΩ/square at 80°. When film thickness was accounted for, there was a less significant increase in resistivity with squeegee angle. Although there was still a gradual increase with angle from 1.7 Ω.cm at 70°, to 1.9 Ω.cm at 75°, then to 2.3 Ω.cm at 80°.

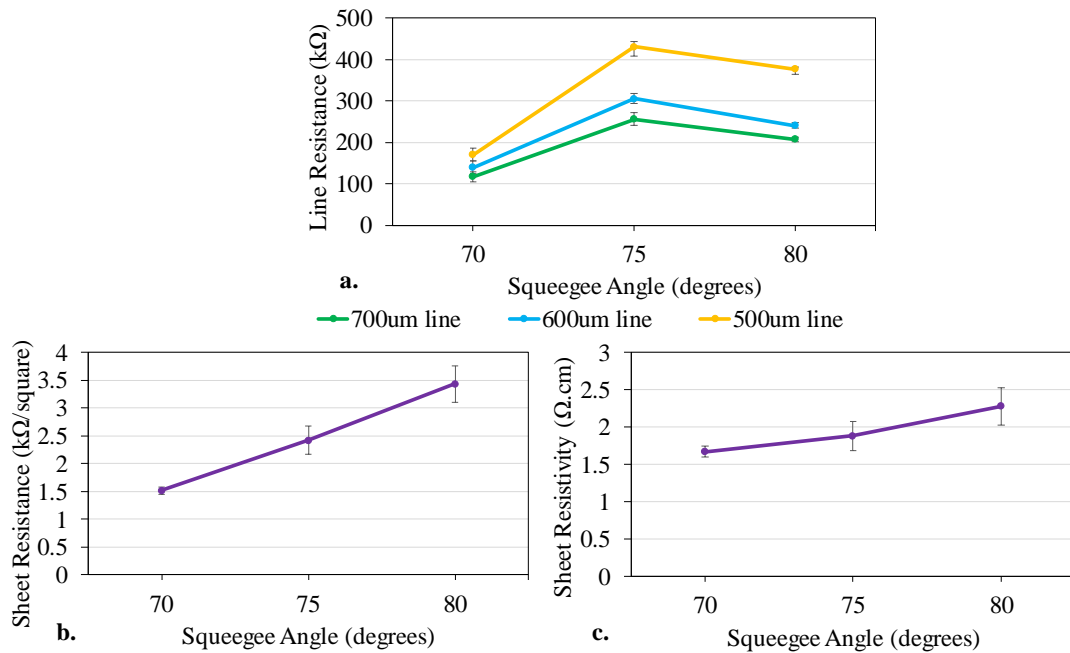


Figure 4.21 Average (a) Line Resistance, (b) sheet resistance and (c) sheet resistivity for the different squeegee angles (error bars for standard deviation).

4.3.4.4. Snap Off

Topography Analyses

The medium snap off distance of 7.5mm was found to produce the most consistent print out of those assessed (Figure 4.22). The lowest snap off distance of 5mm produced the worse print topography, with significant mesh marking with regions containing either large ink deposits or no ink at all, leading to a reduction in the number of conductive pathways across the print. There is insufficient distance between the mesh and substrate for a clean separation leading to ink remaining on the mesh. The highest snap off distance of 10mm did not exhibit mesh marking but did exhibit some areas without any ink deposited as well as large variations in the height of the ink deposited. Although this was not significantly worse than the topography of the print conducted with 7.5mm snap off. This agrees with the changes in average film thickness (Figure 4.23). The film thicknesses were highest for the print conducted at 7.5mm snap off distance and lowest for the prints conducted at 5mm snap off distance. Although there was a more significant difference between the heights for the printed lines than there were for the printed squares. For the printed lines, the average film thicknesses of the prints conducted at a 10mm snap off distance were closer to that of the height produced for a snap off

distance of 7.5mm rather than 10mm. Whereas for the printed square, the film thickness produced for the 10mm snap off distance was 8.9 μm , which is evenly between the film height of the 5mm snap off distance, at 7.8 μm and the 7.5mm snap off distance at a film height of 9.8 μm . There was no significant change in the widths of the printed lines conducted at different snap off distances. The changes in average surface roughness (Sa) were inversely related to the changes in film thickness, with the 7.5mm snap off distance producing the lowest Sa and the 5mm snap off distance producing the highest Sa. The roughness of the 10mm snap off distance lay evenly between the two. This is due to the mesh marking from the 5mm snap off distance creating the greatest roughness, while the 7.5mm snap off distance produced the most consistent film height. There was no significant change in the maximum roughness (Sz) produced as all prints had sections of the print without any ink deposit.

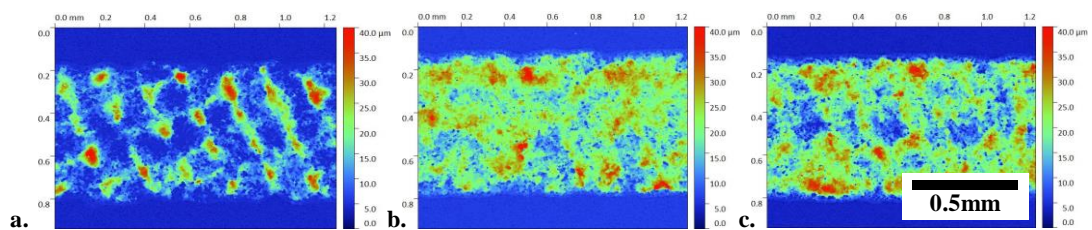


Figure 4.22 White light interferometry images of the 700 μm nominal width lines for the printed graphite-based inks. At (a) 5mm, (b) 7.5mm and (c) 10mm. Conducted at 5 times magnification.

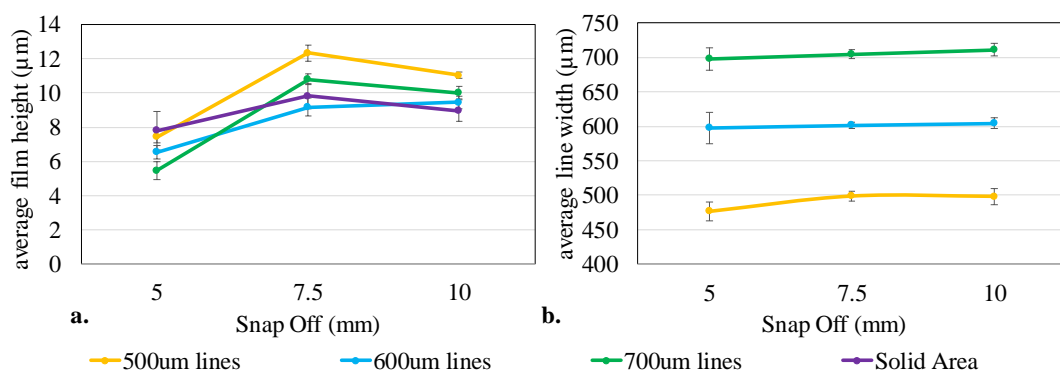


Figure 4.23 Average (a) film thickness and (b) line width for different snap off distances (error bars for standard deviation).

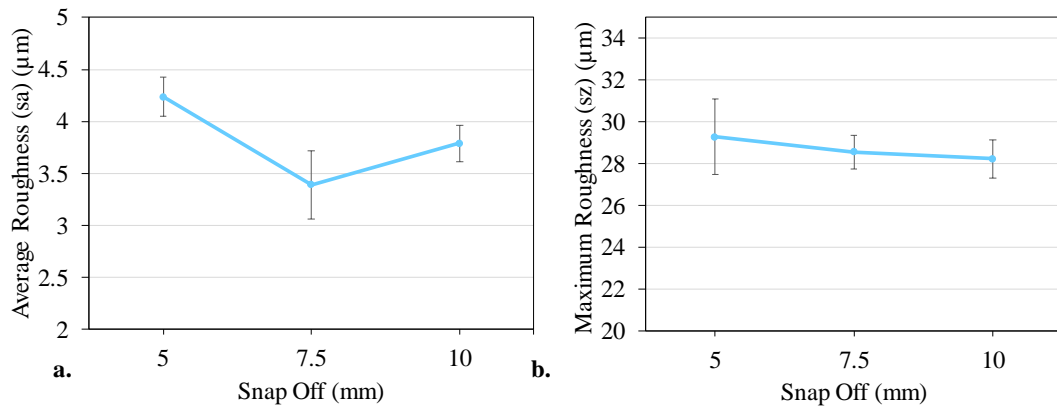


Figure 4.24 Average (a) Surface roughness (Sa) and (b) maximum roughness (Sz) for the different snap off distances (error bars for standard deviation).

Electrical Characterisation

The line and sheet resistances produced were inversely related to the printed film thicknesses, and directly related to the trend in average surface roughness produced for changes in snap off distance (Figure 4.25). In all cases, the 5 mm snap off distance produced the highest line and sheet resistances, while the 7.5mm snap off distance produced the lowest. The line and sheet resistances produced for the 10 mm snap off distance was slightly higher than those produced for 7.5 mm, but significantly lower than those produced for 5mm. However, when film thickness was accounted for, the changes became less significant, with changes in the average sheet resistivities lying within standard deviation. The 5mm snap off distance still had the highest sheet resistivity of 1.9 $\Omega\cdot\text{cm}$ and the 7.5mm snap off distance produced the lowest sheet resistivity of 1.7 $\Omega\cdot\text{cm}$.

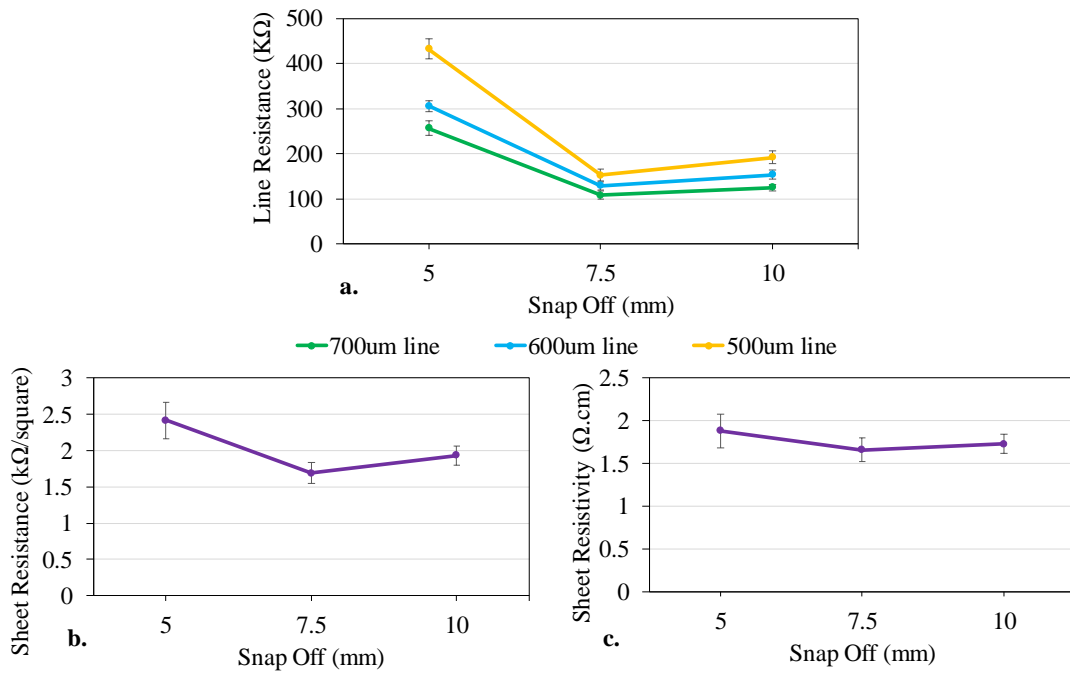


Figure 4.25 Average (a) Line Resistance, (b) sheet resistance and (c) sheet resistivity for the different snap off distances (error bars for standard deviation).

4.3.4.5. Squeegee Hardness and Angle Combined

As the effect of squeegee angle and hardness have been found to be interrelated in past literature, which showed similar trends to those found here, a further study was conducted to assess whether the quantity of ink deposit was further increased when both squeegee angle and hardness were reduced, and if the quantity was further reduced when both were increased.

Topography Analyses

As with the separate squeegee hardness and angle analyses, higher squeegee angles and hardnesses were found to lead to worse print consistency and mesh marking, as shown in Figure 4.26. In this case, increasing both squeegee angle to 80° and squeegee hardness to 80 Shore A produced a lower average film thickness than those produced when only angle or hardness were increased. The average film thickness of the printed square was reduced to 5.0 μm, whereas it was 6.9 μm for a 75 Shore A squeegee at an angle of 80° and 6.6 μm when using an 80 Shore A squeegee at an angle of 75°. However, this was not the case when comparing the film thicknesses of the printed lines. The print conducted with a squeegee angle of 75° with an 80 Shore A hardness squeegee producing the lowest film thickness, of 5.9 μm for the 500 μm line. Compared with a film thickness of 6.2 μm for the 500 μm produced with a

squeegee angle of 80° with an 80 Shore A hardness squeegee. This may be as the print consistency is so bad due to mesh marking with isolated islands of ink, that the print quality cannot get much worse, leading to little change in the average film thickness.

Minimising both squeegee angle and hardness, to 70° and 70 Shore A hardness respectively, produced a consistent print without any mesh marking and few pin holes with a high average film height. Although the average heights were greater than those produced for the 70 Shore A squeegee at an angle of 75°, it was within standard deviation of the average height produced with the 75 Shore A squeegee at an angle of 70°. Therefore, minimising the angle to 70° was beneficial on the print consistency and therefore average film thickness. This is due to there still being print defects such as mesh marking occurring when using a squeegee angle of 75°, even when using a 70 Shore A hardness squeegee, as was shown in Figure 4.14. Whereas there were no signs of mesh marking in the prints conducted with a 75 Shore A hardness squeegee at an angle of 70°, as shown in Figure 4.18, with relatively few pin holes. Therefore, further reductions in squeegee hardness appear to have a less significant effect on the average film thickness. Although the print conducted with a 70° squeegee angle and 70 Shore A hardness squeegee (Figure 4.26) appears to have less pin holes than the print conducted with a 70° squeegee angle and 75 Shore A hardness squeegee which may lead to better electrical pathways.

As with the squeegee hardness analyses, there was no significant change in the line widths produced with maximising or minimising both squeegee angle and hardness (Figure 4.27).

The average surface roughness (S_a) and maximum surface roughness (S_z) was also found to be lowest for the prints produced for the lowest squeegee angle and hardness, due to it producing the most consistent printed film with the least pin holes or gaps in the print (Figure 4.28). The prints produced at medium and maximum squeegee angles and hardnesses produced higher surface roughness's, due to the variation in profiles from the mesh marking.

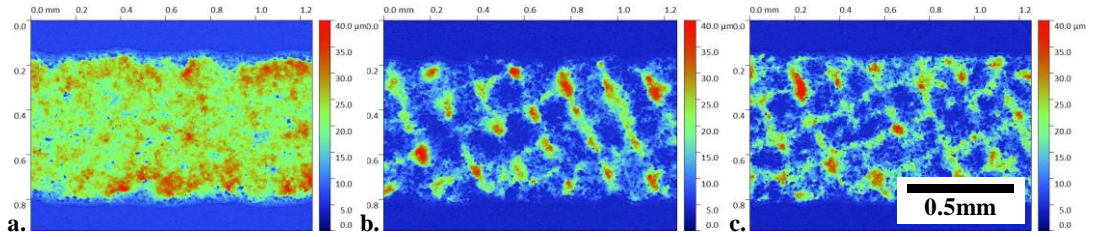


Figure 4.26 White light interferometry images of the 700µm nominal width lines for the printed graphite-based inks. At (a) 70° and 70 Shore A hardness, (b) 75° and 75 Shore A hardness and (c) 80° and 80 Shore A hardness. Conducted at 5 times magnification.

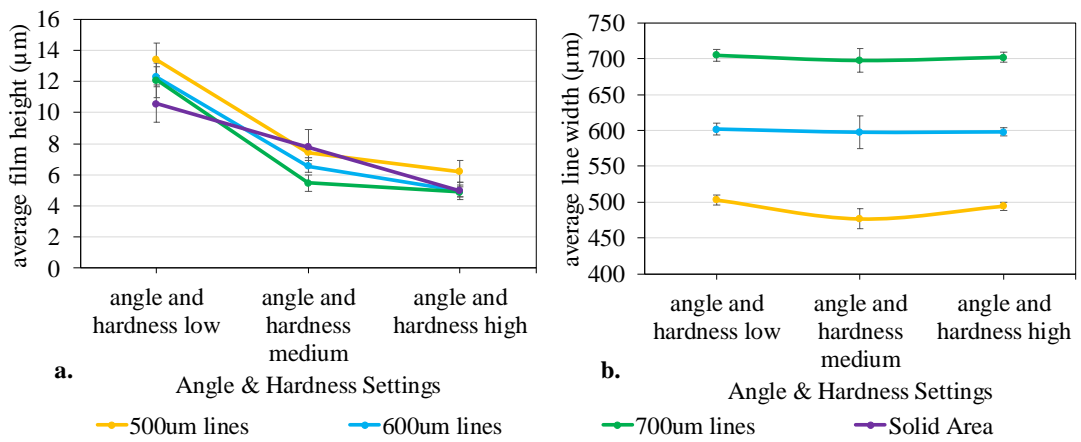


Figure 4.27 Average (a) film thickness and (b) line width for different squeegee hardness's and angles (error bars for standard deviation).

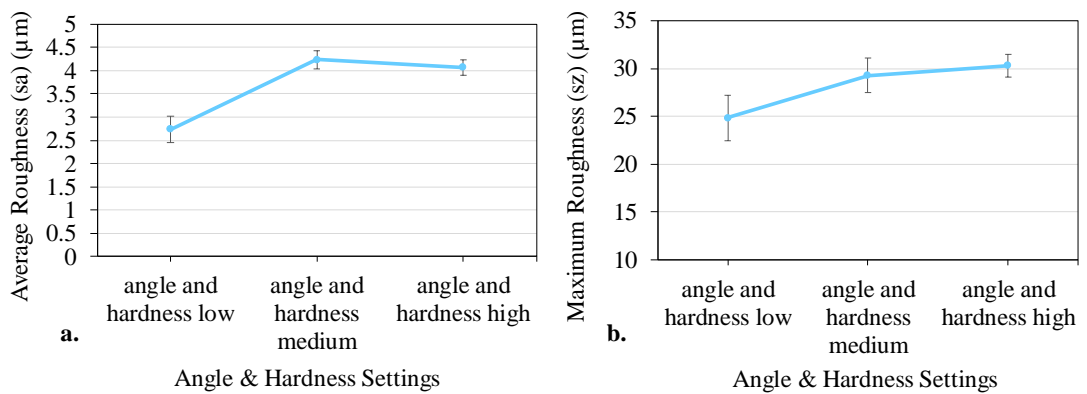


Figure 4.28 Average (a) Surface roughness (Sa) and (b) maximum roughness (Sz) for the different squeegee hardness's and angles (error bars for standard deviation).

Electrical Characterisation

As with the previous experiments, the changes in both line and sheet resistance were inversely related to the changes in film thickness and roughness with changes in squeegee angle, as shown in Figure 4.29. The line resistances produced for the lowest squeegee angle and hardness (70°, 70 Shore A) were found to be lower than those produced for all other combinations. Whereas the line resistances produced for the highest squeegee angle and hardness (80°, 80 Shore A) were higher than those produced for all other combinations assessed in these experiments. There was a linear increase in line resistance with increases in both squeegee angle and hardness, where the line resistances produced for the medium settings with a 75 Shore A squeegee at an angle of 75° lay within the middle of the other settings. Similar trends were seen with sheet resistance, where the lowest settings produced a sheet resistance of 1.6 k Ω /square, and the highest settings produced a sheet resistance of 6.0 k Ω /square. In this case, the sheet resistance for the medium squeegee angle and hardness (75°, 75 Shore A) was closer to that of the lower settings than the higher settings, at 2.4 k Ω /square.

When film thickness was accounted for, similar trends were still seen. The average sheet resistivity produced for the lowest squeegee angle and hardness (70°, 70 Shore A) was 1.7 Ω .cm, the medium settings with a 75 Shore A squeegee at an angle of 75° produced a sheet resistivity of 1.9 Ω .cm and the highest squeegee angle and hardness combination (80°, 80 Shore A) produced an average sheet resistance of 3.0 Ω .cm. Therefore, minimising the squeegee angle and hardness led to the best electrical performance.

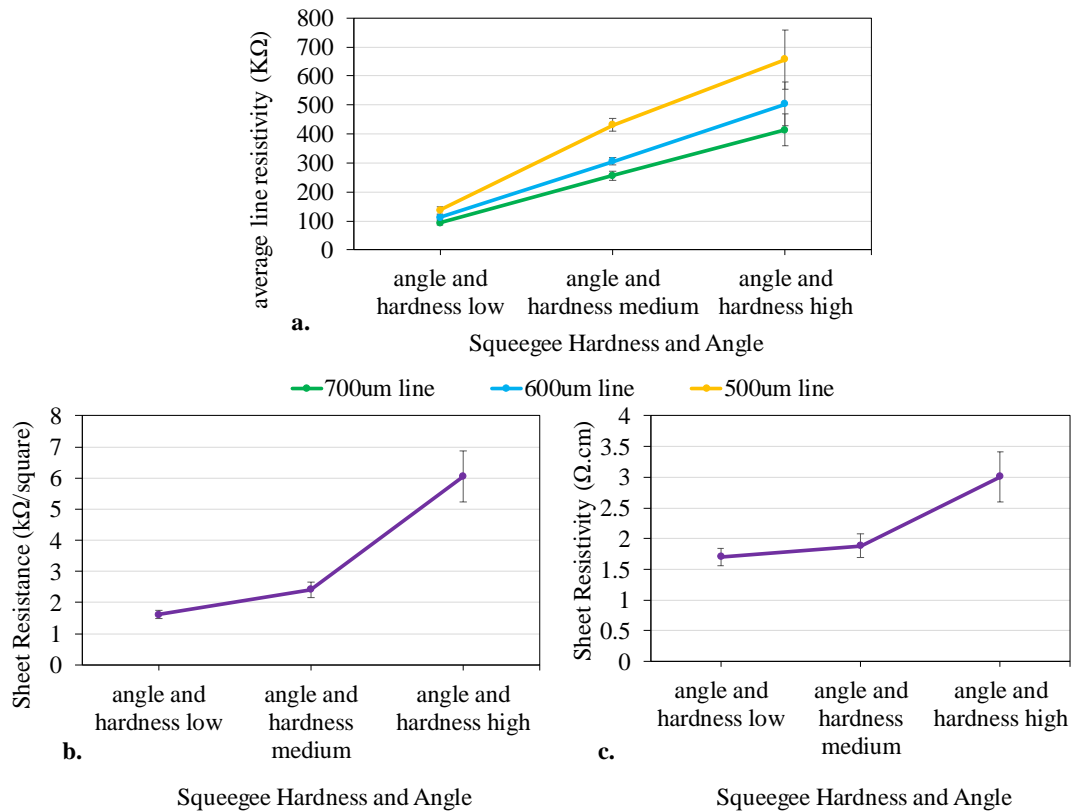


Figure 4.29 Average (a) Line Resistance, (b) sheet resistance and (c) sheet resistivity for the different squeegee hardness's and angles (error bars for standard deviation).

4.3.4.6. Effect of parameters with changes in line orientation

In addition to the line resistance values conducted perpendicular to the print directions which were used for the main analyses, additional lines were printed in the same prints at different orientations. These additional lines were parallel and at 45° to the print direction, printed to verify whether the same trends were observed with changes in parameter settings, irrespective of the print direction. The changes in line resistance for the 700 μm lines produced in all three orientations are compared in Figure 4.30. Analyses were also conducted on the other line widths, with the same trends shown. The changes in print topography were also found to be inversely related to the changes in line resistance, as found with the previous studies.

In Figure 4.30 it was shown that comparable trends were found for most of the studies conducted. However, the extent of the difference between the line resistances produced at the different settings were found to be more significant in some cases, for the lines produced parallel or at 45° to the print direction. In the case of the squeegee speed, shown in graph (a), the lowest speed produced the highest line

resistance and the highest print speed produced the lowest line resistance in all cases. However, the differences between the line resistances produced at the lowest and medium speeds is far more significant for the lines produced parallel or at 45° to the print direction. The changes in line resistance with squeegee hardness were also similar, where the 70 Shore A hardness squeegee produced the lowest line resistance in all cases. However, the lines produced parallel or at 45° to the print direction had far higher sheet resistances than the lines printed perpendicular to print direction, for squeegee hardness's of 75 Shore A and 80 Shore A. The effect of increasing squeegee hardness from 75 Shore A to 80 Shore A also had different effects. Where lines printed parallel to print direction saw reductions in line resistance, while the lines printed 45° to print direction saw a linear increase. The effects of squeegee angle and snap off distance, shown in graphs (c) and (d) respectively showed the same trends for the parallel and 45° lines, as with the perpendicular lines. However, with squeegee angle, the lines produced with a 75° squeegee angle had significantly higher line resistances for those produced parallel or at 45° to the print direction, while the resistances produced at the other squeegee angles were similar to those produced with the perpendicular line. The snap off distance found the resistances produced at 7.5 mm and 10 mm were similar for all line orientations, but the lines produced with a 5mm snap off had significantly higher resistances for those produced parallel or at 45° to the print direction.

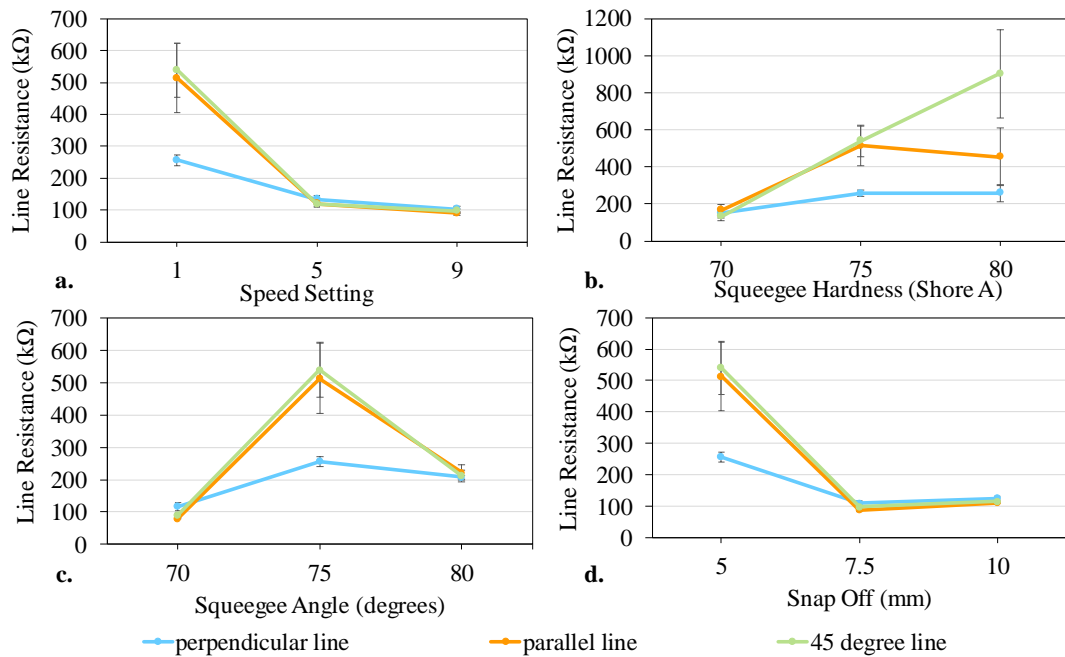


Figure 4.30 Changes in line resistance with line orientation for different (a) squeegee speeds, (b) squeegee hardness's, (c) squeegee angles and (d) snap off distances

4.3.4.7. Discussions of Svecia parameter study

In the parameter studies conducted on the Svecia Matic flatbed screen printer, print speed was found to have a significant effect on print topography, with more ink being deposited at greater speeds due to the rheological profile of the graphite-based ink which was highly pseudoplastic and significantly thinned down over the range of shear rates assessed. The reduction in ink viscosity enabling the ink to flow more readily, leading to more ink being deposited and more homogeneous prints. An ink which shear thins over a smaller shear range may be less susceptible to speed or have a different optimal speed for being printed with, as suggested in the literature.

In the case of squeegee parameters, minimising both squeegee angle and hardness led to increases in the amount of ink deposited and the consistency of the printed film. Along with corresponding reductions in sheet and line resistance. This corresponds with the literature (Section 2.2.2) which found that softer squeegees tend to deposit more ink (23,27,31,32) and that lower angles typically led to a greater film thickness, as illustrated in Figure 2.1 (27,31,32).

With snap off distance, the medium snap off distance was found to produce the thickest and most consistent print. There was an optimal range for snap off rather

than a clear correlation between snap off and a measurable print parameter. The little snap distance would lead to excessive interaction between the mesh and print, which in this case led to mesh marking. While too much snap distance would cause insufficient contact between the mesh and substrate, which in this case caused patches of the print to not transfer across to the substrate. However, the effect of snap off is interlinked with the effect of print pressure, where a given snap off would require pressure to be optimised to ensure sufficient contact. The use of excessive pressure would cause the squeegee to scrape off some of the deposited ink, and too little would prevent the squeegee from providing sufficient contact between the mesh and substrate. In this case, the squeegee pressure was optimised to the contact point for each snap off distance assessed.

There was little variation in the width of the lines produced for the different parameter settings, this is most likely as fluctuations in line width are usually associated with slumping. This is a property of the ink rather than the press parameters.

4.4. Discussions

In the mixing technique experiments, the inks which were Speedmixed produced a more consistent print topography with less defects than those which were stirred. Speedmixing provided an even shear to the whole ink, whereas the traditional overhead stirrer used a blade which only provided localised shear to a given section of the ink at a time leading to sections of the ink containing worse distribution of graphite, which would lead to increases print inconsistencies, as were shown in the results. However, the inks which were triple roll milled prior to Speedmixing produced the best results in terms of both print consistency and electrical performance. This is due to the milling enabling the graphite flakes to be well dispersed in the ink prior to mixing, leading to further improvements in ink homogeneity, which in turn led to better print performance. The ink which was triple roll milled prior to being Speedmixed had the lowest viscosity at all shear rates assessed with one of the lowest phase angles. This would have enabled it to flow better during printing. As triple roll milling followed by Speedmixing was found to produce the most consistent print with the best electrical performance out of the

mixing and milling methods tested, this was used for preparing the inks used in the parameter studies.

Squeegee speed was found to have a significant effect on the print topography and electrical performance of the prints in the study conducted on the Svecia press. This is due to increases in print speed enabling increases in the shear rate of the ink being deposited, which led to reductions in ink viscosity, enabling the ink to flow more readily through the mesh and increasing the amount of ink deposited. Increases in the squeegee speed were found to produce improvements in the print performance up to speeds of around 1.5 m/s. The ink used in this study was highly shear thinning up to 100 s^{-1} and did not show signs of levelling off. This is different to the pseudoplastic profile of many commercial screen-printing inks. Therefore, the optimal speed settings will depend on the rheological profile of the ink. The viscosity of the graphite-based ink at lower shear rates was also a lot higher than many commercial screen-printing inks, including the ink assessed in Chapters 5 and 6. This combined with the ink only containing large graphite flakes may have been the cause of the severe mesh marking observed at low squeegee speeds, as mesh marking is usually caused by the ink viscosity being too high. In all of the prints produced, prints which exhibited mesh marking had far worse electrical performances, with lower average film thicknesses and higher roughness's than those which did not exhibit it.

The hardness and angles of the blade squeegees were both found to have significant effects on the print topography and performance. Reductions in the angle and hardness were found to increase the amount of ink deposited. This corresponds with what was found in the literature for a range of inks (23,27,31,32). The effect of the blade squeegees hardness and angle is irrespective of ink rheology. Where reductions in the squeegee hardness and contact angle of blade squeegees enable the squeegee tip to deflect more during printing. This allows more ink to pass through the mesh, which leads to greater ink deposits. The hardness and pressure of the diamond squeegee had no significant effect. This is most probably as the contact edge of the diamond geometry is at 45° to the mesh and substrate, meaning that the tip will not be deflected away as with a blade squeegee. This makes diamond squeegee more consistent for producing prints of the same performance, but harder to optimise the print performance with.

Snap off distance was also had an effect on the print topography and electrical performance, but to less of an extent than the squeegee speed or hardness and angle of the blade squeegee. The medium snap off distance was found to produce the most consistent print with the best electrical performance for all line orientations and the printed solid areas when assessed with the Svecia trials. This also corresponds with the literature (38), where too low a snap off distance would cause excessive interaction between the mesh and substrate leading to poor ink separation. While too high a snap off distance would lead to distortion of the mesh which would also lead to poor ink separation and therefore worse print quality and electrical performance.

With the prints conducted on the DEK 248, there were gradual improvements in the electrical performances of the printed lines produced perpendicular to the print direction. Although the lines printed parallel or at 45° to the print direction followed the same trend as the Svecia prints. The difference in results is most likely due to the different screen sizes which require different snap off distances. Where the range tested on the Svecia went beyond the optimal snap off distance, leading to worse print consistency and electrical performances at the highest snap off distance for all orientations assessed. While the prints conducted on the DEK did not reach the point where the mesh became distorted or overstretched, therefore producing better prints at greater snap off distances.

In both parameter studies, the printed lines were produced at a range of orientations, perpendicular, parallel and at 45° to the print direction. Similar trends were observed when altering the parameter settings for the differently oriented lines. However, the lines printed perpendicular to the print direction were found to produce lower line resistances than those produced parallel or at 45° to the print direction.

4.5. Conclusions

Optimal mixing techniques for producing a graphite-based ink with best consistency and performance were identified as consisting of triple roll milling followed by Speedmixing as the triple roll milling ensured that flakes were evenly distributed and of even flake sizes while the Speedmixing improved the homogeneity of the ink. Overhead mixing only provides shearing to the centre of the ink pot and can lead to uneven mixing, as was shown in the results where triple roll milling and Speedmixing produced more even prints with less defects. This also led to

improvements in the electrical performance of the prints, as the improvements in ink homogeneity and print consistency directly affect the resistances. This was then used for producing the inks to be assessed for the press parameter studies.

The squeegee speed along with the hardness and angle of a blade squeegee were found to have the most significant effects. The print consistency and electrical performance of the print could be improved by increasing the print speed to enable the ink to reduce in viscosity and flow more regularly, or by reducing the squeegee hardness and angle which reduced the interaction between the squeegee and substrate. Leading to better ink separation from the mesh and a more homogeneous print due to the deflection of the squeegee, if a blade squeegee was used. Snap off distance was also found to have an effect on the print topography and electrical performance in both parameter studies, but to less of an extent.

The hardness and pressure of a diamond geometry squeegee was found to have no significant effects on the print performance, with variation lying within standard deviations from the print cycle and print location. In these studies, mesh marking was found to occur at low print speeds due to low ink viscosity causing poor separation between the mesh and substrate. As well as with low snap off distances, high squeegee angles and harnesses with blade geometry squeegees where excessive interaction between the squeegee and substrate led to poor ink separation. This resulted in low average film thickness's (quantity of ink deposited), high roughness's and poor conductivity. The parameter studies also identified that the line orientation influenced the degree to which parameter settings effected print performance. Where lines produced parallel to, or at 45° to the print direction tended to produce higher line resistances than those produced parallel to the print direction.

In the cases of squeegee speed and snap off distance, the changes in print topography and performance may relate to the ink deposition and separation mechanisms occurring during screen printing. With snap speed, this mechanism will be related to the level of interaction between the mesh and the separating ink. While the optimum print speed is intertwined with the rheological profile of the ink and may cause changes in the ink separation mechanism at different shear rates. Therefore, further work will be conducted in the following chapters to assess whether there are any

notable changes in the actual deposition and separation mechanism with changes in snap off distance and print speed.

As well as this, the ink preparation methods involving triple roll milling followed by Speedmixing will be used as the preparation methods for making other custom-made inks used in this thesis.

This chapter has explored the effects of optimising print performance by improving the parameters settings. However, further improvements could be made by employing post processing methods. These will also be investigated in chapter 7.

Chapter 5. High speed imaging the ink transfer mechanism of screen- printed carbon pastes

5.1. Introduction

This chapter focusses on bridging the knowledge gap in understanding the mechanism by which the ink is transferred through the mesh and onto the substrate during screen printing. The theoretical mechanisms proposed by Messerschmitt (70) and Riemer (39) contradicted one another, dated back to the 1980's before the proliferation of printed electronics and lacked experimental validation.

Riemer (39) proposed that the screen mesh acted like pistons in a syringe, forcing the ink onto the substrate as columns of ink exiting from a tube. After the print stroke, the mesh would be released by its own tension, while the ink remained on the substrate due to adhesive forces between the ink and substrate. The ink would then be able to slump after it had been released from the mesh to form the print, as shown in Figure 2.5. Whereas Messerschmitt (70) proposed that the separation forces would not be able to overcome the adhesion between the ink and mesh in such a way. This would induce a flow, creating a combination of shear and extensional forces which would lead to the ink splitting between the mesh and substrate. This process was described through four key stages consisting of adhesion, extension, flow then separation, as illustrated in Figure 2.5. This chapter presents a unique and novel method which was developed to directly image the ink deposition and separation mechanisms using a custom-made screen-printing visualisation rig. This allowed the screen-substrate separation to be captured during the printing process via a high-speed camera. Thus, providing experimental evidence of the separation mechanisms occurring during screen printing. The design of the rig enabled control of the print

speed and squeegee height to ensure constant squeegee pressure. The design and development of the rig is detailed in Appendix II.

The separation mechanisms were compared against the separation regions proposed in literature and the print topographies. A commercial carbon-based ink was used as it was capable of printing higher quality prints necessary for initial studies used to validate the deposition mechanism than the simple graphite-based ink used in the parameter studies in the previous chapter.

A study on the effect of snap distance and print speed was conducted with the same ink. Print speed was found in both the literature and in Chapter 4 to be related to the rheological properties of the ink. The snap off distance was found previously to be related to the interaction between the mesh and substrate (23,38,40). The effects of both these parameters could be visualised with this technique.

Shear rheology tests were conducted to establish the viscoelastic properties of the ink. The Capillary Breakup Extensional Rheology (CaBER) technique was also used to evaluate the relative amounts of material directed to bottom or top interfaces and flow characteristics as the ink was pulled apart. This is analogous to the extent to which the ink is either transferred to a substrate or retained by the screen mesh, although further testing on the visualisation rig were required to assess the effects of the shear forces of the squeegee, mesh and screen angle. Changes in the mode of capillary thinning and break up with alterations in strain and strain rate were related to the profiles of the filaments formed during the printing process. However, in screen printing there is the additional complexity of the effects of the mesh strands and the stresses occurring in both the x and z axes, due to the angle between the mesh and substrate, which makes it harder to evaluate the relative effects of vertical or horizontal forces and the separation mechanisms. The screen-printing visualisation rig was used to assess how snap off distance and print speed affected the separation mechanisms occurring with changes in print speed and snap off distance.

Topographic analyses of the resulting prints were used to assess whether changes in the ink deposition mechanism affected the resulting ink transfer and print quality. Along with topographic and electrical characterisation of prints produced on a commercial printer to assess whether similar trends are seen in those circumstances.

5.2. Materials and Methods

5.2.1. Rheological and extensional testing

The ink was a commercial carbon ink from Gwent Electronics Materials (GEM C2150317D3 carbon paste (contains a blend of graphite and carbon black, with a solid content of 38-42%)). In common with many commercial inks, limited rheological data was available and insufficient to relate to the flows observed. Therefore, a full Rheological characterisation was carried out using a combination of shear, viscoelastic and extensional measurements. Shear viscosity measurements were carried out on a Malvern Bohlin rotational rheometer (Gemini Bohlin Nano, Malvern Instruments) with a 2° 20 mm stainless steel cone and a parallel plate held at 25 °C. Ink viscosity was measured as the shear rate was gradually increased to 100 s⁻¹ and then reduced back to 1 s⁻¹. Viscoelastic measurements were carried out on a Malvern Kinexus Pro Rheometer (Malvern Instruments) with a 40 mm roughened plate and roughened parallel plate (to minimise the effect of slip). Amplitude (strain) sweep measurements were conducted to establish the linear viscoelastic range at 0.1, 1 and 10 Hz. Then using a stress within the established linear viscoelastic region, a frequency sweep from 0.1 Hz to 10 Hz with 30 logarithmically spaced measurements was conducted.

Extensional testing of the ink was assessed using Capillary breakup extensional rheology (CaBER) testing methods. Ink samples were placed between two parallel 3 mm diameter stainless steel plates held at a 1 mm gap, where the upper plate was then moved upwards at a constant velocity. Once the plates have reached their separation distance, a liquid bridge is formed between the two endplates. As the ink filamented, the resulting change in minimum diameter was then recorded and measured over time until the separation point where upper and lower filaments were formed. As well as this, the relative material flow from bottom to top plates were assessed in terms of cross-sectional area of ink split between the plates, as well as length to separation point from the bottom plate. This provided a 2-dimensional analysis of ink flow during the separation stage in screen printing, which could be compared with existing computational models (Such as those by Kapur et al. (71)) and with those observed in screen printing where other forces are also present. These tests were conducted to mimic the effect of snap distance and print speed on the ink separations mechanisms, but without the effects caused by the mesh, shear forces

from the passage of the squeegee and print angle, which would be related to the separation mechanisms occurring during printing on the rig. To assess the effect of separation distance and speed on the ink separation, this gap was extended by 3 mm, 5 mm and 7 mm by moving the upper plate vertically upwards. For each gap, this was performed at constant velocities of 20 mm s^{-1} , 60 mm s^{-1} and 100 mm s^{-1} . The extension and separation of the cylindrical liquid bridges were captured using a high-speed camera (Photron FastCam Mini High-Speed Camera) at a frame rate of 125 frames per second.

The separation distances were larger than the snap off distances produced, as the 3mm diameter cylinders used would produce filaments of a greater diameter than those produced during separation in screen printing.

5.2.2. Screen-printing visualisation method

Screen-printing visualisation rig allowed the screen-substrate separation to be captured during the print via the high-speed camera (Figure 5.1). The rig used a small screen (100 mm x 130 mm polyester mesh at 22.5° with 61 threads per cm, $64 \mu\text{m}$ thread diameter and $12 \mu\text{m}$ emulsion) (supplied by MCI Precision Screens Ltd.), which enabled imaging within the camera's focal length (80 mm). The print image consisted of a continuous 32mm long line made up of five 6mm long sections (Figure 5.2). Squeegee motion in the x and z axes was controlled by stepper motors powering lead screws on linear actuators to set the speed and distance of the movement. This allowed the squeegee to be brought in to contact with the screen, then brought across the screen to transfer the ink. A 65–70 Shore A hardness diamond squeegee was used. The squeegee had a 10 mm x 10 mm profile and was 10 mm in length to minimise deflection on the screen. For the initial experiment assessing the effect of line width on the $400 \mu\text{m}$, $200 \mu\text{m}$, $100 \mu\text{m}$ and $50 \mu\text{m}$ lines (as the carbon ink would not deposit through the $25 \mu\text{m}$ line), a snap distance of 1.825 mm was used with a squeegee speed of 300 mm min^{-1} (5.0 mm s^{-1}).

In the experiment investigating the effect of snap distance and squeegee speed, the snap distance (distance between screen and substrate) and squeegee speeds (print speeds) were both varied over three settings. With snap distances of 1.125 mm, 1.475 mm and 1.825 mm, which were created by stacking layers of the $175 \mu\text{m}$ substrate to gradually reduce the distance between the mesh and substrate. The

substrates were taped in place to ensure they were flat and secure. Along with squeegee speeds of 100 mm min^{-1} (1.7 mm s^{-1}), 300 mm min^{-1} (5.0 mm s^{-1}) and 500 mm min^{-1} (8.3 mm s^{-1}). These speeds were identified as the best operational speeds for the stepper motors, with greater or lower speeds inducing vibrations within the rig. More increments were tested between these speeds in initial trials but were found to have produce insignificant differences in the prints deposited. The substrate was PET (polyethylene terephthalate—Melinex® 339, DuPont Teijin Films ($175 \mu\text{m}$ thickness) opaque white). The print image consisted of a continuous $200 \mu\text{m}$ wide line in the direction of squeegee travel. This width produced clearer and more consistent prints than those conducted through the narrower lines. As well as having only one gap between threads across the width of the line, unlike thicker lines, so that there were only single filamentations in the y direction.

Imaging of the print cycle was conducted at the interface between the screen and the substrate. It was conducted with the same camera as used in extensional testing, at 125 frames per second with 5 times magnification. A 10,000-lux lamp was placed directly behind the screen-printing rig to provide backlighting for high contrast imaging. Camera images were assessed using ImageJ (126) to measure the lengths of different regions of the print cycles, based on the four regions of flow identified by Messerschmitt (70). These four regions were split up into two quantifiable lengths. Additionally, the length of the paste flow ahead of the squeegee was assessed to make up the full contact region, consisting of the total duration where the ink is simultaneously in contact with the mesh and substrate. The lengths of these flow regions were then measured every 0.024seconds (every third frame) across the print run, where the full contact region (where the ink was in simultaneous contact with the mesh and substrate) could be seen. This produced around 15 measurement sets for each print run, from which an average and standard deviation could be calculated. The filamentation and separation modes displayed during the separation stage were also assessed.

5.2.3. Comparison Screen Printing

Comparison prints on a DEK 248 flatbed screen press were conducted to assess the effect of snap distance and print speed on print topography and electrical performance for a greater range of line widths and printed solid areas. This was to confirm whether the trends in print topography and performance produced on the

visualisation rig were also seen for a greater range of print geometries. The prints were made on to the same substrate using a polyester mesh containing 61 threads per cm, 64 μm thread diameter and 13-micron emulsion with a 65–70 Shore A hardness diamond squeegee of 130 mm length and flood speed of flood speed of 70 mm s^{-1} . The snap off distance was varied from 0.5 mm to 1.5mm with squeegee pressures optimised for each snap off distance (7kg to 9kg), while the squeegee speed was varied from 30 mm s^{-1} to 70 mm s^{-1} . The effects of the settings were assessed as a 3² full factorial, as shown in Table 5.1. The print image included a series of 25-mm-long lines of nominal widths from 100 μm to 700 μm and a 45-mm square solid square for sheet resistance and resistivity assessment. Printed samples were dried in a conveyor dryer at 100°C for 5 minutes. The results from the 700 μm lines are compared in these results as similar trends were seen for all the line widths assessed, with the 700 μm lines producing the lowest standard deviation in line width, height and resistance.

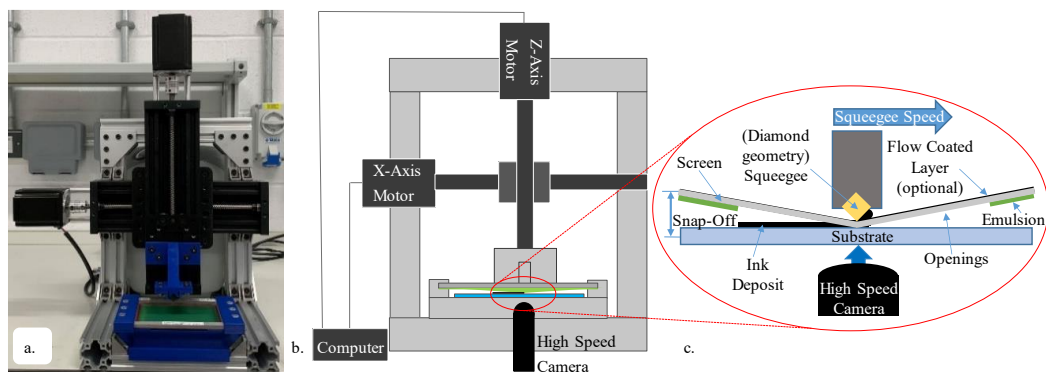


Figure 5.1 Photograph (a) and schematic diagram (b) of the screen-printing simulation rig, showing the positioning of the high-speed camera. The zoomed in schematic diagram (c) shows a cross section through the point of contact during screen-printing as would be observed by the high-speed camera.



Figure 5.2 Print image design consisting of 6mm long sections reducing from 400 μm to 25 μm (400 μm , 200 μm , 100 μm , 50 μm and 25 μm) in line width.

Table 5.1 3² Full factorial analysis of snap off distance and print speed on the DEK 248 screen-printer

Test	Snap off distance (mm)	Print Speed (mm s ⁻¹)
1	0.5	30
2	0.5	50
3	0.5	70
4	1	30
5	1	50
6	1	70
7	1.5	30
8	1.5	50
9	1.5	70

5.2.4. Printed line topography

White light interferometry (NT9300, Veeco Instruments, Inc., Plainview, NY, USA) was used to measure a full three-dimensional surface profile of the printed lines and solid areas produced on both the rig and DEK 248. Five times magnification was used for all scans, giving a measurement area of 1.2 mm by 0.93 mm (at a resolution of 736 × 480 pixels with sampling at 1.67 μm intervals). The lines produced on the rig were each measured in 4 evenly spaced points, with three print samples assessed for each line width or setting. Totalling 12 measurements for each line width and parameter setting, from which the average and standard deviation were calculated.

Comparison prints conducted on the DEK-248 for the snap off distance and print speed studies were also assessed using white light interferometry with 5 times magnification. The 700 μm nominal width lines were measured in 3 points each on 3 print samples with average at standard deviation calculated. For the printed squares, analyses were conducted in the centre of the print for average surface roughness (sa) and average maximum surface roughness (sz) values. As well as over the edge of the

solid print, so that the printed ink film thickness could be evaluated. Twelve measurements were conducted for the surface roughness and film thickness for each parameter setting (from 4 even points around the squares perimeter and 4 even points in the centre for each print, 3 print samples were assessed for each setting). From this, the standard deviation in film thickness and surface roughness was calculated.

To provide an overall image of the printed lines produced on the rig, optical microscopy (Alicona Infinite Focus G5 microscope) was used for its ability to more effectively capture the surface form of carbon ink in true colour for the snap distance and print speed analyses.

5.2.5. Electrical characterisation

For the study on the rig, the effects of snap off distance and print speed on electrical performance were assessed with two-point probe measurements conducted with a Keithley 2400 digital Sourcemeter on the 6 mm long 200 μm lines. Three measurements were conducted on lines from three repeats for each of the parameter settings assessed, producing 9 measurements for each setting from which an average and standard deviation was calculated.

Two- and four-point probe measurements were conducted to find the line resistance, sheet resistance and resistivity values of the printed lines and squares produced on the DEK 248 screen-printer. The sheet resistance measurements were conducted on the printed 45x45 mm squares using a 4-point probe method. A SDKR-13 probe (NAGY Messsysteme GmbH) with a tip distance of 1.3 mm was used with the same Sourcemeter, with subsequent conversion to sheet resistance using the appropriate correction factor from the data table proposed by Smits (124). Sheet resistances are displayed as measured (with the correction factor) and, to account for the variation in film thickness after post processing, resistivities were also calculated as the product of sheet resistance and ink film thickness. A total of 12 sheet resistance values were taken across the centre of each printed square to account for any deviation in print quality across the area. A total of 36 measurements were conducted for each parameter setting, from which the average values and standard deviations were calculated. This was obtained over three print samples. Line resistance was measured using the same Sourcemeter in two-point mode for the 700

μm nominal width lines over three prints for each of the parameter settings to calculate the average value over the print duration and standard deviation.

5.3. Results

5.3.1. Rheological Analyses

5.3.1.1. Shear Rheology

Figure 5.3 shows the viscosity profile during increasing then decreasing shear rates (a) and viscoelastic profiles (b). The ink was highly shear thinning, with a reduction in viscosity as the shear stress was increased, particularly from 1 s^{-1} to 50 s^{-1} . This is desirable as it will allow it to flow more readily when printed, enabling more homogeneous prints. It also showed relatively little hysteresis between 10 s^{-1} and 100 s^{-1} . Where the viscosity values produced when reducing the shear rate back down from 100 s^{-1} were very similar to those produced when increasing the shear rate. Both the elastic component (storage modulus, G') and viscous component (loss modulus, G'') of the shear modulus increased with frequency. G' was consistently larger than G'' for the frequencies tested, although the gap between the two decreased at higher frequencies. This produced a relatively low phase angle (δ), of around 27° at a frequency of 1 Hz , the ink behaving in an elastic manner for the frequencies tested. At higher frequencies, it is possible that the G'' would become greater than the G' . However, this would be above the frequency range relevant to the screen-printing process being used.

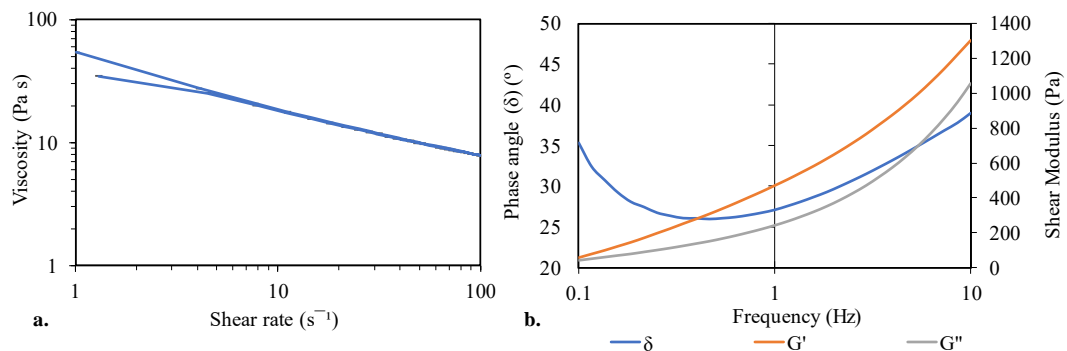


Figure 5.3 Viscosity profile (a) and viscoelastic profile assessing changes in phase angle (δ), storage modulus (G') and loss modulus (G'') with frequency (b) for the carbon ink assessed.

5.3.1.2 Extensional Rheology

The separation mechanism and the relative partition of ink between top and bottom plates during the CaBER tests are shown as a function of separation distance and separation speed, displaying the frames taken at the point of separation (Figure 5.4). The percentage partition of ink between top and bottom plates is described in terms of the cross-sectional area at the point of separation of the ink on the lower plate compared with the total area and length to separation from the bottom plate (Figure 5.5). Depending on settings, between 45 and 60% of the ink was distributed to the bottom plate. As speed was increased the preference of ink to move towards the upper plate (rather than lower plate) was increased, for all separation distances tested. However, the extent of change varied with the separation distances. This is due to the viscoelasticity of the ink, with increases in separation speed causing the ink to behave in a more elastic manner, resulting in more ink being pulled towards the top plate. This can be seen when comparing these results with Figure 3.5, which illustrates the most commonly observed modes of capillary thinning and break up outlined by McKinley (74). Similar observations were also made by Morgan *et al.* (77).

When comparing these trends at the moment of separation (Figure 5.4), the position at which separation occurs reduced with increasing separation speed. The separation position was near the centre of the filamentation region at separation speeds of 20 mm s^{-1} , moving to below the centre point at 100 mm s^{-1} . The capillary thinning break-up mode of the ink was similar to a power law fluid (74), where the ink filaments formed hourglass like profiles prior to separation. However, higher speeds and gaps exhibited profiles more similar to a weakly elastic fluid, exhibiting longer necking regions and more homogeneous extensional flow occurring over the filament (74). As the increased extension rates and longer distances induced higher level of stress within the filament and enabled the ink to flow with a lower viscosity and separate quicker. This is due to the strong shear thinning and viscoelastic nature of the ink, where increases in the strain and strain rate caused the ink to exhibit more elastic behaviours.

The 7 mm gap had the largest reduction of 11% of the total area of ink being separated, and the 5 mm gap had the smallest reduction of 4% of the total area of ink

being separated. However, there was an overall increase in the percentage of ink remaining on the bottom plate when increasing the separation distance from 3 mm to 7 mm. This is due to the larger separation distance, which enables a more even separation profile as the ink separates closer to the centre of the filament. There was a reduction when increasing from 3 mm to 5 mm for all speeds tested. For all speeds tested (Figure 5.5), the length from the bottom plate to the separation point was found to reduce linearly with speed. This is due to the elastic nature of the ink causing it to pull up more towards the top plate with the increasing strain rate, as seen in literature (74,127).

The change in the minimum diameter over time for each of the tests (expressed as the ratio of the final diameter divided by the initial diameter (R_{min}/R_o)) are shown in Figure 5.6. The smallest diameter in each case represents the point at which the filament of ink splits. Ink separated at the slowest speed and over the shortest distance took the longest time to split, due to the low shear rates enabling the ink viscosity to remain high and allowing it to gradually filament, as is characteristic of a power law fluid (74). Whereas the ink separated over the greatest distance at the highest rate took the least time to split. All inks separated at the highest rate of 100 mm s^{-1} took less time to split than those conducted at slower separation rates, for all separation distances. The time taken to separate reduced with increases in separation distance as the increase in shear thinning and elastic response of the ink enabled a more rapid separation. As all tests had the same starting plate separation distance with the same volume of ink between the plates, the expansion would be greater with distance. Therefore, impacting on the shear forces applied to the ink. However, there were some overlaps in the results conducted at 20 mm s^{-1} and 60 mm s^{-1} . Where the inks separated at 20 mm s^{-1} at separation distances of 7 mm and 5 mm took less time to split than those separated at 60 mm s^{-1} over distances of 5 mm and 3 mm. The changes in strain (distance) and strain rate (separation speed) had clear effects on the ink separation mechanism and duration. Increases in separation speed led to a greater preference for ink to separate towards the top rather than bottom plate. The highest separation gap produced a similar effect.

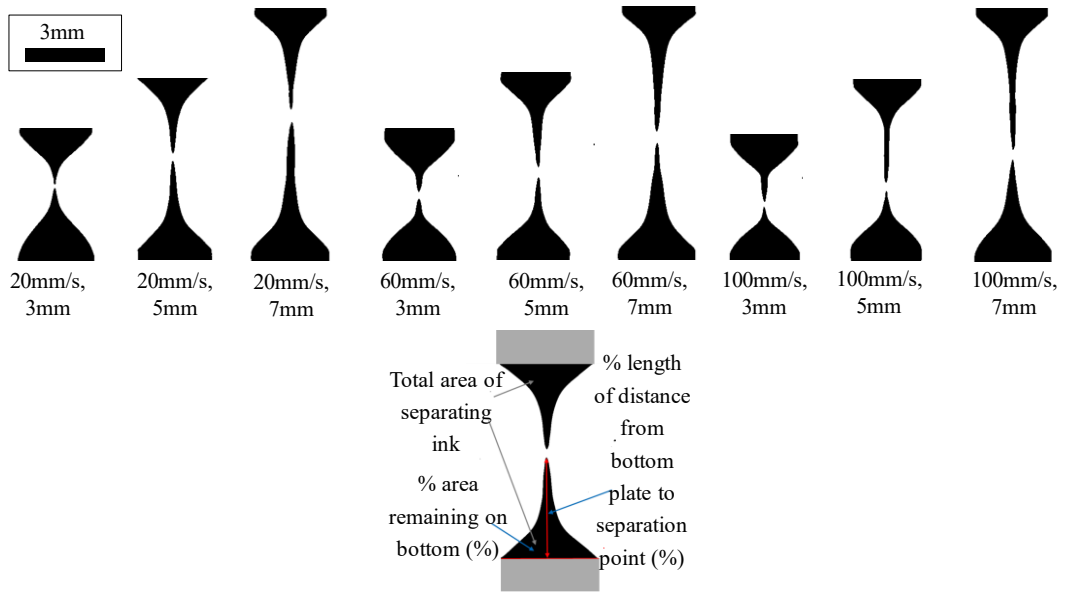


Figure 5.4 High speed images of separation at the point of film splitting with separation speed and separation distance.

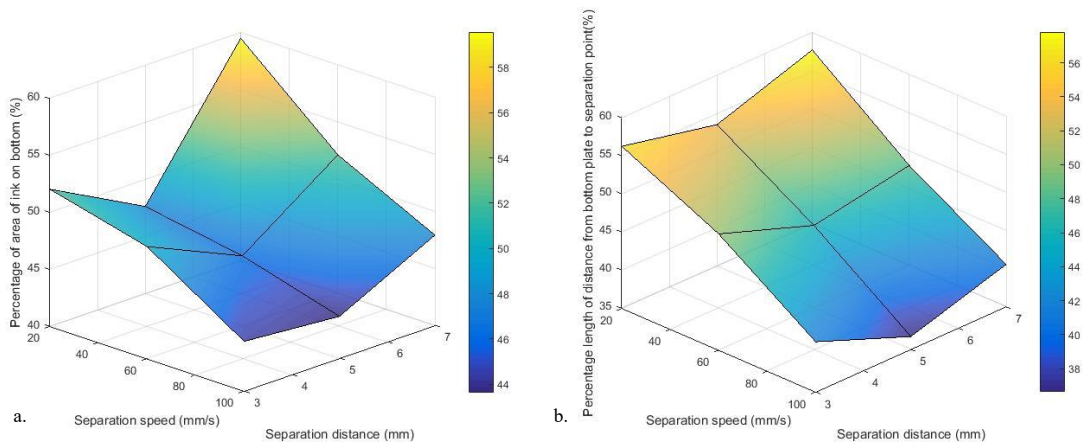


Figure 5.5 Surface response of the percentage of the cross-sectional area of ink remaining on the bottom plate (a) and percentage length to separation point from the bottom plate (b) with changes in separation distance and separation speed.

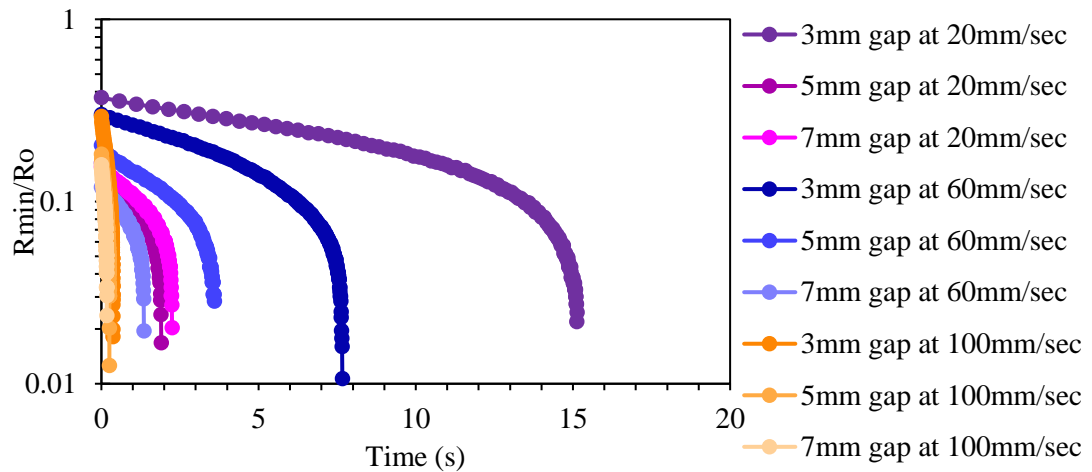


Figure 5.6 Evolution of the minimum radius

5.3.2. Print Topography of different line widths

In order to quantify the lengths of features in the high-speed images, as well as identify how the deposition mechanism relates with the print topography, the topography and microscopy profiles of the 50 μm line were used. The 50 μm width line produced non-continuous ink deposits with notable features, as shown in Figure 5.7, and Figure 5.8 (a) the lengths of these deposits were quantified, to provide a scale for the high speed images, which were all conducted at the same magnification and working distance. The lengths of the deposits and the gaps between them are listed in Table 5.2.

The 100 μm , 200 μm and 400 μm lines produced were all continuous, as shown in Figure 5.8. Both the print consistency and film height increased with line width, as shown in Figure 5.9. Leading to an overall increase in the volume of ink being deposited. Although, as the ink used is optimised for large area prints rather than fine lines, there was a lot of ink slump and spreading around the line edges. This means that greater line widths were produced than the size of the lines on the mesh.

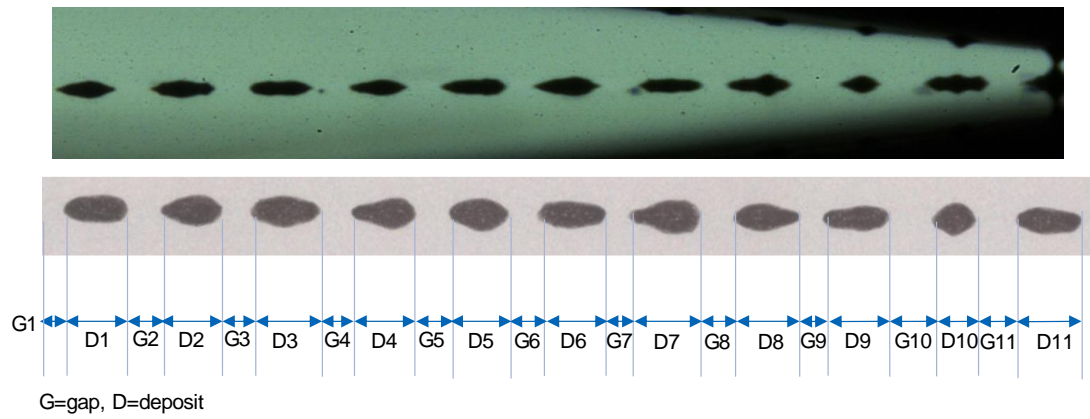


Figure 5.7 Comparison of high-speed image of ink deposition with labelled microscopy image of print produced for 50 μm line.

Table 5.2 Lengths of discrete ink deposits and gaps between deposits for printed 50 μm line.

Discrete ink Deposit	1	2	3	4	5	6	7	8	9	10	11
Prior gap length (G) (μm)	118	147	127	133	130	129	102	140	104	190	180
length (D) (μm)	302	279	328	292	271	308	330	316	300	206	302

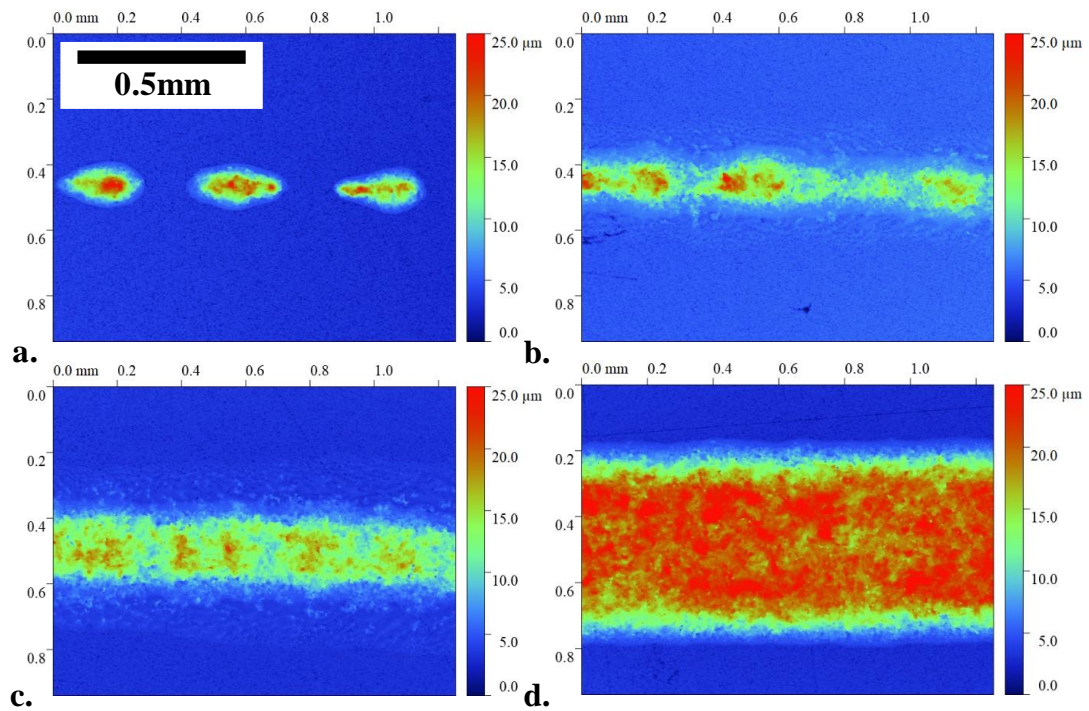


Figure 5.8 White light interferometry images of the prints conducted through the (a) the 50µm line, (b) 100µm line, (c) 200µm line and (d) the 400µm line. Conducted at 5 times magnification.

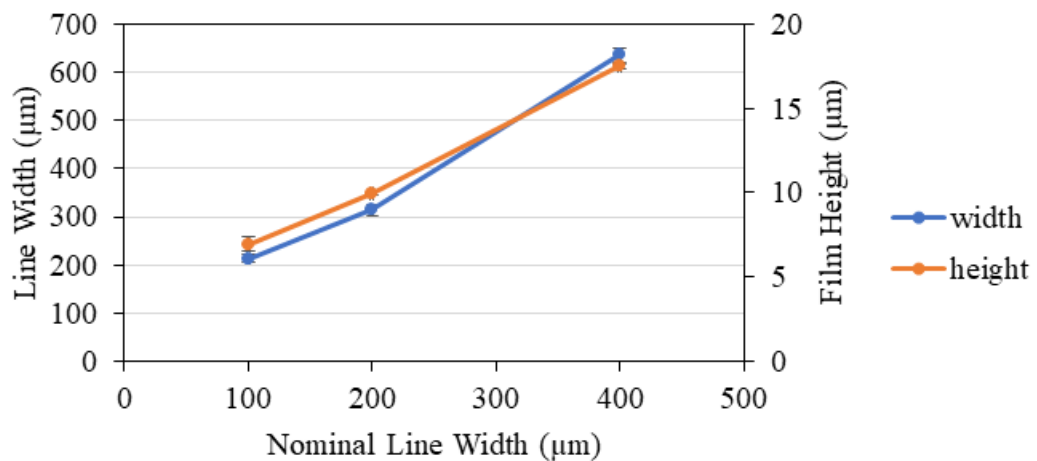


Figure 5.9 Change in average printed film thickness and line width with increases in line width on mesh.

5.3.3. Classification of flow regions during screen-printing

In Figure 5.10 the print direction is from left to right and a mirror image can be seen beneath the point of contact from the reflection on the surface of the substrate. After the squeegee has brought the mesh into contact with the substrate, the ink can then

pass through the gaps in the mesh. During the adhesion stage, the ink forms a continuous bridge between the mesh and substrate directly behind the squeegee contact point. This continues in the extension stage where the ink remains in continuous contact but is stretched over an increasing distance while the mesh moves away from the substrate. The flow stage is where the ink starts to separate from the main body of ink behind the squeegee and form filaments. These then start to display a localised rate of thinning, known as “necking” (29), which then leads to complete separation. These four stages together make up the ink separation stages. The paste flow region ahead of the squeegee was also measured for completeness. In practise, the transitions between stages 1 and 2 and stages 3 and 4 are difficult to measure, so characterisation is in terms of adhesion to extension stages (stages 1 and 2) and flow to separation stages (stages 3 and 4). The overall length of these combined stages, where the ink is in simultaneous contact with the mesh and substrate, are labelled as the full contact region.

The flow observed in Figure 5.10, which show the deposition of a 200 μm line, were best supported by Messerschmitt’s theory (70) with four stages of ink deposition; adhesion, extension, flow and separation. Where the separation forces appear to induce a flow that causes a shearing action at the mesh strands combined with the tensile stresses induced by the increasing distance between the mesh and substrate, leading to the ink splitting (70). There was no clear correlation with Riemer’s theory, where the mesh forces the ink onto the substrate as columns, which remain on the substrate due to adhesion and slump once the mesh is removed (128). However, Messerschmitt’s theory did not outline the length or duration of the four stages, where these analyses enable the lengths of these regions to be quantified. This enables effect of variables on the lengths of these flow regions to be measured. The overall length of the full contact region, including the paste flow region ahead of the squeegee, is outlined in Figure 5.10.

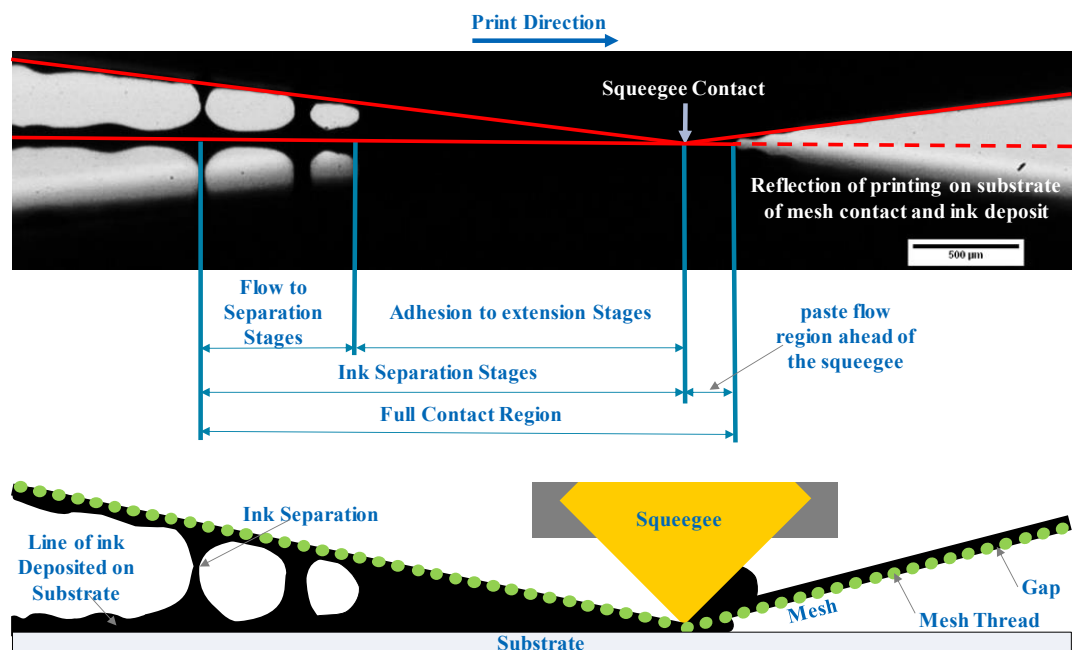


Figure 5.10 Labelled high-speed camera image of the squeegee forcing the mesh into contact with the substrate. Where the ink is deposited from the mesh to the substrate as the squeegee flows across the screen (above). With a cross sectional schematic diagram of the process (below).

5.3.4. Effect of line width on deposition mechanism

The length of the contact regions tended to increase with line width, as shown in Figure 5.11. As the 50 μm line produced a non-continuous line, this line width was assessed only in relation to the points of separation, as shown in Figure 5.12 (a). The other printed line widths were also assessed over regular time intervals with measurements taken every 3 frames (0.024s) to provide a representative study of the print duration, (Figure 5.12 (b)).

The 50 μm line produced the shortest contact region out of the line widths, as shown in Figure 5.11 and Figure 5.12. It also had a flow to separation region which was greater than the adhesion to extension region. The 100 μm line had a larger overall contact region (when measured in relation to separation points) (Figure 5.12 (a)). But had a reduction in the average length of the flow to separation stages with an increase in the average length of the adhesion to extension regions. Along with an increase in the paste flow region ahead of the squeegee. The same trends are seen with the measurements conducted over regular time intervals (Figure 5.12 (b)). This change in the ratio of the lengths of the two ink separation stages are most likely as

the 100 μm line produced a continuous print. When increasing the line width to 200 μm , there is an increase in all the contact regions, when measured both in relation to the filament separation positions and over regular time intervals. This is also observed when increasing the line width further to 400 μm .

There is a near linear increase in the average full contact regions, with an overall increase in the adhesion to extension stages and the flow to separation stages. Where the adhesion to extension stages remained longer than the flow to separation stages for the 100 μm , 200 μm and 400 μm lines. This could be due to increases in the line width leading to increases in the adhesive forces as increases in the contact area would require greater forces to release the larger body of ink. This causes the ink to remain bridging the mesh and substrate until a separation distance capable of producing sufficient force is reached.

The distances between the separation positions (points at which the ink undergoes capillary thinning break up between the mesh and substrate (Figure 5.10)) were also measured over the print cycle for the different line widths. However, these could not be quantified for the 400 μm line as there were multiple openings in parallel across the line width, making it unclear as to which point was separating using 2-dimensional assessments. The average distances between separation points for the line widths assessed are shown in Figure 5.13. The 50 μm line had an average distance of 477 μm between each of the separation points, located on each of the discrete deposits. For the continuous lines, the average distance between separation points was 294 μm for the 100 μm line and 323 μm for the 200 μm line. This variation in the frequency of the occurrence of separation positions, as well as variations in separation region lengths, could be due to fluctuations in ink flow over the print duration. As the inks are pseudoplastic and viscoelastic, changes in the velocity of the flowing ink behind the squeegee would change the viscosity of the ink in that region. As was found in numerical models by Fox *et al.* (42) When combined with the influence of a range of particles sizes within the ink, this would cause variations in the ink viscosity which would influence the separation mechanisms (74). As well as this, the change in snap speed with the reducing angle between the mesh and substrate as the squeegee progresses across the screen would also influence the ink viscosity and extensional forces, which in turn would also affect the separation mechanisms (74,127).

By comparing these lengths with microscope images of the mesh used, separation was found to occur around every two to three threads for these 100 μm and 200 μm lines (Figure 5.13, Figure 5.14). This compliments Messerschmitt's theory (70) as it shows that the ink does not simply pass out of every gap in the mesh and cleanly separate as was believed by Riemer (39). but instead passes through as a body of ink which gradually extends and separated into a series of filaments due to the shearing action of the separating mesh as illustrated in Figure 5.14.

There is also a correlation between the variations in print height and the location of filaments separating during the ink separation between the mesh and substrate, as shown in Figure 5.15. Where the position where the filament separates form a raised area in the print, which can lead to increases in print roughness and reductions in print homogeneity which can have adverse effects on the electrical performance of the print. This is also linked to the recovery time of the ink, which in this case is relatively fast, as shown by the little hysteresis in the viscosity tests. Therefore, this could be worse with inks which recover quicker, but less significant for inks which take longer to recover to their initial viscosity.

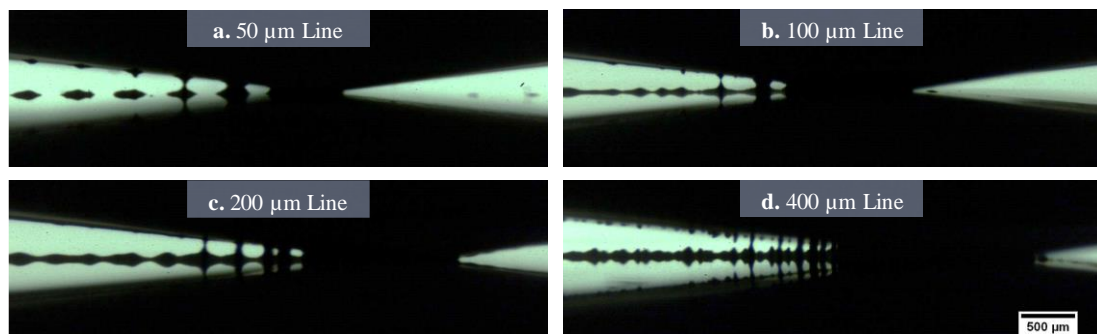
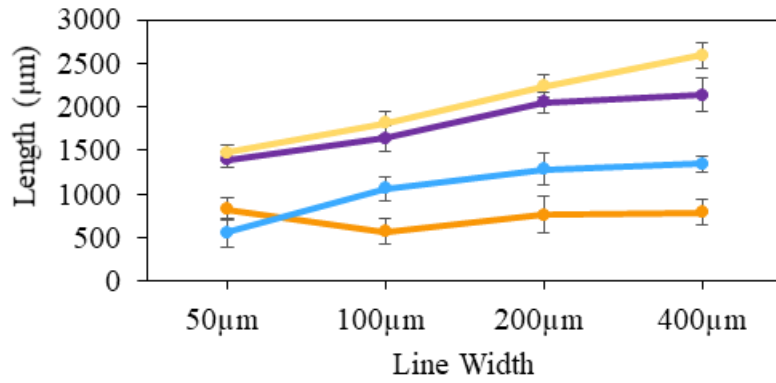
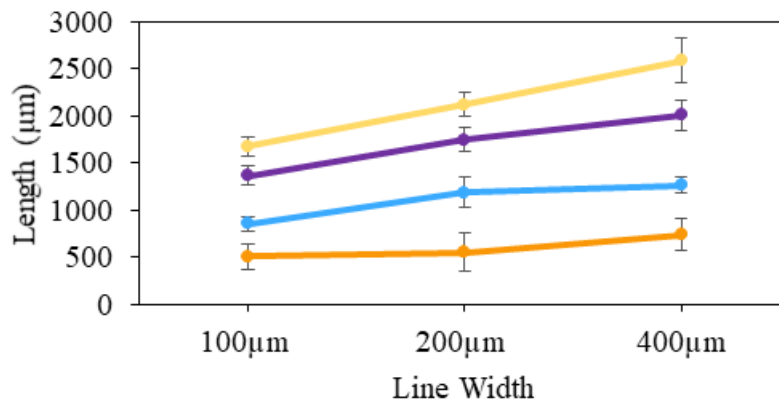


Figure 5.11 High-speed camera images of the deposition of (a) the 50 μm line, (b) 100 μm line, (c) 200 μm line and (d) the 400 μm line conducted at 5x magnification.



a.



—●— Flow to Separation Stages —●— Adhesion to Extension Stages
—●— Ink Separation Stages —●— Full Contact Region

b.

Figure 5.12 Change in contact regions with line width in relation to filament separation positions (a) and when conducted over regular time intervals (measurements conducted every 3 frames) (b).

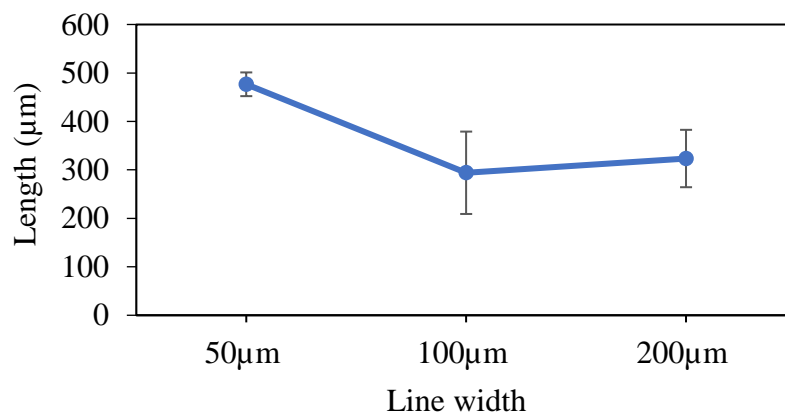


Figure 5.13 Average distance between separation points for different line widths.

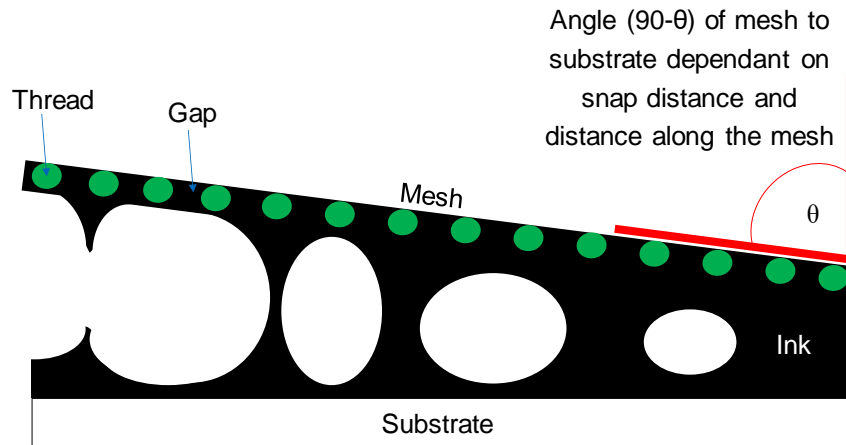


Figure 5.14 Schematic Diagram of the separation mechanisms occurring based on the results for the GEM carbon-based ink when printing a 100 μm or 200 μm line.

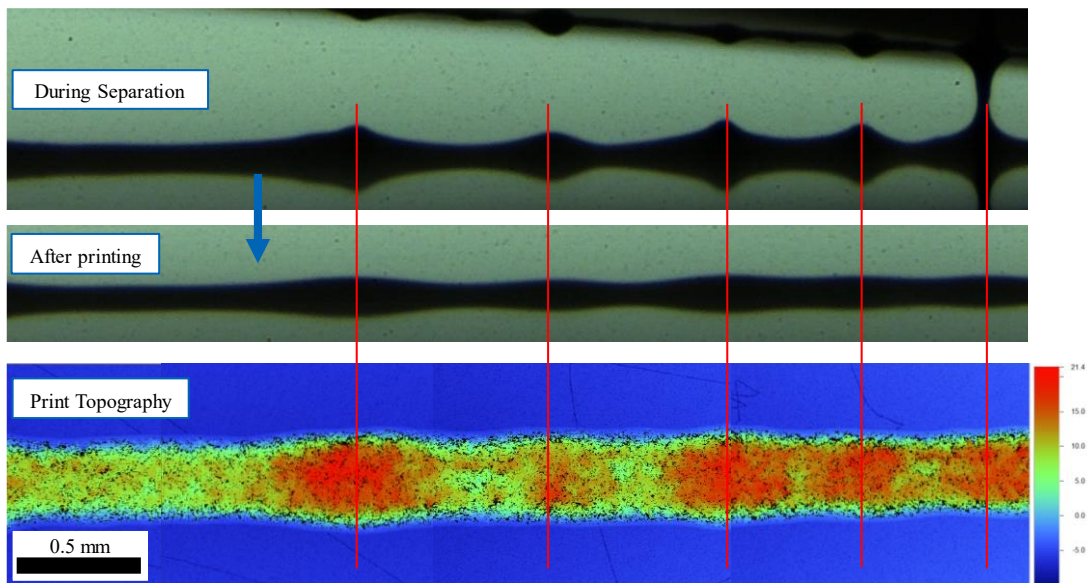


Figure 5.15 Comparison of filament separation positions and the topography profile of the printed 200 μm line

5.3.5. Discussion of effects of line widths

The imaging of the print process demonstrates behaviour is in agreement with the qualitative theory of four stages of ink deposition described by Messerschmitt. Where the separation forces induce a flow causing extensional flows which leads to the ink splitting (70) rather than the passage of the ink through the mesh as a series of columns, as suggested by Riemer. This study has also quantified the relative length and duration of each of the four stages.

The length of the region in simultaneous contact with both the substrate and mesh increased with line width, where the adhesion to extension stages were longer (for lines produced as a continuous print) than the flow to separation stages. Both lengths (adhesion to extension stages and flow to separation stages) were found to increase with line width. The increase in line width also led to increases in the film thickness of the printed lines, where the increase in the full contact length (of the ink in simultaneous contact with the mesh and substrate) corresponded with increases in the quantity of ink deposited. The 200 μm wide line was chosen for further studies as it produced clearer and more consistent lines than the 50 μm and 100 μm lines. As well as having only one gap between threads across the width of the line, unlike the 400 μm wide line, so there were only single filamentations forming across the widths of the lines assessed to avoid confusion in the 2D image analyses.

For fine features, the ink is able to reach sufficient stress states to enable separation, as there is a smaller cross-sectional area of ink to separate from the mesh. However, with the length to separation increasing with the feature size, this would suggest that for large solid areas, it could take a significant distance until sufficient stress states are reached for separation. This corresponds with the cling zone observed by Riemer (39) in experimental studies where the mesh appeared to remain adhered to the substrate for a prolonged period after the squeegee had passed over the area. This may have been a long extension period being observed, as the ink remains in continuous contact with the mesh and substrate, as illustrated by Riemer (39). As this typically occurs for low snap off distances, this also suggests that snap off may influence the length of the adhesion stage, which will be assessed in the next section.

5.3.6. Effect of snap distance and squeegee speed on the length of ink separation stages

The deposition mechanisms observed for the different snap distances and squeegee speeds tested could be characterised using the lengths of the separations stages, as outlined in Section 5.3.3 and illustrated in Figure 5.10.

The snap distance had a greater effect on the lengths of the different flow regions than the squeegee speed, (Figure 5.16) The average print stage lengths are displayed

with the corresponding high-speed images. Reducing the snap distances led to increased length of the adhesion to extension stages. This stage increased from 1617 μm at a snap distance of 1.825 mm to 3328 μm when snap distance reduced to 1.125 mm. There was also an increase in the length of the flow to separation stages, where filaments formed and then separated, with reductions in snap distance. Although these were much shorter in length than the adhesion to extension stage lengths. The flow to separation stage lengths increased from an average of 201 μm to 698 μm when snap off distance was reduced from 1.825 mm to 1.125 mm respectively. As the distance between mesh and substrate was lowered from 1.825 mm to 1.125 mm, the angle between the mesh and substrate at contact point was reduced from 6° to 4° when the squeegee has travelled half way cross the screen, in the centre of the line being assessed. The vertical distance required for the ink to reach sufficient stress states for splitting and forming filaments was not reached until a greater distance behind the squeegee contact point. Leading to an overall increase in the length of the print where the ink is in simultaneous contact with both the mesh and substrate as shown in Figure 5.16.

As print speed was increased from 100 to 500 mm min^{-1} ($1.7 - 8.3 \text{ mm s}^{-1}$), there was an increase in the length of the adhesion to extension stages, from 1410 μm to 2304 μm , (Figure 5.16). There was also a reduction in the length of the flow to separation stages from 465 μm to 177 μm as speeds increased from 100 to 500 mm min^{-1} . However, there was an overall increase in the length of the full contact region with increases in speed, from an average of 2218 μm at 100 mm min^{-1} to 2783 μm at 500 mm min^{-1} . Although there was a slight reduction in the full contact region length to 2158 μm , when increasing speed from 100 mm min^{-1} to 300 mm min^{-1} (1.7 mm s^{-1} to 5.0 mm s^{-1}) as the reduction in the flow to separation stage was greater than the increase in the adhesion to extension stage.

The reduction in the flow to separation stage lengths with increases in print speed may be a result of the increases in shear forces applied to the ink from the increased rate of passage of the squeegee when at higher print speeds. This would allow the ink to shear thin and act in a more elastic manner, which enabled the filaments to develop and separate more rapidly. Whereas the gradual increase in the adhesion to extension stage lengths with increases in print speed may be a result of the increase

in separation speed leading to a greater elastic response in the ink. This is supported by the increase in phase angle with frequency shown in Figure 5.3 (b), which would enable the ink to bridge the mesh and substrate over a longer length prior to filamentation and separation.

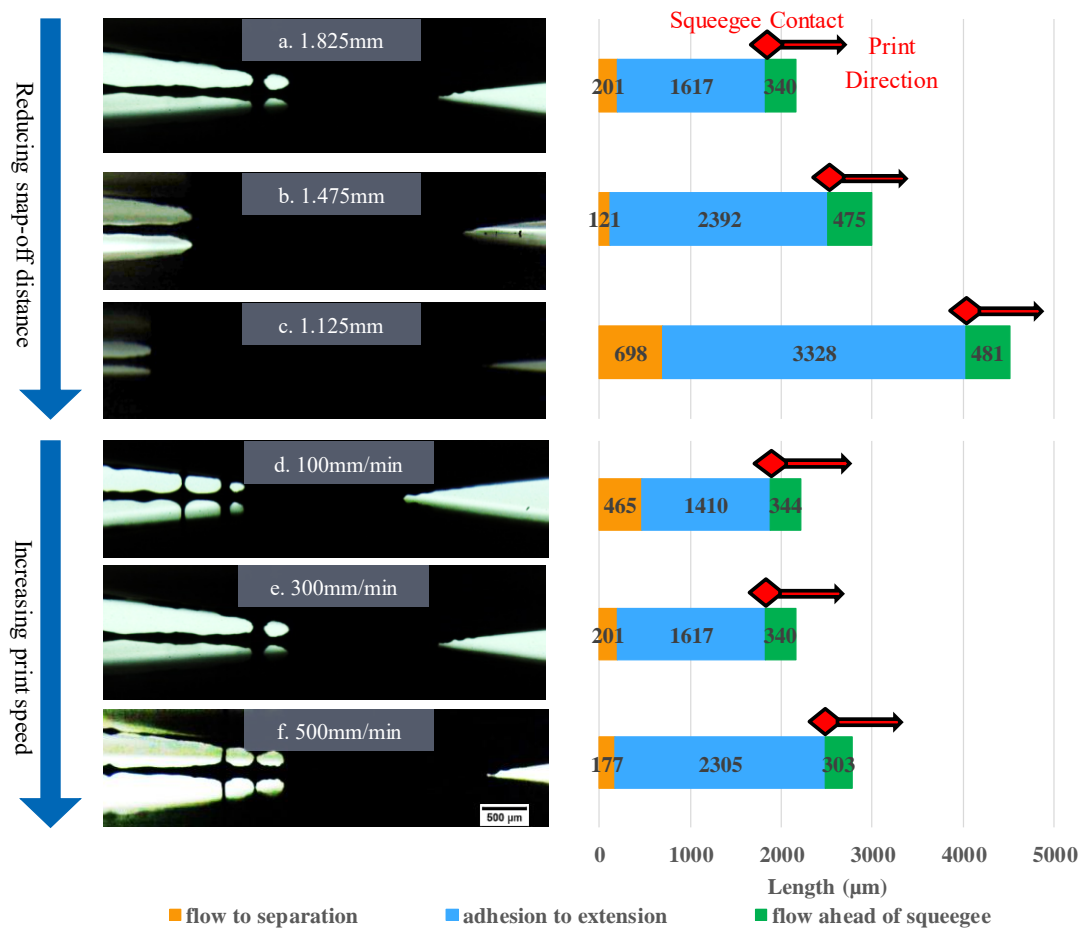


Figure 5.16 Quantification of print stage lengths for deposition using varying snap distances at fixed print speed of 300 mm min⁻¹ (a to c) and at a range of print speeds using a fixed gap of 1.825 mm (d to f).

5.3.7. Assessment of snap off distance and squeegee speed on filamentation behaviour

Consecutive images showing ink flow and separation while the squeegee is at three different positions during the print cycle were compared to show the differences in the ink filamentation and separation mechanism occurring at different snap distances

and speeds (Figure 5.17). There was little effect of snap distance on the number of filaments which formed and separated behind the continuous body of elongating ink. Although the length of ink separating from the main body of ink, transferring from the extension to flow stages, is significantly larger at the lower snap speed, (Figure 5.17). The ink separating to form a filament in the example shown for the 1.475 μm snap off distance separates from the extension stage far closer to the edge of the extension zone and forms a narrower filament. This mechanism can affect the print homogeneity, (Figure 5.15). Therefore, although there was a similar number of separation points across the 5mm length of the prints assessed, ranging from 2 to 5, this could lead to the print conducted at the lowest snap off distance being less homogeneous. The length between these separating points ranged between 965 μm and 3618 μm . Over the print duration of the 1.475 mm and 1.125 mm snap distances, there was the main body of ink in the extension flow region and one filamentation region. The average length of the flow to separation region was far smaller than the average distance between separation points.

For the prints conducted at the higher squeegee speeds, the filaments form a long necking region along the centre of the filament, as highlighted in Figure 5.17. This is capillary thinning and break up which occurs with elastic fluids, as shown in Figure 3.5 (74). This was also seen in the extensional testing at higher speeds. At slower speeds, both the filaments formed during printing and on the extensional rheology tests displayed a mode of capillary thinning and break up similar to the profile of a power law fluid (Figure 3.5). Increasing the print speed, and therefore, strain rate of the ink causes it to behave as an increasingly elastic fluid. The increase in print speed also corresponded with a reduction in the number and frequency of filaments and separation points visible, as the mesh and substrate separated. For example, as speed was increased from 100 to 300 then 500 mm min^{-1} , the number of filaments visible in the image fell from 10 to 5 to 4. This also has an effect on the print profile, as shown in the images where the squeegee is near the end of the print cycle (Figure 5.17). The print conducted at 100 mm min^{-1} displayed more variations in deposit height where the filaments had separated. The locations where the filaments had separated for the print conducted at 500 mm min^{-1} were less raised, producing a more homogeneous print profile. However, this may be due to the filaments formed at 500 mm min^{-1} separating closer to the bottom of the filament. This would result in

more ink remaining on the mesh, resulting in a lower print film thickness. This is comparable with the extensional rheology tests, which found that increases in filament separation speed led to more elastic filament profiles which separated closer to the bottom of the filament, leaving less ink on the bottom plate.

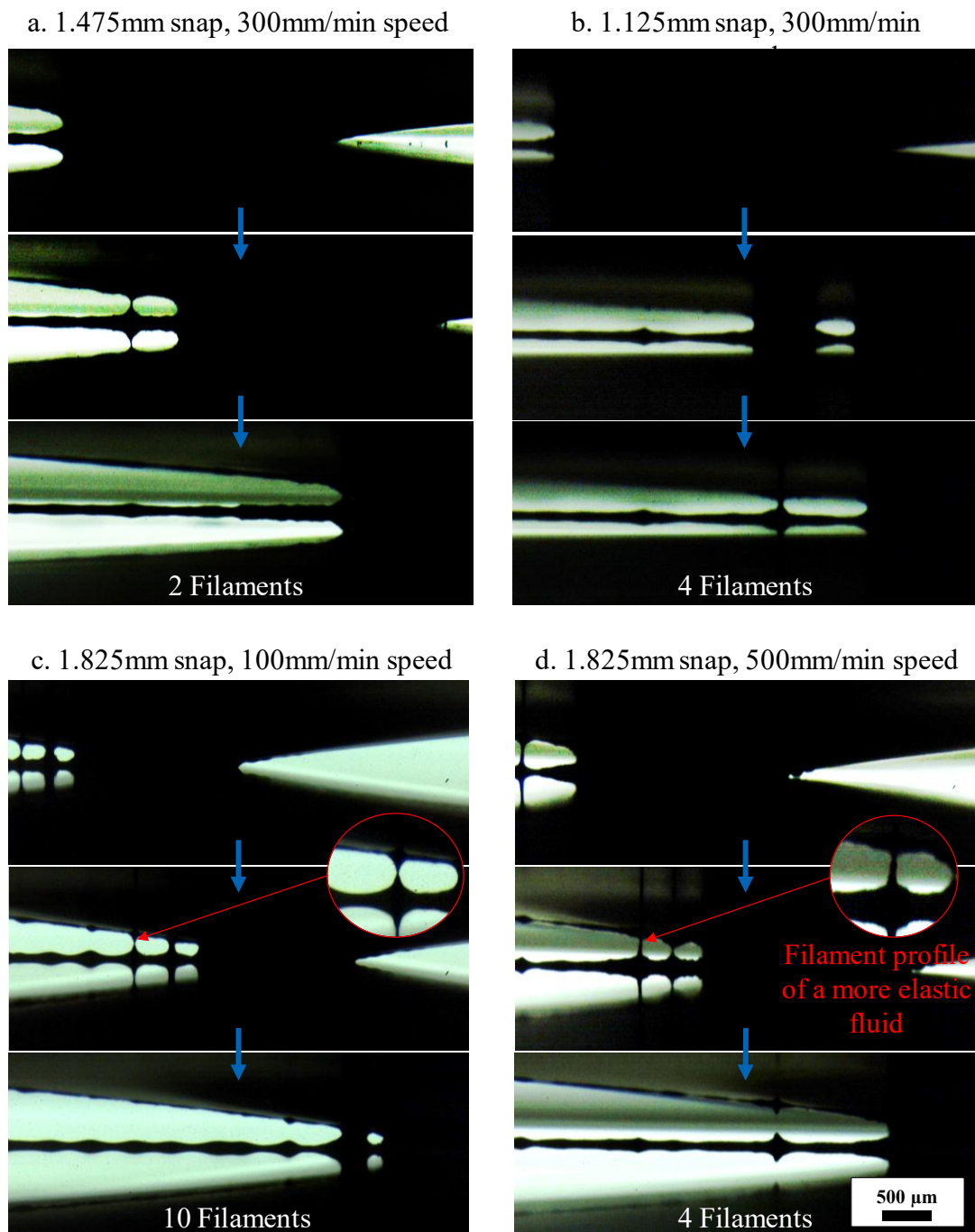


Figure 5.17 High-speed camera images at 5x magnification of different stages of the deposition of the 200 μm line conducted at 300 mm min^{-1} with snap distances of (a) 1.475 mm and (b) 1.125 mm. As well as conducted with a snap distance of 1.825 mm with squeegee speeds of (c) 100 mm min^{-1} and (d) 500 mm min^{-1} .

5.3.8. Effect of snap distance and squeegee speed on print topography

The optical images (Figure 5.18 (a-c)) showed little variation in the evenness and waviness of the edges of the printed lines with snap distance. When comparing these results with the length of the flow regions occurring during the print, the snap distance of 1.475 mm produced fewer filaments and a shorter flow to separation region than the 1.825 mm snap distance (Figure 5.16). It also produced narrower filaments than the 1.125 mm snap distance, where the larger filaments lead to more significant raised areas on the surface of the line conducted at the lowest snap distance (Figure 5.17). The average film thickness and width of the lines produced varied both with changes in snap distance and squeegee speed (Figure 5.19). The mid-range snap distance of 1.475 mm produced the greatest film thickness and line width at 13.6 μm and 316 μm respectively. The 1.475mm snap off distance produced the smallest filamentation region where the majority of the extension region separated evenly without forming filaments, resulting in less ink becoming pulled back up towards the mesh during filamentation and therefore a greater film thickness. The lowest film thickness and line width, of 12.4 μm and 307 μm respectively, were produced at the highest snap distance. However, the reduction in filaments forming appears to have had a less significant effect on the line width, which did not significantly change with snap off distance.

The lowest speed of 100 mm min^{-1} gave the highest ink film thickness and line width of 14.1 μm and 403 μm respectively out of the speeds assessed. It also produced the most consistent and least wavy line edge. The print produced at 300 mm min^{-1} gave the lowest film thickness and line width (12.4 μm and 307 μm respectively). The reduction in deposition with increased print speed and therefore separation speed, corresponds with the filament profiles produced during both the print trials and the CaBER test, where increases in separation speed led to the more elastic filament profile separating closer to the bottom of the filament. Therefore, resulting in more ink being transferred back up to the mesh and producing thinner ink deposits. A further increase in print speed from 300 mm min^{-1} to 500 mm min^{-1} gave a slight increase in deposition.

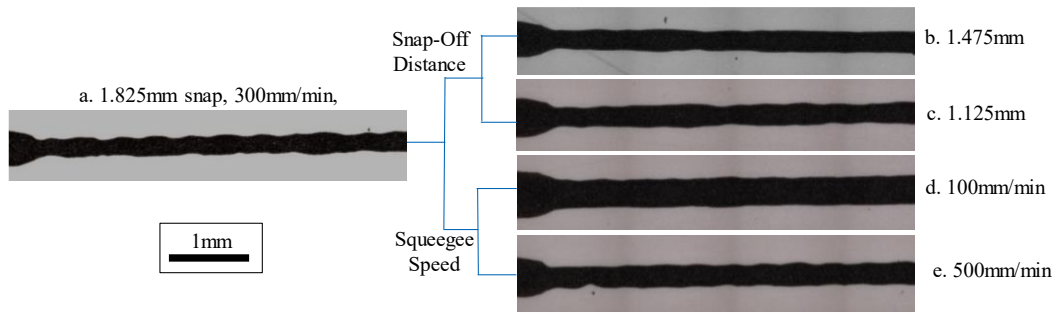


Figure 5.18 Changes in the optical microscopy images (10 x magnification) of the printed lines with standard settings (300 mm min⁻¹, 1.825 mm snap distance and at contact point) (a), with the snap distance reduced to 1.475 μm (b) and 1.125 μm (c). As well as with the print speed reduced to 100 mm min⁻¹ (d) and increased to 500 mm min⁻¹ (e).

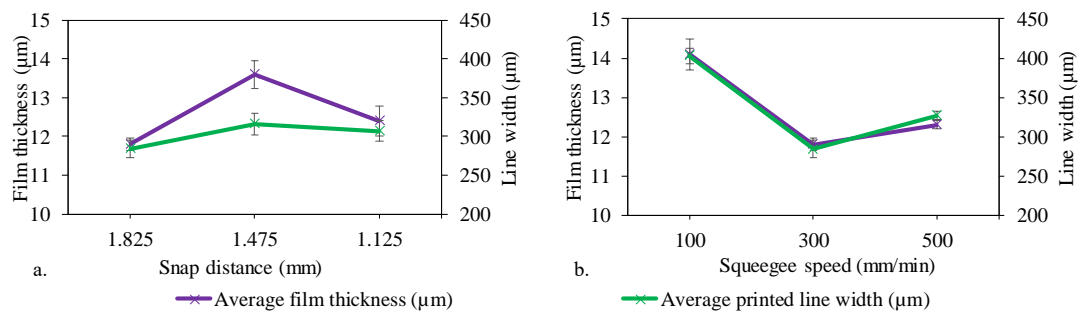


Figure 5.19 Variations in the average film thickness and average printed line width with changes in snap distance (a) and squeegee speed (b) (analysed using white light interferometry) (error bars represent standard deviation).

5.3.9. Effect of snap distance and squeegee speed on electrical performance

The changes in line resistance of the 200 μm printed lines are shown in Figure 5.20. The results are inversely related to the topography profiles of the prints (Figure 5.18). The greater ink deposits, with larger line widths and film thicknesses, had lower line resistance and therefore higher conductivity. The snap distance of 1.825 mm with squeegee speed of 100 mm min⁻¹ which produced the greatest ink deposit, produced the lowest line resistance of 0.239 kΩ.

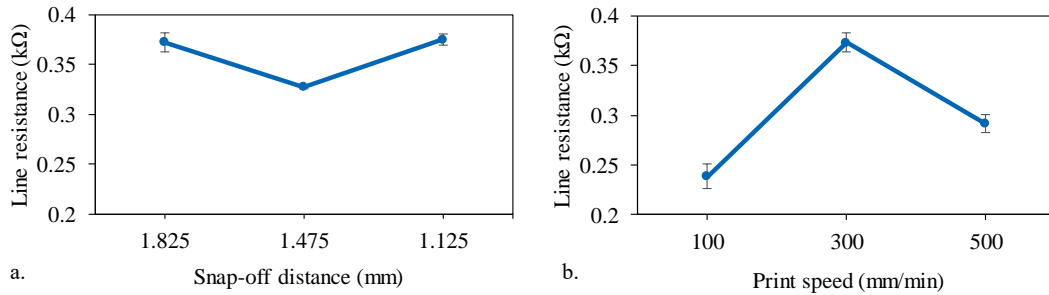


Figure 5.20 Changes in line resistance of the 200 μm lines with changes in snap distance (a) and speed (b) (error bars represent standard deviation).

5.3.10. Full scale Press Comparison for the effects of snap off distance and print speed

5.3.10.1. Print topography and microscopy

The changes in print topography for the 700 μm lines produced on the DEK 248 screen printer for different snap distances and speeds are shown in Figure 5.21, along with changes in average film thickness, line widths and cross sectional areas of ink deposited in Figure 5.22. Increases in snap distance led to increases in the average film thickness deposited, for all print speeds assessed (Figure 5.22 (a)). The highest print speed of 70 mm s^{-1} produced the highest film thickness for all snap distances and the medium print speed of 50 mm s^{-1} was found to produce the lowest. However, the difference between the film thicknesses at 30 mm s^{-1} and 50 mm s^{-1} was greater for the lower snap distances, where the 0.5mm snap distance had an average film thickness of 7.6 μm at 30 mm s^{-1} , which reduced to 6.7 μm at 50 mm s^{-1} , then increased to 7.8 μm at 70 mm s^{-1} . While the 1.5mm snap distance had an average film thickness of 8.2 μm at 30 mm s^{-1} , which reduced slightly to 8.1 μm at 50 mm s^{-1} , that then increased to 8.5 μm at 70 mm s^{-1} .

For the 0.5 mm and 1.0 mm snap distances, the changes in line widths with increases in print speed were the inverse of the changes in film thickness (Figure 5.22 (b)). For these snap distances, the greatest line width was produced at 50 mm s^{-1} and the lowest was produced at 70 mm s^{-1} . The 0.5mm snap distance produced the widest lines for all speeds assessed, with line widths of 830.7 μm at 30 mm s^{-1} , 925.2 μm at 50 mm s^{-1} and 837.0 μm at 70 mm s^{-1} . The 1.0mm snap distance produced similar line widths to the 1.5 mm snap distance at print speeds of 30 mm s^{-1} and 50 mm s^{-1} . However, for the 0.5mm snap off distance, the prints conducted at lower speeds were very irregular around the print edges. Although these prints were wider than those

conducted at 70 mm s^{-1} , due to ink spreading out from the edges of the print this would not improve the electrical performance of the prints. As the large gaps between the ink deposits at the edge of the print which would prevent electrical pathways (Figure 5.21). The 1.0 mm snap produced line widths of $811.5 \text{ }\mu\text{m}$ and $829.3 \text{ }\mu\text{m}$ at speeds of 30 mm s^{-1} and 50 mm s^{-1} respectively. While the 1.5 mm snap distance produced line widths of $811.2 \text{ }\mu\text{m}$ and $825.8 \text{ }\mu\text{m}$ at speeds of 30 mm s^{-1} and 50 mm s^{-1} respectively. However, at 70 mm s^{-1} the 1.0 mm snap distance saw a decrease in width to $799.4 \text{ }\mu\text{m}$, while the 1.5mm snap distance saw an increase in width to $836.8 \text{ }\mu\text{m}$.

Overall, there was an increase in the average cross-sectional area (CSA) of ink deposited for the printed lines with increases in both snap distance and print speed (Figure 5.22 (c)). The greatest average ink deposit of $7131 \text{ }\mu\text{m}^2$ was produced with the highest snap distance of 1.5 mm and the highest print speed of 70 mm s^{-1} . There are fewer pin holes and more raised regions in the print produced at 70 mm s^{-1} (Figure 5.21). There were large variations in the print roughness and less significant changes in the CSA between the lower print speeds and lower snap off distances.

The snap distance had relatively little effect on the average film thickness outside of standard deviation of the printed squares (Figure 5.23 (a)), due to the variation in print topography across the area of the square and over the duration of the print run. The film thickness produced with 1.5 mm snap distance at 70 mm s^{-1} was lower than the film thicknesses produced with 0.5 mm and 1.0 mm snap distances. For the 0.5 mm and 1.0 mm snap distances, the film thickness was lowest at 50 mm s^{-1} and highest at 70 mm s^{-1} . Thicknesses of $7.5 \text{ }\mu\text{m}$ and $7.4 \text{ }\mu\text{m}$ were produced for snap distances of 0.5 mm and 1.0 mm respectively at print speeds of 50 mm s^{-1} and thicknesses of $8.0 \text{ }\mu\text{m}$ were produced for both snap distances of 0.5 mm and 1.0 mm at speeds of 70 mm s^{-1} . Snap distances of 1.5mm saw a reduction from a film thickness of $7.9 \text{ }\mu\text{m}$ at 30 mm s^{-1} to $7.5 \text{ }\mu\text{m}$ at 50 mm s^{-1} and remained at $7.5 \text{ }\mu\text{m}$ at 70 mm s^{-1} .

The average surface roughness (S_a) of the printed squares was affected by both print speed and snap distance (Figure 5.23 (b)). The greatest S_a was produced by the 1.0 mm snap distance, while the lowest was produced by 0.5 mm snap distance for all speeds assessed. For the 0.5 mm snap distance there was a small variation in S_a with

print speed, with Sa ranging between 1.24 μm and 1.29 μm . For 1.0 mm and 1.5 mm snap distances, the lowest Sa was produced at 50 mm s^{-1} , of 1.39 μm and 1.30 μm respectively. For the 1.0 mm snap distance, there was little difference between the Sa produced at 30 mm s^{-1} and 70 mm s^{-1} , with average roughness's of 1.62 μm and 1.63 μm respectively. For the 1.5 mm snap distance, the average roughness produced at 30 mm s^{-1} of 1.49 μm was far larger than the average roughness of 1.35 μm produced at 70 mm s^{-1} .

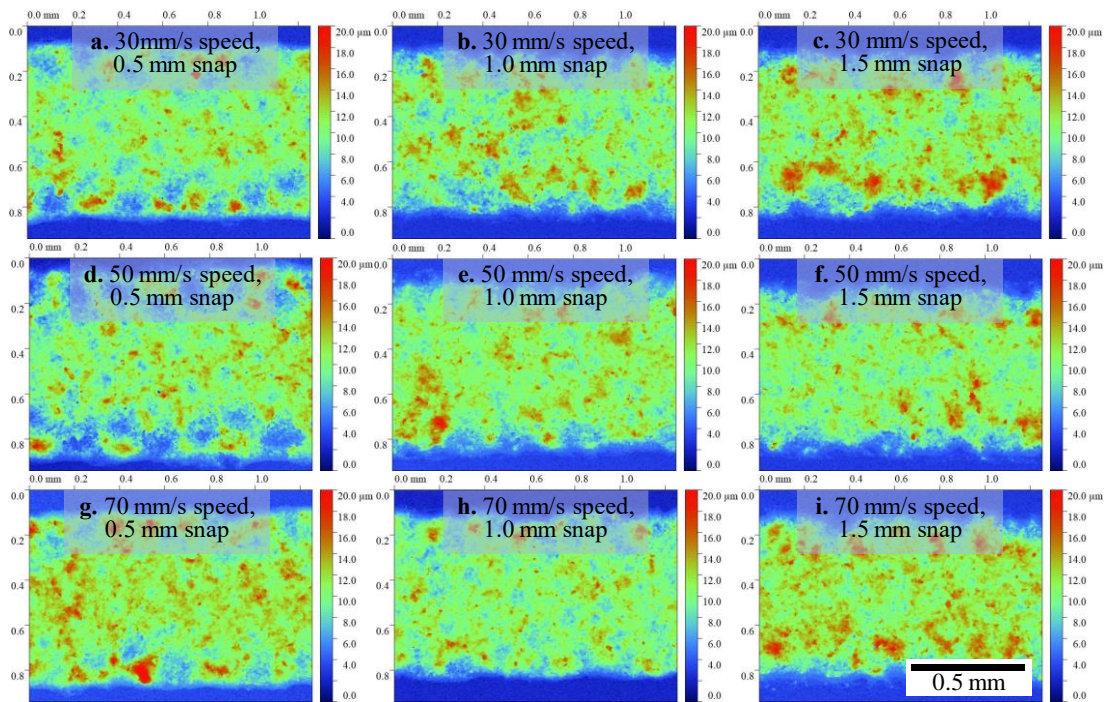


Figure 5.21 White light interferometry topography images of the 700 μm lines conducted on the DEK 248 Screen-printer, for prints conducted at 30mm/s for snap speeds of 0.5mm to 1.5mm (a to c), 50mm/s for snap speeds of 0.5mm to 1.5mm (d to f) and 70mm/s for snap speeds of 0.5mm to 1.5mm (g to i) at 5 times magnification.

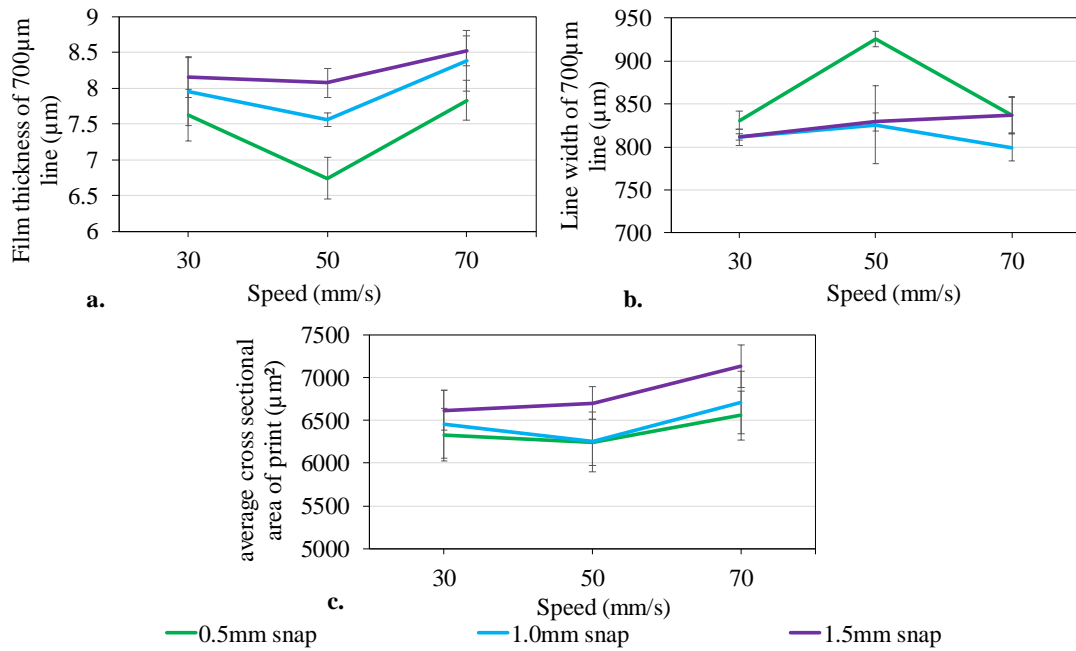


Figure 5.22 Average film thickness (a), line width (b) and cross-sectional area (CSA) of ink deposited (c) for the 700 µm lines produced for combinations of snap off distance and print speed. (error bars for standard deviation)

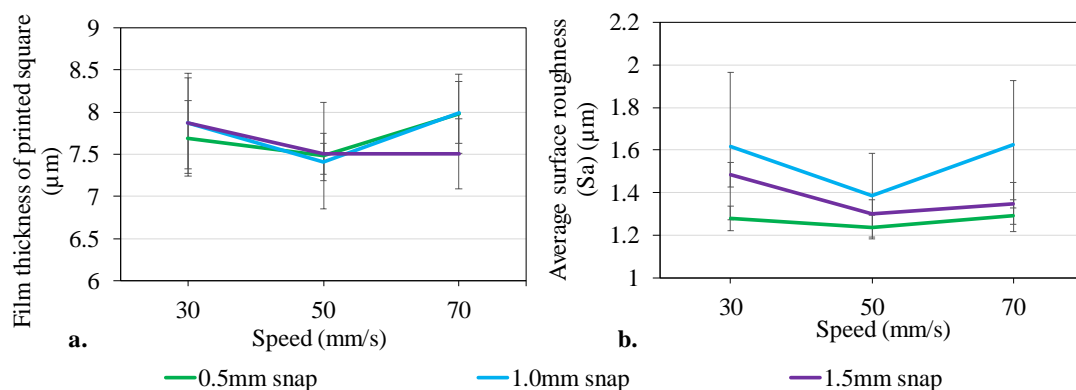


Figure 5.23 Average film thickness (a) and average surface roughness (Sa) (b) for the printed squares produced for combinations of snap off distance and print speed. (error bars for standard deviation)

5.3.10.2. Electrical characterisation

The changes in electrical performance for the prints produced on the DEK 248 screen printer for different snap off distances and speeds are shown in Figure 5.24, which displays the average line resistance for the 700µm lines (a), as well as the average sheet resistance (b) and sheet resistivity (c) of the printed squares. There was

a gradual reduction in line resistance with increases in print speed for the 0.5mm and 1.5mm snap distances. The 0.5 mm snap distance produced the lowest line resistance for all speeds assessed, reducing from 0.84 k Ω at 30 mm s⁻¹ to 0.80 k Ω at 70 mm s⁻¹. While the 1.5mm snap distance produced the highest line resistance out of snap distances assessed at 30 mm s⁻¹ and 50 mm s⁻¹. There was a gradual reduction in line resistance from 0.90 k Ω at 30 mm s⁻¹ to 0.87 k Ω at 70 mm s⁻¹. However, the 1.0 mm snap distance did not display a reduction in line resistance with print speed, where the highest line resistance of 0.93 k Ω was produced at 50 mm s⁻¹ and the lowest was produced at 70 mm s⁻¹, with a line resistance of 0.86 k Ω .

The 0.5mm snap distance also produced the lowest average sheet resistances for speeds of 30 mm s⁻¹ and 50 mm s⁻¹, but a snap distance of 1.5 mm produced the lowest average sheet resistance at 70 mm s⁻¹. For the 0.5 mm snap distance, the lowest sheet resistance of 16.04 Ω /square was produced at 30 mm s⁻¹ and the highest of 16.53 Ω /square was produced at 50 mm s⁻¹. While a sheet resistance of 16.22 Ω /square was produced at 70 mm s⁻¹. A different trend was produced for sheet resistivity when film thickness was accounted for, with the same resistivity of 0.0124 Ω .cm produced for both 30 mm s⁻¹ and 50 mm s⁻¹, which increased to 0.0130 Ω .cm for 70 mm s⁻¹. Although the resistivity values produced at 30 mm s⁻¹ and 50 mm s⁻¹ were lower than those produced by other snap distances at the same speed. The 1.5 mm snap distance produced a reduction in sheet resistance with print speed, from 16.95 Ω /square at 30 mm s⁻¹, to 16.84 Ω /square at 50 mm s⁻¹, then to 6.17 Ω /square at 70 mm s⁻¹. The sheet resistivities for the 1.5 mm snap distance also saw a reduction in resistivity with print speed, from 0.0134 Ω .cm at 30 mm s⁻¹, to 0.0126 Ω .cm at 50 mm s⁻¹, then to 0.0121 Ω .cm at 70 mm s⁻¹, which was the lowest sheet resistivity out of all of the settings assessed. The highest sheet resistance of the settings used was produced with 1.0 mm snap distance at a print speed of 50 mm s⁻¹, of 18.30 Ω /square. While sheet resistances produced at 30 mm s⁻¹ and 70 mm s⁻¹ for the 1.0 mm snap off were significantly lower, at 16.63 Ω /square and 16.65 Ω /square respectively. The highest sheet resistivity was also produced with 1.0 mm snap off distance at a print speed of 50 mm s⁻¹, at 0.0135 Ω .cm. While resistivities of 0.0131 and 0.0133 were produced with 1.0 mm snap distance at 30 mm s⁻¹ and 70 mm s⁻¹ respectively.

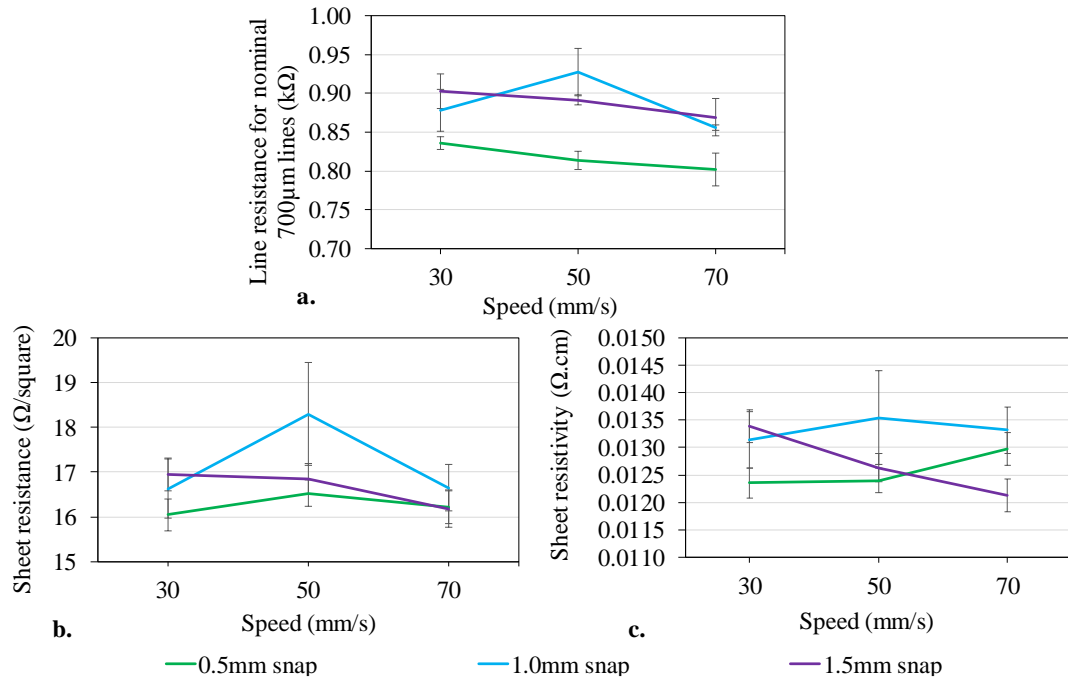


Figure 5.24 Average line resistance for the 700µm lines (a), as well as average sheet resistance (b) and sheet resistivity (c) of the printed squares conducted on the DEK 248 Screen printer for combinations of snap off distance and print speed. (error bars for standard deviation)

5.3.11. Discussion of the effects of snap off distance and print speed

In all the combinations of snap off and speed, the separation mechanisms corresponded with Messerschmitt’s four stages (70), but the lengths of the regions and the necking profiles of the filaments varied with settings.

The flow to separation stages were significantly shorter than the adhesion to extension stages for all settings of snap distance and squeegee speed, ranging from 122 µm to 698 µm in length. The adhesion to extension lengths ranged from 1410 µm to 3328 µm and were most affected by the snap distance. The reducing snap distance led to reductions in the angle between the mesh and substrate, which prolonged the adhesion to extension stages. Therefore, the body of ink behind the squeegee takes longer to reach the length required for sufficient stress states to induce ink splitting. This led to changes in flow stages of ink separation where filamentation typically occurred. At the medium snap off distance, this enabled clean separation directly after the extension stage to occur for the majority of the print, with only a few filaments forming and separating close to the end of the extension

stage. This resulted in a greater average film thickness and a more consistent print than those with either more filament points leading to raised areas in the print, as with the highest snap off distance. Or large extension regions leading to:

- I. The ink splitting further from the edge of the extension stage
- II. The formation of larger filaments
- III. Variations in the print profile.

This increase in the length of ink in simultaneous contact with the mesh and substrate with reductions in snap off distance also corresponds with the cling zone observed by Riemer (39) in experimental studies. Too short a snap off distance would cause the mesh to remain in prolonged contact with the ink adhering to the substrate, leading to separation problems.

Increases in print speed led to changes in the mode of capillary thinning and break up occurring during ink filamentation and subsequent separation. The ink exhibited flow profiles characteristic of a power law fluid at lower speeds and characteristic of weakly elastic fluids at higher speeds, when compared with the filament profiles described by McKinley (74) as illustrated in Figure 3.5. This resulted in an overall reduction in the average quantity of ink deposited with increases in print speed, with corresponding increases in line resistance. Higher separation speeds were also found to cause less ink to remain on the bottom plate in the CaBER tests, with changes in the capillary thinning and break up mode. The ink was found to behave more elastically with increases in strain rate. Assessing changes in the vertical strain rate with extensional rheology tests can indicate how the flow to separation regions of the screen-printing process can be influenced by separation speed. However, imaging of the full deposition process is also required as printing consists of simultaneous shearing and extensional forces, as well as time dependent phenomena.

High print speeds can reduce the viscosity of the ink and display the inherent elasticity of the ink, as demonstrated in the extensional rheology tests. However, the time required for the ink to recover was greater than the short time frames involved in the print cycle. This might negate some of the speed and separation effects seen in purely extensional tests, which do not pre-thin the ink in this way, and thus give fewer clear trends in filamentation behaviours. Overall, the findings in literature along with those presented in this research suggest that the extent to which the print

settings play a role may be influenced by the viscoelasticity and pseudoplasticity of the ink.

Previous studies found increasing snap distance led to greater ink deposits for a range of ink viscosities. (37) However, other studies found there to be an optimal snap distance for a given ink and substrate. (38) whilst others found that snap off distance had no significant effects on the print quality of fine lines. (23) In the case of squeegee speed, increases in print speed led to improvements in print quality (34,37,42,43). However, others found this was only the case up to an optimal value for a given ink and substrate (38). Some reported increases in print speed led to reductions in print quality (23,41). Overall, this suggests the effect of snap distance and squeegee speed depends on their interaction with other parameters, such as ink rheology. There may also be non-linear trends with changes in print topography and performance with snap distance and speed. As the press settings for the Rig and the DEK 248 printers were on different scales, this would explain the variations in the trends observed. As the print speeds of the Rig were slower, this would have caused the ink to be less shear thinned and therefore shown the effects of different ink viscosities to those explored on the DEK 248. Similarly, due to the differences in the size of the screens used, the snap distance required to show excessive snap distance in the DEK 248 prints was not reached, showing the highest snap distance as being best for producing the thickest film. While the smaller screen used in the Rig was tested beyond its optimal snap distance, leading to reductions in print film thickness at the highest snap distance used.

For the prints conducted on the DEK 248, the 0.5mm snap off distance was found to produce the lowest line resistances for the 700 μm lines at all print speeds. As well as the lowest sheet resistances and sheet resistivities at print speeds of 30 mm s^{-1} and 50 mm s^{-1} , with the 1.5 mm snap off distance producing the lowest sheet resistance and resistivity value at 70 mm s^{-1} . Although the 0.5mm snap off distance did not deposit the greatest film thickness or cross-sectional area of ink, it did have the lowest surface roughness for all print speeds assessed which led to consistent electrical pathways across the print. For the lines printed with snap off distances of 0.5 mm and 1.5 mm, there was a reduction in line resistance with increases in print speed. This corresponded with the increase in CSA of ink deposited with increases in

speeds. However, this was not the case with the 1.0 mm snap off distance, which found the highest line and sheet resistances as well as sheet resistivities were produced at 50 mm s^{-1} in all instances. Although this does correspond with print topography, as the lowest CSA of ink and lowest film thickness of printed squares was produced with these settings, with a snap off distance of 1 mm with a print speed of 50 mm s^{-1} .

5.4. Discussion

The ink separation processes during screen printing for all line widths and parameter settings assessed corresponded with the qualitative theory of four stages of ink deposition described by Messerschmitt. Where the separation forces induce a flow causing a shearing action on the mesh strands combined with the tensile stresses induced by the increasing distance between the mesh and substrate which leads to the ink splitting. (70) Rather than the passage of the ink through the mesh as a series of columns, as suggested by Riemer (39). This study has quantified the relative length and duration of the four stages, consisting of adhesion, extension, flow and separation. However, the lengths of the regions and the necking profiles of the filaments varied with the line widths and parameter settings.

The full contact region (full length over which ink is in simultaneous contact with the mesh and substrate) was found to increase gradually with increases in line width from $50 \text{ }\mu\text{m}$ to $400 \text{ }\mu\text{m}$. For changes in line width, both the adhesion to extension stages and the flow to separation stages were found to increase gradually in length with line width for continuous lines ($100 \text{ }\mu\text{m}$ to $400 \text{ }\mu\text{m}$ wide lines). Where the adhesion to extension stages were consistently longer than the flow to separation stage lengths, with both lengths increasing linearly from $100 \text{ }\mu\text{m}$ to $400 \text{ }\mu\text{m}$.

Less length behind the squeegee is required for sufficient shear and extensional forces in the ink to enable filamentation or separation of the ink between the mesh and substrate for printing narrow and fine featured. Whereas thicker lines or large solid areas would not reach sufficient shear and extensional forces for ink separation until a greater distance behind the squeegee, increasing the length of the ink separation stages.

Of the lines produced, the 200 μm wide line produced more consistent lines than the 50 μm and 100 μm lines, but only had one gap between threads across the width of the line, unlike the 400 μm wide line. Therefore, this line width was chosen for the following studies, including the effect of snap off distance and print speed.

As with the changes seen with altering line widths, the adhesion to extension stage lengths were consistently longer than the flow to separation stage lengths, for all snap off distances and print speeds assessed. The full contact region was found to increase gradually with reductions in snap off distance. This is due to reductions in the snap off distance reducing the angle between the mesh and substrate, as measured in Chapter 5.3.6. This would mean that a greater horizontal distance behind the squeegee would be required to produce the same vertical distance between the mesh and substrate. This vertical distance is required to induce sufficient stress states to enable the ink to split off into filaments and can be related to the extensional rheology tests where lower separation distances took substantially longer to separate. These findings correspond with the “cling zone” observed in experimental studies conducted by Riemer (39). Where the mesh appeared to remain adhered to the substrate through the adhesive forces of the ink in simultaneous contact with both the mesh and substrate for a prolonged period after the squeegee had passed over the area. This has been found to lead to separation issues when using too low a snap off distance (39).

For increases in print speed, there was a reduction in the lengths of the flow to separation stages, with a gradual increase in the adhesion to extension stage lengths. This also led to notable changes in the mode of capillary thinning and break up occurring during ink filamentation and separation. The ink exhibited filament profiles characteristic of weakly elastic fluids when printing was conducted at higher speeds, while showing filament profiles more characteristic of power law fluids at lower speeds. Based on the filament profiles described by McKinley (74), as illustrated in Figure 3.5. This change in filament profile also corresponded with the CaBER test results, which also found that the filaments’ profiles went from being characteristic of a power law fluid to an elastic fluid with increases in separation speed. In both instances, the weakly elastic filament profiles tended to separate

closer to the bottom of the filament, resulting in less ink remaining on the bottom plate for the CaBER tests and lower ink deposits for the print trials.

With line width study, the increases in the lengths of the separation stages corresponded with increases in the film thickness and overall cross-sectional area of ink deposited. The medium snap distance produced the greatest ink deposit and lowest line resistance of the prints produced on the rig. Less filaments formed over the duration of the print run and clean separation occurred directly after the extension stage for the majority of the print, with only a few filaments forming and separating close to the end of the extension stage. This resulted in a greater average film thickness and a more consistent print than at the high snap off distance with either more filament points leading to raised areas in the print or large extension regions leading to the ink splitting into filaments further from the edge of the extension stage, resulting in very wide filaments forming which also led to variations in the print profile.

The prints produced on the DEK 248 showed a gradual increase in both the quantity of ink deposited and the roughness of the print, with the lowest snap off distance producing the lowest line and sheet resistances due to better print consistency. Although the overall trends are still comparable. This variation between the results produced on the rig and DEK 248 screen printers is due to the difference in screen size. This would create a very different angle between the mesh and substrate for similar snap off distances, which would cause a difference in the separation mechanism. Resulting in a higher snap off distance being required to go outside of the optimal range. There was also some disparity between the effects of print speed on print topography and performance between the two presses. This is due to the difference in the speed ranges used on the two presses, with the Rig design resulting in far lower print speeds than those used on the DEK 248. This would result in a different amount of shear thinning of the ink and therefore different ink viscosities at which the experiments were conducted. Therefore, further work could be conducted with a rig capable of going at higher speeds to assess a greater range. As well as to assess the effect of using different size meshes at the same snap off distance for a range of print speeds. To assess the effect of screen length on contact angle, along with its resultant interaction with print speed, on the separation mechanism.

5.5. Conclusions

For the first-time High-speed imaging was used with a custom-made screen-printing rig to directly view the deposition of the ink onto the substrate and the subsequent separation of the ink from the mesh during the screen-printing process. Providing visual evidence of the separation mechanisms which occur during screen printing. This enabled the deposition mechanism to be recorded and quantified, providing sufficient experimental evidence to identify key transfer mechanisms and provide contemporary validation for the existing mathematical models using functional ink.

The results support the qualitative theory of four stages of ink deposition described by Messerschmitt (70). Where the separation forces induce a flow, which leads to the ink splitting. The four stages consisted of adhesion, extension, flow and separation and were identified in the high-speed images. There was no clear correlation with Riemer's theory (39), where the mesh forces the ink onto the substrate as columns, which remain on the substrate due to adhesion and slump once the mesh is removed. However, the lengths of these four stages of ink deposition varied with the widths of lines being printed and the settings of the press parameters used.

For the line widths assessed, increases in line width were found to lead to increases in the lengths of the ink separation stages for the commercial carbon-based ink. The 200 μm wide line was found to be suitable for further investigations as it produced a clear and consistent line with, while having only one gap between threads across the width of the line. This enabled clear identification of the different separation stages, which would enable comparisons in the lengths of these stages with changes in press parameters.

Altering the squeegee print speed and snap distance led to variations in the lengths of the ink deposition stages. Reductions in the snap distance led to significant increases in the adhesion to extension stages, with the smaller snap distances causing reductions in the angle between the mesh and substrate. Therefore, for reduction in snap distance, sufficient stress states for separating the ink was not achieved until a greater distance behind the squeegee. Changes in print speed led to alterations in the necking profiles formed during the filamentation stage. Where the ink acted in a more elastic manner at higher speeds. This complimented the CaBER test profiles which observed similar changes in the filamentation profile and found less ink

remaining on the lower plate as separation speed was increased. However, the CaBER tests were insufficient to simulate the whole of the screen-printing separation mechanisms. As it cannot capture mesh effects, shear forces from the squeegee motion, the contact angle between the mesh and substrate, or their effects on the adhesion to extension stages. The changes in snap distance and print speed also led to changes in the print topography produced.

Chapter 6. The effect of ink composition on ink transfer mechanisms

6.1. Introduction

This chapter continued work on the visualisation of ink deposition mechanisms conducted in Chapter 5. It investigates the effect of changing the rheological properties of carbon-based inks on the deposition and separation mechanisms occurring during screen printing. As well as whether the mechanisms observed in Chapter 5 were still applicable when the ink rheology and carbon morphologies were altered.

The literature identified that a range of carbon morphologies and carbon concentrations have been used in screen printing inks, for tailoring the print quality and electrical performance of a variety of printed electronics applications. This produces a wide range of rheological profiles of screen-printing carbon-based inks, each requiring different press settings for optimal performance. However, due to limitations in modelling the complex rheological properties of screen-printing inks and the contradicting theories by Messerschmitt and Riemer, there have not been predictive models available to assist in identifying the optimal parameters to use. Where Messerschmitt believed the separation forces induced a flow causing a shearing action of the mesh strands combined with the tensile stresses induced by the increasing distance between the mesh and substrate, which leads to the ink splitting. (70) While Riemer believed that the ink passed through the mesh as a series of columns with the wires in the mesh acting in the manner of that Riemer described as acting like “pistons of a syringe” (39). Which would then slump and join together to form a print after the mesh had released the ink (39).

The work conducted in Chapter 5 identified a method for assessing the ink separation mechanism. As well as identified similarities in the ink deposition mechanism observed with that described by Messerschmitt, enabling the ink

separation stages to be split up into two quantifiable regions. Consisting of adhesion to extension for the first region and flow to separation in the second region. The lengths of these separation regions quantifiably varied with changes in line width, snap off distance and print speed, which related to the quantity of ink deposited and the homogeneity of the print.

Therefore, changing the rheological profile of the ink should also create quantifiable changes in the ink separation stages which could be related to the print quality and performance. The aim was to improve the understanding of how the rheological profiles of carbon-based inks influence the ink deposition and separation mechanisms in screen printing.

The first part of this chapter continued investigations conducted on the commercial carbon ink, assessed in Chapter 5. This experiment assessed the effect of making gradual changes to the viscosity and viscoelasticity of the ink (by producing a range of dilutions of the ink), on the lengths of the separation mechanisms identified in the previous chapter. It also assessed whether all four stages of ink separation were still present for all of the rheological profiles.

However, the commercial carbon-based ink contained a combination of different carbon morphologies which could influence the separation mechanisms due to the influence of particle size and geometry on ink flow. P2CAR2 (Printing Process Control by Advanced Rheology 2) project, a flagship project of the EPSRC Centre for Innovative Manufacture of Large Area Electronics being run in the Welsh Centre for Printing and Coating, was investigating the effect of carbon black, graphite and graphite nanoplatelets (GNPs), each in three different concentrations on printability. The project was developed by Prof. Tim Claypole with initial research conducted by Dr James Claypole with initial experiments conducted by myself. Bespoke inks were developed by Dr Tatyana Korochkina, who also printed the inks and measured the print topography and electrical properties, while the rotational shear rheological analysis was undertaken by Dr Alex Holder, both of whom provided their results to enable comparative analysis to be presented. While the SEM images were conducted by myself. The inks developed for the P2CAR2 project were further evaluated using CaBER tests and the Screen-printing Visualisation Rig used in the previous chapters. The P2CAR2 project provided a range of both shear and extensional rheological

profiles which could be compared to the resultant deposition and separation mechanisms occurring during screen-printing.

6.2. Materials and Methods

6.2.1. Inks

6.2.1.1. *Dilution study of commercial carbon-based ink*

The commercial carbon ink from Gwent Electronics Materials (GEM C2150317D3 carbon) as used in Chapter 5, was used to assess the effect of gradually changing the rheological profile of a commercial carbon-based ink. It was diluted between 0 wt% and 10 wt% with 1-Methoxy-2-propanol (solvent choice and dilution percentage range advised by manufacturer).

6.2.1.2. *Inks containing various carbon morphologies and loadings*

Bespoke inks containing graphite, graphite nanoplatelets (GNP) and carbon black were made to assess the effect of carbon morphologies and loadings on the ink separation process. Materials used were as follows: graphite (Timrex® SFG15, Imerys Graphite and Carbon; typical D90 17.9 μm according to manufacturer); carbon black (TIMCAL ENSACO™ 250G Conductive Carbon Black Compounds; with diameter distribution from 20 to 50 nm and specific surface area of 65 m^2/g according to the manufacturer) and graphite nanoplatelets (GNPs) functionalised with oxygen (GNP-O2 produced by Haydale Ltd. with average flake diameter around 5 μm). All inks used the same ethyl cellulose resin base (with 12.5% by weight dry polymer, ethyl cellulose (200697 Aldrich, Sigma–Aldrich) in 4-hydroxy-4-methylpentan-2-one (H41544 Aldrich, Sigma–Aldrich)).

Each carbon morphology was produced in three concentrations, which were demonstrated in preliminary experiments to be capable of producing a consistent 200 μm line. These concentrations are expressed in weight percentage (wt%) in Table 6.1, where an x in the matrix denotes loading percentage used in the experiments. This produced a total of 9 inks to be assessed. When making the inks, the carbon materials were gradually added and stirred in to the pre-made resin by hand. The ink slurries were then left to wet overnight before triple roll milling. Milling was conducted with an EXAKT80E three roll mill (EXAKT Advanced Technologies GmbH) with the same processing conditions used for all inks, as

presented in Table 6.2. Mixing was then conducted prior to printing, using a Speedmixer (Speedmixer™ DAC 150.1 (FVZ-K)), for 5 minutes at 2500 rpm.

Table 6.1 Ink batch composition for carbon-based inks

Carbon material loading in terms of mass %	10	15	20	25
Graphite wt%	-	x	x	x
Carbon Black wt%	x	x	x	-
GNP wt%	-	x	x	x
Resin base wt%	90	85	80	75
(of which 12.5 wt% solid, 87.5 wt% solvent)				

Table 6.2 Triple roll mill settings

Pass number	Band Gap (µm)	Front Gap (µm)	Speed (rpm)
1	60	15	200
2	40	10	200
3	20	5	200

6.2.2. Rheological and extensional testing

6.2.2.1. Shear Rheology for commercial carbon-based ink

For the commercial carbon-based ink, the same rheological tests were conducted as outlined in Section 5.2.1.

6.2.2.2. Shear Rheology for varying carbon morphologies and concentrations

Rheological evaluation was carried out using a combination of shear, viscoelastic and extensional measurements on the inks containing various carbon morphologies in a range of weight loadings as a part of the P2CAR2 project, by Alex Holder.

Analyses were conducted with a TA Instruments AR-G2 Rheometer. A roughened 60 mm stainless steel parallel plate geometry held at 20 °C was used for conducting the tests. Prior to conducting the tests, viscosity measurements were conducted over a range of gap distances to establish a suitable gap height between the plates to prevent slip from occurring. Ink viscosity was measured as the shear rate was increased from 0.01 s⁻¹ to 100 s⁻¹ with 5 logarithmically spaced measurements per decade. Small amplitude oscillatory shear (SAOS) was used to measure the quiescent viscoelastic profile of each ink between 0.01 Hz and 10 Hz. Measurements were performed within the linear viscoelastic region (LVR) of the inks.

6.2.2.3. *Extensional Rheology*

Extensional testing of the ink was assessed using Capillary breakup extensional rheology (CaBER) testing methods, as outlined in Section 5.2.1. In these analyses, the upper plate was then moved upwards at a constant velocity of 20 mm s⁻¹ by a further 5mm.

6.2.3. **Screen-printing visualisation method**

Printing on the screen-printing visualisation rig was conducted as outlined in Section 5.2.2. Along with a snap off distance of 1.825 mm and squeegee speed of 300 mm min⁻¹ (5.0 mm s⁻¹).

6.2.4. **Printing on a commercial press**

Comparison prints were also conducted for all inks to assess changes in print topography and electrical performance for a greater range of line widths and printed solid areas, on the DEK 248 flatbed screen printing press as described in Section 5.2.3, with a snap off distance of 1 mm, a downward squeegee force of 9 kg and a print speed of 70 mm s⁻¹.

6.2.5. **Printed line topography**

White light interferometry (NT9300, Veeco Instruments, Inc., Plainview, NY, USA) was used to measure a full three-dimensional surface profile of the prints produced on both the rig and DEK 248 at 5 times magnification, as described in Section 5.2.4. Where the 500 μm lines were measured the same way as the 700 μm, as described in Section 5.2.4.

The microstructures of the prints were also assessed, using a JEOL JSL 7800F FEG Scanning Electron Microscope (SEM) at 3000 times magnification.

6.2.6. Electrical characterisation

Two- and four-point probe measurements were conducted to find the line resistance, sheet resistance and resistivity values of the 500 μm and 700 μm printed lines, as well as the squares produced on the DEK 248 screen-printer, as described in Section 5.2.5. The 500 μm lines were measured using the same methods conducted on the 700 μm lines.

6.3. Results

6.3.1. Rheological analyses

6.3.1.1. Dilution study

The viscosity and viscoelasticity profiles of the inks are shown in Figure 5.1. All the inks were highly shear thinning, so would flow more readily when subjected to higher shear rates during printing. The most significant reductions in viscosity occurred between 1 s^{-1} to 50 s^{-1} . As the inks were diluted with increasing concentrations of 1-Methoxy-2-propanol from the plain carbon ink to 10 wt% dilution, the shear thinning (pseudoplasticity) profile was found to reduce in viscosity at a similar rate but with gradually reducing initial and final viscosity values. Increasing dilution percentages produced gradually lower viscosity values at all shear rates assessed. However, the rate of change in viscosity with shear rate was found to be similar in all inks. All dilutions also showed relatively little hysteresis over the shear rates assessed, when shear was reduced back down to 1 s^{-1} from 100 s^{-1} .

The phase angles of the carbon inks were found to increase with increasing dilution percentages (Figure 5.1 (b)), from 27° for the plain ink to 32° for the 10 wt% diluted ink at a frequency of 1Hz. Due to the increase in solvent concentration and resultant lower concentration of carbon causing the inks to behave in a more viscous manner as there are less carbon to carbon interactions. There was little change in phase angle between the plain ink and 2.5 wt% dilution, as well as between the 7.5 wt% and 10 wt% dilutions across the frequencies tested. All inks produced similar trends across the frequencies tested. In terms of the elastic (storage modulus, G') and

viscous (loss modulus, G'') shear modulus components (Shown in Figure 5.1 graphs (c) and (d) respectively), both components increased with frequency for all inks. The G' was found to be greater than the G'' for all dilutions tested across the frequency range of 0.1Hz to 10Hz. However, the G' is nearer the value of the G'' at the lower and higher frequencies in all dilutions tested. Although there is a far larger relative gap between the G' and G'' at the lower dilutions than with the higher dilutions. At 10 wt% dilution, there is the smallest relative gap between the G' and G'' for all frequencies, with the intersect point between G' and G'' being far closer at 10Hz than with lower dilutions. This raises the phase angle at 10Hz from around 39° with the plain ink to around 44° when diluted with 10 wt% thinner. This increase in phase angle reduced the elasticity of the inks, although all dilutions would behave in a predominantly elastic manner with such phase angles.

The separation mechanism during the CaBER tests are shown as a function of dilution percentage (Figure 6.2 (a) to (e)). The corresponding changes in the minimum diameter of the filament over time to the point of separation are also given (Figure 6.2 (f)). There was little change in the filamentation profile and separation position with changes in dilution percentage. However, the time to separation was found to range between around 1 and 5 seconds. The ink diluted by 2.5 wt% took the longest to separate, at 5.0 seconds. Increases in the dilution percentage led to gradual reductions in the time taken for ink separation, with the ink diluted by 10 wt% taking the least time to separate at 1.0 second. This is due to increases in the solvent concentration leading to a lower ink viscosity and therefore enabling the ink to separate faster. However, the non-dilute ink did not follow this trend, taking 2.2 seconds to separate. A possible mechanism to cause this may be that the initial addition of the diluting solvent leads to a change in the carbon to carbon interactions which caused it to separate over longer time period than with the undiluted ink.

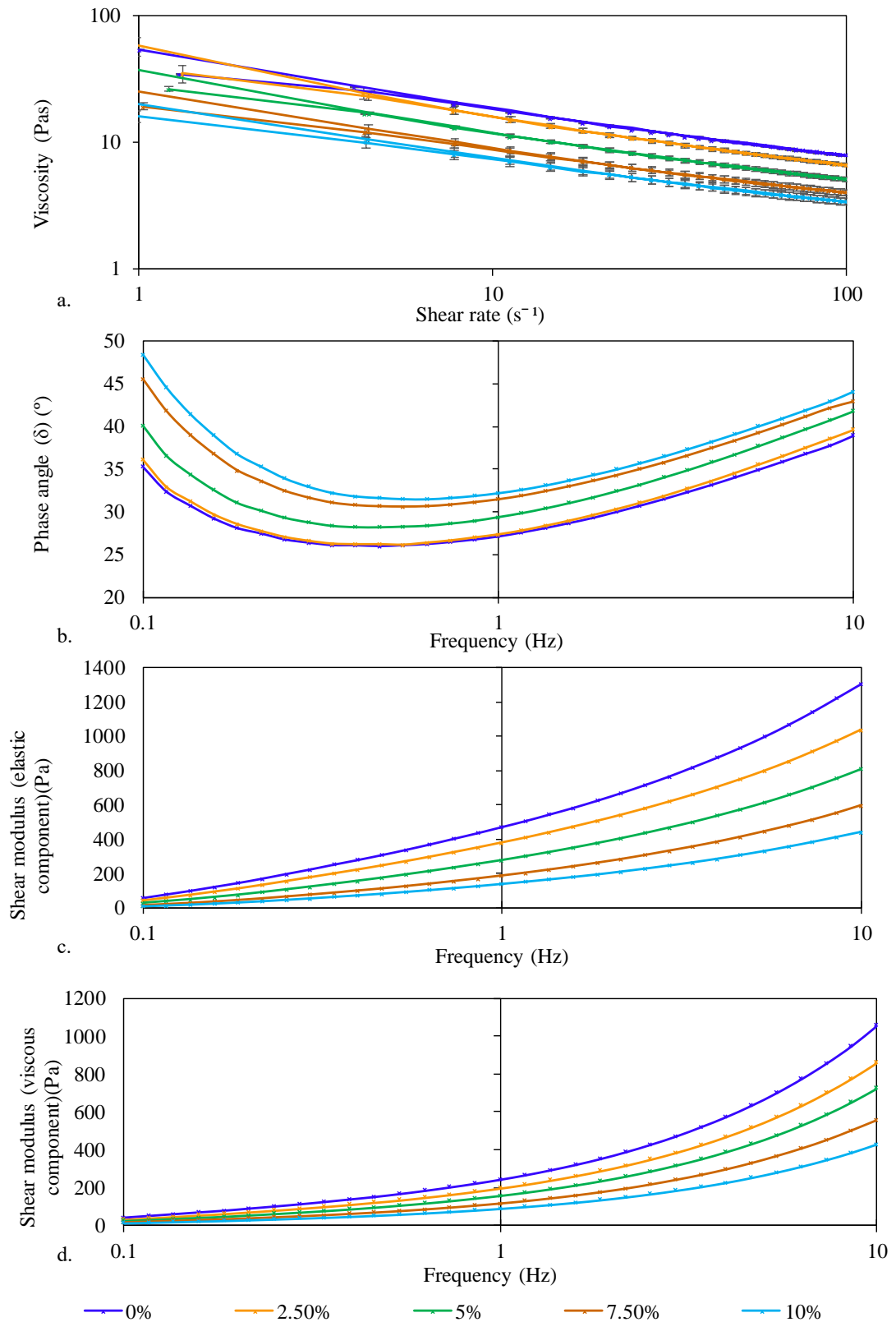


Figure 6.1 Viscosity profiles (a) and viscoelastic profiles assessing changes in phase angle (δ) (b), storage modulus (G') (c) and loss modulus (G'') (d) of the different dilutions of the carbon ink.

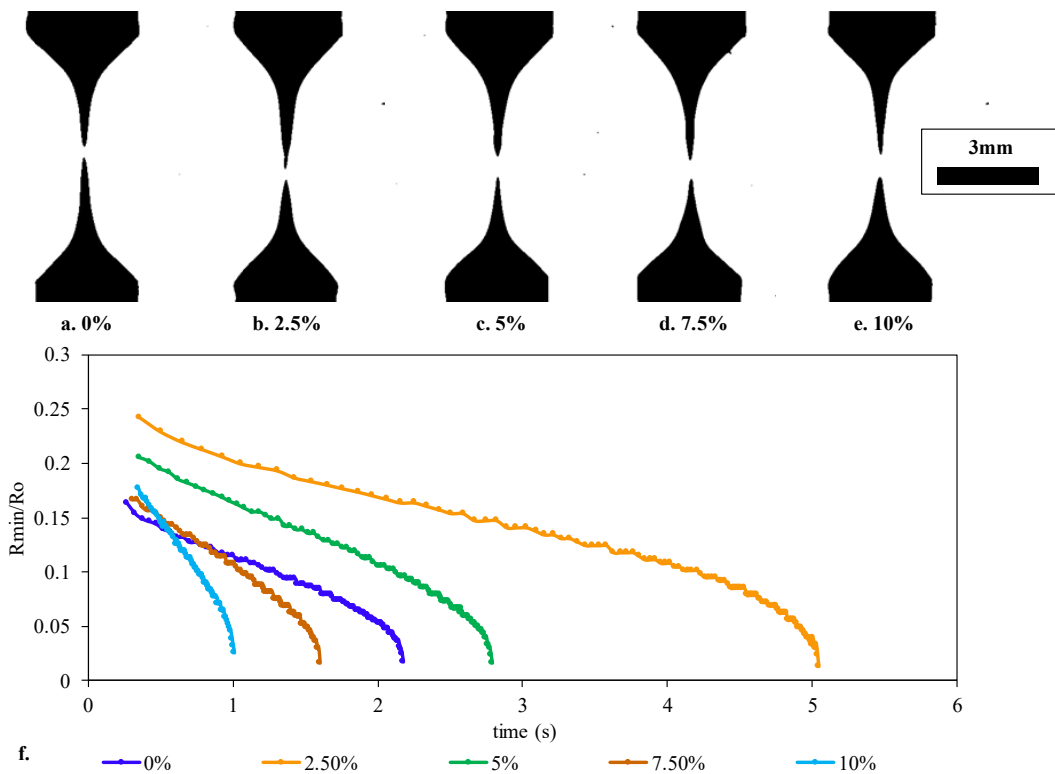


Figure 6.2 High speed images of the separation mechanism for inks diluted by (a) 0 wt%, (b) 2.5 wt%, (c) 5 wt%, (d) 7.5 wt% and (e) 10 wt% and a graph of the evolution in the (dimensional) radius as a function of time (f).

6.3.1.2. Carbon morphology and loading study

The viscosity and viscoelasticity profiles of the inks are shown in Figure 6.3. The viscosity graph (Figure 6.3 (a)) shows that all of the inks assessed and the plain resin were shear thinning, with the greatest reductions in viscosity occurring before 20 s^{-1} . For all carbon morphologies, increasing the loading percentage of carbon led to increases in viscosity over all shear rates. Although the inks containing 25 wt% of graphite and 20 wt% carbon black could not be assessed for shear rates beyond 10 s^{-1} and 15 s^{-1} as the high viscosities of the inks prevented the rheometer from rotating at these speeds, with viscosities of 95.5 Pas and 48.5 Pas respectively at these final shear rates. These two inks also had the highest initial viscosities.

The inks containing carbon black were found to shear thin to a greater degree at the lower shear rates than the inks containing graphite or GNPs. Although the carbon black based inks had a far higher initial viscosity due to the interactions of the small spherical particles. The inks containing 15 wt% and 10 wt% carbon black reduced to

viscosities of 8.0 Pas and 7.1 Pas respectively at shear rates of 100 s^{-1} . The graphite-based inks with 20 wt% and 15 wt% loading have viscosities of 11.3 Pas and 6.6 Pas respectively at 100 s^{-1} . While the GNP-based inks have the lowest viscosities over the shear rates tested for their respective loadings. Where the inks loaded with 25 wt%, 20 wt% and 15 wt% GNP's have viscosities at 100 s^{-1} of 11.0 Pas, 7.5 Pas and 5.5 Pas respectively. The high aspect ratios of the graphite flakes and GNP's with random orientation in the ink may enable the inks to have a lower viscosity than the carbon black based inks which have more surface area in contact with neighbouring particles. The ink containing 15 wt% GNPs has the viscosity profile most similar to that of the plain resin, which had a viscosity of 4.9 Pas at a shear rate of 100 s^{-1} . The higher aspect ratio of the GNPs compared with the other geometries may have enabled the platelets to act in a lubricating manner, enabling them to flow at a similar viscosity to the resin when at low concentrations. When comparing the viscosity profiles of these inks with the dilutions of the commercial ink, the lower concentrations of GNPs and the 15 wt% concentration of graphite have the most similar profiles. Although the commercial ink contains higher concentrations of carbon, the combination of graphite with carbon black and a different resin enable it to have a lower viscosity range than with the higher concentrations of graphite, GNPs and all of the carbon black based inks used in this study.

When comparing the viscoelastic profiles of the inks, the inks containing GNPs produced the highest phase angles at all frequencies assessed. The 15 wt% GNP ink produced the highest phase angle over the range of frequencies assessed, with a phase angle of 77.3° at a frequency of 1 Hz. The phase angles of the inks containing 20 wt% and 25 wt% GNPs were the next highest at 70.9° and 67.6° at 1 Hz respectively. The lowest phase angles were produced by the ink containing 20 wt% carbon black, followed by the ink containing 15 wt% carbon black with phase angles of 18.6° then 29.5° at 1 Hz respectively. The ink containing 10 wt% carbon black had a higher phase angle of 52.2° at 1 Hz, which was similar to the phase angle produced by the ink containing 25 wt% graphite, with a phase angle of 47.1° at 1 Hz. The other graphite-based inks lay in the middle, with the 15 wt% and 20 wt% graphite-based inks having phase angles of 65.3° and 62.1° at 1 Hz respectively.

In terms of the elastic (storage modulus, G') and viscous (loss modulus, G'') shear modulus components (Shown in Figure 6.3, graphs (c) and (d) respectively), both

increased with frequency for all inks. For the carbon black-based inks, the ink containing 10 wt% loading showed cross over points between G' and G'' at two frequencies, first at 0.01 Hz where G' becomes greater than G'' , then at 0.5 Hz, where G'' becomes greater than G' , causing it to behave in a more liquid like manner at higher frequencies. The 15 wt% loaded carbon black-based ink had one cross over point where G'' becomes greater than G' at 5Hz, meaning that it only behaved in a liquid like manner at the higher frequencies assessed. While the 20 wt% carbon black-based ink never reached a cross over point between the two moduli over the frequency range assessed, meaning that it behaved in an elastic manner for all frequencies.

The GNP based inks also did not exhibit any cross over points between G' and G'' , where G'' remained consistently greater than G' for the full range of frequencies assessed, leading to predominantly liquid like behaviour in the inks. The graphite-based inks showed similar trends to the GNP-based inks for the lower percentage loadings, although the gap between G' and G'' was narrower for the 20 wt% graphite-based ink. For the 25 wt% graphite-based ink, G' is greater than G'' at the lower frequencies, but G'' becomes greater than G' at 1.5 Hz, leading to predominantly liquid like behaviour at the higher frequencies.

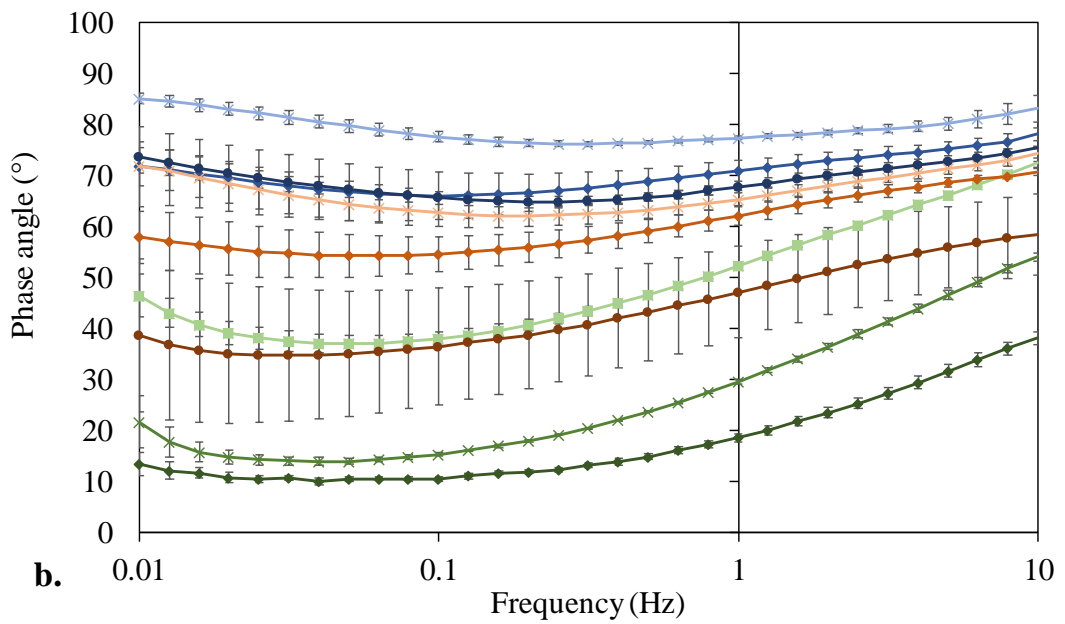
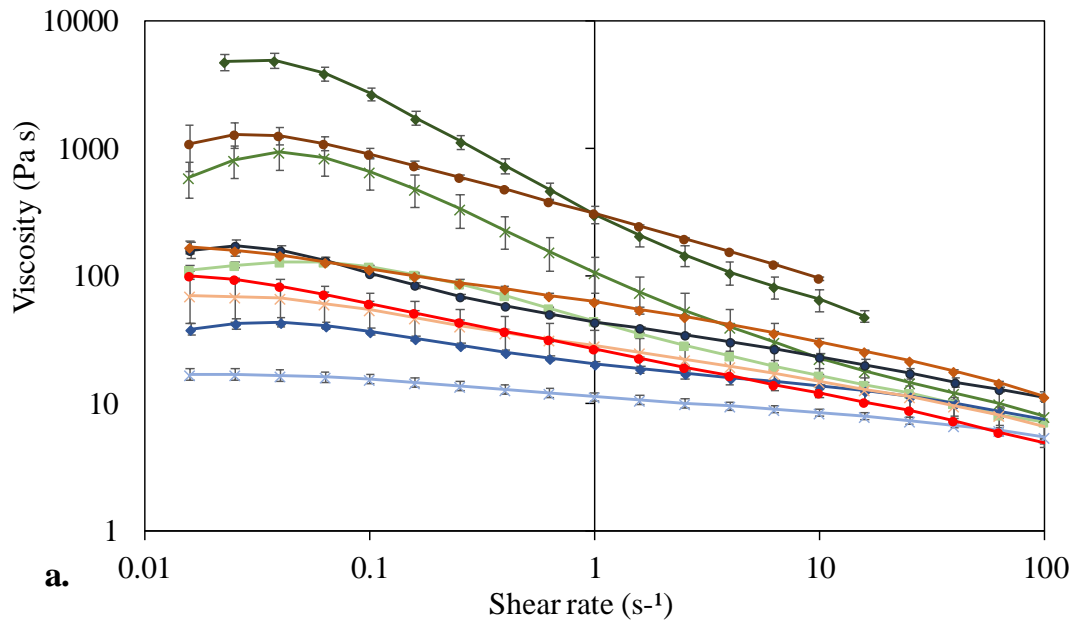
Therefore, the GNP-based inks exhibited more liquid like behaviour and the carbon black-based inks exhibited more elastic behaviours as the small, spherical carbon black particles had more surface area in contact with one another than the high aspect ratio, randomly oriented GNPs. The graphite-based inks exhibited more liquid like behaviours at lower concentrations and behaved in a more elastic manner at higher concentrations as the surface area of the flakes interacting increased. As well as this, lower particle concentrations led to higher phase angles with more liquid like behaviours.

Figure 6.4 shows the changes in the separation mechanism from the CaBER tests with changes in the carbon morphology and loading (Figure 6.4 (a) to (i)). The corresponding changes in the minimum diameter of the filament over time to the point of separation were also shown (Figure 6.4 (j)). The graphite-based inks were typically found to take the longest to separate for their given loading percentage, due to the large graphite flakes gradually aligning and flowing past one another. The

rough texture of the graphite flakes can be seen on the edges of the filaments in Figure 6.4, particularly in image (c) of the 20 wt% loaded graphite ink. The 25 wt% graphite-based ink took 16.5 seconds to separate, followed by the 20 wt% graphite-based ink which took 11.8 seconds. While the 15 wt% graphite-based ink took 4.9 seconds, which was comparable with the 20 wt% GNP based ink, which took 4.8 seconds. The other GNP inks were also faster at separating than the higher loaded graphite-based inks, where the 25 wt% GNP ink took 8.6 seconds and the 15 wt% GNP-based ink took the least time to separate out of all of the inks, at 2.4 seconds. This is likely due to the smaller size of the GNPs compared with the graphite flakes, enabling them to flow more readily and separate faster. The 10 wt% and 15 wt% carbon-black based inks took similar times to that of the GNP based inks, taking 3.2 and 4.8 seconds to separate respectively. This is likely due to the small size of the carbon black particles, enabling them to flow and separate easier than the larger carbon morphologies. However, the ink containing 20 wt% carbon black would not break, even after one minute, as shown in Figure 6.4 image (f). This is due to the high elasticity of the ink causing it to behave more like an elastic solid and preventing it from flowing well enough to enable separation. This is a result of the increased volume of carbon black leading to smaller interparticle distances and therefore more particle-particle interactions which elastically store energy, as shown by its low δ in Figure 6.3 (b).

In terms of the separation profiles produced, all carbon morphologies produced long necking regions with homogeneous extensional flow over the filament. However, the inks containing higher concentrations of carbon tended to produce filaments which formed more hourglass like profiles prior to separation and tended to separate with larger final diameters, or not separate at all in the case of the highly loaded carbon black ink.

Overall, inks containing higher carbon loading percentages took longer to separate and separated with larger diameters than those with lower loading percentages.



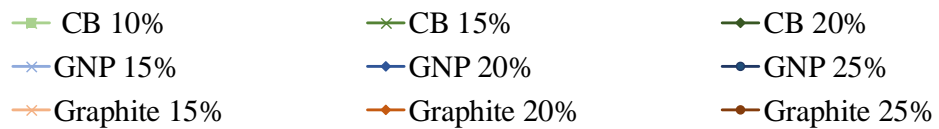
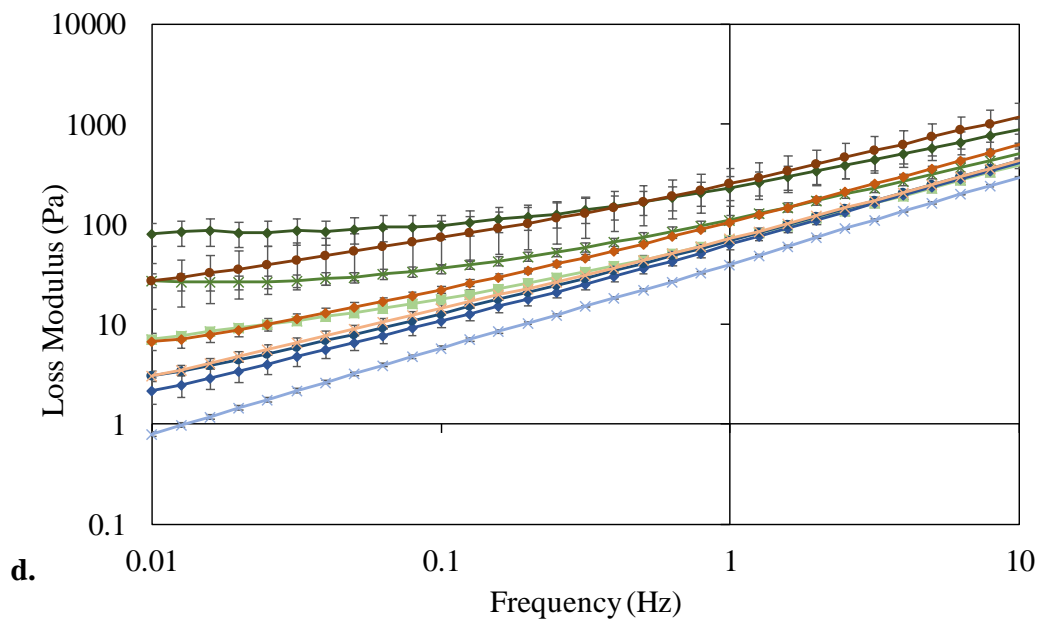
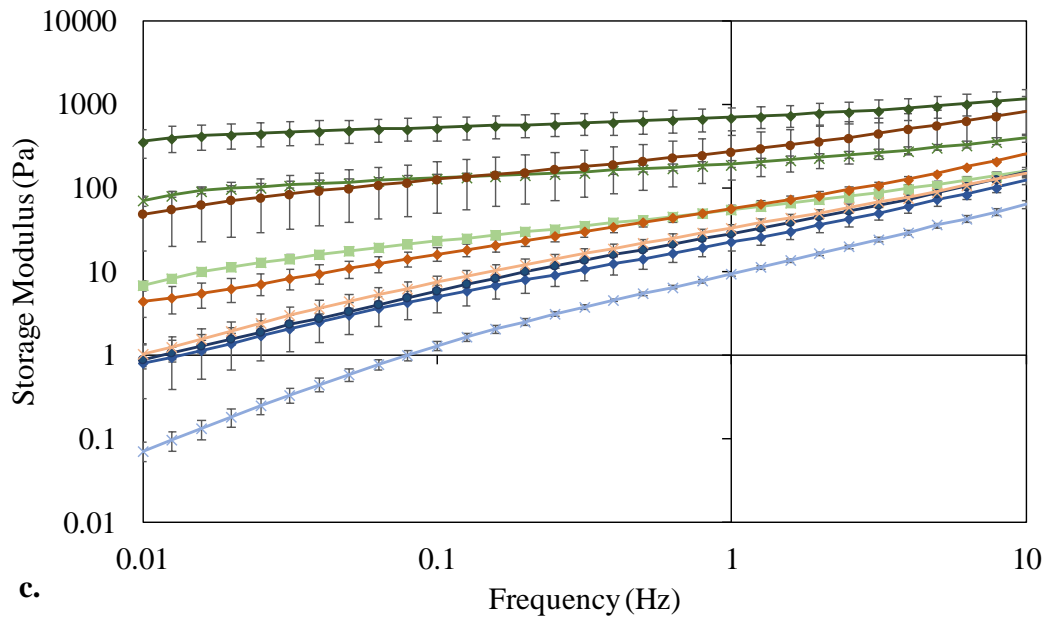


Figure 6.3 Viscosity profiles (a) and viscoelastic profiles assessing changes in phase angle (δ) (b), storage modulus (G') (c) and loss modulus (G'') (d) of the varying carbon morphologies and loading percentages. (Error bars represent standard deviation)

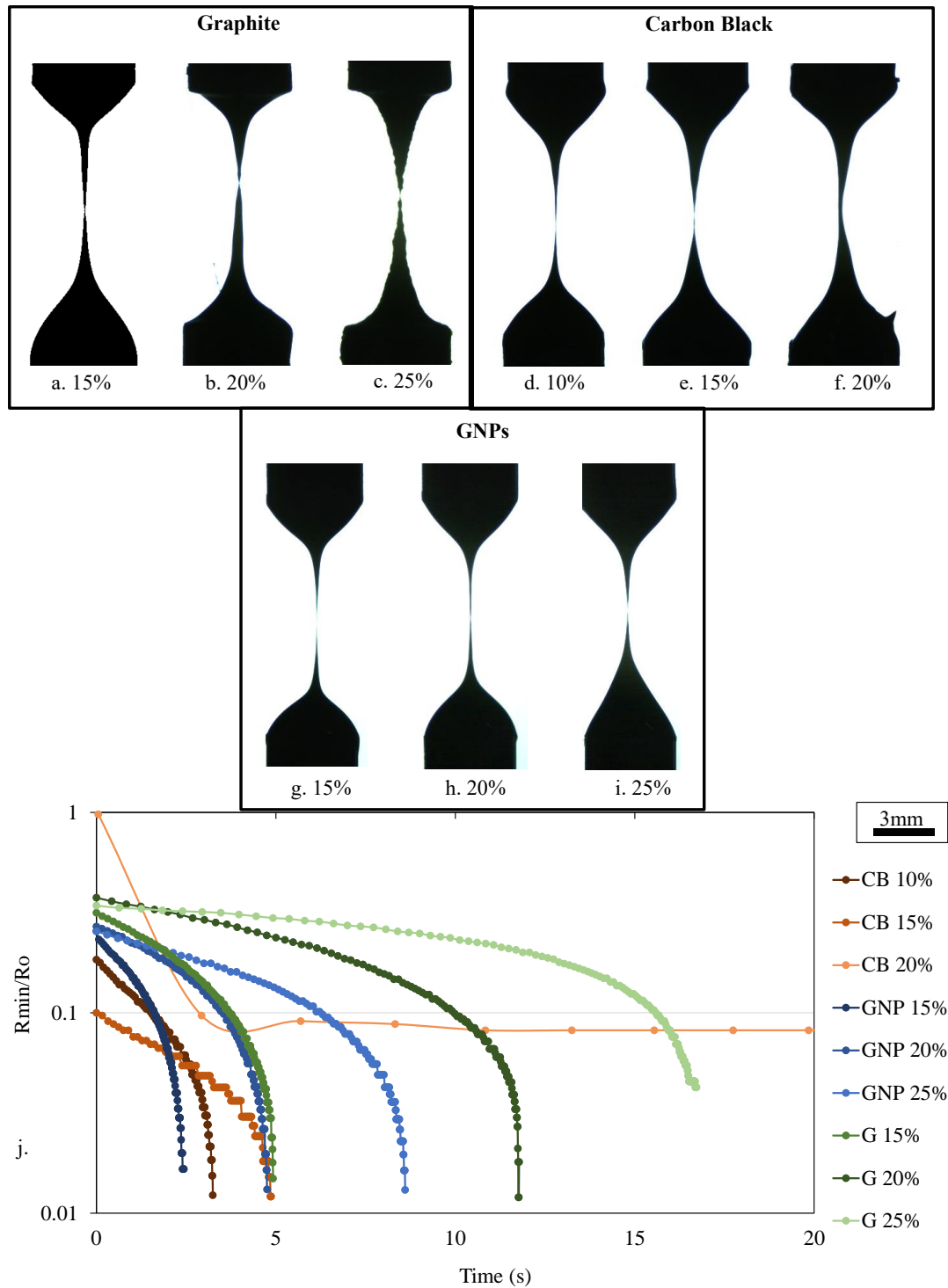


Figure 6.4 High speed images of the separation mechanism for the ethyl cellulose-based carbon inks loaded with varying amounts of graphite (a to c), carbon black (d to f) and GNPs (g to i), with a graph of the evolution in the (dimensional) radius as a function of time (j).

6.3.2. Print contact regions

6.3.2.1. Dilution study

The deposition mechanisms observed for the different ink dilutions were characterised using the lengths of the separation stages, as outlined in Section 5.3.3 and illustrated in Figure 5.10.

Increasing the dilution percentage of the carbon inks led to small increases in the lengths of the adhesion to extension stages. More significantly, the flow to separation stages were found to cease at higher dilution percentages (Figure 6.5). Between the plain ink (0 wt%) and 2.5 wt% diluted ink, there was a relatively small increase in the average adhesion to extension stage lengths, from 1428 μm to 1499 μm and an increase in the average flow to separation stage lengths from 392 μm to 757 μm . Both inks showed similarities in deposition patterns, where both print cycles exhibited regular filamentations after the extension stage. They both produced an average of around 10 filaments over the print cycle assessed, which led to subsequent necking and ink splitting across the flow to separation stages. This is in line with the rheological profiles of the inks as there was little change in the viscosity or phase angle between these two inks, when compared with the other dilutions.

Some inks with higher dilutions of 1-Methoxy-2-propanol were found to have a clean separation behind the adhesion to extension zone without any individual filaments leading to necking regions. This was the case with the 5 wt% and 10 wt% diluted inks. Where only stages 1 and 2 of Messerschmitt's 4 stages of ink separation were exhibited during with these dilutions. This is due to the increases in solvent percentage leading to lower ink viscosity as the interparticle distance increases, leading to a reduction in the particle-particle interactions, which reduced the amount of stress required for separation. This enables a clean separation without the need for filament formation.

The 7.5 wt% ink produced a few filaments with subsequent necking regions on two of the three prints conducted, while the third did not exhibit any. Producing an average of 4 filaments and subsequent separation points across the print runs assessed.

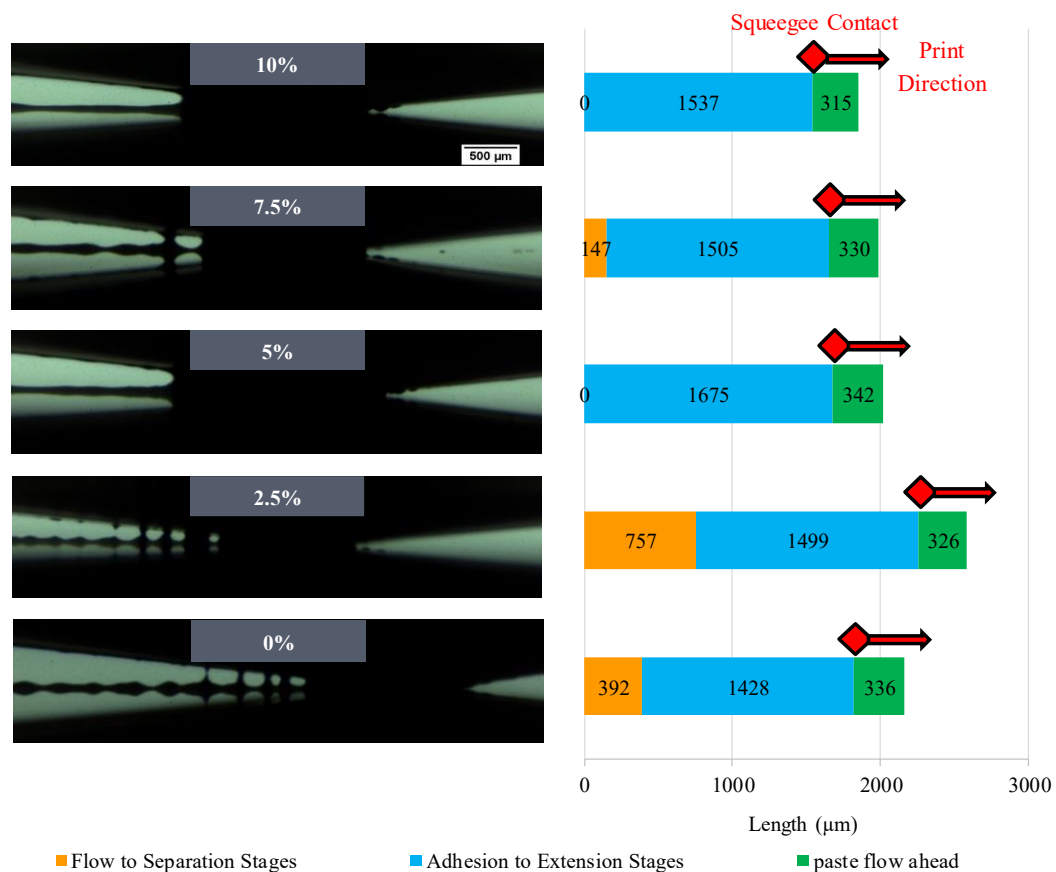


Figure 6.5 High-speed camera images at 5x magnification and quantification of the average print stage lengths for deposition of the carbon ink diluted by 0 wt% to 10 wt%.

6.3.2.2. Carbon morphology and loading study

The ink separation mechanisms observed for the inks containing various loading percentages of carbon black, GNPs and graphite were characterised using the lengths of the separation stages, as outlined in Section 5.3.3 and illustrated in Figure 5.10.

The plain resin exhibited all four stages of ink separation, as described in Section 5.3.3., adhesion, extension, flow and separation (Figure 6.6). The plain resin had an average adhesion to extension stage length of 976 μm, average flow to separation stages length of 478 μm, along with a 479 μm long paste flow region ahead of the squeezegee. However, the filaments forming during the flow to separation stages exhibited a dominos like effect. Where the outermost filaments would flow back towards the print direction and merge with the next filament forming on most occasions, rather than continuing to elongate and then separate. This is shown in

more detail in Figure 6.7, which shows the filaments moving back towards the main body of the extended ink over the duration of the squeegee moving across the mesh during printing.

The graphite-based inks containing 15 wt% and 20 wt% carbon loading behave in a manner closest to that of the plain resin, (Figure 6.6). The dominos like effect was also seen with these inks during separation, where the filaments forming at the end of the separation stages would flow into the next forming filaments. However, the lengths of the flow to separation stage lengths of the 15 wt% and 20 wt% graphite-based inks were slightly shorter than those observed with the plain resin and their adhesion to extension stages were slightly longer. The average adhesion to extension stage lengths of the 15 wt% and 20 wt% graphite-based inks were around 1091 μm and 1127 μm respectively. With average flow to separation stages lengths of around 308 μm and 337 μm for the 15 wt% and 20 wt% graphite-based inks respectively. The 25 wt% graphite-based ink had a similar average adhesion to extension stage length of around 1094 μm , but with a far larger average flow to separation stage length of around 820 μm . The 25 wt% loaded ink exhibited a greater number of filaments formed behind the adhesion to extension stages and took longer to separate than with the lower concentrations of graphite. In this case, the dominos like effect where the end filaments reformed with newly forming filaments did not occur. Instead, the filaments gradually necked and separated, as with the filaments formed in the extensional rheology tests. There was an overall increase in the average full contact region length with increases in graphite concentration and increases in ink viscosity and elasticity. There was no significant change in the lengths of the paste flowing ahead of the squeegee, although it could be seen that the ink was starting to flow through the holes in the mesh ahead of the squeegee due to the ink flowing ahead of the squeegee on top of the mesh.

The full contact region of the ink in simultaneous contact with the mesh and substrate was typically longer for the inks containing GNPs. However, the 15 wt% and 20 wt% loaded inks exhibited a clean separation behind the adhesion to extension zone without any individual filaments forming. As a result, these inks did not exhibit any flow to separation stages but did have relatively long adhesion to extension lengths of 1905 μm and 2063 μm for the 15 wt% and 20 wt% loaded inks respectively. The 25 wt% GNP ink did exhibit filaments forming, necking and

separating after the adhesion to extension stages. Although these filaments were far larger and more spread out than in the graphite-based inks, with an average flow to separation stage length of 602 μm . The 25 wt% GNP ink also had a relatively long average adhesion to extension stage length of 1825 μm . As with the graphite based inks, increases in the GNP concentration led to increases in the full contact region as the ink increases in viscosity and elasticity. Although there were also no significant changes in the length of the paste flow region ahead of the squeegee, there was less ink coming through the mesh prior to deposition. As shown by the lack of ink droplets emerging from the mesh prior to transferring to the substrate. This may be due to the lower viscosities of the GNP based inks.

The carbon black-based inks exhibited the broadest range of deposition profiles out of the carbon morphologies assessed. The 10 wt% loaded ink had the shortest full contact region length out of the carbon black based inks, at 2029 μm . Along with a relatively short average flow to separation stage length of 92 μm and an average adhesion to extension stage length when compared with the other inks, of 1561 μm . The 15 wt% carbon black-based ink did not exhibit a flow to separation stage. As with the 15 wt% and 20 wt% GNP inks, there was a clean separation behind the adhesion to extension zone without any individual filaments forming. However, the ink still had a large full contact region, due to having the largest average adhesion to extension stage of all the inks assessed, of 2837 μm . Unlike the 15 wt% carbon black ink, the 20 wt% carbon black ink did exhibit filamentation after the adhesion to extension stage, with the largest average flow to separation stage length of all the inks assessed, of 2027 μm . In this case, there were several filaments formed behind the adhesion to extension stage at one time. In addition to this, the 20 wt% carbon black ink had an average adhesion to extension length of 1203 μm and paste flow region ahead of the squeegee of 514 μm . Therefore, this ink produced the largest full contact region length of the inks assessed, of 3744 μm . As with the other morphologies, there is an increase in the average full contact region length with increases in the concentration of carbon black and resultant increases in viscosity and elasticity. There were no significant changes in the lengths of the paste flow region ahead of the squeegee across all nine inks, however, the carbon black based ink showed the most ink emerging from the mesh strands prior to the ink contacting the substrate. This may be due to the hydrodynamic pressure of the ink flow front ahead

of the squeegee forcing it through the mesh being greater in the carbon black based inks, which were more viscous and elastic than the other inks.

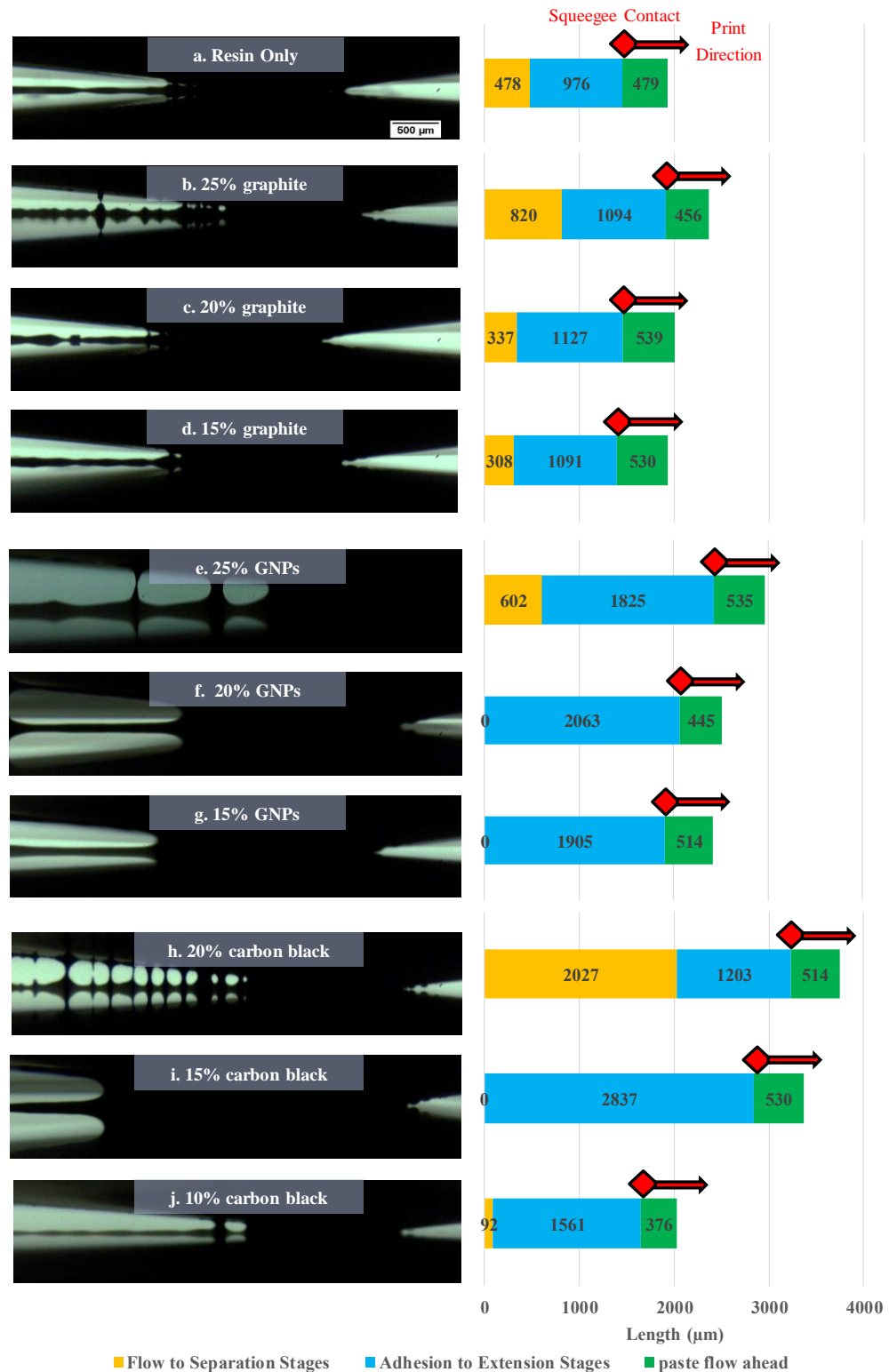


Figure 6.6 High-speed camera images at 5x magnification and quantification of the average print stage lengths for deposition of the plain resin (a) along with the ethyl

cellulose-based carbon inks loaded with varying amounts of graphite (b to d), GNPs (e to g) and carbon black (h to j).

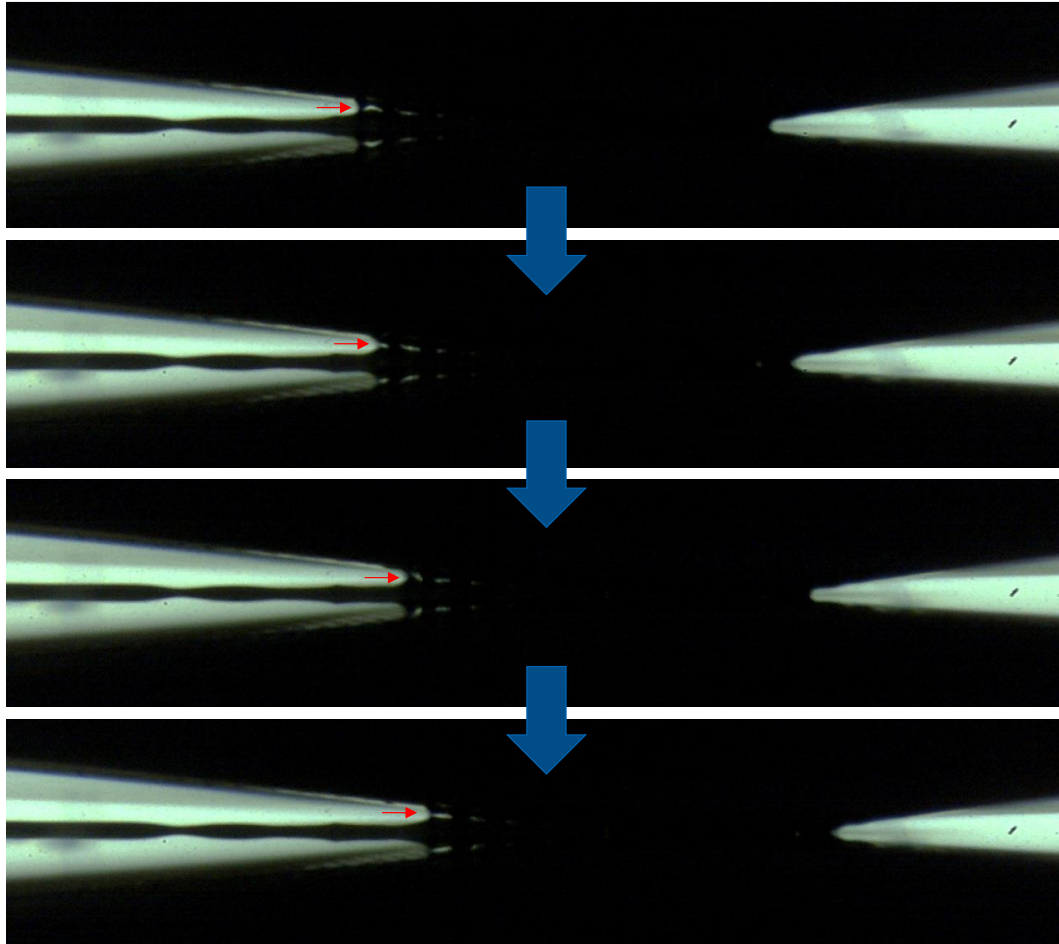


Figure 6.7 High-speed camera images at 5x magnification of different stages of the deposition of the plain resin showing the merging of the filaments forming during separation.

6.3.3. Print Characterisation

6.3.3.1. Dilution study

The ink film thickness and line widths of the prints produced for each of the ink dilutions on the screen-printing rig are compared in Figure 6.8, with corresponding topography images of the prints (Figure 6.8 (a-e)). There was an overall reduction in the average film thicknesses and line widths of the printed lines, as the dilution percentage of the carbon inks was increased. The cross-sectional area (CSA) of ink deposited, calculated by multiplying the film thickness by the line width, was found

to reduce from an average of $3966 \mu\text{m}^2$ for the plain ink, to an average of $2927 \mu\text{m}^2$ for the ink diluted by 10 wt% 1-Methoxy-2-propanol (Figure 6.9).

However, there were some fluctuations in the average amount of ink deposited, where the 2.5 wt% diluted ink produced a greater ink deposit than the plain ink. As well as this, the 7.5 wt% dilution produced a greater ink deposit than the 5 wt% dilution. While the 5 wt% and 10 wt% dilutions produced similar average ink deposit quantities. The 5 wt% dilution produced a line width of $284.1 \mu\text{m}$ and a film thickness of $10.5 \mu\text{m}$, while the 10 wt% dilution produced a line width of $284.4 \mu\text{m}$ and a film thickness of $10.3 \mu\text{m}$.

When comparing these results with the lengths of the ink separation stages, there was a correlation between the changes in ink deposition quantity and the length of the flow to separation stages, as shown in Figure 6.9. The increase in ink deposition between the plain ink and 2.5 wt% diluted ink, from an average CSA of $3966 \mu\text{m}^2$ to $4409 \mu\text{m}^2$, corresponded with the increase in the average flow to separation stage lengths from $392 \mu\text{m}$ to $757 \mu\text{m}$. When increasing dilution percentage to 5 wt%, there was a reduction in average CSA down to $2980 \mu\text{m}^2$. This also corresponded with a reduction in the average flow to separation stage lengths down to nothing, where there were no filaments forming behind the extension stage. At 10 wt%, a similar average CSA of $2927 \mu\text{m}^2$ was produced. This dilution also produced no filaments behind the extension stage. Additionally, the increase in average CSA from $2980 \mu\text{m}^2$ to $3684 \mu\text{m}^2$, when increasing dilution percentage from 5 wt% to 7.5 wt%, was found to correspond with the increase in the average flow to separation stage length from nothing to $147 \mu\text{m}$.

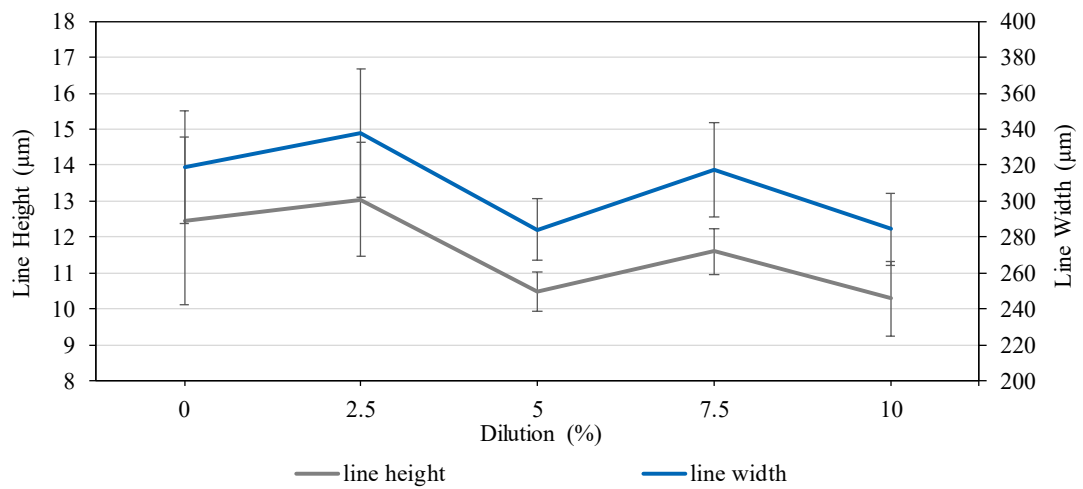
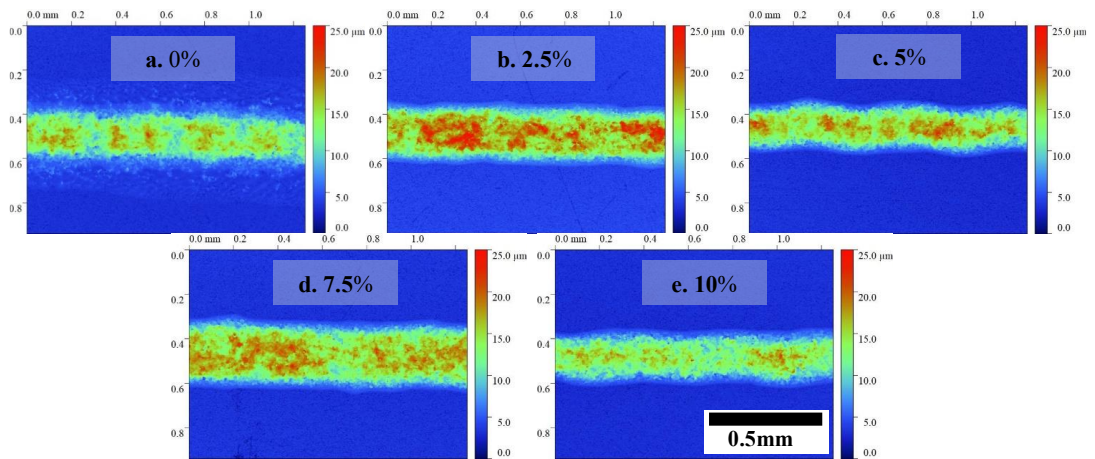


Figure 6.8 White light interferometry topography images of the printed lines diluted by (a) 0 wt%, (b) 2.5 wt%, (c) 5 wt%, (d) 7.5 wt% and (e) 10 wt%, with a graph of the corresponding changes in film thickness and width below. (error bars represent standard deviation).

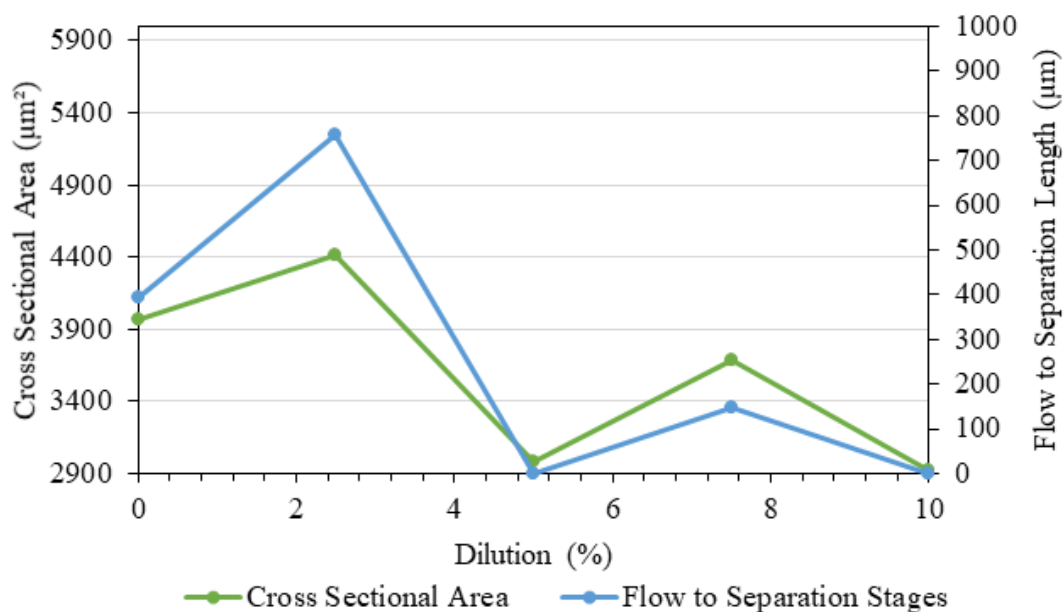


Figure 6.9 Comparison of the average cross sectional area of the printed line with the average flow to separation stage length during printing of the line.

6.3.3.2. Carbon morphology and loading study

The ink film thickness and line widths of the prints produced for each of the carbon morphologies and carbon concentrations printed on the screen-printing rig are compared in Figure 6.10 and Figure 6.11. For all carbon morphologies, increases in the carbon loading percentage led to increases in the ink film thickness and cross-sectional area of ink deposited overall. This also corresponds with changes in the lengths of the full contact regions (all stages of ink separation where the ink is in simultaneous contact with the mesh and substrate) of the inks during deposition. Where higher carbon loadings of all morphologies led to both increases in the cross-sectional area (CSA) of the printed lines and increases in the length of the full contact regions during printing (Figure 6.12).

For the carbon-black based inks, there was a linear increase in the average film thickness of the printed lines with increases in carbon loading, from 4.1 µm for 10 wt% loading to 14.5 µm for 20 wt% loading (Figure 6.11 (a)). There was also a linear increase in the film thickness of the prints containing GNPs, although with a less significant increase, from 5.1 µm at 15 wt% loading to 11.4 µm at 25 wt% loading. The graphite-based inks saw a slight reduction in the average film thickness between 15 wt% and 20 wt% loading from 5.3 µm to 5.1 µm. However, this was

then followed by an increase in the average film thickness to 16.9 μm at 25 wt% graphite loading.

The average line widths of the GNP and graphite-based inks were found to only vary within the standard deviation of the line widths across the lengths of the lines and over repeat prints (Figure 6.11 (b)). The graphite-based inks containing 20 wt% and 25 wt% graphite had more consistent line widths than those containing 15 wt%. Whereas the line widths produced for the carbon-black based inks were found to have variations greater than standard deviations, where the line width produced for the 15 wt% loaded ink was found to be narrower than those produced for the 10 wt% and 20 wt% loaded inks. However, the effect of line width was less significant than that of the film thickness on the quantity of ink deposited, leading to an overall increase in the amount of ink deposited, with increases in carbon loading percentages (Figure 6.11 (c)).

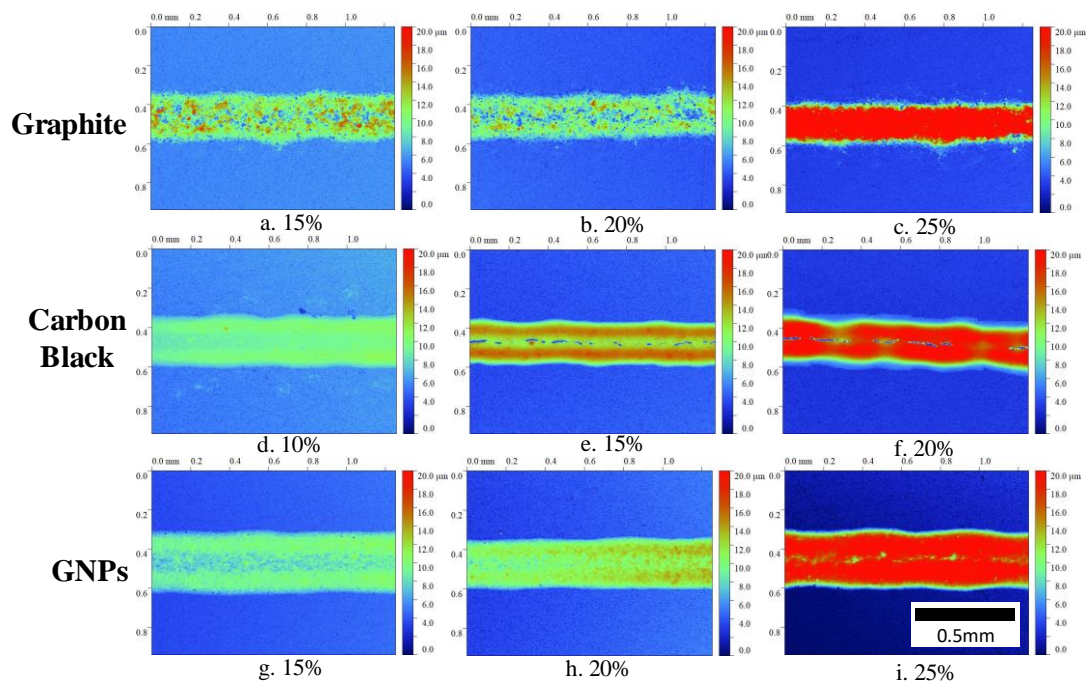


Figure 6.10 White light interferometry topography images of the printed lines produced with the ethyl cellulose-based carbon inks loaded with varying amounts of graphite (a to c), carbon black (d to f) and GNPs (g to i).

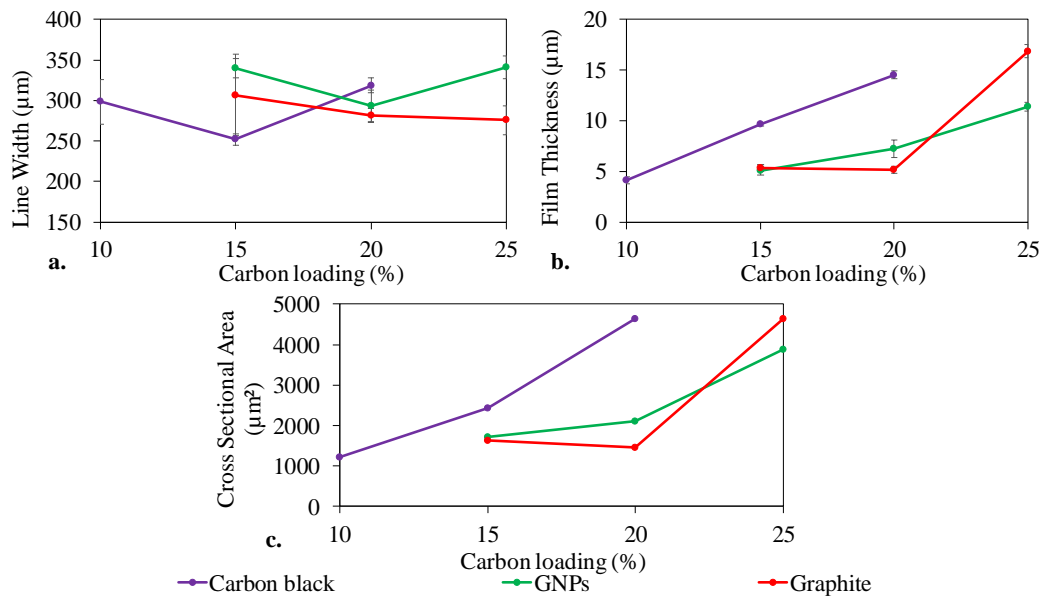


Figure 6.11 Changes in line width (a), film thickness (b) and the cross-sectional area of ink deposited (c) with ethyl cellulose-based carbon inks containing different carbon morphologies and different loading ratios.

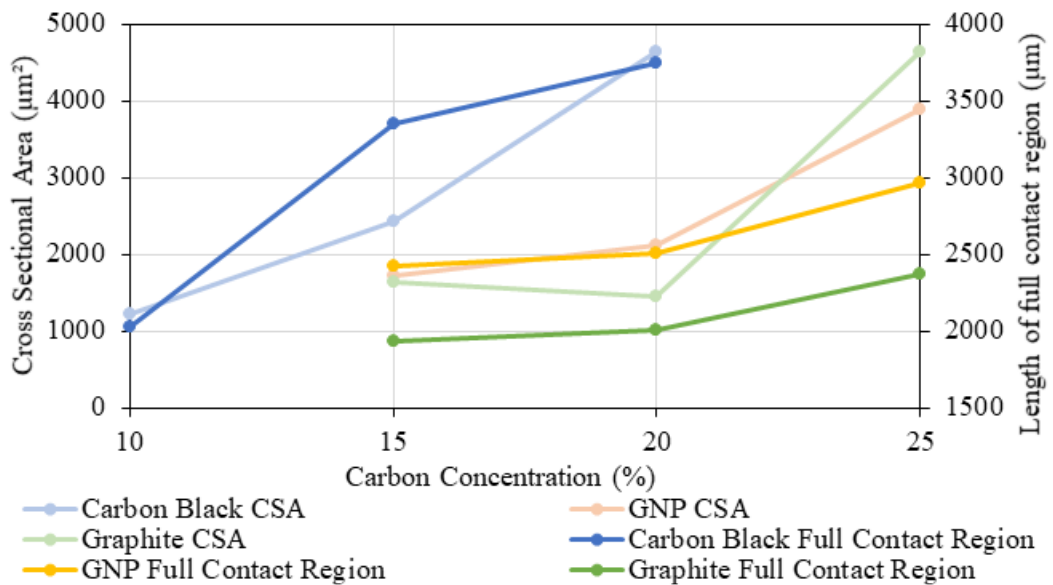


Figure 6.12 Comparison of the average cross sectional area of the printed line with the average full contact region (stages 1-4) during printing of different carbon morphologies and concentrations.

6.3.4. Commercial Press Comparison

6.3.4.1. Dilution Study

The average film thickness and line widths of the 500 µm and 700 µm lines, along with the film thickness of the printed solid squares produced on the commercial

screen printer for each of the ink dilutions are shown in Figure 6.13. Corresponding topography images of the 500 μm lines were also shown (Figure 6.13 (a-e)). There was a gradual reduction in the average film thickness of both the printed lines and squares (Figure 6.13 (g)). The average film thickness of the 500 μm reduced from 8.1 μm for the plain ink to 5.4 μm for the ink diluted by 10 wt%. There was also an overall reduction in the average line width from 799 μm to 779 μm for the nominal 700 μm line and from 644 μm to 611 μm for the 500 μm line, when going from the plain ink to the ink diluted by 10 wt% respectively (Figure 6.13, (f)). There was no clear trend with the changes in the average printed line widths for both the 500 μm and 700 μm nominal lines. The line widths of the 2.5 wt% and 5 wt% diluted inks were greater than that of the plain ink, while the line widths of the 7.5 wt% and 10 wt% diluted inks were lower than those produced for the plain ink. However, when the total cross-sectional area (CSA) of ink deposited was considered, the trend was comparable with the changes in film thickness. There was a gradual reduction in CSA after each increase in dilution percentage. This can also be observed in the white light microscopy images shown in images (a) to (e) of Figure 6.13. Displaying a reduction in the film thickness with increases in dilution percentage, but little visible change in the line width or print consistency and roughness. This is supported by the surface roughness values in Figure 6.14, measured on the centre of the printed squares, which show little change. Fluctuations in roughness lay within the standard deviation (illustrated by error bars), due to changes in print topography over the position of the printed square and over the duration of the print run.

The variations between the trends in the printed lines produced between the rig and the commercial press are due to the changes in the line widths produced, with the line widths produced on the commercial press more representative of those produced in industry. As well as the different screen sizes and press speeds which all interact and influence the print quality. Although both presses show an overall reduction in the film thickness deposited with increases in solvent percentage as the film thickness is related to the carbon concentration of the ink.

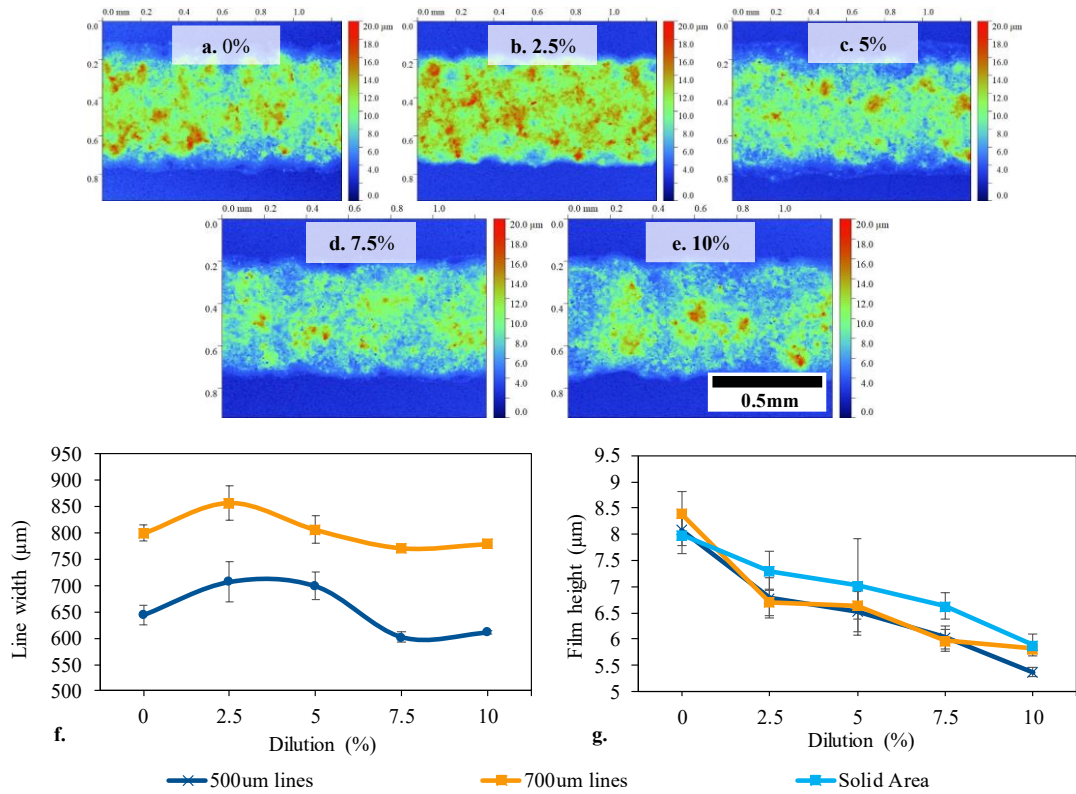


Figure 6.13 White light interferometry topography images of 500µm printed lines conducted on the DEK 248 Screen-printer at 5 times magnification, diluted by (a) 0 wt%, (b) 2.5 wt%, (c) 5 wt%, (d) 7.5 wt% and (e) 10 wt%, with a graph of the corresponding changes in line width (e) and film thickness (f) below for the 500µm and 700µm lines, as well as the film thickness of the printed squares (error bars represent standard deviation).

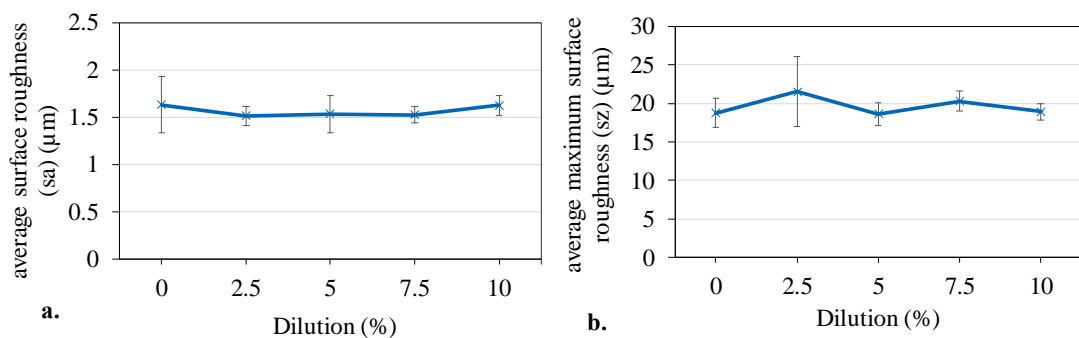


Figure 6.14 The average surface roughness (sa) (left graph) and average maximum surface roughness (sz) (right graph) of the printed squares conducted on the DEK 248 Screen printer for the printed carbon inks diluted between 0 wt% and 10 wt%.

The electrical characterisation of the prints conducted on the commercial press for the series of ink dilutions is shown in Figure 6.15. Displaying the average line

resistance for the 500 μm and 700 μm lines (a), as well as the average sheet resistance (b) and sheet resistivity (c) of the printed squares. Changes in both line and sheet resistance were found to be inversely related to the changes in ink deposition quantity. Reductions in the quantity of ink deposited were found to cause increases in line and sheet resistances. However, there was relatively little change in line resistance for both widths assessed between the plain ink (0 wt%) and 5 wt% diluted ink, as shown in Figure 6.15 (a). The nominal 700 μm line produced an average line resistance of 0.86 k Ω for the plain ink, 0.83 k Ω for the 2.5 wt% diluted ink and 0.86 k Ω for the 5 wt% diluted ink. This shows that small dilutions in the ink up to 5 wt% have a negligible effect on the line resistance, which are within standard deviation. However, this then increased to 1.01 k Ω for the 7.5 wt% diluted ink, with a less significant further increase to 1.02 k Ω for the 10 wt% diluted ink. Similar trends were found for the 500 μm nominal width lines, where the average line resistance was 1.10 k Ω for the plain ink, 1.13 k Ω for the 2.5 wt% diluted ink and 1.16 k Ω for the 5 wt% diluted ink. This then increased to 1.42 k Ω for the 7.5 wt% diluted ink and to 1.52 k Ω for the 10 wt% diluted ink.

The sheet resistance values gradually increased across all dilutions, from the plain ink to 10 wt% dilution, as shown in Figure 6.15 (b). However, there was relatively little fluctuation in the average sheet resistivity, where the film thickness was accounted for (Figure 6.15 (c)). Variations in average sheet resistivity for the various ink dilutions were found to be within standard deviation, due to fluctuations in sheet resistance and film thickness across the area of the printed squares and changes over the print run (represented as error bars). The 2.5 wt% diluted ink was found to produce the lowest average sheet resistivity of 0.013 $\Omega\cdot\text{cm}$ and the 10 wt% diluted ink produced the highest average sheet resistivity of 0.014 $\Omega\cdot\text{cm}$.

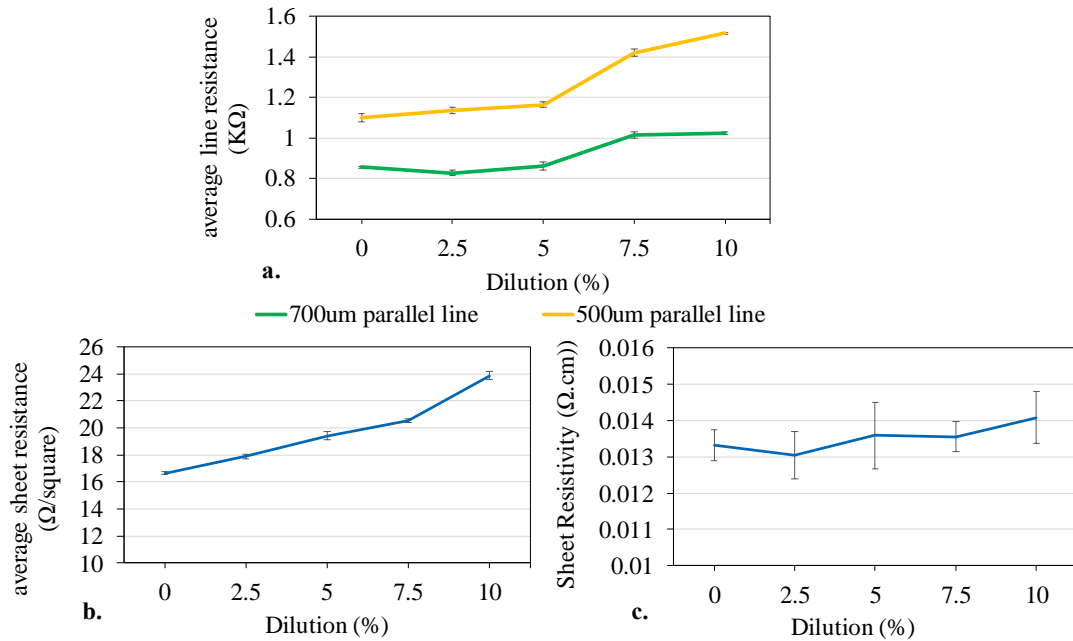


Figure 6.15 Average line resistance for the 500 μm and 700 μm lines (a), as well as average sheet resistance (b) and sheet resistivity (c) of the printed squares conducted on the DEK 248 Screen printer for the printed carbon inks diluted between 0 wt% and 10 wt%.

6.3.4.2. Carbon morphology and loading study

As with the prints conducted on the rig, there were significant increases in the film thicknesses of the 500 μm and 700 μm lines, as well as the printed square with increases in the percentage of the carbon mass in the inks (Figure 6.16 (a), Figure 6.17 (a) and Figure 6.18). However, there was a reduction in the line width of the 500 μm and 700 μm lines produced with increases in carbon concentrations for all morphologies, leading to less significant increases in the overall amount of ink deposited (Figure 6.16 (a)).

There were also changes in the average surface roughness (Sa) of the prints produced with different carbon morphologies and loadings (Figure 6.17 (b)). For the graphite-based inks, there was a gradual increase in the average surface roughness (Sa) of the prints. With increases from 15 wt% to 25 wt% loading leading to increases in Sa from 1.77 μm to 2.86 μm respectively. For the GNP based inks, there were relatively little changes in the Sa, going from 0.61 μm at 15 wt% loading, to 0.78 μm at 20 wt% loading, then to 0.73 μm at 25 wt% loading. The carbon black-based inks had a relatively small difference between the Sa of the 10 wt% and 15 wt% loaded

inks, with roughness's of 0.26 μm and 0.34 μm respectively. This then increased to 0.71 μm at 20 wt% due to the high viscosity of the ink leading to mesh marking, shown in Figure 6.18 (f).

The graphite-based inks have a consistently greater Sa than the other morphologies. This is due to the relative size of the graphite flakes which are far bigger than the GNPs and carbon black particles, as well as the orientation of the graphite flakes (Figure 6.19). For both 15 wt% and 25 wt% loading, the flakes are shown to be deposited in a random orientation, ranging between 0° and 90° to the planer of the substrate, as shown in the SEM images (Figure 6.19 (a and b)). Similar results were found for the GNP based inks, where both 15 wt% and 25 wt% loadings showed the GNPs to be well dispersed and lying at a range of orientations (Figure 6.19 (c and d)). However, both the 15 wt% loaded graphite and GNP based inks displayed more binder between the flakes and nanoplatelets than in the 25 wt% loaded inks.

The carbon black-based inks displayed the most significant reduction in the amount of binder insulating particles from each other, as shown in Figure 6.19 (e) and (f). In the 10 wt% carbon black-based ink, the carbon black particles are all surrounded by resin, insulating agglomerates of carbon black particles from each other. Whereas the 20 wt% ink displayed most particles interacting with one another, with small patches of resin across the surface, leading to more electrical connections, as shown in Figure 6.19.

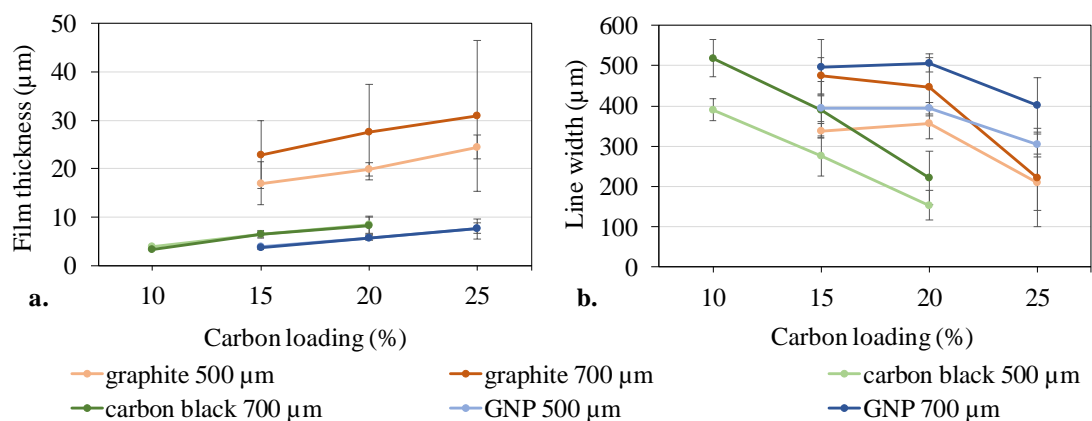


Figure 6.16 Average film thickness (a) and line width (b) of the 500 μm and 700 μm lines produced by the ethyl cellulose-based carbon inks containing different carbon morphologies and different loading ratios. (error bars for standard deviation)

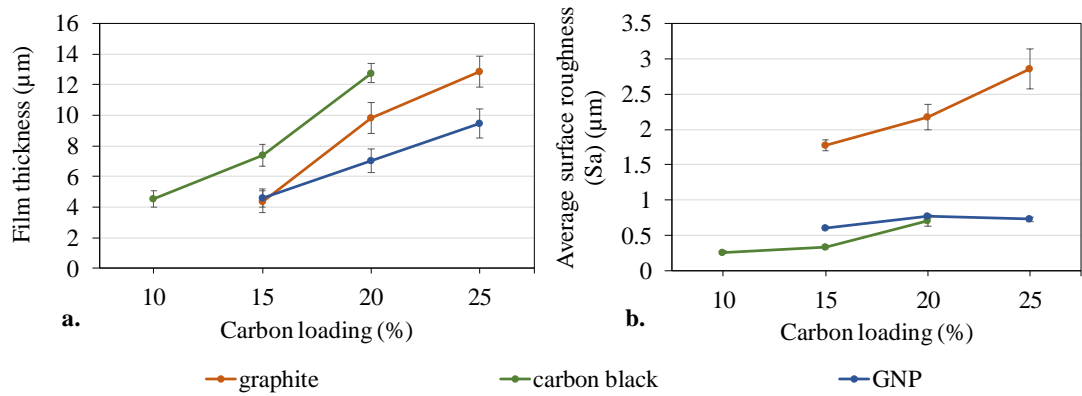


Figure 6.17 Average film thickness (a) and average surface roughness (S_a) (b) of the printed squares produced by the ethyl cellulose-based carbon inks containing different carbon morphologies and different loading ratios. (error bars for standard deviation)

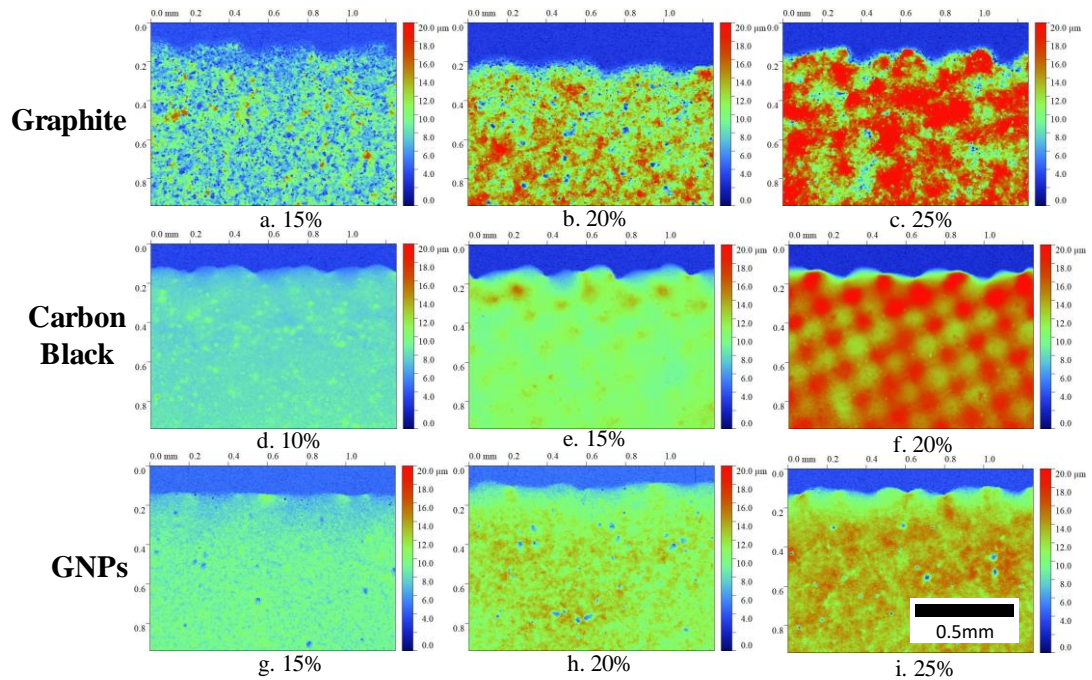


Figure 6.18 White light interferometry topography images of the printed solid area conducted on the DEK 248 Screen-printer, for the ethyl cellulose-based inks containing 15 wt% (a) and 25 wt% (b) graphite, 15 wt% (c) and 25 wt% (d) GNPs, as well as 10 wt% (e) and 20 wt% (f) carbon black at 5 times magnification.

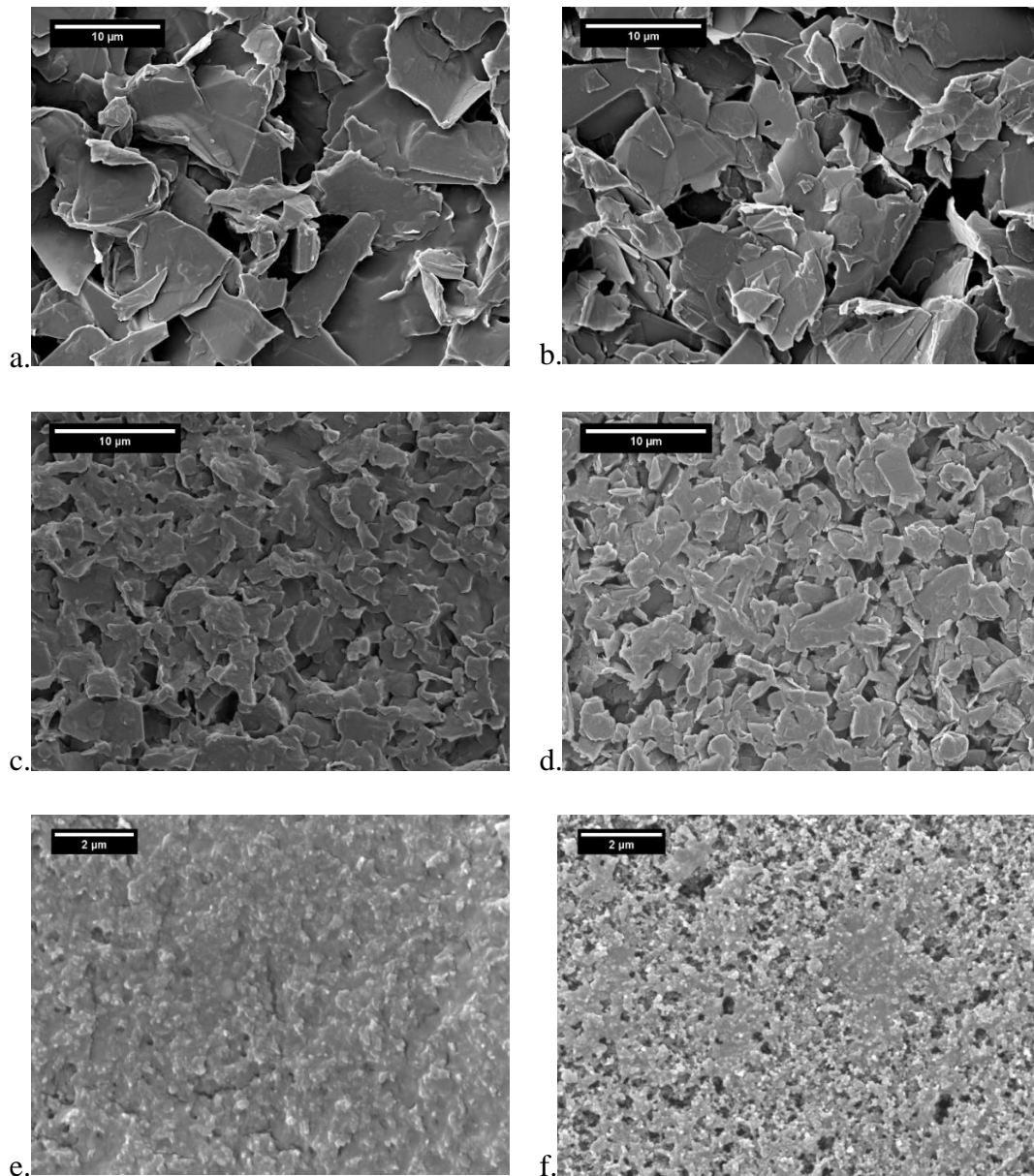


Figure 6.19 Scanning Electron Microscope (SEM) images showing the microstructure of the ethyl cellulose-based inks containing 15 wt% graphite (a), 25 wt% graphite (b), 15 wt% GNPs (c) and 25 wt% GNPs (d) at 3,000 times magnification. As well as the inks containing 10 wt% carbon black (e) and 20 wt% carbon black (f) at 10,000 times magnification.

The electrical characterisation of the prints conducted on the commercial press for the different carbon morphologies and loadings are shown in Figure 6.20. Displaying the average line resistance for the 500 μ m and 700 μ m lines (a), as well as the average sheet resistance (b) and sheet resistivity (c) of the printed squares. Both the line and sheet resistances of the carbon-black based inks were found to be the most

conductive, followed by the graphite-based inks, with the GNP based inks producing the highest line and sheet resistances for all loading percentages assessed.

For the carbon black based inks, there was no significant difference between the line resistances produced for the 10 wt% and 15 wt% loading with the 500 μm line but saw a slight reduction from 30.5 $\text{k}\Omega$ to 26.0 $\text{k}\Omega$ for the 700 μm line. Both line widths then saw an increase in line resistances between 15 wt% and 20 wt% loading, rising to 35.3 $\text{k}\Omega$ for the 700 μm line. There was a gradual reduction in the sheet resistance with increases in carbon-black loading, from 0.30 $\text{k}\Omega/\text{square}$ at 10 wt% loading, to 0.21 $\text{k}\Omega/\text{square}$ at 15 wt% loading, then to 0.16 $\text{k}\Omega/\text{square}$ at 20 wt% loading. When film thickness was accounted for, there was a slight increase in the sheet resistivity from 0.14 $\Omega\cdot\text{cm}$ at 10 wt% loading, to 0.16 $\Omega\cdot\text{cm}$ at 15 wt% loading, followed by a larger increase to 0.21 $\Omega\cdot\text{cm}$ at 20 wt% loading. Therefore, both the 15 wt% and 20 wt% concentrations are within the range of optimal concentrations of carbon black for electrical performance, with 15 wt% plateauing at the lowest resistance values. Where further increases in carbon concentration to 20 wt% led to reductions in performance due to it causing reductions in print quality as shown in the topography images.

For the GNP based inks, there was a significant reduction in the line resistance of both the 500 μm and 700 μm lines between 15 wt% and 20 wt% loading, reducing from 1384 $\text{k}\Omega$ to 180 $\text{k}\Omega$ for the 700 μm . But there was no significant difference between the line resistance of the 20 wt% and 25 wt% loaded inks for either line width as the resistance plateaus. This is due to the optimal GNP concentration for electrical pathways having been reached, with further increases having no significant effects on electrical performance. Likewise, sheet resistance saw a significant reduction between 15 wt% and 20 wt% loading, from 7.35 $\text{k}\Omega/\text{square}$ to 1.88 $\text{k}\Omega/\text{square}$, followed by a smaller reduction to 1.31 $\text{k}\Omega/\text{square}$ at 25 wt% loading. Similar trends were still shown after film thickness was accounted for, with resistivity significantly reducing from 3.38 $\Omega\cdot\text{cm}$ at 15 wt% loading to 1.32 $\Omega\cdot\text{cm}$ at 20 wt% loading, followed by a less significant reduction to 1.25 $\Omega\cdot\text{cm}$ at 25 wt%.

For the graphite-based inks, the 20 wt% loaded ink was found to produce the lowest line resistance and the 15 wt% loading was found to produce the highest line resistance for both the 500 μm and 700 μm lines. The line resistance of the 700 μm

line was found to reduce from 368 k Ω at 15 wt% loading to 102 k Ω at 20 wt% loading, then increase to 137 k Ω at 25 wt%. The sheet resistance also saw a significant reduction between 15 wt% to 20 wt% loading, from 2.77 k Ω /square to 0.76 k Ω /square. However, this was followed by a further reduction in resistance, to 0.58 k Ω /square at 25 wt% loading. The 20 wt% was the best loading percentage out of those tested, with lower concentrations having insufficient conductive pathways and further increases leading to reductions in print quality without increasing the number of pathways. A similar trend was shown when the film thickness was accounted for, with resistivity reducing from 1.19 Ω .cm at 15 wt% loading, to 0.74 Ω .cm at 20 wt% loading, but with no change at 25 wt% loading which also had an average sheet resistivity of 0.74 Ω .cm.

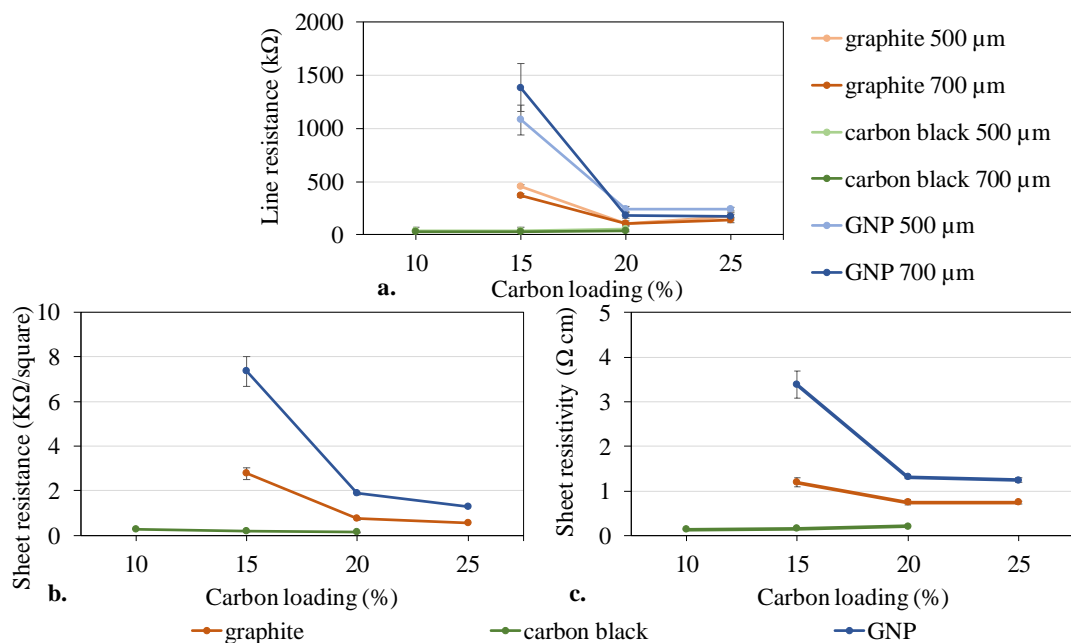


Figure 6.20 Average line resistance for the 500 μ m and 700 μ m lines (a), as well as average sheet resistance (b) and sheet resistivity (c) of the printed squares conducted on the DEK 248 Screen printer for the ethyl cellulose-based carbon inks containing different carbon morphologies and different loading ratios. (error bars for standard deviation)

6.4. Discussions

The higher viscosity inks (<5 wt% diluted) containing less of the solvent thinner exhibited all four stages. Consisting of the ink adhering to the mesh, then extending between the mesh and substrate as one continuous body of ink followed by filaments

of ink separating off from the main body of ink behind the squeegee, which subsequently necked and separated. However, the inks diluted with 5 wt% and 10 wt% thinner did not show any sign of filamentation. Where the ink fully separated at the back of the body of ink being extended between the mesh and substrate.

This is due to the increase in interparticle distance with increasing dilution concentration which resulted in less particle-particle and particle-polymer interactions which result in the storage of elastic energy. This resulted in more liquid like behaviour which enabled the dilutions to separate after a shorter full contact region. The 5 wt% and 10 wt% dilutions spitted fully after the extension zone, rather than split off into filaments while remaining in simultaneous contact with both the mesh and substrate over a greater distance behind the squeegee. This was the case for the higher viscosity, more elastic undiluted ink and 2.5 wt% dilution, which had a similar δ . Resulting in the undiluted ink and 2.5 wt% dilution having a larger full contact region length than the 5 wt% and 10 wt% dilutions.

Although these higher dilutions did have a slightly longer adhesion to extension length up to the separation point. This correspondence between longer adhesion to extension lengths and a lack of filamentation during ink separation was also observed in Chapter 5 when assessing the effect of snap off distance. Where lower snap off distances were found to produce longer adhesion to extension lengths, which enabled the inks to yield at a lower force, typically leading to clean separation without the formation of filaments. In both cases, this may be due to the elastic response of the ink. With the greater snap off distances subjecting the ink to larger snap speeds, which is a product of horizontal print speed and snap off distance, as the horizontal distance remained constant while separating the ink over a larger distance.

However, the 7.5 wt% dilution did not follow this trend, producing some filaments during separation. Although these were significantly less frequent and occurred for a far shorter distance after the extension stage than those produced during the separation of the 2.5 wt% dilution and undiluted ink. As well as this, the full contact distance was still shorter than that of the 5 wt% dilution with the short distance of filaments forming occurring alongside a shorter adhesion to extension length than those produced by the 5 wt% and 10 wt% dilutions.

For the study assessing the effect of carbon morphologies and their loading concentrations, the plain resin exhibited all four of Messerschmitt's stages of ink separation, although the filaments appeared to exhibit a domino effect, with the majority flowing into the next forming filament rather than necking and separating.

The graphite-based inks behaved most like the resin, with all four stages of separation present and of similar lengths to those produced for the deposition of the resin. The lower graphite concentrations also exhibited this domino effect in the filaments forming prior to separation. The carbon black-based inks showed significant deviations from the deposition profile of the plain resin. As well as notable changes in the deposition stages with changes in the weight percentage of carbon black in the inks. The ink containing 15 wt% carbon black was found to produce the largest average adhesion to extension stage lengths with no flow to separation stage. The ink remained in simultaneous contact with mesh and substrate over a long length, until producing a clean separation between the two without forming any filaments. The 20 wt% carbon black ink had an average adhesion to extension stage length, but the largest flow to separation stage length out of the nine inks, producing multiple filaments which gradually separated over a long length. While the ink containing 10 wt% carbon black exhibited a short flow to separation stage and slightly longer adhesion to extension stage than the 20 wt% loaded ink, producing the shortest overall separation length of the three concentrations of carbon black inks assessed. The GNP-based inks also showed deviation from the separation profile of the resin. As with the 15 wt% carbon black ink, the 15 wt% and 20 wt% GNP-based inks also exhibited a clean separation behind the adhesion to extension stage with no filament's formations, although these adhesion to extension lengths were shorter.

The interactions of the small carbon black particles had the most significant effect on the separation profiles out of the morphologies assessed. This also corresponds with the shear and extensional rheology tests, where carbon black led to significant increases in the elasticity of the ink and at 20 wt% loading, took longer to separate in CaBER tests than the other inks. To the extent where it would sometimes neck into a point and then remain connected. In the dilution study of the commercial ink containing graphite and carbon black, the dilution of the carbon black particles may have been the main cause of the change in the separation profile.

The prints produced both on the visualisation rig and the DEK 248 screen printing presses found that higher solid contents of carbon typically led to increases in the amount of ink deposited.

However, for the carbon concentration and loading study, the widths of the printed lines were found to reduce with increases in the carbon loading. This is most likely due to increases in the carbon loading leading to increases in the ink viscosity. This would cause the inks to flow less after deposition, leading to narrower lines.

Although there was still an overall increase in the cross-sectional area of ink deposited.

There was also an increase in the surface roughness of the graphite-based ink with increases in loading. This is due to the geometries, particle interactions and random orientation of the graphite flakes in the inks. Although there was no significant change in the roughness of the GNP-based inks and only a significant increase in the roughness of the carbon black-based inks between 15 wt% and 20 wt% loading which was due to the presence of mesh marking as the particles formed agglomerates. The graphite-based inks had the greatest roughness for all concentrations due to the relatively large size of the flakes. Therefore, increases in the mass of flakes lead to increases in film thickness along with increases in roughness due to the random orientations of stacks of flakes. The carbon black-based inks had the lowest roughness's as the particles were significantly smaller than the other morphologies. Increasing the mass of carbon black particles had relatively little effect on the print roughness, until 20 wt% loading. At which point the optimal loading had been exceeded and mesh marking had started to appear due to the high viscosity of the ink.

When comparing the print topography profiles with the ink separation stage lengths, the greater cross-sectional areas of ink deposited corresponded with longer overall lengths of the flow to separation stages in the screen-printing process as well as higher ink viscosities. The electrical performance was typically proportional with the quantity of ink deposited, where greater deposits led to lower resistances. For both the graphite and GNP-based inks, there was a significant reduction in electrical performance between 15 wt% and 20 wt%, but little improvement with further increases. Therefore, at 15 wt%, there were insufficient particles interacting to form

enough conductive pathways. At 20 wt% there are sufficient conductive pathways between the graphite flakes or GNPs. Further increases led to increases in surface roughness and greater numbers of filaments forming during ink separation, resulting in worse print quality and reductions in electrical performance. There were sufficient conductive pathways across the carbon black prints for all concentrations assessed, leading to less significant changes in the electrical performance of the carbon black inks. The 15 wt% ink was found to be the point where improvements in electrical performance with carbon concentration plateaued. Further increase to 20 wt% leading to reductions in print consistency which in turn led to increases in line and sheet resistance as well as sheet resistivity.

Overall, these findings show that changes in the carbon concentration and morphologies, with resultant changes in the viscosity and viscoelasticity profiles, had notable effects on the deposition mechanisms occurring. As well as on the print topography and electrical performances of the prints produced. Where different carbon morphologies have different rheological profiles, with carbon black producing more elastic, highly viscous inks which can lead to features such as mesh marking in high concentrations. Therefore, optimal loadings of the carbon morphologies must be identified to compromise between conductivity and print topography.

6.5. Conclusions

These studies have used high-speed imaging to identify the effect of altering the carbon morphologies and concentrations in carbon-based screen-printing inks on the deposition and separation mechanisms in screen printing.

The results correlated with the deposition theory by Messerschmitt. However, the final two stages of Messerschmitt's ink deposition theory, where the ink between the mesh and substrate formed filaments which gradually led to necking and separation, were not present in all inks assessed. This was the case for the inks which were diluted by 5 wt% or 10 wt% solvents in the dilution study and for the inks containing low concentrations of GNPs or 15 wt% of carbon black. Whereas the inks containing higher carbon concentrations and all of the graphite-based inks displayed all four stages of separation.

The lengths of the flow to separation stages, where filamentation occurs, were found to correspond with the quantity of ink deposited. Overall, inks containing higher weight concentrations of carbon particles and flakes were found to deposit greater quantities of ink. This led to reductions in line and sheet resistances.

Altering the carbon morphologies and concentrations of carbon-based screen-printing inks can alter the lengths of the separation stages occurring in screen printing.

Chapter 7. Effect of photonic flash-annealing with subsequent compression rolling on the performance of carbon-based inks

7.1. Introduction

The previous chapters have investigated the effect of ink mixing, ink formulation and parameter optimisation on print quality and performance. However, further improvements in the print performance of carbon-based inks can be achieved after the printing.

This chapter focusses on post processing methods which can lead to electrical performance enhancement for a range of carbon-based inks. There have been a range of studies conducted into identifying the effects of modifying the ink formulations of graphite and carbon black based inks on enhancing the print quality and electrical performance. However, despite these improvements, significant gains in conductivity might not be possible through formulation alone due to trade-offs between particle loading and printability. In the case of altering the ratios of different carbon forms, the small carbon black particles were able to fill the gaps between the large graphite flakes (26). Therefore, identifying post processing methods which could be used to reduce the physical size of these gaps, rather than altering the print formulation, might also help drive further improvements to the print performance. This could enable print topography and conductivity to be enhanced without changing the ink formulation, as changing the formulation could compromise the quality of dispersion, shelf-life and print performance. From an electrochemical perspective, the binders in inks can block the active surfaces and thus result in slower reaction kinetics (16). Therefore, utilising methods capable of reducing the

binder in the print without compromising the print performance are desirable. Post processing methods which have shown promise in literature include photonic flash annealing followed by subsequent compression rolling.

Photonic methods, in the form of intensive pulsed light (IPL) sintering and annealing, have been used to provide a rapid burst of high energy to heat materials such as metal nanoparticles, copper oxide and carbon morphologies such as graphene. This allows them to sinter and become more conductive. It can also selectively heat the print to high temperatures without damaging low cost substrates, such as polymer films or paper (48,49). This provides opportunities for low cost electronics printed onto polymers and has already been used for a range of applications including RFID (radio frequency identification) tags and photovoltaic applications.

Despite improvements in electrical performance, photonic annealing also resulted in a reduction in layer adhesion and cohesion. Compression rolling could be used after photonic annealing to improve the structural integrity of the prints, as well as provide further improvements in the electrical performance. This also enables reductions in the print film thickness and roughness. Compression rolling alone has also been investigated as a possible post processing method for a range of applications, to improve the electrical and thermal conductivity of devices by improving the flake alignment.

The analyses conducted in the literature assessed the effect of photonic annealing and compression rolling on single morphologies of carbon or copper. However, these processes could also provide an effective method for improving the electrical performance of inks containing a range of carbon morphologies, without having to change the ink formulations.

Therefore, this chapter investigates the effect of photonic annealing and compression rolling on inks containing a range of common, low cost forms of carbon. Inks were made with the following carbon morphologies dispersed in solvent and polymeric binder: 1) graphite only, 2) graphite nanoplatelets (GNPs) only and 3) graphite with carbon black. The inks were manufactured, screen printed, thermally dried then post treated. The effects of post treatment were established using topography and resistance

measurements of both printed solid areas and printed lines, as well as SEM (scanning electron microscopy) imaging after each of the stages. Thermogravimetric Analysis (TGA) tests were also conducted to establish the equivalent temperatures and durations required to remove the binder using traditional thermal drying methods.

The effect of compression rolling on inks containing binder in comparison to those which have had their binder removed has also not been fully assessed. To establish whether the removal of binder is required to enable optimisation of print conductivity, the graphite only ink was used to assess the effect of compression rolling both with and without prior photonic annealing. These methods could provide a feasible technique for enhancing the print consistency and conductivity of low-cost carbon inks. This could lead to improvements in printed carbon electrodes for a host of devices, without increasing the cost or practicality of the ink formulation.

7.2. Materials and Methods

7.2.1. Ink formulation

Inks with graphite only, graphite nanoplatelets (GNP) only and a combination of graphite with carbon black were made for the study. Materials used were as follows: graphite (Timrex® SFG15, Imerys Graphite and Carbon; typical D90 17.9 μm according to manufacturer); carbon black (TIMCAL ENSACO™ 250G Conductive Carbon Black Compounds; with diameter distribution from 20 to 50 nm and specific surface area of 65 m^2/g according to the manufacturer) and graphite nanoplatelets (GNPs) functionalised with oxygen (GNP-O₂ produced by Haydale Ltd. with average flake diameter around 5 μm). All inks used the same vinyl resin base (with 15% by weight dry polymer, VINNOL (Wacker Chemie AG) in 4-hydroxy-4-methylpentan-2-one (H41544 Aldrich, Sigma–Aldrich)) (as used in Chapter 3) but with different loadings to suit processing and printing characteristics.

The graphite and GNP based inks were produced with 22.5 % carbon concentrations (i.e. 22.5 % carbon and 77.5 % polymer dispersion by mass) as this was found to produce a good compromise between print quality and conductivity. Higher particle loadings were found to produce thicker and rougher print films with minimal improvements in line and sheet resistance and increases in resistivity. The ink

containing a combination of carbon black and graphite was formulated based on optimal loading and ratios described previously by Phillips *et al.*(26): 29.4% carbon concentration, with 2.6 parts graphite to 1 part carbon black. The mass contents of all inks are described in Table 7.1. When making the inks, the carbon materials were gradually added to the pre-made resin and stirred in by hand, with the carbon black added before the graphite in the case of the graphite and carbon black ink. The ink slurries were then left to wet overnight before three roll milling. Milling was conducted with an EXAKT80E three roll mill (EXAKT Advanced Technologies GmbH) with the same processing conditions used for all inks, as presented in Table 7.2. Mixing was then conducted prior to printing using a Speedmixer (Speedmixer™ DAC 150.1 (FVZ-K)), for 5 minutes at 2500 rpm.

Table 7.1 Ink formulations for graphite, GNP and combined graphite and carbon black-based inks.

Inks	Dry resin %	Solvent %	Graphite%	Carbon Black %	GNP %
Graphite based ink	11.6	65.9	22.5	-	-
GNP based ink	11.6	65.9	-	-	22.5
Graphite and Carbon Black based ink	10.6	60	21.3	8.1	-

Table 7.2 Triple roll mill settings

Pass number	Band Gap (µm)	Front Gap (µm)	Speed (rpm)
1	60	15	200
2	40	10	200
3	20	5	200

7.2.2. Printing Methodology

Printing was carried out on a DEK 248 flatbed screen printing machine using a polyester mesh with 61 threads per cm, 64 µm thread diameter and 13-micron

emulsion, 2 mm snap-off, 65–70 Shore A hardness diamond squeegee of 130 mm length with a 12-kg squeegee force and print/flood speeds of 70 mm s⁻¹. The substrate was PET (polyethylene terephthalate—Melinex® 339, DuPont Teijin Films (175 µm thickness) opaque white). The print image included a series of 25-mm-long lines of nominal widths from 100 µm to 700 µm and a 45-mm square solid patch for sheet resistance assessment. Printed samples were dried in a conveyor dryer at 100°C for 4 minutes as this had been found sufficient for drying the samples and removing solvents from the print.

7.2.3. Print characterisation before and after processing

Print topography, microscopy analyses and electrical characterisation were conducted after printing and after each stage of post processing. White light interferometry (NT9300, Veeco Instruments, Inc., Plainview, NY, USA) was used to measure a full three-dimensional surface profile over the edge of the solid print so that the printed ink film thickness could be evaluated. 5 times magnification was used, giving a measurement area of 1.2 mm by 0.93 mm (at a resolution of 736 × 480 pixels with sampling at 1.67 µm intervals). The ink film thickness was calculated as the average height of the substrate subtracted from the average height of the ink, excluding the print edges where there tended to be a lip or a decline in ink film thickness depending on the print orientation. A total 36 measurements were taken for each ink type/processing combination. This was obtained over three print samples with 12 evenly spaced points around the perimeter of the printed square for each print. Average surface roughness measurements (Sa) over the printed area were also taken away from the edges. The microstructures of the prints were also assessed, using a JEOL JSL 7800F FEG Scanning Electron Microscope (SEM) at 3000 times magnification.

Printed line geometry was also assessed at five times magnification with the white light interferometer. 700µm nominal width lines were each measured in 3 evenly spaced points. Geometric features were assessed by taking discrete measurements over the 1.2-mm-length sections measured by the interferometer (736 measurements at 1.67-µm intervals for each measured section). From this the standard deviation in line width and thickness was calculated.

Sheet resistance measurements were conducted on the printed 45x45 mm squares using a 4-point probe method. A SDKR-13 probe (NAGY Messsysteme GmbH) with a tip distance of 1.3 mm was used with a Keithley 2400 digital Sourcemeter, with subsequent conversion to sheet resistance using the appropriate correction factor from the data table proposed by Smits (124). Sheet resistances are displayed as measured (with the correction factor) and, to account for the variation in film thickness after post processing, resistivities were also calculated as the product of sheet resistance and ink film thickness. A total of 12 sheet resistance values were taken across the centre of each printed square to account for any deviation in print quality or effects of compression across the area. Line resistance was measured using the same multimeter in two-point mode for 700 μm nominal width lines. These measurements were conducted on three samples from each of the print runs to obtain averages and standard deviations.

7.2.4. Post Processing – photonic annealing and compression

Photonic annealing was performed using a PulseForge® 1200 (NovaCentrix, Austin, TX, USA). A preliminary study was used to optimise voltage, pulse pattern and duration to produce the greatest improvement in conductivity in the prints. The pulse envelope of 2000 μs in length and 260 volts was used to provide a total energy of 1.10 J/cm^2 to the samples. A single pulse of high energy resulted in catastrophic ablation and delamination of the print due to rapid gasification of binders within the ink. Therefore, an envelope comprised of 10 micro pulses and a duty cycle of 80 % of total energy was used to raise the temperature of the printed features more gradually to remove the binders in a more controlled manner.

Using NovaCentrix's SimPulse thermal simulation package, the peak temperature of the ink during photonic annealing was estimated to be 307°C. This was based on measured layer thickness and a database of thermal characteristics of the materials. As the carbon-based prints were black and the PET substrate was opaque white, light absorbance in the visible spectrum was far greater for the print than it was for the substrate. This allowed the PulseForge to selectively heat the printed features to a high temperature whilst the unprinted area remained below its glass transition temperature and was not distorted.

Compression rolling was performed using a Durston DRM 150 Rolling Mill (W Durston Ltd, UK). The compression pressure could not be directly measured but was manipulated by setting the gap between the rollers. Gap sizes from 0.05mm to 0.25mm were assessed and a gap size of 0.125mm was found in preliminary studies to generate the greatest improvement in conductivity without causing warpage of the substrate.

To evaluate the relative effects of photonic annealing followed by compression and compression alone, samples of printed graphite ink were also compression rolled without prior photonic annealing.

7.2.5. Thermogravimetric analysis of ink and binder

Thermogravimetric analysis (TGA) was used to provide an indication of the temperatures required to reduce the amount of binder in the inks using thermal treatment. Samples of the resin binder (15% polymer by mass) and graphite ink were analysed. Testing was carried out by a Perkin Elmer STA 6000 with a temperature ramp to 500°C, over the duration of 50 minutes (10°C/min) in a nitrogen atmosphere.

7.3. Results

7.3.1. Topography and microstructure of printed solid squares

Topographies of the prints for the various ink systems are shown before and after photonic annealing with subsequent compression rolling in Figure 7.1. The resulting film thickness and surface roughness data are shown in Figure 7.2 and scanning electronic microscope images of the surfaces are shown for graphite only, GNP only and graphite-carbon black in Figure 7.3, Figure 7.4 and Figure 7.5 respectively. Summary data is also provided in Table 7.3 together with data for graphite print compression only. For all inks, the print surface was relatively rough after thermal drying alone, with evidence of features such as voids, agglomerations and ‘mesh marking’ due to the interaction of the ink with the mesh during deposition (Figure 7.1 images a to c). The features of mesh marking correspond with the frequency of the mesh used (61 threads per cm) and are more prevalent in higher viscosity inks which do not settle and slump after deposition, as was the case with these inks.

7.3.1.1. Graphite only ink

Prior to post processing, the graphite ink had the highest ink film thickness at 9.8 μm and average surface roughness of 2.8 μm (Figure 7.2), with signs of mesh marking, agglomerations and pinholes. This high surface roughness is due to low frequency effects from the mesh but also the relatively large graphite flakes seemingly randomly orientated in the print. Flakes were orientated at a range of angles, between 0° and 90° to the horizontal axis, with large gaps between flakes and only small sections of the flakes in contact with neighbouring flakes, as shown in the SEM images (Figure 7.3 (a)). When the graphite ink prints were compression rolled directly after thermal drying, there was a reduction in both film thickness and average surface roughness, down to 6.2 μm and 0.9 μm respectively. The SEM images (Figure 7.3 (b)) demonstrate that compression rolling alone resulted in a significant increase in the area of the flakes in contact with one another, with flakes becoming aligned with the horizontal plane and filling in gaps between flakes. However, some gaps between flakes remained.

Prior to compression, the graphite ink prints that were photonic annealed, showed an initial increase in film thickness and surface roughness up to 13.5 μm and 3.2 μm respectively. These increases corresponded with a change in microstructure as shown in the appropriate SEM image (Figure 7.3(c)). As with the print which had been thermally dried only, the flakes were seemingly randomly orientated with only small areas of graphite flakes in contact with their neighbours. However, after photonic annealing there were more flakes aligned towards the vertical plane and the texture and edges of the flakes and gaps became more apparent.

When photonic annealing was followed with compression rolling, there was reduction in both average film thickness and surface roughness down to 4 μm and 1.2 μm respectively. These reductions are due to the flakes becoming densely compacted together, as shown in the appropriate SEM image (Figure 7.3 (d)). This was apparent to a greater extent than for prints compression rolled without photonic treatment (Figure 7.4 (b)). This resulted in smaller and fewer gaps between the flakes and alignment of the flakes with the horizontal plane, producing a smoother and thinner print when compared with compression alone.

7.3.1.2. *Graphite nanoplatelet only ink*

Prior to post processing, the GNP ink had an average film thickness and surface roughness of 8.7 μm and 0.8 μm respectively (Figure 7.2). Irregular edges were apparent in the print (Figure 7.1 (b)) but the roughness was the lowest of all the inks due to the smaller size of the GNPs when compared with graphite. As with the graphite flakes, the GNPs in the print were randomly orientated at various angles to the substrate. There was also a relatively large number of voids between the nanoplatelets, as shown in the SEM image (Figure 7.4 (a)). As with the graphite inks, after photonic annealing, there was an increase in both film thickness and surface roughness to 10.3 μm and 1.0 μm respectively. After subsequent compression rolling, this was followed by a reduction in both film thickness and surface roughness to 4.7 μm and 0.5 μm respectively, with significant reductions in mesh marking (Figure 7.1 (e)). SEM images of the photonic then compression treated prints showed that GNPs were aligned to the horizontal axis, lying flat with respect to the substrate (Figure 7.4 (b)). The boundaries between individual nanoplatelets were less clear than they were prior to postprocessing, where gaps between the GNPs appeared smaller.

7.3.1.3. *Graphite and carbon black ink*

The graphite and carbon black based ink had an initial film thickness and surface roughness of 8.3 μm and 1.7 μm respectively (Figure 7.2). Prior to processing, as with the graphite only ink, there were graphite flakes randomly orientated with small areas of the flakes in contact with one another (Figure 7.5). However, the gaps between the flakes were partially filled with carbon black particles. Despite the carbon black acting as a filler material, the samples were relatively rough, with some peaks of the relatively large graphite flakes protruding out of the carbon black matrix. Along with troughs between graphite flakes that were not filled with carbon black. As with the other inks, after photonic annealing only, there was an increase in the film thickness and surface roughness to 11.1 μm and 2.4 μm respectively. Compression reduced both film thickness and surface roughness to 5.9 μm and 0.7 μm respectively. After both photonic annealing with subsequent compression rolling, the graphite flakes became aligned to the horizontal plane with carbon black particles filling in gaps between the flakes, as shown in the SEM image (Figure 7.5 (b)). Despite these improvements, there appeared to be removal of carbon black from around the graphite particles.

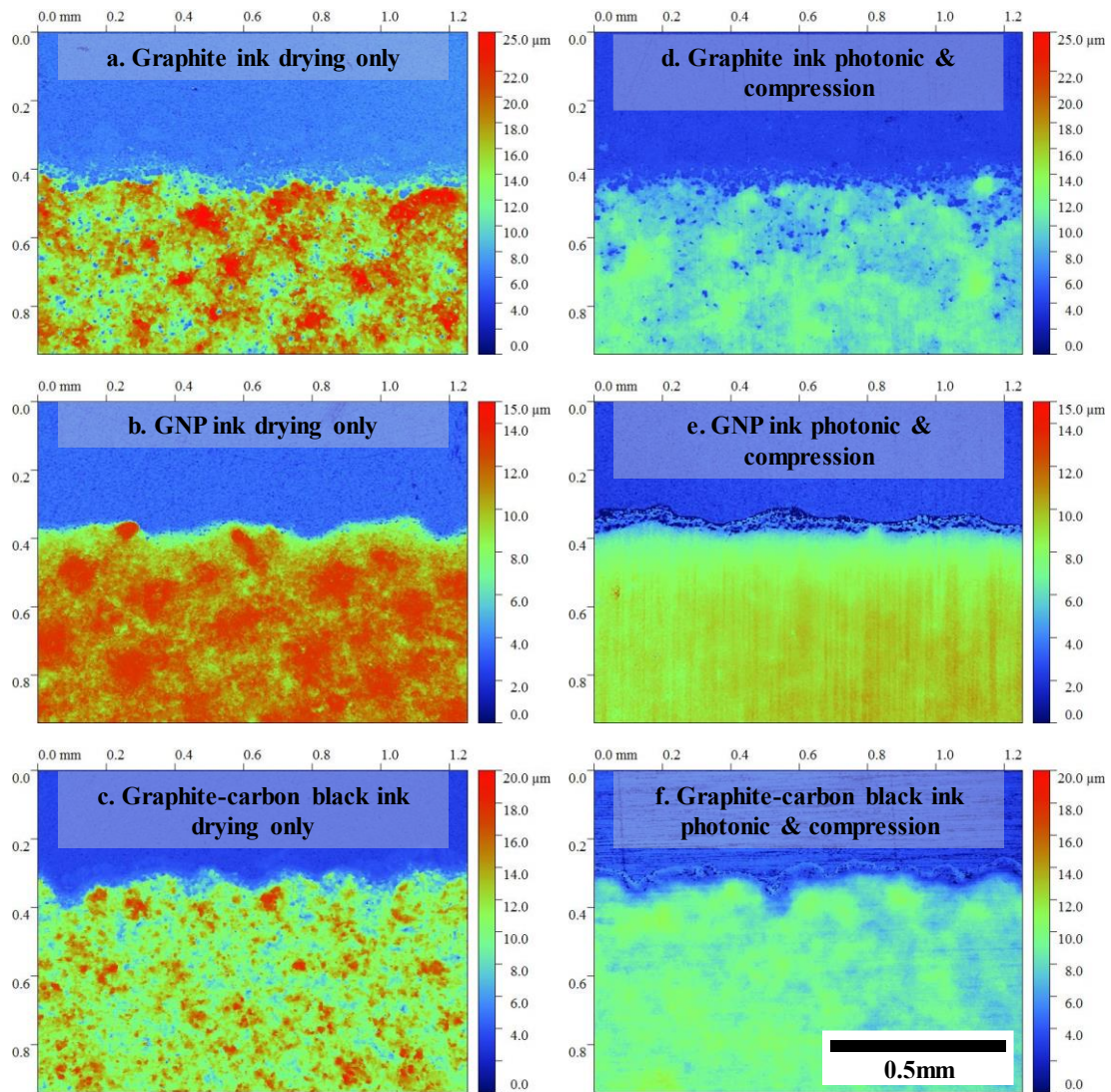


Figure 7.1 White light interferometry images of the edges of the printed squares for the printed graphite, GNP, graphite with carbon black inks both before post treatment (images a to c respectively) and after both photonic annealing and compression rolling (images d to f respectively) at 5 times magnification.

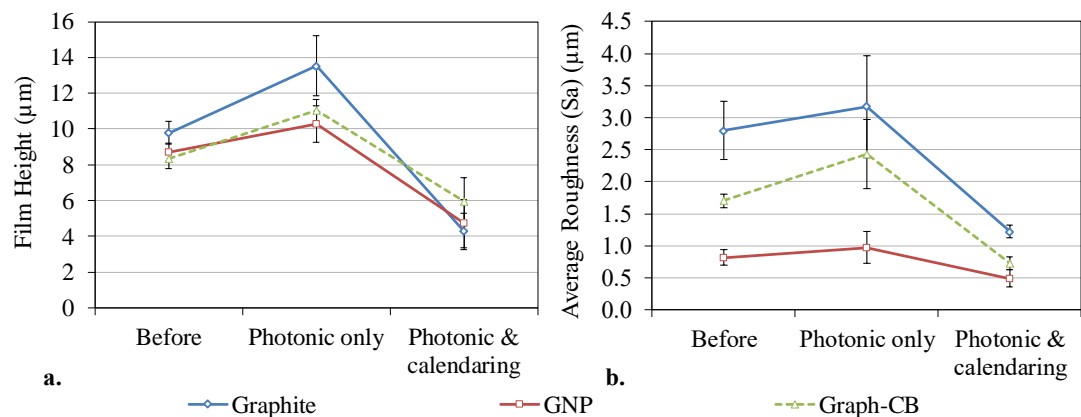


Figure 7.2 Film thickness (a) and Average surface roughness (Sa) (b) for the various inks before and after photonic annealing and compression rolling (error bars show standard deviation).

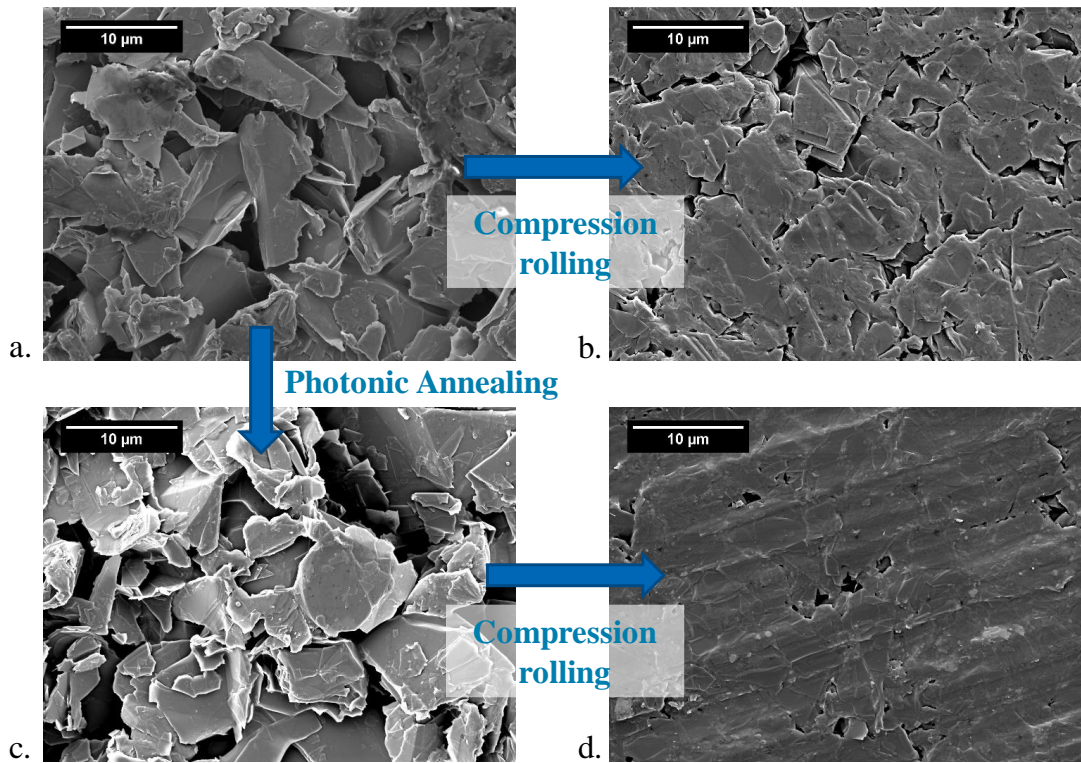


Figure 7.3 Scanning Electron Microscope (SEM) images at 3000 times magnification showing the microstructure of the graphite-based inks which have received no post processing (a), after compression rolling only (b), after photonic annealing only (c) and after both photonic annealing and compression rolling (d).

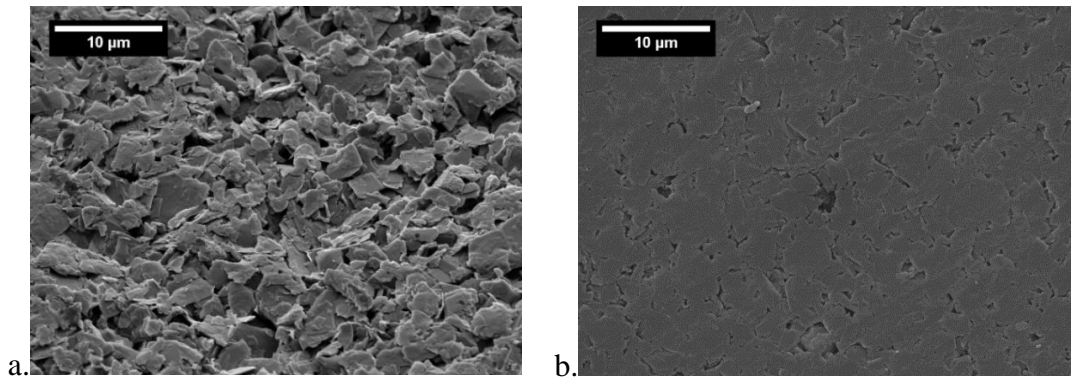


Figure 7.4 Scanning Electron Microscope (SEM) images at 3000 times magnification showing the microstructure of the graphite nanoplatelet (GNP)-based inks which have received no post processing (a) and which have undergone both photonic annealing and compression rolling (b).

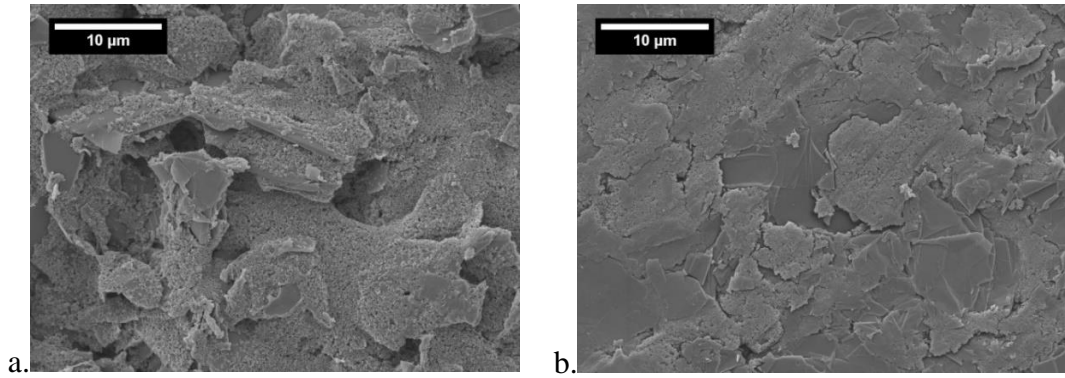


Figure 7.5 Scanning Electron Microscope (SEM) images at 3000 times magnification showing the microstructure of the graphite and carbon black -based inks which have received no post processing (left) and which have undergone both photonic annealing and compression rolling (right).

Table 7.3 Summary of changes in ink film thickness and roughness of solid area data – standard deviation in parentheses.

	Changes in ink film thickness compared with before value (μm) (standard deviation)			Changes in roughness of solid compared with before value ($S_a \mu\text{m}$) (standard deviation)		
	Graphite	GNP	Graphite - CB	Graphite	GNP	Graphite - CB
Before	9.78 (0.64)	8.68 (0.51)	8.33 (0.57)	2.80 (0.46)	0.82 (0.12)	1.70 (0.11)
Compression only	-3.57 (1.20)	-	-	- 1.90 (0.2)	-	-
Photonic only	+ 3.75 (1.69)	+ 1.61 (1.01)	+ 2.73 (0.61)	+ 0.37 (0.80)	+ 0.15 (0.25)	+ 0.73 (0.54)
Photonic then compression	- 5.51 (1.01)	- 3.97 (1.34)	- 2.39 (1.32)	-1.58 (0.10)	- 0.33 (0.14)	- 0.98 (0.10)

7.3.2. Sheet Resistance of printed squares

Sheet resistance and resistivity are compared before and after post processing for each of the inks in Figure 7.6 and Figure 7.7 respectively. Summary data is also provided in Table 7.4 with data for graphite print compression only. Sheet resistance is not affected by ink film thickness, but the resistivity values allow for the changing thickness of the ink. The graphite-based ink had an initial resistivity of $1.91 \Omega \text{ cm}$ after thermal drying only and displayed a substantial reduction in sheet resistivity after all post processes. In the case of the prints which were compression rolled directly after thermal drying, there was a reduction in resistivity down to $0.74 \Omega \text{ cm}$. The prints which were photonic annealed underwent a reduction to $0.96 \Omega \text{ cm}$, then after following subsequent compression rolling, there was a further reduction to $0.23 \Omega \text{ cm}$, which represented a resistivity of around 12 % of the initial value. Similarly, sheet

resistance fell from 1.95 k Ω /square to 1.49, 0.71 and 0.55 k Ω /square for compression only, photonic annealing and photonic then compression respectively. These changes are lower in magnitude as they do not take the change in ink film thickness into account. The compression rolling led to an improvement in resistivity due to the increase in contact area between the conductive flakes and particles as they were aligned to the horizontal plane during compression.

The GNP ink had an initial resistivity of 2.37 Ω cm after thermal drying only which was slightly higher than that of the graphite ink. However, the GNP ink also showed a substantial reduction after both photonic annealing and subsequent compression rolling. There was a reduction in resistivity to 1.38 Ω cm after photonic treatment, followed by a further reduction to 0.32 Ω cm after compression rolling. Both post treated resistivities were higher than for the graphite only ink. As with the graphite ink, this is due to the significant improvement in the flatness and contact area between the nanoplatelets. Sheet resistances fell from an initial 2.73 k Ω /square to 1.35 and 0.67 k Ω /square for photonic annealing and photonic then compression respectively.

The graphite and carbon black based ink had an initial resistivity of 0.037 Ω cm which was substantially lower than the graphite and GNP based inks. Post processing only gave a small reduction in sheet resistance at each stage of processing. Compared with the other inks, there was a smaller but still significant improvement in resistivity upon processing, with a reduction in resistivity to 0.019 Ω cm after photonic annealing and subsequent compression rolling. However, there was an increase in resistivity to 0.042 Ω cm after photonic annealing only (although there was a reduction in sheet resistance). This is due to the photonic annealing process causing an increase in surface roughness and therefore average film thickness. Although this increase in film thickness also occurred with the graphite and GNP inks, the reduction in sheet resistance was more significant, thus counteracting this change in thickness. Nevertheless, the subsequent compression rolling led to an overall improvement in the electrical performance, as the graphite flakes were preferentially aligned towards the horizontal plane and the carbon black was compacted into the gaps between the flakes. This led to a greater area of conductive flakes and particles in contact. Sheet

resistances fell from an initial 0.044 k Ω /square (44 Ω /square) to 0.039 and 0.031 k Ω /square for photonic annealing and photonic then compression respectively.

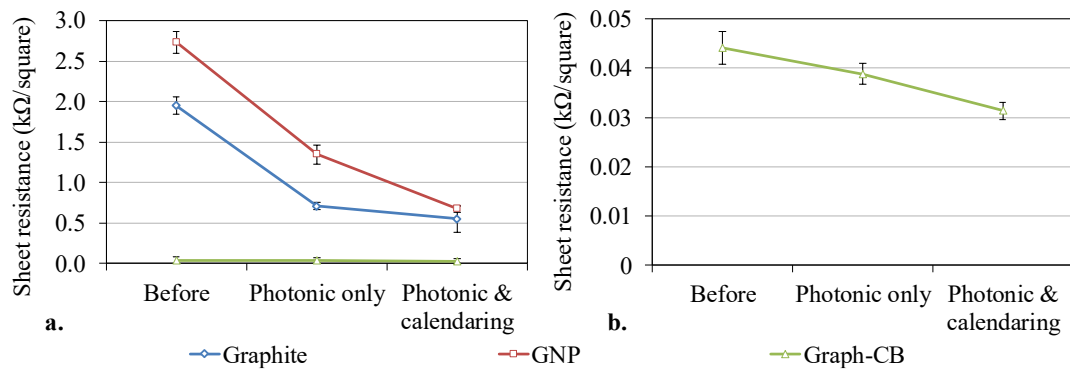


Figure 7.6 Sheet resistance of the printed squares before and after photonic curing and compression rolling for all inks (left) and graphite and carbon black based ink only (right).

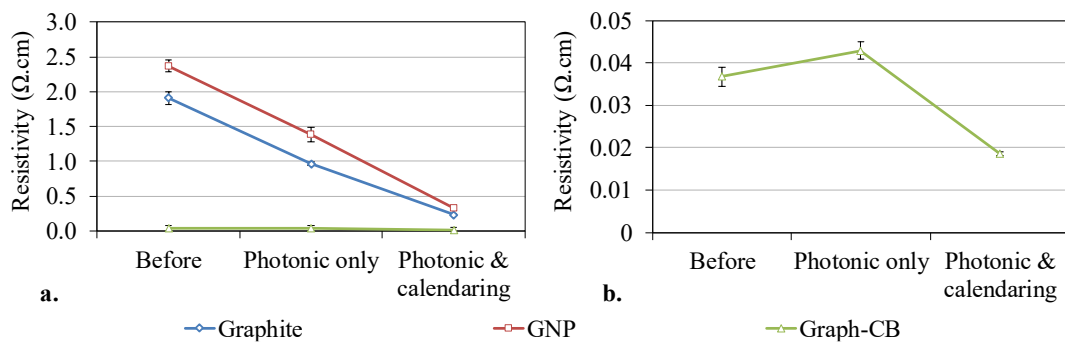


Figure 7.7 Resistivity of the printed squares before and after photonic curing and compression rolling for all inks (left) and graphite and carbon black based ink only (right).

Table 7.4 Summary sheet resistance and resistivity of solid area data – standard deviation in parentheses.

	Sheet resistance (k Ω /square)			Resistivity (Ω .cm)		
	Graphite	GNP	Graphite - CB	Graphite	GNP	Graphite - CB
Before	1.95 (0.11)	2.73 (0.14)	0.044 (0.003)	1.91 (0.09)	2.37 (0.09)	0.037 (0.002)
Compression only	1.49 (0.30)	-	-	0.74 (0.10)	-	-
Photonic only	0.71 (0.04)	1.35 (0.12)	0.039 (0.002)	0.96 (0.03)	1.39 (0.11)	0.043 (0.002)
Photonic then compression	0.55 (0.17)	0.68 (0.04)	0.031 (0.002)	0.24 (0.02)	0.32 (0.004)	0.019 (0.000)

7.3.3. Printed Lines

The film thicknesses produced for the 700 μ m nominal width lines (of 25mm in length) from each of the ink types are shown before and after postprocessing in Figure 7.8. The resulting resistance values are shown in Figure 7.9. The trends in both film thickness and resistance were similar to those produced for the printed squares for all inks. There was an increase in ink film thickness with photonic annealing, followed a reduction due to compression rolling, but line widths did not change significantly. Line resistances fell from 151.6 to 27.2 k Ω for graphite only, 317.6 to 64.9 k Ω for GNPs only and 2.3 to 1.7 k Ω for graphite-carbon black.

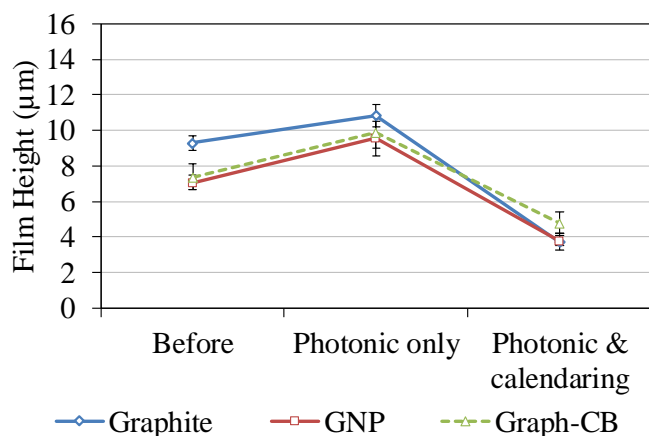


Figure 7.8 Ink film thickness for the printed 700 µm nominal width lines before and after photonic curing and compression rolling.

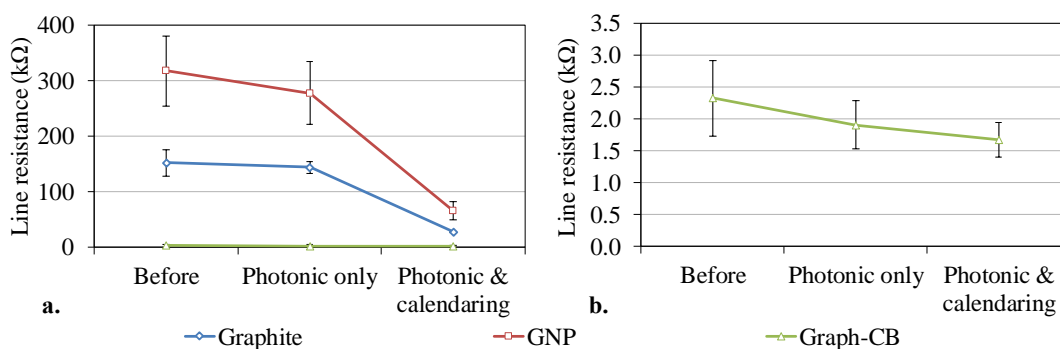


Figure 7.9 Resistance of the printed 700 µm nominal width lines before and after photonic curing and compression rolling for all inks (left) and graphite and carbon black based ink only (right).

7.3.4. TGA analysis of ink and binders

Plots of mass percentage versus temperature from the TGA analysis of the graphite-based ink and binder only are shown in Figure 7.10. Mass loss began gradually from 30°C and accelerated until peaking between 100°C and 200°C. Both the graphite ink and binder alone then showed a plateau in weight loss at 200°C, when the majority of the solvent had been evaporated. This is supported by the 63% mass loss from the ink, which contained approximately 66 % solvent in wet form, and 81% mass loss in the binder which initially contained approximately 85% solvent. At approximately 250°C, the rate of mass loss started to increase before plateauing from around 330°C for the ink and 360°C for the binder. By this point, all of the solvents will have been evaporated off and the observed mass loss most probably represents thermal degradation of the binder.

During thermal drying, a temperature of 100°C was used so that structural damage and warping of the PET substrate did not occur. However, photonic treatment is able to rapidly heat the ink to a high temperature. This is sufficient to decompose the binder without degrading the substrate. The photonic annealing simulation software gave an indicative peak temperature of 307°C which corresponded with a TGA mass loss of 71 and 90 % for ink and dry resin respectively. Although the thermal profiles of the two techniques are dissimilar, this suggests that photonic annealing the prints could lead to a significant reduction in the remaining resin in carbon inks.

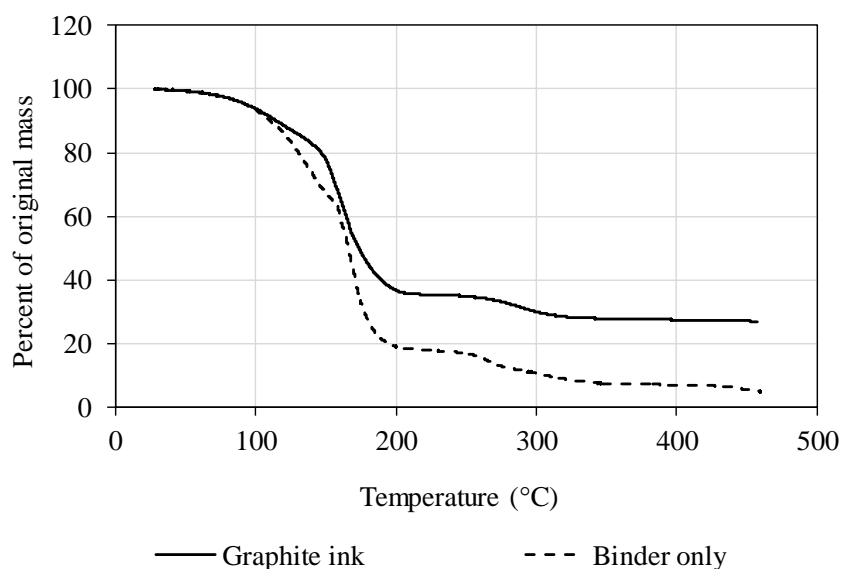


Figure 7.10 TGA Analysis of the graphite ink and binder only up to 500°C.

7.4. Discussions

In the case of the graphite-based ink, reductions in surface roughness, film thickness and resistivity were apparent for both samples which were compression rolled with and without prior photonic annealing. However, more significant improvements were seen for the samples which were photonic annealed with subsequent compression rolling. TGA analysis suggests that photonic annealing is able to reduce the binder in the print. This complements the results by Secor *et al.* which found that photonic annealing was able to reduce the resistance of printed graphene inks by exceeding the threshold temperature required for decomposition of the polymer binder without damaging the substrate, as it was conducted on a short timescale (86). This removal of insulating barriers between the graphite flakes could enable more direct contact

points between the conductive carbon flakes. As well as provide more space for the flakes to be compacted into during compression. Thus, leading to significantly smoother prints with the graphite flakes aligned to the horizontal plane, enabling these more substantial improvements. For electrochemical applications, such as sensors, the rougher surface produced by photonic annealing only will provide a greater number of exposed edges and potentially increase electron transfer rate, (129,130) but this must be weighed against durability and stability issues.

Similar improvements were shown in surface roughness and resistivity for the GNP based inks, these similarities are likely due to the similarities in the morphologies of the materials, i.e. layered planar structures which are initially randomly orientated and aligned. The random orientation of the GNPs provided large gaps between nanoplatelets from which binder could easily escape during photonic annealing and allow the GNPs to be compacted into during compression rolling. These changes in the print microstructure and improvements in the print conductivity seen for the graphite and GNP based inks are in line with the trends found for the graphene-based inks assessed by Arapov *et al* (88).

Graphite and carbon black ink was substantially more conductive than the GNP and graphite-based inks and therefore had lower potential for improvement in the conductive matrix. The carbon black particles acted as conductive bridges between the graphite flakes, with the graphite to carbon black ratio optimised for conductivity by Phillips *et al*. (26). However, there were still improvements seen in the print topography which may have potential benefits. For example, Lee *et al*. suggested that polishing of an electrode surface would extend its working life and potentially make single use sensors reusable (131). There were reductions in surface roughness from 1.7 μm to 0.7 μm of the graphite and carbon black based prints and reductions in resistivity from 0.037 $\Omega\text{ cm}$ to 0.019 $\Omega\text{ cm}$ after photonic annealing and subsequent compression rolling. However, the SEM images (Figure 7.5) show some carbon black had been removed from the graphite flakes as a result of processing. So, although there is an overall improvement in print topography and electrical performance for the print, due to an improvement in the area of carbon flakes and particles in contact with one another, it is done at the expense of removing some of the uppermost carbon black

particles. The high surface area and small size of these particles makes them likely to be entrained in the vapour when the binder is degraded.

Overall, these post processing methods could provide a quick and simple method to enhance conductivity with low cost, easy to process materials. However, further improvements in conductivity could be made by using thicker printed layers, as found by Secor *et al.* where the resistivity reduced from around 0.0075 Ω cm after one print layer to around 0.0039 Ω cm after eight print passes (86). These methods could be used to improve the electrochemical performance of a range of redox couples for electrochemical sensors. As well as improve the performance of battery electrodes, to assess whether these post processing methods can lead to advantages other than improvements in electrical conductivity.

7.5. Conclusions

The photonic annealing and compression rolling can provide a suitable post processing method for improving the topography and electrical performance of carbon-based inks of a range of carbon morphologies. These processes can both be integrated into a roll to roll production of printed electronics and may be beneficial for a range of applications. As well as potentially widening the range of uses for low-cost carbon inks, so that they can displace some of the applications using earth metal inks. Future work could be conducted to assess the effect of photonic annealing and compression rolling on the electrochemical performance of a range of redox couples for and electrochemical sensors, as well as battery electrodes, to assess whether these post processing methods can lead to advantages other than improvements in electrical conductivity.

Chapter 8. Conclusions and Future Work

8.1. Introduction

Screen-printing is the most widely used process in the production of printed electronics due to its ability to consistently transfer highly viscous inks containing large functional materials and large concentrations of functional materials. However, despite this surge in the number of functional applications, the science of screen printing is rooted in the graphics era with a limited understanding of the ink deposition mechanism, or the requirements of functional inks containing larger particles and higher concentrations than traditional inks. The work conducted in this thesis focussed on carbon inks as they are widely used in the manufacture of a range of printed electronics applications due to their electrical conductivity, relatively low cost, chemical inertness and ability to be modified or functionalised. Carbon is also available in a range of morphologies, making it viable for use in a wide range of applications. This made carbon the most viable material for conducting a range of investigations within this thesis.

This thesis has identified methods for optimising the print topography and electrical performance of carbon-based inks. A multifaceted approach encompassing all aspects of the production of printed electronics from ink formulation, through screen-printing, to drying and post processing was undertaken. A specially designed screen-printing visualisation rig was developed for ink and process evaluation, which was used alongside traditional methods such as shear and extensional rheometry. This was also used to provide validation to existing theories of ink transfer mechanisms. The overall aim of this thesis was to fully understand cause and effect in the printing process, to work towards repeatable and predictable outcomes.

8.2. Conclusions

The key findings are summarised below and described in more detail in the following paragraphs:

- Optimal mixing techniques for producing a graphite-based ink with best consistency and performance were identified as consisting of triple roll milling followed by Speedmixing.
- Parametric studies found that with blade squeegees, lower angles and softer blades led to increases in ink deposition, irrespective of the ink's rheological properties and determined by deflection of the blade. However, the effects of print speed and snap distance were related to the rheology of the inks. With higher print speeds producing greater ink deposits due to the pseudoplasticity of the graphite-based ink and the snap distance depending on the elasticity and viscosity of the ink which influence the separation mechanism.
- Extensional CaBER testing provided qualitative indications of the effect of separation speed and distance on deposition but could not evaluate the influence of shear forces caused by the passage of the squeegee and screen mesh. For this purpose, a screen-printing visualisation rig was constructed, allowing the ink transfer mechanism to be captured for the first time, validating and quantifying the theory proposed by Messerschmidt consisting of four key stages: adhesion, extension, flow and separation.
- The parameters of print speed, snap distance, solid loading and ink rheology affected mesh/substrate contact time and filamentation behaviour with a quantifiable effect on ink deposition, in terms of the amount of ink transfer, roughness and therefore conductivity.
- Photonic annealing and subsequent compression rolling were found to enhance the conductivity of carbon inks by removing binder between particles and consolidating the ink film. Leading to 8 times reduction in resistivity for the graphite-based ink and halving in resistivity for the ink containing a combination of carbon black and graphite, where there was less potential for improvement due to the conductive bridges between the graphite flakes.

A simple graphite-based ink was used for parametric studies to minimise the number of variables. A combination of triple roll milling followed by Speedmixing was found to produce the smoothest and most conductive prints out of methods assessed. This was as the milling enabled the graphite flakes to be well dispersed in the ink prior to mixing. Speedmixing provided more even shear to the entirety of the ink,

while traditional mixing techniques such as overhead stirring only provided localised shear. These methods produced a more homogeneous ink, which led to smoother and more conductive prints. Therefore, these methods were used for preparing the inks for the parametric studies.

In the case of blade squeegees, the variations in ink deposition and print roughness were related to the deflection of the blade which was influenced by the hardness and angle of the squeegee. As these are mechanical effects, these trends were found to be independent to the rheological profile of the ink being printed. Softer squeegee blades positioned at shallower angles were found to cause to greater deformation, leading to greater ink deposits and subsequently better conductivity of the graphite-based ink assessed. Harder squeegees at too high an angle led to the squeegee and mesh applying excessive force to the squeegee which led to poor ink transfer. Altering the hardness and pressure of diamond squeegees only led to changes in the area of the tip in contact as they were 45° to the mesh, meaning the squeegee could not deflect to the degree where it would lose contact with the mesh as with blade squeegees. This resulted in less significant effects on ink deposition and print performance. A diamond squeegee would enable more consistent print roughness and conductivity irrespective of the squeegee hardness but would make it harder to optimise print conductivity.

The effect of print speed and snap off distance were related to the rheological profile of the ink, where increases in print speed led to increases in ink deposit and consequent reductions in resistance, as the graphite-based ink was highly pseudoplastic. A medium snap distance produced the smoothest and most conductive print while too little snap distance caused poor ink separation between the mesh and substrate and too high a snap distance caused poor contact between the mesh and substrate and mesh warping, leading to insufficient ink transfer. This optimal snap distance was dependent on the elasticity and viscosity of the ink and altered depending on the inks rheological profile. CaBER tests enabled the effect of separation distance and speed on ink separation to be assessed. For the commercial carbon ink, increases in speed led to an overall reduction in the amount of ink transferred and changes in the necking profile of the filament during separation from a profile typical of a power law fluid to that of a weakly elastic fluid, as the ink behaved in a more elastic manner at high speeds.

However, the CaBER method could not assess the effect of mesh features, the combination of shear and extension forces, or the angle between the mesh and substrate. For this purpose, a screen-printing visualisation rig was constructed, enabling direct imaging of the deposition of the ink onto the substrate and the subsequent separation of the ink from the mesh during the screen-printing process, using high speed imaging. This enabled the ink separation mechanism in screen printing to be recorded and quantified for the first time. Providing sufficient experimental evidence to identify key transfer mechanisms and provide validation for the theory suggested by Messerschmitt (70). Where the four stages of ink deposition, consisting of adhesion, extension, flow and separation were identified and quantified. During the adhesion stage, the ink forms a continuous bridge between the mesh and substrate directly behind the squeegee contact point. This continues in the extension stage where the ink remains in continuous contact but is stretched over an increasing distance while the mesh moves away from the substrate. The flow stage is where the ink starts to separate from the main body of ink behind the squeegee and form filaments. These then start to display a localised rate of thinning (necking) which then leads to complete separation. There was no clear correlation with Riemer's theory, where the mesh forces the ink onto the substrate as columns, which remain on the substrate due to adhesion and slump once the mesh is removed. However, Messerschmitt's theory did not outline the length or duration of the four stages, where these analyses enabled the lengths of these regions to be quantified, with increases in line width leading to the ink taking longer to separate and forming more filaments during separation. This also led to corresponding increases in the amount of ink deposited for the carbon-based ink assessed.

When assessing the effect of altering snap distance and print speed, some observations were common to both types of test. As with the CaBER tests, higher print speeds on the screen-printing visualisation rig led to less ink deposited for the commercial carbon ink. With the filaments forming during the flow to separation stages also showing changes in the necking profile from that typical of a power law fluid to a weakly elastic fluid, as the ink behaved in a more elastic manner at higher speeds due to its viscoelastic profile. Changes in ink separation with separation distance on the CaBER tests did not correspond with the changes caused by altering snap distance seen on the screen-printing rig. The CaBER tests could not mimic the

effects of the angle between the mesh and substrate on the shear and extensional forces which enabled ink separation in screen printing. On the rig, snap distance had significant effects on the adhesion to extension stages, as reductions in snap distance led to shallower angles between the mesh and substrate. This led to increases in the adhesion to extension stages as at these lower angles, sufficient stress states for separating the ink was not achieved until a greater distance behind the squeegee. As with the graphite-based ink, the largest ink deposit conductivity was achieved at the medium snap off distance assessed, at which distance, the minimum number of filaments occur during separation, which would lead to less rough and therefore more conductive prints.

The applicability of the various stages of the model proposed by Messerschmitt differed depending on the ink properties. When assessing the effect of altering carbon morphologies and concentrations in carbon-based screen-printing inks, less viscous inks containing lower concentrations of carbon only displayed the first two stages of Messerschmitt's 4 stages of ink separation theory. In these cases, the ink fully separated between the mesh and substrate at the back of the body of ink being extended between the mesh as substrate, rather than forming filaments which necked and led to subsequent separation. Whereas the inks containing higher carbon concentrations and all of the graphite-based inks displayed all four stages of separation. The inks containing higher concentrations of carbon typically took longer to separate between the mesh and substrate and formed more filaments during separation and produced greater ink deposits in prints which were subsequently more conductive. The smaller carbon black particles with more particle to particle interactions had more significant effects on the ink separation mechanism than the larger morphologies such as graphite. The inks containing graphite separated in a manner most similar to the plain resin, whereas the ink containing carbon black showed the most variance in separation mechanisms. Where the 15 wt% carbon black ink produced a large adhesion to extension stage, with a clean separation after this stage without any filaments formed. While the 20 wt% carbon black ink produced many filaments, with the largest flow to separation stages lengths out of all the inks assessed. Where the 15% carbon black ink produced smoother and more conductive prints than the 20% carbon black ink. This also corresponds with the

shear and extensional rheology tests, which found that carbon black lead to significant increases in the elasticity of the ink and at 20 wt% loading, took longer to separate in CaBER tests than the other inks.

Photonic annealing and compression rolling reduced print roughness and improving the conductivity of carbon-based inks of a range of morphologies. Photonic annealing removed some of the remaining binder between the particles and flakes, while the compression rolling reconsolidated the print, reduce print roughness and improve interactions between the carbon flakes and particles. Inks containing single morphologies were found to have the most significant improvements in conductivity, with reductions in resistivity from 1.908 Ω cm to 0.235 Ω cm for the graphite-based ink. The ink containing a combination of morphologies was more conductive than the other inks as the carbon black particles acted as conductive bridges between the graphite flakes, but still saw an improvement in resistivity from 0.037 Ω cm to 0.019 Ω cm. Compression rolling without photonic annealing was also found to improve resistivity by increasing interactions between flakes but to less of a degree as the binder was still left between them. With improvements in resistivity of 61% for the graphite ink, rather than 88% when photonic annealing was applied prior to compression. These processes could both be integrated into a roll to roll production of printed electronics and may be beneficial for a range of applications. They could also potentially widen the range of uses for low-cost carbon inks, so that they can displace some of the applications using earth metal inks.

Overall, this work has increased the understanding and predictability of the screen process for the modern age of printed electronics, identifying how carbon morphologies and loadings affect the ink deposition process and conductivity of prints, how press parameter settings are influenced by the inks rheological profile and finally how post processing methods offer further enhancement. The quantitative results from the high-speed imaging analyses could also form the basis for the development of numerical simulations and predictive methods. This work highlighted that there was no correspondence between the model suggested by Riemer while supporting the theory suggested by Messerschmitt. However, previous computational models have simplified this theory so that there are only vertical forces acting on the ink with ink separation occurring on each individual mesh

strand. Whereas the experimental results from this work identified that the ink separated over multiple mesh strands, with the four stages of ink separation described by Messerschmitt varying in length and duration according to the ink and press parameter settings used.

8.3. Future Work

The work conducted in this thesis assessed the effect of a range of press parameters on carbon-based inks containing a variety of carbon-based morphologies. This has provided a range of experimental results which have improved the understanding of the ink deposition and separation process in screen printing. This ink separation process was quantified into four significant lengths which vary with ink rheology and press parameter settings. However, to understand how these ink separation stage lengths vary with a greater range of inks, substrates and settings, further experiments should be conducted to assess the effect of:

- Different inks – other functional materials and graphics-based ink of a range of rheological profiles
- Different substrates – assess the effect of surface energy and roughness
- Different screen sizes
- Mesh coarseness – different thread diameters and separation distances
- Mesh material – stainless steel, trampoline meshes as well as other polyesters
- Emulsion thickness
- Squeegee geometries
- Squeegee angles
- Squeegee hardness
- Squeegee pressure
- Printing multiple layers- of the same ink or a range of inks to replicate multilayer printed electronics

With these results, computational models can be developed, based on the boundary conditions that can be derived from the experimental results. These can be used to enable the effects of different ink rheologies and press conditions to be predicted computationally.

In the case of using photonic annealing and subsequent compression rolling for enhancing the electrical performance of prints, future work could be conducted to assess the effect of these post processes on the electrochemical performance of a range of redox couples for and electrochemical sensors. As well as battery electrodes, to assess whether these post processing methods can lead to advantages other than improvements in electrical conductivity.

I. Appendix I Quantifying and controlling variables on Svecia Matic

This appendix presents supplementary data for work reported in Chapter 3. It comprises of two sections, the first being the method by which the squeegee pressure was controlled for the parameter studies conducted on the Svecia Matic. While the second describes the equipment, which was designed and made to measure the speeds of the Svecia Matic at each of its arbitrary speed settings.

Controlling squeegee pressure

For the Svecia Matic, as the squeegee pressure was controlled through vertical distance with a set interaction distance rather than pressure exerted by the squeegee, it was hard to keep the pressure constant, therefore creating a source of variability between print runs.

During set up, to assess the squeegee and substrate interaction, a piece of substrate, (of the same material and dimensions as those being printed on) would be placed half below the screen and half coming off of the back of the print bed. The squeegee would then be engaged onto the mesh, bringing the mesh into contact with the substrate. After which, a “tug test” would be conducted, where the substrate would be tugged and the interaction adjusted until it could just about be moved by tugging. As it can be hard to imagine the amount of force being exerted to move the squeegee, this was not sufficient for maintaining consistent pressure between trials, although the interaction distance would be recorded.

To try and minimise variation, the test substrate was modified to contain a series of evenly spaced, eyelets (14mm Hemline nickel plated eyelets) were inserted to the bottom of the substrate, as shown in Figure I.1. The substrate was folded over into a hem with the last inch of material, to provide more strength and avoid the eyelets tearing the substrate. A pair of spring balance scales were then hooked into the eyelets. When the squeegee was engaged and the substrate was forced onto the

substrate, the tug test could then be used with the spring scales attached to the substrate to measure the horizontal force exerted to move the substrate. The spring scales were either used in pairs, with one each of the outer eyelets to ensure even pressure across the substrate. Or with one in the centre to measure the total force, as shown in Figure I.1.

Although this still does not provide the actual value of squeegee pressure, it enabled more consistency between print runs.



Figure I.1 Substrate with eyelets and spring balance to measure horizontal interaction force between squeegee, mesh and substrate.

Quantifying print speed

In order to quantify the arbitrary speed settings on the Svecia Matic Screen-printing press, an LDR (light dependent resistor) based design was created which could be used with an Arduino Uno and based in an FDM printed casing. The prototype was created for two LDRs which would be triggered by a LED (light emitting diode) fixed to the printing arm, as shown in Figure I.2. Where the triggering of the first LDR with the passage of the LED would start the timer and the passage of the LED over the second LDR would stop it. As the LDRs were separated in the casing, designed on Solidworks™ and printed using a Raise 3D FDM printer, which fixed

the LDRs at 10cm apart. The print speed was then calculated by dividing the distance in mm (100mm) by the time in seconds. However, as the printer was located in a bright room, the LED was not always detected, making the process unreliable.

To overcome this, the final design incorporated a cantilever beam onto the side of the printing arm, as shown in Figure I.3. In this design, the LDR would be triggered when the lighting was below a set threshold, which was determined through trial and error. The final design incorporated six LDRs where pairs which were each placed 10mm apart. Where the first LDR of each pair would start the timer and the second would stop it, with speed calculated in the Arduino code using distance divided by time. This provided three speeds to be collected from each test so that any acceleration could be noted, with the speeds displayed on a LED screen so that the speed tested could be used without a computer if necessary, using the USB port to only supply mains power. The casing was designed in Solidworks™ and printed with a Raise 3D FDM as with the prototype (Figure I.4).

Each print speed setting was tested 3 times, with 3 speeds produced per test, producing a total of 9 readings to average from which an overall average and standard deviation was produced. Table I.1 shows the average print speeds from each of the 3 tests conducted on the 10 print speed settings as well as the overall average for each setting. As there was no notable acceleration in speed over the lengths assessed, the average speed of each of the tests is shown. Print speeds were found to range from around 55 mm s⁻¹ at speed setting 1 to around 1857 mm s⁻¹ at speed setting 10. There was a relatively linear increase in print speed with speed setting increments, as shown in Figure I.5.



Figure I.2 Prototype for speed tester



Figure I.3 Speed tester design

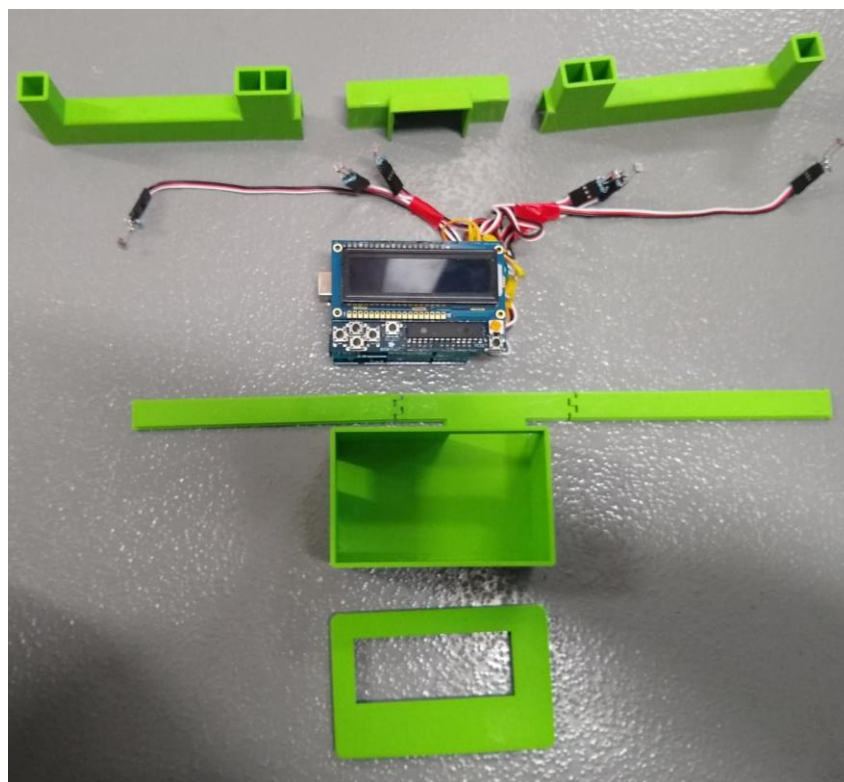


Figure I.4 Components for speed tester displaying the FDM printed casing, Arduino, LCD screen and LDRs with resistors.

Table I.1 Table of average speeds for different settings on the Svecia Matic screen-printer.

Speed Setting	Average Speed 1 (mm/s)	Average Speed 2 (mm/s)	Average Speed 3 (mm/s)	Average of all speeds (mm/s (standard deviation))
1	55.10	56.30	55.80	55.73 (± 0.60)
2	259.95	260.05	259.90	259.97 (± 0.08)
3	507.85	505.95	505.95	506.58 (± 1.10)
4	708.65	710.00	706.75	708.47 (± 1.63)
5	880.75	888.70	867.30	878.92 (± 10.82)
6	1048.95	1017.35	999.20	1021.83 (± 25.18)
7	1234.85	1198.55	1198.55	1210.65 (± 20.96)
8	1412.90	1424.25	1424.25	1420.47 (± 6.55)
9	1593.70	1619.65	1577.25	1596.87 (± 21.38)
10	1847.45	1862.05	1861.30	1856.93 (± 8.22)

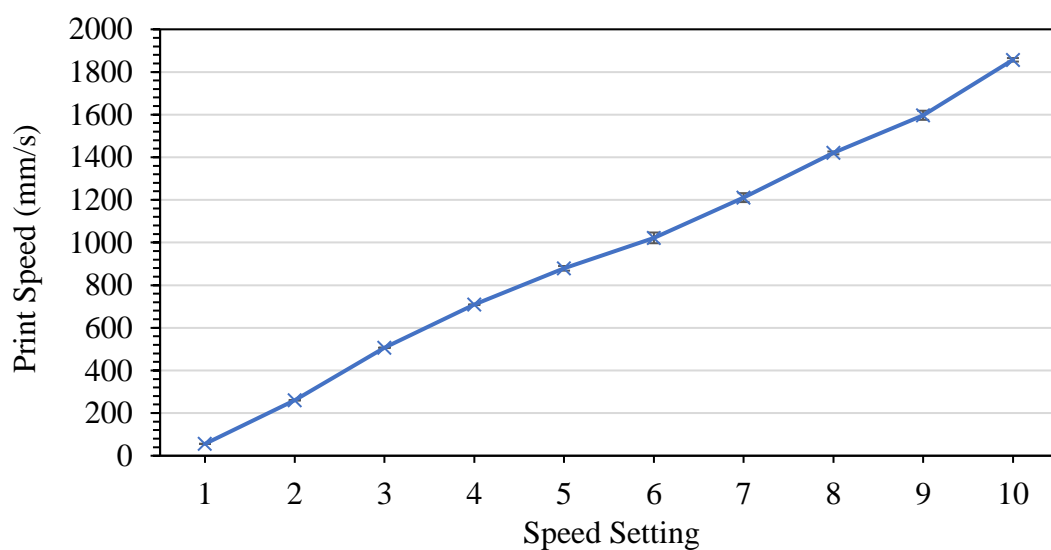


Figure I.5 Average speeds for different settings on the Svecia Matic screen-printer.

II. Appendix II Development of Screen-Printing Visualisation Rig

This appendix presents supplementary data for work reported in Chapters 4 and 5. It describes the design stages involved in developing and building the screen-printing visualisation rig which was used for high speed imaging of the ink separation mechanisms in screen printing.

Prototype 1

The first prototype for imaging ink separation in screen printing comprised of a small screen made to fit in a DEK 248 Screen-printer (290x240mm). It was mounted onto a transparent laser cut raised platform with spacers supporting the screen on top of the print bed, held in place with clamps. A 10,000-lux lamp was placed directly behind the screen-printing rig to ensure sufficient back lighting for high-speed imaging. The transparent support structure was designed to allow as much of the light through as possible so that the deposition could be clearly visualised, as shown in Figure II.1.

Printing was conducted by hand while the imaging technique was set up to film at the side of the screen. Imaging was attempted using a high-speed camera (Photron FastCam Mini High-Speed Camera). However, the features being assessed were at around 120mm from the edge of the screen, while the focal length of the camera at the desired zoom of around five times magnification was around 80mm.

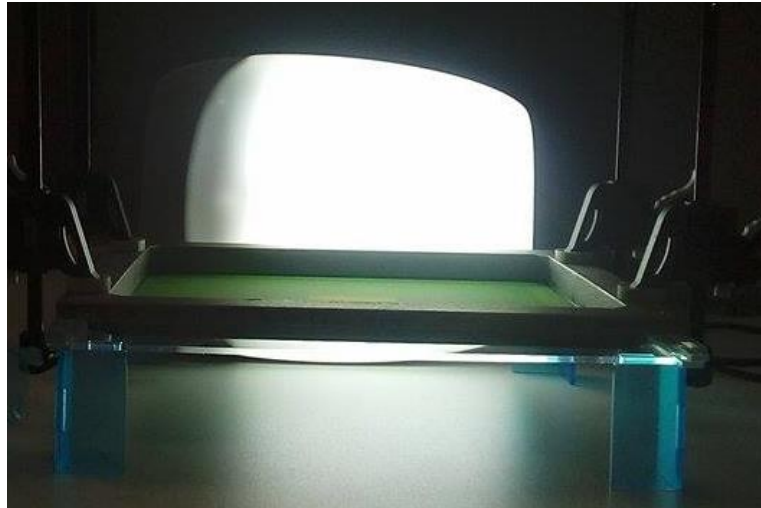


Figure II.1 Prototype 1 for the screen-printing visualisation jig

Prototype 2

To overcome this issue, a custom design was created, which could be fitted on to the existing extensional rheology jig which would provide computational control over the z axis with movement provided by stepper motors.

To ensure the feature position would align with the focal length of the high-speed camera available at the desired magnification, a custom screen was designed in SolidWorks™ (SOLIDWORKS Student Edition 2014-2015(Dassault Systèmes SolidWorks (DS SolidWorks))), as shown in Figure II.2 (Top diagram). The SolidWorks finite element analysis (FEA) software was also used to select the material and thickness of the frame when it was put under tension and had the downward force of the squeegee applied to it, when supported by the screen holder design (modelled as a 12kg downward remote force load, with supports placed in the location of the screen holder it would be held on). This resulted in a 100x300mm stainless steel frame with 10mm offset, which was 5mm thick (Figure II.2) as it had a relatively small deflection and maximum stress well below the yield stress of stainless steel. The frame was then made in the university workshop as specified. The screen mesh was made of polyester with 61 threads per cm, 64 µm thread diameter and 13-micron emulsion. This mesh size was chosen as it was appropriate for the carbon-based inks which I wished to assess. The print design consisted of a 30mm long line with 5 different width lines joined together, each 6mm long and

400um, 200um, 100um, 50um and 30um wide, as shown in Figure II.3 The mesh was made mounted onto the pre-made frame by MCI Precision Screens Ltd.

The screen and substrate holder along with the squeegee holder were also designed in Solidworks™, as shown in Figure II.4 They were also assessed with FEA, with the designs optimised to be able to withstand 12kg of downward force. 12kg was chosen as it is the upper squeegee forces used on the Dek 248 screen-printing press, leading to assumptions that this smaller rig would not require squeegee forces in excess of this to be exerted. Both sections were designed and optimised using Polylactic acid (PLA) as the material choice, so that it could be created using Fused Deposition Modelling (FDM) (also known as Fused Filament Fabrication (FFF)) forms or rapid prototyping to allow the custom designs to be quickly made.

The screen and substrate holder (Figure II.5) was designed to be clamped onto the bottom plate of the extensional rheology jig which would remain stationary. It had a 2mm offset bed in which the substrate could be positioned, where the snap gap would be varied by placing spacers between the bed and substrate. The flanges on the sides of the holder were designed to support the screen, leaving a gap at the front and back of the holder for visualising deposition and separation as well as enabling sufficient light to image the print occurring.

The squeegee holder (Figure II.6) was designed to slotted onto another FDM produced rectangle (10mm thick) with interference fits to ensure it was secure so that the it could be clamped onto the upper plate of the extensional rheology jig which would provide movement in the z axis. A 75 shore A hardness, 1mm wide squeegee with a double-sided bevel edge was fixed flat onto the squeegee holder slider to provide a 45° squeegee contact angle, providing a similar profile to a diamond squeegee to remove the variable of squeegee angle (Figure II.4). The squeegee was mounted onto a slider with a small handle to enable manually controlled squeegee motion to enable printing to occur by sliding the handle from one side to the other.

The prototype was set up as shown in Figure II.7 with the jig lit from behind and the camera placed in from of the jig where it was in best focus. The jig was successful in imaging the deposition and separation of the carbon ink tested. However, as this jig only had manual control over the squeegee, the rate of squeegee motion was not controllable or consistent across the print duration.

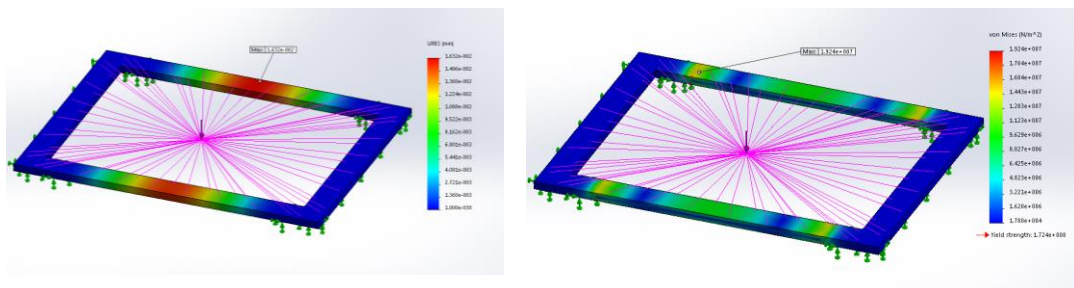
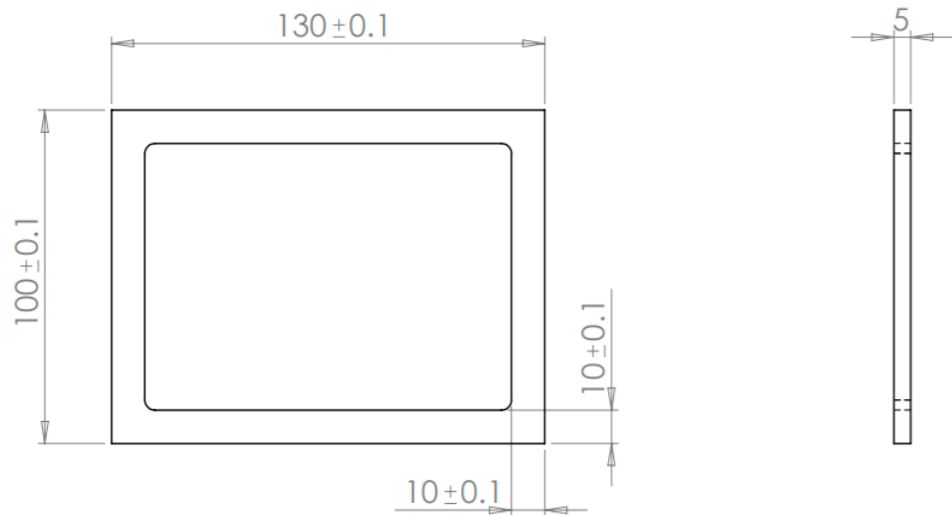


Figure II.2 Dimensions of Screen Frame (Top) with the deflection (bottom left) and von mises stress (bottom right) distributions caused by a point load when supported by the jig design.

Figure II.3 Print Design

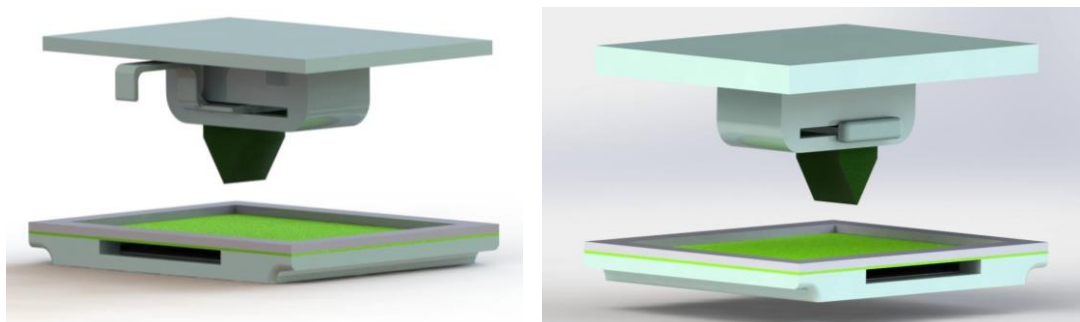


Figure II.4 Prototype 2 design in SolidWorks from the front (left) and rear (right) views.

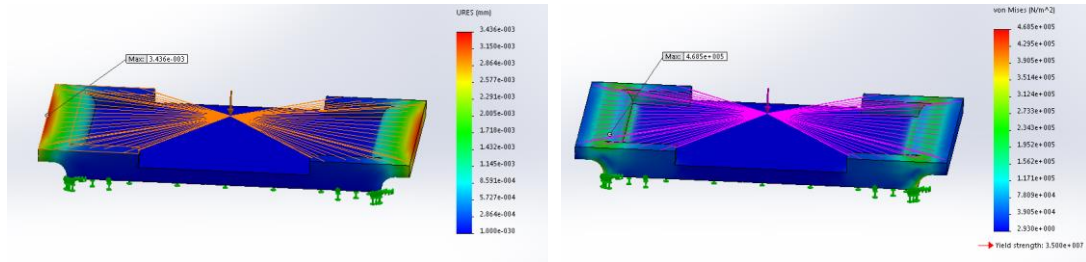


Figure II.5 Prototype 2 screen and substrate holder design with the deflection (left) and von mises stress (right) distributions caused by a point load.

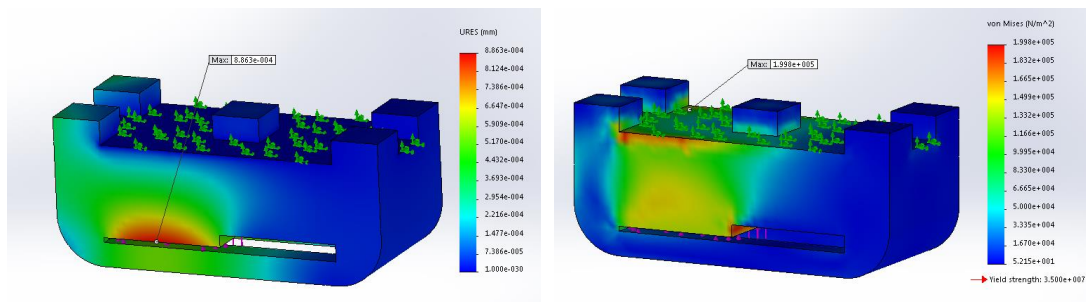


Figure II.6 Prototype 2 squeegee holder on moving slider design with the deflection (left) and von mises stress (right) distributions caused by the reaction of the downward squeegee force with the holder fixed from above.



Figure II.7 Prototype 2 clamped in position with backlighting and high-speed camera positioned to the side.

Motorised Screen-Printing Visualisation Rig

To provide a controllable and consistent print speed, a motorised rig design was created using a pair of Nema 23 stepper motors with lead screw driven linear actuators to produce both x and z axis motion for the squeegee movement. A sturdy frame made up of 40mmx40mm v slot aluminium extrudes was also designed to provide sufficient support and stability for the motors, linear actuators, squeegee holder and screen holder. The movement of the linear actuators powered by the stepper motors was controlled by a pair of HALJIA Single 1 Axis Controller Stepper Motor Drivers: TB6560 3A driver board CNC Routers which were controlled by Arduino. Along with the Grbl Controller 3.0 (open source) software to set the speed and distance of the movement.

As with prototype 2, the screen and squeegee holders were designed in SolidWorks™, optimised using FEA and produced in PLA using FDM. The screen holder design was similar to the one used in Prototype 2, except it had been altered to be clamped onto the V slot frame. It had also been optimised to enable more light to illuminate the ink deposition by curving the back of the substrate bed and had removed the back supports for the screen (Figure II.8). While FEA was used to alter the design so that it could still withstand the forces from the screen and squeegee. To remove the need for clamping the screen on top of the holder, additional parts were produced so that the screen could be secured and screwed in place to prevent movement during printing.

The squeegee holder was designed to be screwed onto the gantry plate providing the z motion as shown in Figure II.9. The holder was designed to fit a diamond geometry squeegee of up to 30mm in width, which was sufficient for the experiments being conducted. It was designed so that the squeegee could be secured in place using nuts and bolts, making it easy to remove and clean the squeegee. FEA was also conducted on the squeegee holder design to ensure minimal deflection and that the design would withstand sufficient downward forces.

The jig was set up as shown in Figure II.10 with the camera placed in front of the jig and back lighting provided by a 10,000-lux lamp which was secured into the back of the frame. This provided sufficient control to adjust the squeegee interaction distance and therefore the squeegee pressure applies as well as the squeegee print speed.

Thus, enabling repeatable prints to be produced with a range of squeegee interaction forces, print speeds as well as snap distances which were altered by placing spacer sheets between the base and substrate.

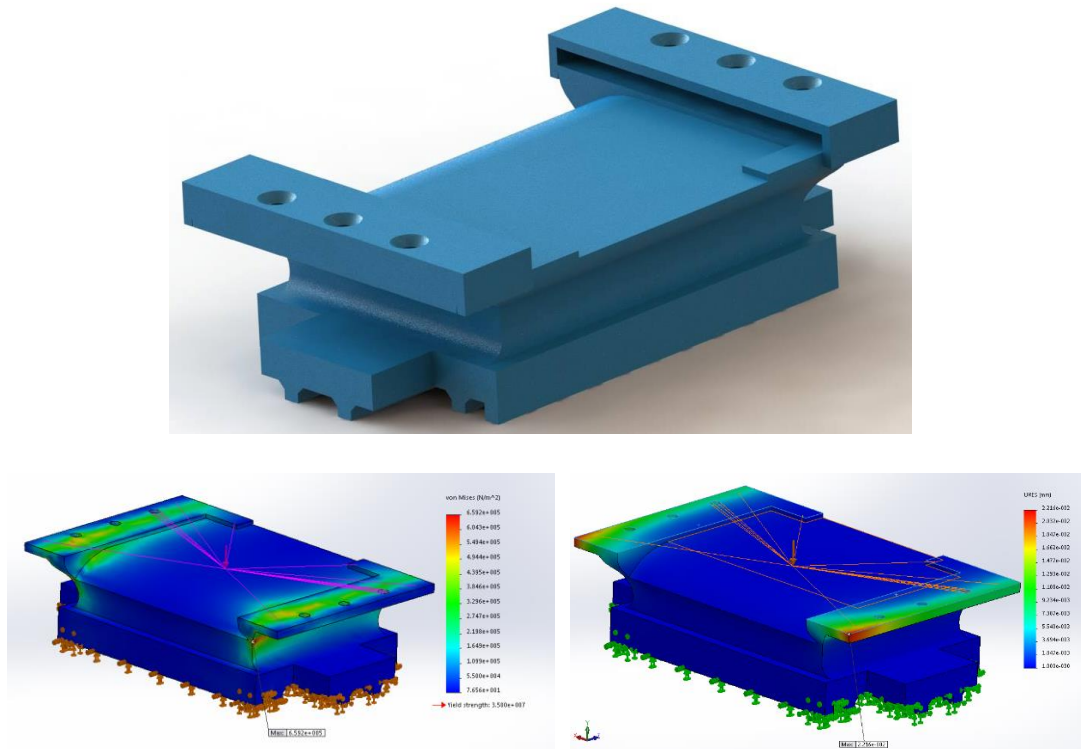
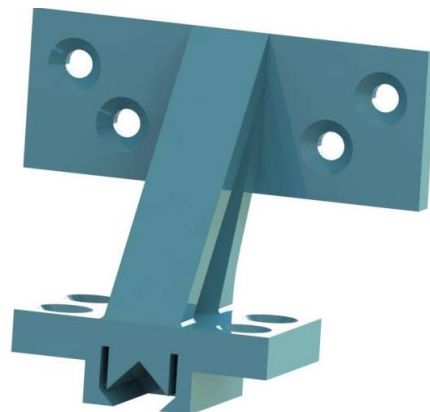


Figure II.8 Screen and substrate holder for motorised jig (Top) with the deflection (bottom left) and von mises stress (bottom right) distributions caused by a point load estimated as the squeegee and screen forces.



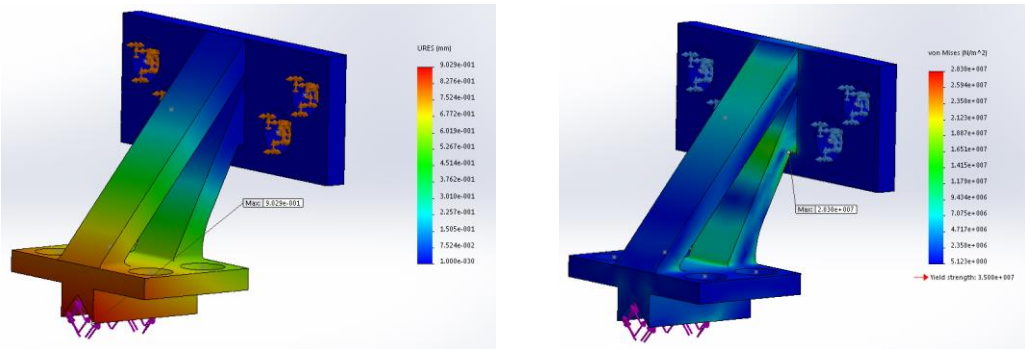


Figure II.9 Squeegee holder for motorised jig (Top) with the deflection (bottom left) and von mises stress (bottom right) distributions caused by a point load estimated as the squeegee and screen forces.

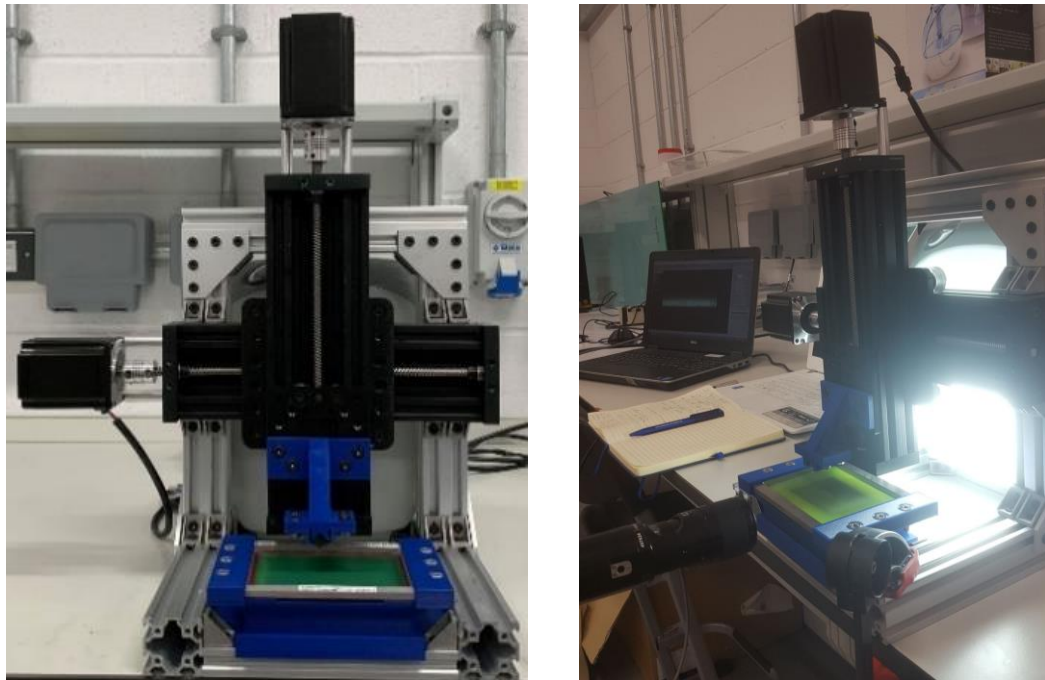


Figure II.10 Motorised screen-printing visualisation rig from the front (left) and when in use (right).

References

1. Schwalbach M V., Schwalbach JA. Silk-Screen Printing for Artists and Craftsmen. Courier Corporation; 2012. 150 p.
2. Griffiths A. Prints and Printmaking: An Introduction to the History and Techniques. University of California Press; 1996. 160 p.
3. Weigeldt K, Jewell EH, Phillips CO, Claypole TC, Hubler AC. Bidirectional mouldable electroluminescent lamps fabricated by screen printing K. J Print Media Technol Res. 2012;I(2):97–102.
4. Philip B, Jewell E, Greenwood P, Weirman C. Material and process optimization screen printing carbon graphite pastes for mass production of heating elements. J Manuf Process [Internet]. 2016;22(1):185–91. Available from: <http://dx.doi.org/10.1016/j.jmapro.2016.03.001>
5. Park HK, Kim SM, Lee JS, Park JH, Hong YK, Hong CH, et al. Flexible plane heater: Graphite and carbon nanotube hybrid nanocomposite. Synth Met [Internet]. 2015;203(1):127–34. Available from: <http://dx.doi.org/10.1016/j.synthmet.2015.02.015>
6. Baker J, Hooper K, Meroni S, Pockett A, McGettrick J, Wei Z, et al. High throughput fabrication of mesoporous carbon perovskite solar cells. J Mater Chem A. 2017;5(35):18643–50.
7. Zhang L, Liu T, Liu L, Hu M, Yang Y, Mei A, et al. The effect of carbon counter electrodes on fully printable mesoscopic perovskite solar cells. J Mater Chem A [Internet]. 2015;3(17):9165–70. Available from: <http://xlink.rsc.org/?DOI=C4TA04647A>
8. Cinti S, Arduini F. Graphene-based screen-printed electrochemical (bio)sensors and their applications: Efforts and criticisms. Biosens Bioelectron [Internet]. 2017;89:107–22. Available from: <http://dx.doi.org/10.1016/j.bios.2016.07.005>
9. Tehrani Z, Burwell G, Azmi M a M, Castaing A, Rickman R, Almarashi J, et al. Generic epitaxial graphene biosensors for ultrasensitive detection of cancer

risk biomarker. *2D Mater* [Internet]. 2014;1(2):025004. Available from:
<http://stacks.iop.org/2053-1583/1/i=2/a=025004?key=crossref.72a450317bd58517cf23ed273d546139>

10. Khan S, Lorenzelli L, Dahiya RS. Technologies for printing sensors and electronics over large flexible substrates: A review. *IEEE Sens J*. 2015;15(6):3164–85.
11. Biegeleisen JJ. *The Complete Book of Silk Screen Printing Production*. Courier Corporation; 1963. 253 p.
12. Tehrani Z, Korochkina T, Govindarajan S, Thomas DJ, Mahony JO, Kettle J, et al. Ultra-thin flexible screen printed rechargeable polymer battery for wearable electronic applications. *Org Electron* [Internet]. 2015;26(1):386–94. Available from: <http://dx.doi.org/10.1016/j.orgel.2015.08.007>
13. Zabek D, Seunarine K, Spacie C, Bowen C. Graphene Ink Laminate Structures on Poly(vinylidene difluoride) (PVDF) for Pyroelectric Thermal Energy Harvesting and Waste Heat Recovery. *ACS Appl Mater Interfaces*. 2017;9(10):9161–7.
14. Cao Z, Koukharenko E, Tudor MJ, Torah RN, Beeby SP. Flexible screen printed thermoelectric generator with enhanced processes and materials. *Sensors Actuators A Phys*. 2016;238:196–206.
15. Izdebska J, Thomas S, Novaković D, Kašiković N, Vladić G, Pál M. Printing on Polymers: 15 Screen Printing [Internet]. *Printing on Polymers*. Elsevier; 2016 [cited 2016 Jan 21]. 247–261 p. Available from: <http://www.sciencedirect.com/science/article/pii/B9780323374682000154>
16. Jewell EH. *MSc in Printing and Coating Technology Principles of Screen Printing*. The MSc in Printing and Coating Technology Lecture Notes. 2005.
17. Peterson I. *CONTRIBUTIONS TO IMPROVED INK CONTROL IN SCREEN PRINTING*. Vol. 1. Swansea University; 2015.
18. Anderson JT. *An Investigation In To The Physical Aspects Of The Screen Printing Process*. Swansea University; 1997.
19. Horvath E, Harsanyi G, Henap G, Torok a. *Mechanical Modelling and Life*

- Cycle Optimisation of Screen Printing. *J Theor Appl Mech.* 2012;50(4):1025–36.
20. Jewell E, Hamblyn S, Claypole T, Gethin D. Deposition of High Conductivity Low Silver Content Materials by Screen Printing. *Coatings* [Internet]. 2015;5(2):172–85. Available from: <http://www.mdpi.com/2079-6412/5/2/172/>
 21. Philip B, Jewell E, Worsley D. The impact of solvent characteristics on performance and process stability of printed carbon resistive materials. *J Coatings Technol Res.* 2016;13(5):911–20.
 22. Jewell EH, Hamblyn SM, Claypole TC, Gethin DT. The impact of carbon content and mesh on the characteristics of screen printed conductive structures. *Circuit World* [Internet]. 2013;39(1):13–21. Available from: <http://www.emeraldinsight.com/10.1108/03056121311298918>
 23. Pan J, TONKAY GL, QUINTERO A, Ave WP. Screen Printing Process Design of Experiments for Fine Line Printing of Thick Film Ceramic Substrates. *J Electron Manuf* [Internet]. 1999 Sep 7 [cited 2016 Feb 5];9(3):203–13. Available from: <http://www.worldscientific.com/doi/abs/10.1142/S096031319900012X>
 24. Anderson J, Appleton W, Claypole T., Jewell EH. An investigation into the effect of squeegee design and print speed on ink transfer. *Gloscat Screen Printing Project.* 1996.
 25. Willfahrt A. Screen Printed Thermoelectric Devices. *Linköping Stud Sci Technol.* 2014;(1663):49.
 26. Phillips C, Al-Ahmadi A, Potts S-J, Claypole T, Deganello D. The effect of graphite and carbon black ratios on conductive ink performance. *J Mater Sci* [Internet]. 2017;52(16). Available from: <http://link.springer.com/10.1007/s10853-017-1114-6>
 27. Jewell EH, Barden T, Claypole TC. The effect of flat bed screen printing parameters on ink film thickness. *Screen Print Technol Group, Rep no 00-01-SPTG.* 2000;
 28. Woan Yi S. *The Manufacture of Bioscaffolds by Printing.* University of

Wales Swansea; 2010.

29. E.H. Jewell, T. Barden, T. C. Claypole and DTG. Characterisation of Fine Lines. Swansea; 2003.
30. Jewell E, Philip B, Greenwood P. Improved Manufacturing Performance of Screen Printed Carbon Electrodes through Material Formulation. Biosensors [Internet]. 2016 Jun 27;6(3):30. Available from: <http://www.mdpi.com/2079-6374/6/3/30>
31. Jewell EH, Barden T, Claypole TC. The effect of flat bed screen printing parameters . Part II : Tone gain and solid density. Screen Printing Technology Group. Report no : 00 – 04- SPTG. Swansea; 2000.
32. Jewell EH, Claypole TC. The role of squeegee deformation on ink transfer Screen Printing Technology Group. Report no : 02 – 02- SPTG. Swansea; 2002.
33. Barden TJ. The application of three-dimensional profiling to the measurement and characterisation of screen printed fine lines. University of Wales Swansea; 2008.
34. Molamphy TA, Stephenson MI, Murphy EA. Application of Experimental Design to the Solder Paste Screen Printing Process. Solder Surf Mt Technol. 1992;11:4–6.
35. Jewell EH, Claypole TC, Gethin DT. The effect of exposure to inks and solvents on squeegee performance. Surf Coatings Int Part B Coatings Trans [Internet]. 2004;87(4):235–308. Available from: <http://link.springer.com/article/10.1007/BF02699673>
36. Phillips C, Beynon D, Hamblyn S, Davies G, Gethin D, Claypole T. A Study of the Abrasion of Squeegees Used in Screen Printing and Its Effect on Performance with Application in Printed Electronics. Coatings [Internet]. 2014;4(2):356–79. Available from: <http://www.mdpi.com/2079-6412/4/2/356/>
37. Jewell EH, Claypole TC, Gethin DT. The Impact of ink rheology on the image transfer mechanism in screen printing. In: Proceedings of Institute of Non Newtonian fluid mechanics. Cardiff; 2003.

38. Cao K, Cheng K, Wang Z. Optimization of Screen Printing Process [Internet]. IEEE, 7th International Conference on Electronics Packaging Technology. 2006 [cited 2016 Jan 27]. Available from:
https://www.google.co.uk/search?q=Optimization+of+Screen+Printing+Process&oq=Optimization+of+Screen+Printing+Process&aqs=chrome..69i57.525j0j4&sourceid=chrome&es_sm=93&ie=UTF-8
39. Riemer DEE. The Theoretical Fundamentals of the Screen Printing Process. *Microelectron Int* [Internet]. 1989 Jan 13 [cited 2016 Dec 6];6(1):8–17. Available from: <http://dx.doi.org/10.1108/eb044350>
40. Fox IJ. *Ink Flow Within The Screen-Printing Process*. Swansea University; 2002.
41. Jewell EH, Claypole TC, Gethin DT. Viscosity control in the screen printing of ceramic transfers. *Surf Coatings Int Part B Coatings Trans* [Internet]. 2003 Jun [cited 2016 Feb 10];86(2):155–63. Available from:
<http://link.springer.com/10.1007/BF02699628>
42. Fox IJ, Bohan MFJ, Claypole TC, Gethin DT. Film thickness prediction in halftone screen-printing. *Proc Inst Mech Eng Part E J Process Mech Eng* [Internet]. 2003;217:345–59. Available from:
<http://pie.sagepub.com/lookup/doi/10.1243/095440803322611705>
43. Mannan SH, Ekere NN, Ismail I, Lo EK. Squeegee Deformation Study In The Stencil Printing Of Solder Pastes. *IEEE Trans Components Packag Manuf Technol Part A*. 1994;17(3):470–6.
44. Żółek-Tryznowska Z. Rheology of Printing Inks [Internet]. *Printing on Polymers*. 2016. 87–99 p. Available from:
<http://linkinghub.elsevier.com/retrieve/pii/B9780323374682000063>
45. Pan J, Tonkay GL, Storer RH, Sallade RM, Leandri DJ. Critical Variables of Solder Paste Stencil Printing for Micro-BGA and Fine-Pitch QFP Jianbiao. *IEEE Trans Electron Packag Manuf*. 2004;27(2):125–32.
46. Pekarovicova A, Husovska V. *Printing on Polymers: 3 Printing Ink Formulations* [Internet]. *Printing on Polymers: Fundamentals and*

Applications. Elsevier Inc.; 2015. 41–55 p. Available from:
<http://linkinghub.elsevier.com/retrieve/pii/B9780323374682000038>

47. Liang J, Tong K, Pei Q. A Water-Based Silver-Nanowire Screen-Print Ink for the Fabrication of Stretchable Conductors and Wearable Thin-Film Transistors. *Adv Mater* [Internet]. 2016 Jul [cited 2016 Dec 7];28(28):5986–96. Available from: <http://doi.wiley.com/10.1002/adma.201600772>
48. Salmeron JF, Molina-Lopez F, Briand D, Ruan JJ, Rivadeneyra A, Carvajal MA, et al. Properties and printability of inkjet and screen-printed silver patterns for RFID antennas. *J Electron Mater*. 2014;43(2):604–17.
49. Albrecht A, Rivadeneyra A, Abdellah A, Lugli P, Salmerón JF. Inkjet printing and photonic sintering of silver and copper oxide nanoparticles for ultra-low-cost conductive patterns. *J Mater Chem C*. 2016;4(16):3546–54.
50. Kenfack A, Vemo BN, Ngoula F, Anyangwe FF, Chombong JK, Et Joseph Tchoumboué AMMT. Comparison of laser and intense pulsed light sintering (IPL) for inkjet-printed copper nanoparticle layers. *Sci Rep* [Internet]. 2015;5(8832):2–11. Available from: <http://dx.doi.org/10.1038/srep08832>
51. Sengupta R, Bhattacharya M, Bandyopadhyay S, Bhowmick AK. A review on the mechanical and electrical properties of graphite and modified graphite reinforced polymer composites. *Prog Polym Sci* [Internet]. 2011;36(5):638–70. Available from: <http://dx.doi.org/10.1016/j.progpolymsci.2010.11.003>
52. He L, Tjong SC. Low percolation threshold of graphene/polymer composites prepared by solvothermal reduction of graphene oxide in the polymer solution. *Nanoscale Res Lett*. 2013;8(1):2–8.
53. Pantea D, Darmstadt H, Kaliaguine S, Roy C. Electrical conductivity of conductive carbon blacks : influence of surface chemistry and topology. *Appl Surf Sci*. 2003;217(1):181–93.
54. Oxfall H, Ariu G, Gkourmpis T, Rychwalski RW, Rigdahl M. Effect of carbon black on electrical and rheological properties of graphite nanoplatelets/poly(ethylene-butyl acrylate) composites. *Express Polym Lett*. 2015;9(1):66–76.

55. Lei H, Pitt WG, McGrath LK, Ho CK. Resistivity measurements of carbon-polymer composites in chemical sensors: Impact of carbon concentration and geometry. *Sensors Actuators, B Chem.* 2004;101(1–2):122–32.
56. Lux F. Models proposed to explain the electrical conductivity of mixtures made of conductive and insulating materials. *J Mater Sci.* 1993;28(2):285–301.
57. Zallen R. The Percolation Model. *Phys Amorph Solids.* 2005;135–204.
58. Lin HW, Chang CP, Hwu WH, Ger M Der. The rheological behaviors of screen-printing pastes. *J Mater Process Technol.* 2008;197(1–3):284–91.
59. Chen D, Zhao L, Diao H, Zhang W, Wang G, Wang W. Rheological properties and related screen-printing performance of low-temperature silver pastes for a-Si:H/c-Si heterojunction solar cells. *J Mater Sci Mater Electron.* 2014;25(12):5322–30.
60. Riemer DE. Analytical engineering model of the screen printing process: Part I. *Solid State Technol.* 1988;8(1):107–11.
61. Riemer DE. Analytical engineering model of the screen printing process: Part II. *Solid State Technol.* 1988;9(1):85–90.
62. Owczarek J a., Howland FL. A Study of the Off-Contact Screen Printing Process- Part I: Mode of the Printing Process and Some Results Derived From Experiments. *IEEE Trans Components, Hybrids, Manuf Technol.* 1990;13(2):368–75.
63. Owczarek JA, Howland F. A study of the off-contact screen printing process. II. Analysis of the model of the printing process. *Components, Hybrids, Manuf Technol IEEE Trans.* 1990;13(2):368–75.
64. Glinski GP, Bailey C, Pericleous KA. A non-Newtonian computational fluid dynamics study of the stencil printing process. *Proc Inst Mech Eng Part C J Mech Eng Sci [Internet].* 2001;215(4):437–46. Available from: <http://journals.sagepub.com/doi/abs/10.1243/0954406011520869?journalCode=picb>
65. Clements DJ, Desmulliez MPY, Abraham E. The evolution of paste pressure

- during stencil printing. *Solder Surf Mt Technol.* 2007;19(3):9–14.
66. Jewell EH, Claypole TC. The significance of the ink roll in front of the squeegee Screen Printing Technology Group. Report no : 04 – 01- SPTG. Swansea; 2001.
 67. Dowson D. A generalized Reynolds equation for fluid-film lubrication. *Int J Mech Sci.* 1962 Mar 1;4(2):159–70.
 68. Riemer DE. The Direct Emulsion Screen as a Tool for High Resolution Thick Film Printing. In: *Electronic Component Conference Proceedings.* Washington, DC, USA.; 1971. p. 463–7.
 69. Riemer DE. Ein Beitrag zur Untersuchung der physikalisch-technischen Grundlagen des Siebdruckverfahrens [Internet]. na; 1988 [cited 2016 Apr 26]. 95 p. Available from:
https://books.google.co.uk/books/about/Ein_Beitrag_zur_Untersuchung_der_physika.html?id=uxWpuAAACAAJ&pgis=1
 70. Messerschmitt E. Rheological considerations for screen printing inks. *Screen Print.* 1982;72(10):62–5.
 71. Kapur N, Abbott SJ, Dolden ED, Gaskel PH. Predicting the Behavior of Screen Printing [Internet]. *EEE TRANSACTIONS ON COMPONENTS, PACKAGING AND MANUFACTURING TECHNOLOGY, VOL. 3, NO. 3.* 2013 [cited 2016 Jan 27]. p. 508–15. Available from:
https://www.google.co.uk/_/chrome/newtab?espv=2&ie=UTF-8
 72. Fox IJ, Claypole TC, Gethin DT. An experimental investigation into ink transfer using a roller squeegee in high-speed screen printing. *Proc Inst Mech Eng E, J Process Mech Eng.* 2003;217(E4):307–21.
 73. Webster MF, Matallah H, Sujatha KS, Banaai MJ. *Journal of Non-Newtonian Fluid Mechanics* Numerical modelling of step – strain for stretched filaments. 2008;151:38–58.
 74. McKinley GH. Visco-Elasto-Capillary Thinning and Break-Up of Complex Fluids [Internet]. *Rheology Reviews.* 2005. Available from:
<http://mit.dspace.org/handle/1721.1/18085>

75. Fagan JE, Tirtaatmadja V, Lester DR, Boger D V. Drop formation dynamics of constant low-viscosity , elastic fluids. 2002;106:29–59.
76. Tuladhar TR, Mackley MR. Filament stretching rheometry and break-up behaviour of low viscosity polymer solutions and inkjet fluids. *J Nonnewton Fluid Mech* [Internet]. 2008 Jan [cited 2019 Aug 6];148(1–3):97–108. Available from: <https://linkinghub.elsevier.com/retrieve/pii/S0377025707000973>
77. Morgan ML, Holder A, Curtis DJ, Deganello D. Formulation, characterisation and flexographic printing of novel Boger fluids to assess the effects of ink elasticity on print uniformity. *Rheol Acta* [Internet]. 2018 Feb 7 [cited 2019 Apr 25];57(2):105–12. Available from: <http://link.springer.com/10.1007/s00397-017-1061-9>
78. Xu C, Willenbacher N. How rheological properties affect fine-line screen printing of pastes: a combined rheological and high-speed video imaging study. *J Coatings Technol Res* [Internet]. 2018; Available from: <http://link.springer.com/10.1007/s11998-018-0091-2>
79. Holmes DM, Tegeler F, Clegg WJ. Stresses and strains in colloidal films during lateral drying. *J Eur Ceram Soc*. 2008;28(7):1381–7.
80. Katsumata R, Ata S, Kuboyama K, Ougizawa T. Evaporation rate effect on starting point of shrinkage stress development during drying process in solvent cast polymer film. *J Appl Polym Sci*. 2013;128(1):60–5.
81. Druffel T, Dharmadasa R, Lavery BW, Ankireddy K. Intense pulsed light processing for photovoltaic manufacturing. *Sol Energy Mater Sol Cells*. 2018;174(1):359–69.
82. Troughton J, Carnie MJ, Davies ML. Photonic flash-annealing of lead halide perovskite solar cells in 1 ms. *J Mater Chem A*. 2016;4(1):3471–6.
83. Galagan Y, Coenen EWC, Abbel R, Lammeren TJ Van, Sabik S, Barink M, et al. Photonic sintering of inkjet printed current collecting grids for organic solar cell applications. *Org Electron* [Internet]. 2013;14(1):38–46. Available from: <http://dx.doi.org/10.1016/j.orgel.2012.10.012>

84. Amin Y, Chen Q, Zhen LR, Tenhunen H. Design and fabrication of wideband archimedean spiral antenna based ultra-low cost “green” modules for RFID sensing and wireless applications. *Prog Electromagn Res.* 2012;130(1):241–56.
85. Turki BM, Abbel R, Barbosa S, Tate DJ, Oyeka D, Batchelor JC, et al. Inkjet printed paper based frequency selective surfaces and skin mounted RFID tags : the interrelation between silver nanoparticle ink , paper. *J Mater Chem C.* 2015;3(1):2132–40.
86. Secor EB, Ahn BY, Gao TZ, Lewis JA, Hersam MC. Rapid and Versatile Photonic Annealing of Graphene Inks for Flexible Printed Electronics COMMUNICATION. *Adv Mater.* 2015;27(1):6683–8.
87. Kim H, Dhage SR, Shim D, Hahn HT. Intense pulsed light sintering of copper nanoink for printed electronics. *Appl Phys A.* 2009;97(1):791–8.
88. Arapov K, Bex G, Hendriks R, Rubingh E, Abbel R, de With G, et al. Conductivity Enhancement of Binder-Based Graphene Inks by Photonic Annealing and Subsequent Compression Rolling. *Adv Eng Mater.* 2016;18(7):1234–9.
89. Coscia U, Palomba M, Ambrosone G, Barucca G, Cabibbo M, Mengucci P, et al. A new micromechanical approach for the preparation of graphene nanoplatelets deposited on polyethylene. *Nanotechnology.* 2017;28(19).
90. Malekpour H, Chang KH, Chen JC, Lu CY, Nika DL, Novoselov KS, et al. Thermal conductivity of graphene laminate. *Nano Lett.* 2014;14(9):5155–61.
91. Huang X, Leng T, Zhang X, Chen JC, Chang KH, Geim AK, et al. Binder-free highly conductive graphene laminate for low cost printed radio frequency applications. *Appl Phys Lett.* 2015;106(20).
92. El Baradai O, Beneventi D, Alloin F, Bongiovanni R, Bruas-Reverdy N, Bultel Y, et al. Microfibrillated Cellulose Based Ink for Eco-Sustainable Screen Printed Flexible Electrodes in Lithium Ion Batteries. *J Mater Sci Technol [Internet].* 2016;32(6):566–72. Available from: <http://dx.doi.org/10.1016/j.jmst.2016.02.010>

93. Sheng Y, Fell CR, Son YK, Metz BM, Jiang J, Church BC. Effect of Calendering on Electrode Wettability in Lithium-Ion Batteries. *Front Energy Res* [Internet]. 2014;2(December):1–8. Available from: <http://journal.frontiersin.org/article/10.3389/fenrg.2014.00056/abstract>
94. Gnanaraj JS, Cohen YS, Levi MD, Aurbach D. The effect of pressure on the electroanalytical response of graphite anodes and LiCoO₂ cathodes for Li-ion batteries. 2001;516:89–102.
95. Wang C, Yi Y, Sastry AM, Shim J, Striebel KA. Particle Compression and Conductivity in Li-Ion Anodes with Graphite Additives. *J of The Electrochem Soc*. 2004;151(9):A1489–98.
96. Willenbacher N, Georgieva K, Ulrich Bröckel by, Meier W, Wagner G. Rheology of Disperse Systems [Internet]. 2013 [cited 2019 Aug 2]. Available from: https://application.wiley-vch.de/books/sample/3527332200_c01.pdf
97. Howard A. Barnes. A HANDBOOK OF ELEMENTARY RHEOLOGY. Vol. 6, Polymer Composites. The University of Wales Institute of Non-Newtonian Fluid Mechanics, Department of Mathematics, University of Wales Aberystwyth; 2000. 1–210 p.
98. Wu Y-S, Wu Y-S. Immiscible Displacement of Non-Newtonian Fluids. *Multiph Fluid Flow Porous Fract Reserv* [Internet]. 2016 Jan 1 [cited 2019 Aug 3];127–66. Available from: <https://www.sciencedirect.com/science/article/pii/B9780128038482000076>
99. Sadd MH. Chapter 6 - Constitutive relations and formulation of classical linear theories of solids and fluids. In: *Continuum Mechanics Modeling of Material Behavior*. 2019. p. 159–261.
100. AliAshter S. 6. Mechanics of materials. In: *Thermoforming of Single and Multilayer Laminates*. William Andrew Publishing; 2014. p. 123–45.
101. Meyers MA, Chawla KK. *Mechanical Behaviour of Materials* [Internet]. 2nd ed. Cambridge University Press; 2009 [cited 2019 Aug 5]. 882 p. Available from: <https://the-eye.eu/public/Books/Materials%20science%20and%20engineering/M>

304%2520Mechanical%2520behavior%2520of%2520materials/Marc%2520A
ndr%25C3%25A9%2520Meyers%252C%2520Krishan%2520Kumar%2520C
hawla-Mechanical%2520Behavior%2520of%2520Materials-Cambr

102. Haines BM, Mazzucato AL. A Proof of Einstein's Effective Viscosity for a Dilute Suspension of Spheres. *SIAM J Math Anal* [Internet]. 2012;44(3):2120–45. Available from: <http://epubs.siam.org/doi/10.1137/100810319>
103. Einstein A. Eine neue Bestimmung der Moleküldimensionen. *Ann Phys* [Internet]. 1906 Jan 1 [cited 2019 Aug 2];324(2):289–306. Available from: <http://doi.wiley.com/10.1002/andp.19063240204>
104. Mendoza CI, Santamaría-Holek I. The rheology of hard sphere suspensions at arbitrary volume fractions: An improved differential viscosity model [Internet]. 2008 [cited 2019 Aug 2]. Available from: <https://arxiv.org/pdf/0810.5111.pdf>
105. Krieger IM, Dougherty TJ. A Mechanism for Non-Newtonian Flow in Suspensions of Rigid Spheres. *Trans Soc Rheol* [Internet]. 1959 Mar [cited 2019 Aug 2];3(1):137–52. Available from: <http://sor.scitation.org/doi/10.1122/1.548848>
106. Quemada D. Rheology of concentrated disperse systems and minimum energy dissipation principle. *Rheol Acta* [Internet]. 1977 Jan [cited 2019 Aug 2];16(1):82–94. Available from: <http://link.springer.com/10.1007/BF01516932>
107. Hudson RE, Holder AJ, Hawkins KM, Williams PR, Curtis DJ. An enhanced rheometer inertia correction procedure (ERIC) for the study of gelling systems using combined motor-transducer rheometers. *Phys Fluids*. 2017;29(12).
108. Bae JE, Lee M, Cho KS, Seo KH, Kang DG. Comparison of stress-controlled and strain-controlled rheometers for large amplitude oscillatory shear. *Rheol Acta*. 2013;52(10–12):841–57.
109. Dimic-Misic K, Hummel M, Paltakari J, Sixta H, Maloney T, Gane P. From colloidal spheres to nanofibrils: Extensional flow properties of mineral

- pigment and mixtures with micro and nanofibrils under progressive double layer suppression. *J Colloid Interface Sci* [Internet]. 2015;446:31–43. Available from: <http://dx.doi.org/10.1016/j.jcis.2015.01.004>
110. Vadodaria SS, English RJ. Extensional rheometry of cellulose ether solutions: flow instability. *Cellulose*. 2016;23(1):339–55.
 111. Rodd LE, Scott TP, Cooper-White JJ, McKinley GH. Capillary break-up rheometry of low-viscosity elastic fluids. *Appl Rheol*. 2005;15(1):12–27.
 112. Anna SL, Mckinley GH. Elasto-capillary thinning and breakup of model elastic liquids. 2001 [cited 2019 Aug 6]; Available from: <http://web.mit.edu/nmf/publications/GHM49.pdf>
 113. Morgan MLC of morphological and electrical properties of flexographic printed electronics through tailored ink rheology, Curtis DJ, Deganello D. Control of morphological and electrical properties of flexographic printed electronics through tailored ink rheology. *Org Electron physics, Mater Appl*. 2019;73:212–8.
 114. BAZILEVSKY AV, ENTOV VM, ROZHKOVA AN. Liquid filament microrheometer and some of its applications. In: *Proceedings of Third European Rheology Conference and Golden Jubilee Meeting of the British Society of Rheology*. 1990. p. 41–3.
 115. Niedzwiedz K, Buggisch H, Willenbacher N. Extensional rheology of concentrated emulsions as probed by capillary breakup elongational rheometry (CaBER). *Rheol Acta*. 2010;49(11):1103–16.
 116. Tiwari MK, Bazilevsky A V., Yarin AL, Megaridis CM. Elongational and shear rheology of carbon nanotube suspensions. *Rheol Acta*. 2009;48(6):597–609.
 117. Doshi P, Basaran OA, Introduction I. Self-similar pinch-off of power law fluids. 2004;16(3):585–94.
 118. Gresty JL. Chapter 15 Surface Profilers, Multiple Wavelength, and White Light Interferometry. In: MALACARA D, editor. *Optical Shop Testing*. Hoboken, New Jersey Published: John Wiley & Sons, Inc.; 1979. p. 667–755.

119. Moroni G, Syam WP, Petrò S. A simulation method to estimate task-specific uncertainty in 3D microscopy. *Measurement* [Internet]. 2018 Jul 1 [cited 2018 Jul 9];122:402–16. Available from:
<https://www.sciencedirect.com/science/article/pii/S0263224118300320?via%3Dihub>
120. Billah A. Investigation of multiferroic and photocatalytic properties of Li doped BiFeO₃ nanoparticles prepared by ultrasonication. BANGLADESH UNIVERSITY OF ENGINEERING AND TECHNOLOGY; 2017.
121. Marturi N. Vision and visual servoing for nanomanipulation and nanocharacterization in scanning electron microscope. [Internet]. Université de Franche-Comté; 2013 [cited 2019 Jul 5]. Available from:
https://www.researchgate.net/publication/281534044_Vision_and_visual_servoing_for_nanomanipulation_and_nanocharacterization_in_scanning_electron_microscope
122. Allen JJ, Barron AR, Bott S, Bovet C, Bratt A, Chiang P-T, et al. 8.3 SEM and its applications for Polymer Science. In: Barron AR, editor. *Physical Methods in Chemistry and Nano Science*. Rice University, Houston, Texas: Connexions; 2012. p. 639–50.
123. Ghorbani MM, Taherian R. Methods of Measuring Electrical Properties of Material. In: *Electrical Conductivity in Polymer-Based Composites: Experiments, Modelling and Applications*. 2018.
124. Smits FM. Measurement of Sheet Resistivities with the Four-Point Probe. *Bell Syst Tech J* [Internet]. 1958 May [cited 2018 Jun 7];37(3):711–8. Available from:
<http://ieeexplore.ieee.org/lpdocs/epic03/wrapper.htm?arnumber=6773368>
125. Jewell EH, Barden T, Claypole TC. The effect of flat bed screen printing parameters on ink film thickness. Screen Printing Technology Group, Report no. 00-01-SPTG. Swansea; 2000.
126. Rueden CT, Schindelin J, Hiner MC, DeZonia BE, Walter AE, Arena ET, et al. ImageJ2 : ImageJ for the next generation of scientific image data. 2017;1–26.

127. Mckinley GH, Anna SL, Tripathi A, Yao M. Extensional rheometry of polymeric fluids and the uniaxial elongation of viscoelastic filaments [Internet]. 1999 [cited 2019 May 22]. Available from: <http://web.mit.edu/nnf/publications/GHMconf1.pdf>
128. Riemer DE. The Theoretical Fundamentals of the Screen Printing Process. *Microelectron Int.* 1989;6(1):8–17.
129. Kadara RO, Jenkinson N, Banks CE. Characterisation of commercially available electrochemical sensing platforms. *Sensors Actuators, B Chem.* 2009;138(2):556–62.
130. Fanjul-Bolado P, Hernández-Santos D, Lamas-Ardisana PJ, Martín-Pernía A, Costa-García A. Electrochemical characterization of screen-printed and conventional carbon paste electrodes. *Electrochim Acta.* 2008;53(10):3635–42.
131. Lee J, Arrigan DWM, Silvester DS. Mechanical polishing as an improved surface treatment for platinum screen-printed electrodes. *Sens Bio-Sensing Res* [Internet]. 2016;9:38–44. Available from: <https://doi.org/10.1016/j.sbsr.2016.05.006>